Universität Potsdam

HELMHOLTZ
SPITZENFORSCHUNG FÜR
GROSSE HERAUSFORDERUNGEN

GFZ
Helmholtz-Zentrum
POTSDAM

Innovative Technologien
für Ressourceneffizienz
Bereitstellung wirtschafts-
strategischer Rohstoffe

Constraining the Hydrology at Minas da Panasqueira W-Sn-Cu Deposit, Portugal

Kumulative Dissertation
zur Erlangung des akademischen Grades
"doctor rerum naturalium"
(Dr. rer. nat.)
in der Wissenschaftsdisziplin Geochemie

eingereicht an der
Mathematisch-Naturwissenschaftlichen Fakultät der
Universität Potsdam

vorgelegt von
Marta Sofia Ferreira Codeço
geb. in Arcos de Valdevez, Portugal
Potsdam, im Juni 2019

Datum der Disputation: 18.04.2019

Marta Sofia Ferreira Codeço: *Constraining the Hydrology at Minas da Panasqueira W-Sn-Cu deposit, Portugal*

Erster Betreuer: Priv. Doz. Dr. Philipp Weis
Zweiter Betreuer: Prof. Dr. Jörg Erzinger

Gutachter:

Priv. Doz. Dr. Philipp Weis
Deutsches GeoForschungsZentrum Potsdam GFZ, Potsdam Deutschland
Universität Potsdam, Institut für Erd- und Umweltwissenschaften, Potsdam, Deutschland

apl. Prof. Dr. Uwe Altenberger,
Universität Potsdam, Institut für Erd- und Umweltwissenschaften, Potsdam, Deutschland

Prof. Dr. Axel K. Schmitt,
Institut für Geowissenschaften, Ruprecht-Karls-Universität Heidelberg, Deutschland

https://doi.org/10.25932/publishup-42975
https://nbn-resolving.org/urn:nbn:de:kobv:517-opus4-429752

Constraining the Hydrology at Minas da Panasqueira W-Sn-Cu Deposit, Portugal

Cumulative dissertation
for the academic degree
”Doctor of Philosophy”
in the scientific discipline of Geochemistry

submitted to the
Faculty of Science of the
University of Potsdam

by
Marta Sofia Ferreira Codeço
born in Arcos de Valdevez, Portugal
Potsdam, June 2019

Defense date: 18.04.2019

Marta Sofia Ferreira Codeço: *Constraining the Hydrology at Minas da Panasqueira W-Sn-Cu deposit, Portugal*

First supervisor: Priv. Doz. Dr. Philipp Weis
Second supervisor: Prof. Dr. Jörg Erzinger

Referees:

Priv. Doz. Dr. Philipp Weis,
German Research Center for Geosciences Potsdam GFZ, Potsdam, Germany
Institute of Earth and Environmental Science, University Potsdam, Germany

apl. Prof. Dr. Uwe Altenberger,
Institute of Earth and Environmental Science, University Potsdam, Germany

Prof. Dr. Axel K. Schmitt,
Institute of Earth Sciences, Ruprecht-Karls-Universität Heidelberg, Germany

Ao meu marido e aos meus pais.

To my husband and my parents.

Declaration of Authorship

I hereby confirm, that I have authored this thesis entitled ”Constraining the Hydrology at Minas da Panasqueira W-Sn-Cu deposit, Portugal” independently and without use of others than the indicated sources. This work was accomplished during the PhD candidature at the University of Potsdam. I am aware of the University's regulations concerning plagiarism, including those regulations concerning disciplinary actions that may result from plagiarism. Any use of the works of any other author, in any form, is properly acknowledged at their point of use. I further declare that I have not submitted this thesis at any other institution in order to obtain a degree.

Signature:

M.Sc. Marta Sofia Ferreira Codeço

Date:

Abstract

This dissertation combines field and geochemical observations and analyses with numerical modeling to understand the formation of vein-hosted Sn-W ore in the Panasqueira deposit of Portugal, which is among the ten largest worldwide. The deposit is located above a granite body that is altered by magmatic-hydrothermal fluids in its upper part (greisen). These fluids are thought to be the source of metals, but that was still under debate. The goal of this study is to determine the composition and temperature of hydrothermal fluids at Panasqueira, and with that information to construct a numerical model of the hydrothermal system. The focus is on analysis of the minerals tourmaline and white mica, which formed during mineralization and are widespread throughout the deposit. Tourmaline occurs mainly in alteration zones around mineralized veins and is less abundant in the vein margins. White mica is more widespread. It is abundant in vein margins as well as alteration zones, and also occurs in the granite greisen. The laboratory work involved in-situ microanalysis of major- and trace elements in tourmaline and white mica, and boron-isotope analysis in both minerals by secondary ion mass spectrometry (SIMS).

The boron-isotope composition of tourmaline and white mica suggests a magmatic source. Comparison of hydrothermally-altered and unaltered rocks from drill cores shows that the ore metals (W, Sn, Cu, and Zn) and As, F, Li, Rb, and Cs were introduced during the alteration. Most of these elements are also enriched in tourmaline and mica, which confirms their potential value as exploration guides to Sn-W ores elsewhere.

The thermal evolution of the hydrothermal system was estimated by B-isotope exchange thermometry and the Ti-in-quartz method. Both methods yielded similar temperatures for the early hydrothermal phase: 430° to 460°C for B-isotopes and 503° ± 24°C for Ti-in-quartz. Mineral pairs from a late fault zone yield significantly lower median temperatures of 250°C . The combined results of thermometry with variations in chemical and B-isotope composition of tourmaline and mica suggest that a similar magmatic-hydrothermal fluid was active at all stages of mineralization. Mineralization in the late stage shows the same B-isotope composition as in the main stage despite a ca. 250°C cooling, which supports a multiple injection model of magmatic-hydrothermal fluids.

Two-dimensional numerical simulations of convection in a multiphase NaCl hydrothermal system were conducted: (a) in order to test a new approach (lower dimensional elements) for flow through fractures and faults and (b) in order to identify conditions for horizontal fluid flow as observed in the flat-lying veins at Panasqueira. The results show that fluid flow over an intrusion (heat and fluid source) develops a horizontal component if there is sufficient fracture connectivity. Late, steep fault zones have been identified in the deposit area, which locally contain low-temperature Zn-Pb mineralization. The model results confirm that the presence of subvertical faults with enhanced permeability play a crucial role in the ascent of magmatic fluids to the surface and the recharge of meteoric waters. Finally, our model results suggest that recharge of meteoric fluids and mixing processes may be important at later stages, while flow of magmatic fluids dominate the early stages of the hydrothermal fluid circulation.

Zusammenfassung

In dieser Dissertation werden Feldbeobachtungen und geochemische Analysen mit numerischer Modellierung kombiniert, um die Bildung von Sn-W-Cu- Mineralisation in der Erzlagerstätte Panasqueira in Portugal zu verstehen. Panasqueira gehört zu den 10 größten Sn-W Lagerstätten weltweit, sie befindet sich oberhalb eines Granitkörpers, der im oberen Bereich durch magmatisch-hydrothermale Fluide alteriert ist (Greisenbildung). Es wird postuliert, dass magmatisch Fluide die Quelle für Metalle sind, das wurde aber bislang nicht eindeutig bestätigt. Das Ziel dieser Arbeiten ist es, die Zusammensetzung und Temperatur der hydrothermalen Fluide in Panasqueira zu bestimmen und mit diesen Informationen ein numerisches Modell des hydrothermalen Systems zu erstellen. Der Schwerpunkt liegt auf der Untersuchung von Turmalin und Hellglimmer, welche bei der Mineralisation gebildet wurden und in der gesamten Lagerstätte weit verbreitet sind. Turmalin kommt hauptsächlich in Alterationszonen um die vererzten Quarzgänge vor, sowie weniger häufig im Randbereich der Gänge. Hellglimmer dagegen ist stärker verbreitet. Es kommt sowohl in Quarzgangrändern und Alterationszonen vor als auch im Greisenkörper. Die Laborarbeiten umfassten in-situ Mikroanalytik der Haupt- und Spurenelementgehalte von Turmalin und Hellglimmer sowie die Analyse der Bor-isotopen in beiden Mineralen mittels Sekundärionen-Massenspektrometrie (SIMS).

Die Bor-Isotopenzusammensetzung von Turmalin und Hellglimmer deuten auf eine magmatische Quelle hin. Der Vergleich von hydrothermal-überprägten mit unveränderten Gesteinsproben aus Bohrkernen zeigt, dass die Erzmetalle (W, Sn, Cu, Zn) sowie As, F, Li, Rb und Cs während der Alteration hinzugefügt wurden. Die meisten dieser Elemente sind

auch in Turmalin und Glimmer angereichert, womit ihre Nützlichkeit als Explorationshilfe für Sn-W-Erze in anderen Gebieten bestätigt wird.

Die thermische Entwicklung des Hydrothermalsystems wurde durch B-Isotopenaustausch-Thermometrie sowie durch die Ti-in-Quarz- Methode bestimmt. Beide Methoden ergaben für die frühe Hydrothermalphase ähnliche Temperaturen: 430° – 460°C für B-Isotope und 503° ± 24 °C für Ti-in-Quarz. Mineral Paare aus einer späten Verwerfungszone ergaben deutlich niedrigere B-Isotopentemperaturen von durchschnittlich 250°C. Die Kombination der Thermometrie mit den chemischen und B-Isotopenvariationen in Turmalin und Glimmer deutet darauf hin, dass ein ähnliches magmatisch-hydrothermales Fluid in allen Mineralisierungsstufen beteiligt war. Die Mineralisierung im späten Stadium zeigt dieselbe B-Isotopenzusammensetzung wie die Hauptphase trotz der Abkühlung um ca. 250°C, was ein Mehrfachinjektionsmodell des magmatisch-hydrothermalen Fluids unterstützt.

Zwei-dimensionale numerische Simulationen der Konvektion in einem mehrphasen NaCl System wurden durchgeführt um: a) eine neue Methode (lower dimensional elements) für hydrothermales Fließen durch Brüche und Störungszonen zu testen und b) die Voraussetzungen für die in Panasqueira dominierende horizontale Fluidbewegung in den flach liegenden Gängen zu identifizieren. Die Ergebnisse zeigen, dass Fluidströmungen immer dann eine starke horizontale Komponente haben wenn ausreichende Bruchverbindungen im Gestein vorhanden sind. Späte, steile Bruchzonen sind in der Umgebung der Lagerstätte identifiziert worden, welche lokal niedrig-temperierte Zn-Pb Mineralisierungen führen. Die Modellergebnisse bestätigen, dass das Vorhandensein subvertikaler Störungszonen mit höherer Permeabilität eine entscheidende Rolle für den Aufstieg magmatischer Fluide zur Oberfläche und das Eindringen von meteorischen Fluiden spielen. Schließlich schlagen unsere Simulationsergebnisse vor, dass das Eindringen meteorischer Fluide und Mischungsprozesse in späteren Phasen der hydrothermalen Zirkulation wichtig sind, während magmatische Fluide in frühen Phasen dominieren.

Resumo

O estudo apresentado na presente dissertação combina análises e observações campo e geoquímica (e.g. multi-elementar, mineral, isotópica) com modelação numérica por forma a compreender a evolução do sistema hidrotermal da Panasqueira e a formação dos filões sub-horizontais. O jazigo filoniano da Panasqueira, localizado em Portugal, encontra-se entre os dez maiores depósitos do tipo a nível mundial e é o maior produtor de W na União Europeia. O depósito desenvolveu-se a topo de um granito Varisco do tipo S, cuja cúpula se encontra greisenizada devido a circulação de fluidos de carácter magmato-hidrotermal. Pensa-se que estes fluidos sejam a fonte dos metais para a génese do jazigo, contudo esta questão tem constituído matéria de grande debate. Por forma, a compreender a evolução hidrotermal e construir um modelo numérico capaz de simular a hidrologia do sistema hidrotermal da Panasqueira, este trabalho envolveu a determinação da composição e temperatura dos fluidos hidrotermais. Para o efeito, este estudo concentrou-se na caracterização geoquímica e isotópica de turmalina e mica branca, as quais se formaram durante os processos iniciais de alteração hidrotermal e/ou mineralização, ocorrendo em diversos contextos. A turmalina ocorre essencialmente nos halos de alteração hidrotermal que encerram os veios mineralizados e está predominantemente associada aos estádios pré-mineralização. Em contraste, a mica branca ocorre em diversos contextos: greisen, filões (salbandas), e halos de alteração hidrotermal, estando associada quer aos estádios precoces, quer aos estádios principais de mineralização. O trabalho laboratorial envolveu análises in-situ de elementos maiores e traço em turmalina e mica, e análises isotópicas (isótopos de boro) em ambas as fases minerais através de espectrometria de massa por iões secundários (SIMS).

As composições isotópicas da turmalina e mica branca sugerem uma fonte magmática para os fluidos hidrotermais. A comparação dos dados de litogeoquímica dos metassedimentos alterados e não alterados mostra que os metais (W, Sn, Cu e Zn), assim como em As, F, Li, Rb e Cs foram introduzidos durante o processo de alteração hidrotermal. Parte substancial destes elementos encontram-se também enriquecidos na mica e turmalina, o que confirma o seu potencial valor como vectores de prospecção mineral para os depósitos de W-Sn.

A evolução térmica do sistema hidrotermal da Panasqueira foi estimada utilizando geotermómetros minerais. O geotermómetro do quartzo (Ti-in-quartz) indica temperaturas de 503° ± 24°C para a alteração precoce das rochas encaixantes, o que é consistente com as temperaturas médias de 430° a 460°C obtidas através da geotermometria isotópica de boro em turmalina e mica branca nas salbandas micáceas. As zonas de falha estudadas através da utilização de pares-minerais indicam temperaturas médias substancialmente mais baixas (250°C). A combinação dos estudos de geotermometria mineral com as variações químicas e isotópicas obtidas para a turmalina e mica sugerem que um fluido magmático-hidrotermal relativamente homogéneo esteve activo durante todos os estádios de mineralização. Durante estádios tardios, a os fluidos mineralizantes possuem as mesmas composições isotópicas obtidas para os estádios principais, embora que registando um arrefecimento de ca. 250°C, o que suporta um modelo dinâmico com múltiplas injecções de fluidos magmático-hidrotermais.

Simulações numéricas bidimensionais da convecção num sistema hidrotermal multifásico salino foram conduzidas: (i) para testar uma nova metodologia ("lower dimensional elements") capaz de traduzir o fluxo de fluidos através de fracturas e falhas e, (ii) para identificar as condições do fluxo horizontal observado nos filões sub-horizontais da Panasqueira. Os resultados mostram que o escoamento dos fluidos em associação com uma intrusão (fonte de calor e fluidos) desenvolve uma componente horizontal, desde que haja conectividade suficiente. Falhas tardias inclinadas identificadas na área contem localmente mineralização de Zn e Pb de baixa temperatura. Os resultados dos modelos numéricos confirmam que a presença de falhas sub-verticais de permeabilidade acrescida tem um papel crucial na ascensão de fluidos magmáticos até a superfície e na infiltração de águas meteóricas. Por fim, os resultados das simulações sugerem que a infiltração de águas meteóricas e processos de mistura de fluidos possam ser importantes durantes os estádios tardios, enquanto os fluidos de carácter magmático dominam os estádios iniciais da circulação hidrotermal dos fluidos.

Contents

List of Figures

List of Tables

Acknowledgments

This thesis is part of the project ”GRAMME” Granites, Models and Metals (033R149) under the ”r4 – Innovative Technologies for Resource Efficiency – Research for the Supply of Strategic Raw Materials” – *”r4 – Innovative Technologien für Ressourceneffizienz – Forschung zur Bereitstellung wirtschaftsstrategischer Rohstoffe”* funding measure. The project was financially supported by funding from the German Federal Ministry of Education – *Bundesministerium für Bildung und Forschung* (BMBF) granted to PD Dr. Philipp Weis.

I am indebted to PD Dr. Philipp Weis and Dr. Robert B. Trumbull for providing me with the opportunity to pursue my doctoral studies and for supporting me throughout its duration in the form of stimulating discussion and scientific and often personal guidance. Additionally, I am thankful for their support and encouragement towards the continuation of my career in academic research and involvement in other projects. I would like to express my sincere gratitude to Prof. Dr. Vincent van Hinsberg for providing his lab for the LA-ICP-MS analyses and hospitality during my stay in Montreal. I am also deeply grateful for his support of in providing discussion and inspiration, as well as in sharing with me his expertise and scientific methods. Pilar Lecumberri-Sanchez is acknowledged for her many contributions, from the conceptualization, to the many discussions undertaken during the course of this study.

I would like to thank Beralt Tin & Wolfram (Portugal) S.A. for the logistical support over two field seasons, not only by making personnel available to accompany me on the descent to the mine but also by providing maps, all necessary equipment, accommodation,

etc. A special thanks go the Mine Geologist, Filipe Pinto, for the continuous support over these 3,5 years. I also thank all nice people that helped me during my stays at Barroca Grande and Cabeço do Peão, never forgetting the delicious meals served in the Restaurant ”O Gasómetro”.

Many staff members at the GFZ Potsdam, University of Potsdam and University McGill contributed to the work presented in this thesis. I thank Elke Lewerenz and Uwe Dittmann for the many thin sections prepared during the course of this project. I am also grateful to Franziska D.H. Wilke and Onna Appelt for their help with the electron microprobe and Frédéric Couffignal, Michael Wiedenbeck, Alex Rocholl and Ziliang Jin for the assistance in the SIMS analyses. I am thankful for the help of Hartmut Liep and Frank Rosendahl in sample preparation; Anja Maria Schleicher, Andrea Gottsche and Heike Rothe for performing the XRF and ICP-MS analyses; and Uwe Altenberger, Melanie Lorenz and Ilona Schäpan for the SEM imaging. I further would like to thank Prof. Dr. Rolf Romer, Johannes Glodny and Bettina Hübner for the MC-IPC-MS analyses of the reference material that allowed the publication of the second article in this thesis. I am grateful to Dr. Bernd Wunder for the encouragement and help during the preparation of the second manuscript. I further acknowledge Dr. Kirsten Elger for all support provided during the preparation of the Data Publication. I am grateful to Anna Jung and Vincent van Hinsberg for teaching me how to run the LA-ICP-MS and all assistance during the measurements.

Special thanks goes to the 3.1 GFZ Section’s secretary Julia Fechner and Frauke Stobbe (Welcome Center) for helping on most of the administrative issues and personal support (housing, insurances, contracts, etc.) especially when it involves the German language, which have been very helpful and kind all the times when I needed. I also acknowledge Katja Heeschen for the many conversations, for the advice and the words of encouragement. I would like to express my deepest and sincere gratitude to my project and PhD colleague Maximiliam Korges (and his lovely fiancée Lydia), who helped me from the first day that I arrived in Germany. I am grateful to Christine Andersen for the

help with the numerical simulations and the words of encouragement.

Last, but most certainly not least, this doctoral program would not have been as enjoyable, or arguably possible, without the ongoing encouragement of my mentors, friends and family. In particular, I would like to thank Prof. António Mateus for his continued mentorship and support in multiple facets of my life. I also would like to thank Filipa Luz for all the advice, encouragement, scientific discussions and friendship. I thank my dear best friend Erica Godinho for being always there for me in all moments of my life. I also thank Edgar Murphy (and Erica) for the relaxing afternoons/evenings playing Fortnite and for the many idiotic conversations that made me laugh for hours. A special acknowledgment goes to my parents that made my jump to Germany possible and that always supported my decisions. Obrigada pai e mãe por tudo o que tendes feito por mim, por todos os esforços e por todas as palavras de encorajamento; obrigada por teres tornado possível eu mudar para a Alemanha e prosseguir como meu doutoramento. I also thank all the other members of my family for the support, especially aunt Cristina and my cousins Carina and Madalena for being always ready for helping. Finally, I would like to thank Ricardo Barros Codeço for cheerfully taking care of everything during my long nights writing this thesis. Also for trying to dress the skin of a Geologist to discuss Geology with me; for responding with enthusiasm when I decided to move to Germany and leave his entire life behind and joining me: I think all the words in the world are not enough to describe how grateful I am for everything.

To everyone who had a positive impact on my doctoral experience, including those I have not directly mentioned: *Thank you!*

List of Publications

The contents of this doctoral thesis listed below, have been published, accepted or are being prepared for publication in peer-reviewed journals:

[1] **Chapter 3**: Codeço, M.S.; Weis, P.; Trumbull, R.B.; Pinto, F.; Lecumberri-Sanchez, P. (2017). Chemical and boron isotopic composition of hydrothermal tourmaline from the Panasqueira W-Sn-Cu deposit, Portugal. Chemical Geology 468C: 1–16. doi: `https://doi.org/10.1016/j.chemgeo.2017.07.011`

[2] **Chapter 4**: Codeço, M.S.; Weis, P.; Trumbull, R.B.; Glodny, J.; Wiedenbeck, M.; Romer, R.L. (2019). Boron-isotope muscovite-tourmaline geothermometry indicates fluid cooling during magmatic-hydrothermal W-Sn-ore formation. Economic Geology 114(1), 153–163. doi: `https://doi.org/10.5382/econgeo.2019.4625`

[3] **Chapter 5**: Codeço, M.S.; Weis, P.; Trumbull, R.B.; van Hinsberg, V.; Pinto, F.; Lecumberri-Sanchez, P.; Schleicher, A.M. (submitted to *Geochimica et Cosmochimica Acta*). The chemical footprint of the Panasqueira W-Sn-Cu deposit (Portugal), and thei value of white mica and tourmaline as pathfinders

Codeço, Marta. S.; Weis, Philipp; Trumbull, Robert B.; van Hinsberg, Vincent; Pinto, Filipe; Lecumberri-Sanchez, Pilar; Schleicher, Anja Maria (2019): Trace elements in white mica and tourmaline from the Panasqueira W-Sn-Cu deposit (Portugal). GFZ Data Services. doi: `http://doi.org/10.5880/GFZ.3.1.2019.001`

[4] **Chapter 6**: Codeço, M.S.; Weis, P.; Anderson, C. (in preparation for *Geochemistry, Geophysics, Geosystems*). Numerical simulations of the fluid flow patterns in the Panasqueira W-Sn-Cu deposit

In addition to above mentioned, I was also involved in the preparation of following publication, to which I contributed with data reduction, discussion and editing :

[1] Trumbull, R.B., Garda, G.M., Xavier, R.P., Cavalcanti, J.A.D., Codeço, M.S. (2019). Tourmaline in the Passagem de Mariana gold deposit (Brazil) revisited: in-situ boron isotope and trace element compositions. Mineralium Deposita 54(3):395-414. doi: `https://doi.org/10.1007/s00126-018-0819-z`

Presentations

Some of the results obtained during the development of this doctoral study have been exposed as posters or oral presentations in several national and international scientific meetings. The contributions are listed below:

[1] Codeço, M.S.; Trumbull, R.B.; Weis, P.; Pinto, F.; Lecumberri-Sanchez, P. (2017). Hydrothermal tourmaline from the Panasqueira W-Sn-Cu deposit, Portugal: chemical and B-isotope constraints on fluid source and evolution. Tourmaline 2017 International Symposium, Skalský Dvůr, Czech Republic, 23-25.

[2] Codeço, M.S.; Weis, P.; Trumbull, R.B.; Pinto, F.; Lecumberri-Sanchez, P. (2017). Fluid sources of the Panasqueira W-Sn-Cu Deposit (Portugal): evidence from chemical and boron isotopic compositions of tourmaline. Goldschmidt 2017, Paris, France.

[3] Codeço, M.S.; Weis, P.; Trumbull, R.B.; Pinto, F.; Lecumberri-Sanchez, P. (2017). Chemical and $\delta^{11}B$ compositions of tourmaline from the Panasqueira W-Sn-Cu deposit, Portugal: considerations on fluid source and evolution. GeoBremen 2017, Bremen, Germany.

[4] Codeço, M.S.; Weis, P.; Trumbull, R.B.; van Hinsberg, V; Pinto, F.; Lecumberri-Sanchez, P. (2018). Early ore-forming fluids at the world-class Panasqueira W-Sn-Cu deposit (Portugal). Insights from in situ micro-analytical techniques. EGU Vienna 2018, Vienna, Austria.

[5] Codeço, M.S.; Weis, P.; Trumbull, R.B.; van Hinsberg, V; Pinto, F.; Lecumberri-Sanchez, P. (2018). Using geochemistry and B-isotopes of hydrothermal tourmaline and mica to trace metals and fluid sources in the world-class class Panasqueira W-Sn-Cu deposit (Portugal). SEG Keystone 2018, Colorado, USA.

In addition, the contents of this doctoral thesis have been presented at the following invited talks and seminars:

June 16, 2017

Universität Potsdam

Title: "Fluid sources of the Panasqueira W-Sn-Cu deposit (Portugal): evidence from chemical and boron isotopic compositions of tourmaline"

MinPet Seminar

November 15, 2017

Helmholtz Centre Potsdam - GFZ German Research Centre for Geosciences

Title: "In-situ boron isotope studies of tourmaline by SIMS. An application to the Panasqueira W-Sn-Cu deposit (Portugal)"

Invited by: Dr. Michael Wiedenbeck for the Short SIMS course 2017

November 29, 2017

McGill University

Title: "Fluid sources of the Panasqueira W-Sn-Cu Deposit (Portugal). Insights from chemical and boron isotopic compositions of hydrothermal tourmaline"

Invited by: Prof. Dr. Vincent Van Hinsberg

"Wisdom must be intuitive reason combined
with scientific knowledge.

–Aristotle, Nicomachean Ethics, VI.7

1

Introduction

1.1 Preamble

Minerals are fundamental for economic advancement, for the functioning of society and for sustaining the XXI century human lifestyle, and it is the necessity or desire for a given product that generates demand for a particular mineral or minerals. Metallic ore deposits constitute the most significant geochemical anomalies within Earth's crust. The study of the geochemistry of ore deposits is essential for (i) understanding the ore formation, (ii) mineral deposit classification, (iii) extractive metallurgy or mineral processing and (iv) geoenvironmental studies (Carranza, 2012). The combination of high-resolution geochemistry (mineral chemistry and stable isotopes), whole-rock chemistry, and numerical simulations constitute powerful tools to constrain the origin and flow paths of the hydrothermal fluids that generate mineral deposits. This thesis focuses on the study of the geochemistry of gangue minerals associated with the formation of tin and tungsten ores from the Panasqueira deposit (Portugal). The following sections present a summary of the economical relevance of W and Sn and a short overview of W-Sn deposits and numerical modeling of hydrothermal systems.

1.2 Economic importance of the W and Sn commodities

The abundance of metals in the crust varies greatly and affects the costs involved in locating, mining and preparing the metals for use (Graedel et al., 2013). The ability of mineral deposits to satisfy future demand has been widely debated, with several authors having concluded that metal scarcity and, ultimately depletion may occur over a relatively short timescale of a few decades and are unpreventable (Cohen, 2007; Ragnarsdóttir, 2008). These predictions are grounded on the estimation of resources and/or reserves divided by present or expected demand and consequently fail to recognize that reserves are both poorly-known and adjustable (Cohen, 2007; Gilbert, 2009; Graedel et al., 2013; Sverdrup and Robert, 2009). Furthermore, reserves strongly depend on scientific advances and the price of metals or minerals. The scientific knowledge has a significant influence on the definition of reserves, which are continuously replenished through new discoveries, by developments in mining and processing technology or by improved access to the deposits (Graedel et al., 2013). Hence, market mechanisms are a central control in overcoming supply shortages. Rising metal prices result in the inclusion of low-grade ore in the reserves but also motivates increased substitution, recycling, and resource efficiency, and consequently improved supply security (Graedel et al., 2013).

Metals are critical for our modern society, and without continued technological development for mineral exploration, processing, and manufacturing, we could not benefit from a panoply of products, such as airplanes, computers, mobile phones, and other trending portable personal electronic devices. Nonetheless, the concept of metal criticality is complex and depends on its physical and chemical properties, as well as on several factors influencing its supply and demand (Graedel et al., 2013). An important step to define metal criticality in Europe was initiated by the European Commission (EC) in 2009 (European Commission, 2013). The ad-hoc working group defined metal criticality based on the supply risk and the potential economic impact of supply disruption in the European industry (Figure 1.1). The supply risk includes the political stability of the producing countries, the potential to substitute the metal and the extent to which metals can be recycled (European Commission, 2013; Graedel et al., 2013). A total of twenty critical raw materials (thirteen metals and seven non-metals) were identified as critical from a list of fifty-four candidates (European Commission, 2013, 2014). In 2017 the European Union (EU) reevaluated a new list of sixty-one materials and produced the third list of critical raw materials. The new list includes nine more materials than the 2014 list: barite, bismuth, hafnium, helium, natural rubber, phosphorus, scandium, tantalum, and vanadium (Figure 1.2) (European Commission, 2017).

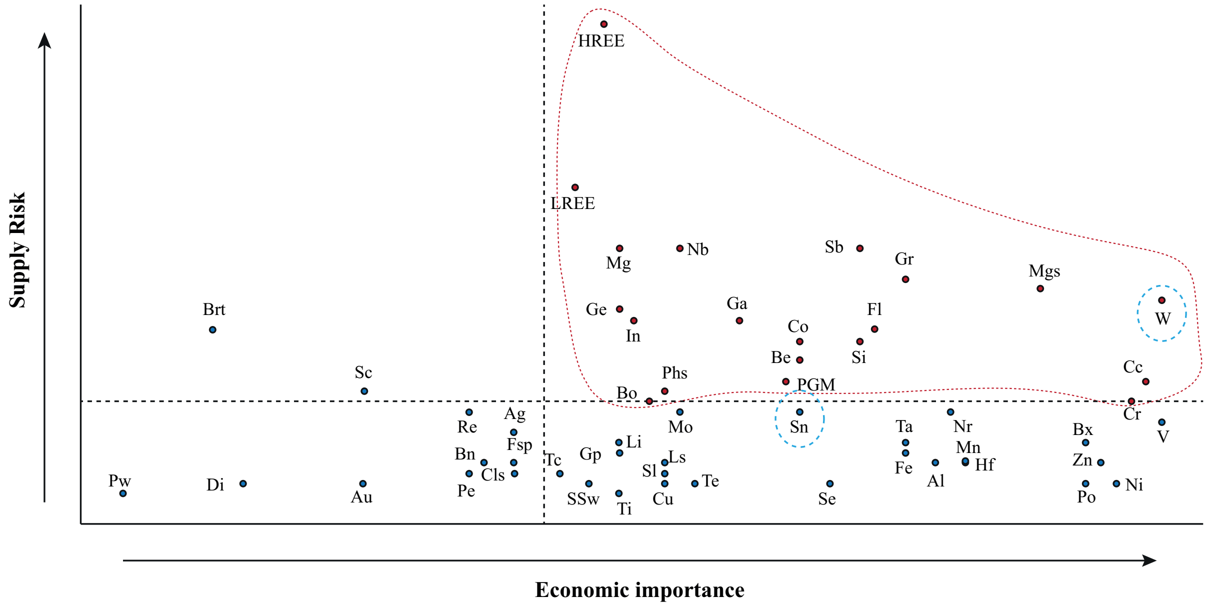

Figure 1.1: Criticality metals matrix of the European Commission (2014). The horizontal axis reflects the economic impact of supply restriction on a broad group of European industries and the vertical axis the supply risk. The metals falling within the top-right cluster are regarded as critical to the European Union (modified from European Commission, 2014). Agg: Aggregate, Brt: Baryte, Bx: Bauxite, Bn: Bentonite, Bo: Borate, Cls: Clays, c: Coking coal, Di: Diatomite, Fsp: Feldspar, Fl: Fluorspar, Gp: Gypsum, Kc: Kaolin clay, Ls: Limestone, Mgs: Magnesite, NC: Natural cork, Gr: Natural graphite, Nr: Natural rubber, Nt: Natural teak wood.

Tungsten is part of the critical raw materials list as defined by the EC, and it is one of the metals with the most significant economic importance to the European industry. W is used in a wide range of industrial applications: (1) manufacturing of cemented carbides (58%) for the metal-working, mining and petroleum industries; (2) production of special steel and other alloys (23%), such as high-speed, heat-resistant and tool steels, widely used

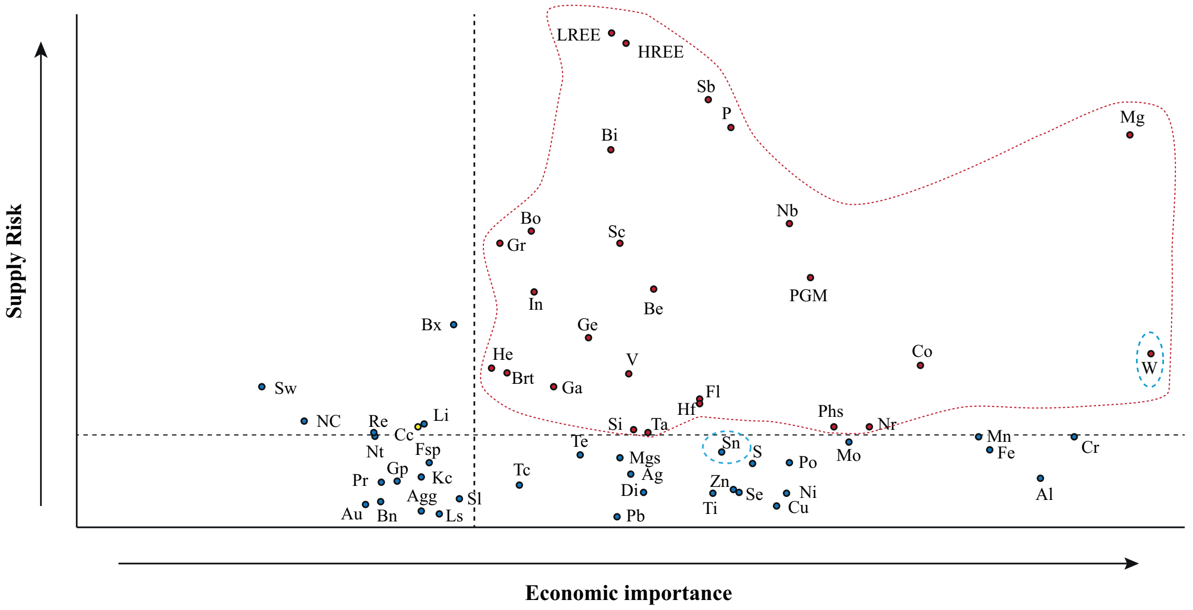

Figure 1.2: Criticality metals matrix of the European Commission (2017). The horizontal axis reflects the economic impact of supply restriction on a broad group of European industries and the vertical axis the supply risk. The metals falling within the top-right cluster are regarded as critical to the European Union (modified from European Commission, 2017). Agg: Aggregate, Brt: Baryte, Bx: Bauxite, Bn: Bentonite, Bo: Borate, Cls: Clays, c: Coking coal, Di: Diatomite, Fsp: Feldspar, Fl: Fluorspar, Gp: Gypsum, Kc: Kaolin clay, Ls: Limestone, Mgs: Magnesite, NC: Natural cork, Gr: Natural graphite, Nr: Natural rubber, Nt: Natural teak wood.

in metal cutting and specialized engineering applications where hardness and strength are required; and, (3) "mill products", i.e. tungsten wire, sheets or rods for electrical and electronic applications (8%). Tungsten can also be used as a catalyst, pigment, or reagent for chemical analyses (9%) (Wolf Minerals, 2012 in Brown and Pitfield, 2013). Demand for tungsten has increased by an annual average of 5.8% since 2003, driven by high economic growth in Asia, the Commonwealth of Independent States (CIS) and other emerging markets (Marten & Co, 2016). According to Roskill Information Services, in 2013 the world demand for tungsten was 93,000 t (tons), rising to over 105,000 t by 2018 (Figure 1.3). Similarly, although a little more conservative, Argus Media forecasts global demand for tungsten growing up to approximately 99,000 t by 2020 (Marten & Co, 2016). China represents the world's largest consumer of W with approximately half of total world consumption, followed by Europe (ca. 20%), North America (ca. 17%) and Japan (ca. 5%) (Figure 1.3). On top of that, China represents the dominant player on the production side, accounting for over 80% of world production in 2013 (Figure 1.4). Other significant producers are Russia, Austria, Bolivia, Portugal, and Vietnam. However, W production in Europe remains minor and is not sufficient to supply the European industry, whose annual W importation increases every year (Figure 1.4).

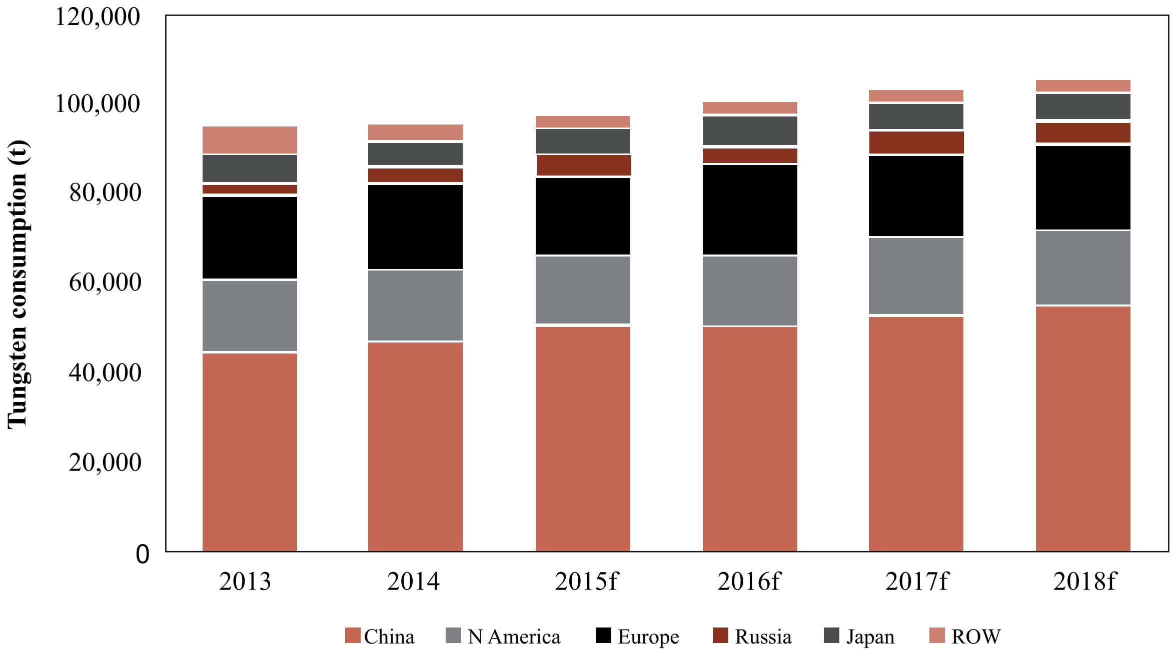

Figure 1.3: Actual and forecast tungsten consumption (t). Source: Roskill Information Services (adapted from Marten & Co, 2016). ROW – rest of world.

Secondary supply from recycling is believed by market analysts to have reached a ceiling of about 50% (Marten & Co, 2016), which is, however, far from being able to sustain the European demand. In this scenario, it is critical for Europe to discover new deposits as well as to invest in the re-evaluation of former deposits. Except for Mittersill (Austria) and Panasqueira (Portugal), tungsten production practically ceased in Europe for more than 25 years. Recently, new exploration projects were started in Spain (Los Santos, Valtreixal, Morille, La Parilla and Barruecopardo), Portugal (Covas, Borralha, Bejanca, Vale das Gatas, Regua and Tarouca), France (Loc Envel, Couflens, Merlac) and England (Redmoor, Drakelands), showing that Europe is investing once again in the mining industry.

Contrary to tungsten, **tin** has a lower economic importance and critical supply risk for Europe,but it is still part of the critical list of the EU (Figure 1.1 and 1.2). Tin is a fairly resistant metal to corrosion, durable and malleable. It is for example used

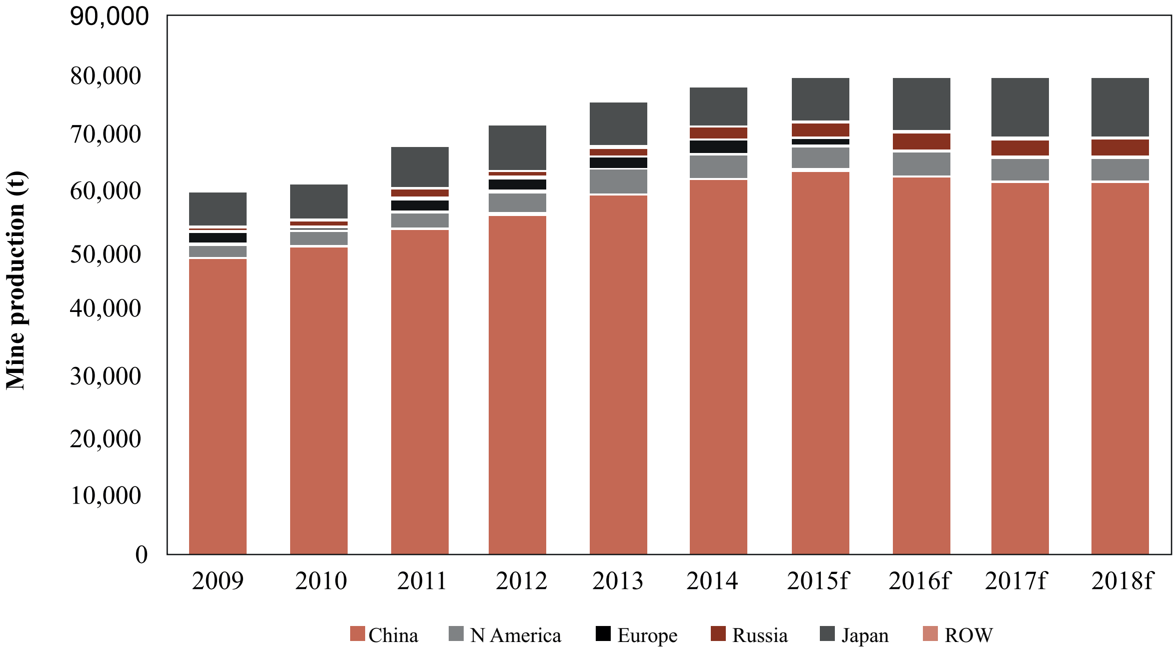

Figure 1.4: Tungsten mine production: historical, actual-estimated (e) and forecast (f). Source: Roskill Information Services (adapted from Marten & Co, 2016). ROW – rest of world.

to coat harder metals (*e.g.*, iron and steel) to prevent corrosion (*e.g.*, tin cans) and as an alloy with other metals (*e.g.*, tin-copper alloys to produce bronze, soft solder, pewter, phosphor bronze). Tin is an indispensable ingredient in a variety of industrial sectors (*e.g.*, consumer goods, packaging, construction, vehicles). Therefore, the main uses include

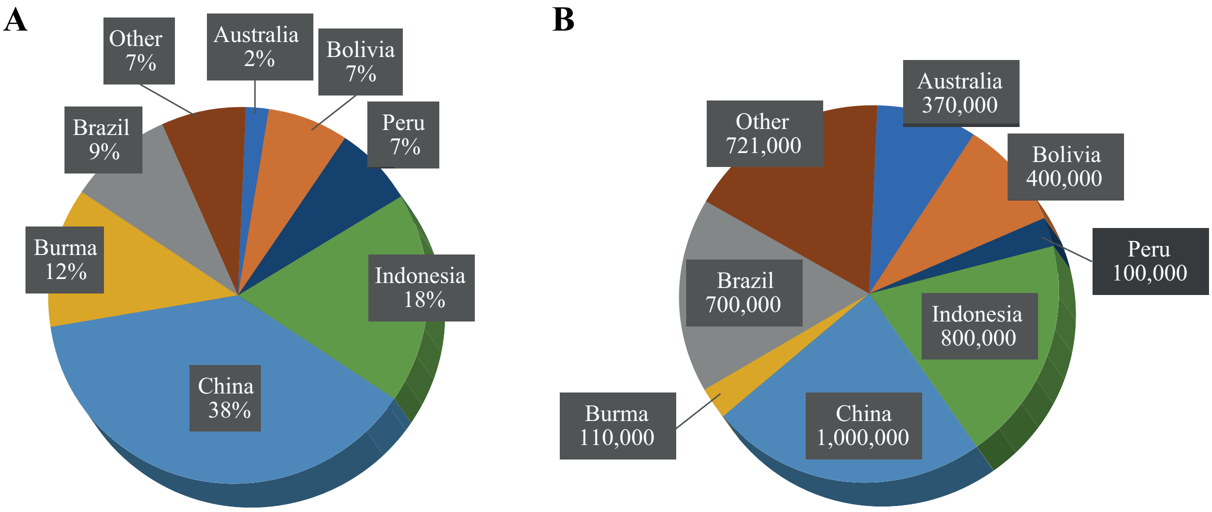

Figure 1.5: **(a)** World mine tin production (in 2015) and **(b)** reserves [in t (tons)]. Source: US Geological Survey (2017).

solder (47%), chemicals (18%), tinplate (14%), lead acid batteries (8%), and copper alloys (5%). Other applications (8%) include tin and bronze powders, wine capsules, pewter, tin coatings, and float glass (ITA, 2018). The demand for tin runs at roughly 340,000 t per year, with China as a major consumer (147,000 t), followed by the USA (30,000 t) and Japan (25,500 t) (DonkeyStock, 2017). According to reports from the United States Geological Survey (USGS), China is the world's leading tin producer (2015) with 38%. Indonesia and Burma emerge as second (18%) and third (12%), respectively (Figure 1.5a). South American countries account together for 23% of the tin produced in the world (US Geological Survey, 2017). There is hardly any tin production in the EU, except for limited quantities in Portugal (69 t, 2016) (Wheeler, 2016), but there is great potential for future mining [*e.g.*, Gottesburg (112,407 t), Hammerlein-Tellerhäuser (101,660 t), Oropesa (69,100 t) (ITRI, 2016)]. China has the largest Sn reserves as well, followed by Indonesia and Brazil (Figure 1.5b).

Tin is recycled back to pure tin ingots, and in the form of tin-based alloys, however, no firm data exists on the quantities of tin recycled per year worldwide. According to USGS, the recycling rate in the USA was 30%, i.e., about 12,000 t of tin recovered both from new and old scrap (US Geological Survey, 2017).

1.3 Tin-tungsten ore deposits

Tungsten and tin deposits usually occur within, or near to, orogenic belts and result from subduction-related plate tectonics. All major deposit types are associated with granitic intrusions (Figure 1.6) or with medium-to high-grade metamorphic rocks (Romer and Kroner, 2016, and references therein). Granite emplacement typically has an orogenic to post-orogenic timing, in some cases localized along deep fault systems that can coincide with major metamorphic and tectonic boundaries (Hart, 2007). Also, different types of W-Sn primary deposits depend on the evolution of the associated magma, depth of the intrusion, country rocks, structural control, and nature and evolution of the hydrothermal fluids (*e.g.*, Audétat et al., 2000; Heinrich, 1990; Jackson et al., 2000; Linnen, 1998; Sanderson et al., 2008). Tin and/or tungsten are generally related to highly fractionated I-type or S-type granites with distinctive trace element signatures commonly showing pronounced enrichments in Sn, W, Be, Cs, F, B, Li, Rb, Ta, and U and a marked depletion in Fe, Ti, Mg, Ca, Sr, Eu, Ba, and Zr (*e.g.*, Bouchot et al., 2005; Breiter et al., 2005; Förster et al., 1999; Lehmann, 1990*b*; Stussi, 1989). These geochemical signatures are mainly favored by high-temperature and high-degree of melting that will mobilize the rare metals into the melt. In contrast, extreme fractional crystallization will enrich the melts in those elements (Romer and Kroner, 2016, and references therein). High-temperature melting of W-Sn enriched-source rocks may be favored not only by the mobilization of rare metals but also the inheritance of geochemical fingerprints from these source rocks (*e.g.*, Lehmann, 1987; Romer and Kroner, 2016). Thus, melting a Sn-W-enriched source increases the potential for W and/or Sn deposits to form, where the enriched source controls the spatial distribution, and the magmatic processes control whether the deposit eventually forms (Romer and Kroner, 2016). Consequently, the formation of such type of deposits results from a sequence of processes, including: (i) source enrichment, (ii) source accumulation and (iii) metal extraction from the source rocks, followed by metal concentration via fractional crystallization and late-stage fluid-controlled processes (Romer and Kroner, 2016, 2015).

During the crystallization of a granitic magma, water saturation increases, resulting in the exsolution of a distinct aqueous fluid, that rises and concentrates at the roof or shell of the magma chamber (Figure 1.7A) (*e.g.*, Robb, 2005). At shallow levels, when

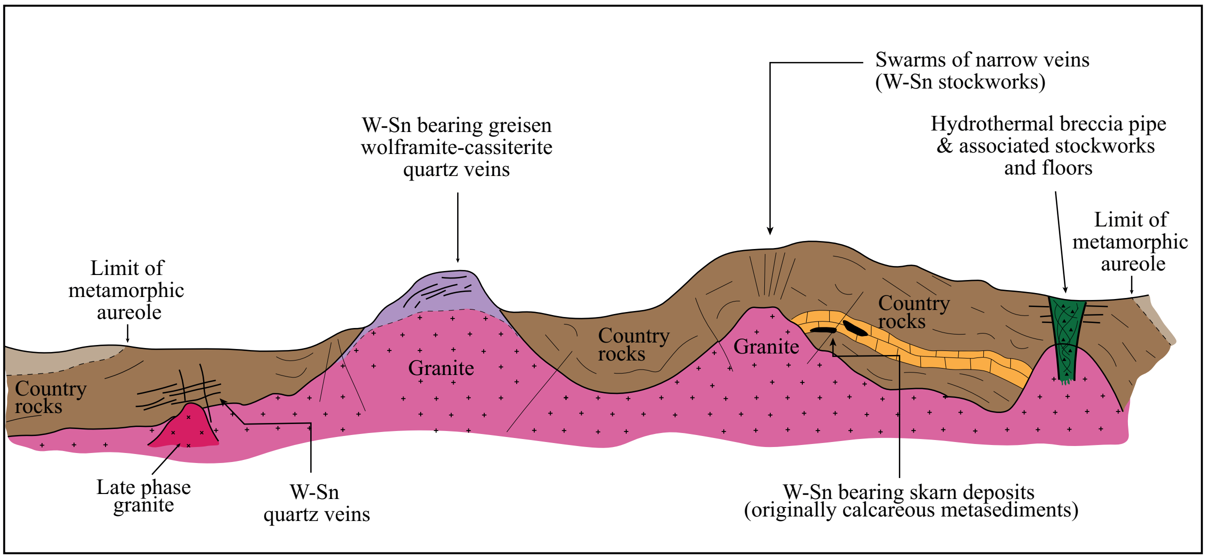

Figure 1.6: Main W-Sn deposit types (adapted from Hosking 1969 *in* Taylor 1979).

vapor pressure equals the load pressure on the magmatic system, vapor saturation can occur due to pressure drop. The volume change accompanying the water fluid production reaches up to 30% (at P = 1 kbar), resulting in the overpressure of the chamber interior and causing brittle failure of the sounding rocks (hydrofracturing) (Figure 1.7B) and providing excellent ground preparation for the efficient circulation of ore-bearing fluids (Robb, 2005). In reduced S-type granites, most lithophile elements (*e.g.*, W, Sn, Rb, Ta, Li, B, F, Be) behave as incompatible and as a consequence are concentrated in the residual melt by fractional crystallization and are exsolved during later stages (*e.g.*, Robb, 2005). In many cases, the percolation of such hot fluids through fractured media leads to the formation of potentially mineralized quartz-veins (Figure 1.7B), which are filled by successive pulses of magmatic-hydrothermal fluids.

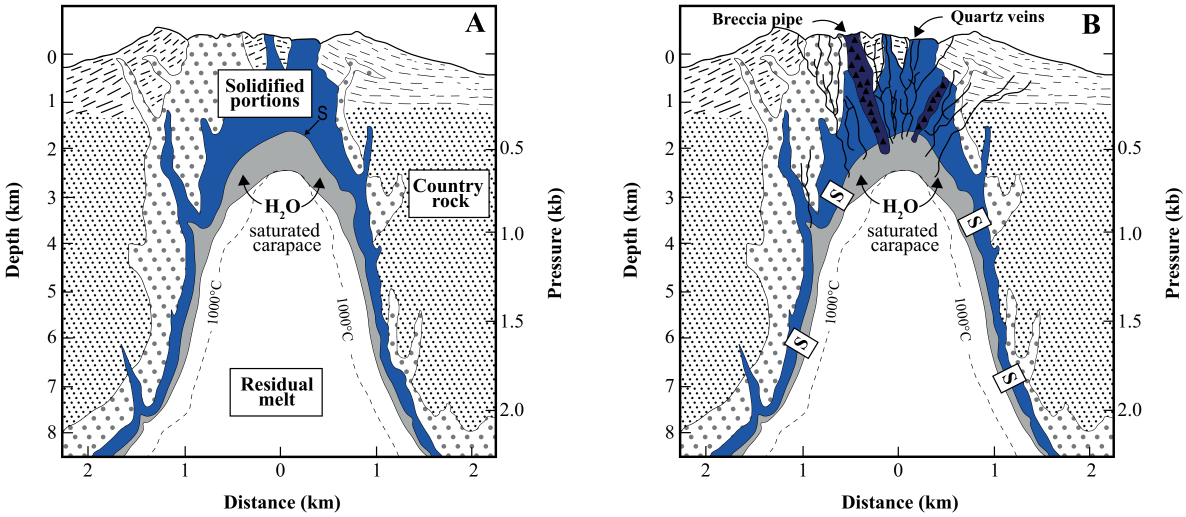

Figure 1.7: Section through a high-level granitic intrusion **(A)** undergoing progressive crystallization and showing the hypothetical H_2O-saturated granite solidus line (S) and the zone of aqueous fluid saturation (in light grey) and **(B)** showing the nature of hydrofracturing and breccia pipe formation that can form around the apical portion of the granite body (after Burnham, 1997; Lehmann, 1990*a*)

The style of mineralization in these deposits varies from disseminated ores in highly fractioned granites to pegmatites, swarms of veins/lodes and stockworks within the granites, greisen and/or country rocks (Figure 1.6) (*e.g.*, Štemprok, 1980; Romer and Kroner, 2016; Sinclair, 1996). Classically, lode-type deposits include wolframite and cassiterite, as well as scheelite, molybdenite, bismuthinite, chalcopyrite, sphalerite, galena, tetrahedrite, pyrite, arsenopyrite, and native bismuth in variable amounts. These can also include U-

Pb-REE oxides and phosphates. Gangue minerals encompass fluorite, muscovite, biotite, feldspar, beryl, tourmaline, topaz, apatite and chlorite (*e.g.,* Cox and Bagby, 1986; Hosking, 1969; Kelly and Rye, 1979). Greisen-type deposits primarily consist of cassiterite (disseminated, veinlets, stockwork, lenses, breccia and/or pipes) precipitated together with minerals resulting from the greisenization process (*e.g.*, quartz, mica, fluorite, and topaz). Arsenopyrite constitutes an important accessory phase (*e.g.,* Cox and Bagby, 1986). As a general rule for these deposits, the oxides correspond to the high-temperature paragenesis phase, followed by a lower-temperature sulfide stage. The alteration processes usually affect the host rocks and include greisenization, albitization and/or tourmalinization. Minor argillic, potassic and propylitic alteration, silicification and hematitization can also be found (*e.g.,* Cox and Bagby, 1986).

In Western Europe, W and Sn metallogenic provinces are bound to the European Variscan Belt, particularly, the Iberian Massif, French Massif Central, Armorican Massif, Cornwall, and Bohemian Massif (Derré, 1982). The metallogenic province contains many quartz-cassiterite and quartz-wolframite ores associated with highly evolved Variscan S-type granites and to a lesser extent, I-type granites, which consist of granite/greisen-hosted or metasedimentary-hosted mineralization in close association with granitic cupolas. Breccia pipe-type (*e.g.,* Breiter et al., 1999; Gonçalves et al., 2018a; Harlaux et al., 2015), and skarn deposits are also recognized (*e.g.,* Cheilletz et al., 2005; Gomes, 2016; Lefebvre et al., 2019; Ramos et al., 2017; Spruzeniece et al., 2018).

1.4 Numerical modeling of magmatic-hydrothermal deposits

The formation of magmatic-hydrothermal and hydrothermal deposits results from the interaction of several structural, hydrological, thermal and geochemical processes (*e.g.*, Hobbs et al., 2000; Oliver and Bons, 2001; Zhang et al., 2008). Spatial and temporal scales exceed those that are experimentally accessible and PTX conditions are challenging to deal with (*e.g.*, Emmanuel and Berkowitz, 2006; Menand et al., 2003). Thus, numerical simulations can play an essential role in clarifying the dynamic controls and behavior of magmatic-hydrothermal systems by testing different hypothesis and scenarios in such complex systems. Nonetheless, those numerical simulations deal with several assumptions and have many limitations. Thus, extensive knowledge of the system of interest is crucial.

There are numerous existing multiphase simulators, with TOUGH2 and FEHM being widely used and adapted to a variety of applications and HYDROTHERM remaining as a hydrothermal modeling research tool (see reviews by Ingebritsen et al., 2010). Other models, such as PFC2D, PANDAS, FLAC2D, and FLAC3D were also employed to simulate fault systems, geothermal systems and ore-forming processes (*e.g.*, Liu et al., 2015; Zhang et al., 2011, 2008). Nonetheless, archiving full coupling of all four processes in numerical models remains a computational challenge. On the other hand, most simulators are still of limited applicability to magmatic-hydrothermal systems, either because they are restricted to fluid properties of pure water, or temperatures below 350 °C (see Ingebritsen et al., 2010; Weis et al., 2014). Efforts have been instigated to overcome such limitations. Two more recently developed codes, Complex Systems Modeling Platform (CSMP++) and Fully Implicit Seafloor Hydrothermal Event Simulator (FISHES), can simulate high-temperature multiphase flow of NaCl-H_2O fluids and mass and heat transport in porous media (*e.g.*, Coumou et al., 2008*a*,*b*; Geiger et al., 2006*a*,*b*; Lewis and Lowell, 2009*a*,*b*; Matthäi et al., 2007; Weis et al., 2014). In the last decade, several studies attempted to model the physical hydrology (*e.g.*, Fekete et al., 2018; Schardt et al., 2005; Schardt and Large, 2009; Weis, 2015; Weis et al., 2014, 2012) and structural processes (Li et al., 2015; Liu et al., 2014; Zhang et al., 2011) of fossil ore deposits.

1.5 Aim and significance of the thesis

Panasqueira is a W-Sn-Cu lode-type deposit located in the Central Iberian Zone of Portugal, where several mines have been producing during the 20th century (*e.g.*, Borralha, Carris, Murçós, Segura). Nowadays, Panasqueira is the only active tungsten mine in Portugal, the main tungsten producer in Europe and the 9th worldwide (Wheeler, 2016). The deposit has been the subject of many geological, mineralogical, geochemical and structural studies for more than half a century. Nonetheless, many questions remain open. Those questions include not only the genetic link between the mineralization and the opening of the horizontal swarm of veins but also the origin and source of metals and the temporal evolution of the hydrothermal system. Furthermore, the physical flow processes that lead to the enrichment of metals such as W, Sn, Cu, Zn and Pb at Panasqueira are poorly understood. The understanding of the interplay between the hydrothermal circulation of metal-rich solutions and rock mechanics is of critical importance to comprehend the processes operating in ore deposits. The permeability of the rock largely determines the flow regime of hydrothermal fluids; the configuration and large number of veins and pathways in hydrothermal ore deposits, show that hot fluids flow through fractures, fissures and faults, and seal them by precipitation of ore and gangue minerals. Numerical simulations allow quantifying the physical and chemical processes involved in ore deposition.

This doctoral thesis aims to understand and constrain the hydrology of the Panasqueira W-Sn-Cu deposit in Portugal. In this study, high-resolution geochemical analyses of trace elements and isotopic signatures, and numerical process modeling were used to constrain the origin and flow paths of the hydrothermal fluids. To address this problematic, the following main scientific objectives were formulated:

(a) The first objective is to investigate the chemical and B-isotope variations of coexisting tourmaline and white mica from Panasqueira in order to better understand the source and evolution of the hydrothermal fluids, as well as the fluid-rock interaction processes involved. The alteration halos in the metasediments that host Panasqueira deposit contain large amounts of tourmaline (up to 70 vol.%), whereas mica is an accessory mineral. This alteration is interpreted to be the result of hydrothermal alteration dominantly predating the ore-forming event (Foxford et al., 2000, 1991; Marignac, 1982). Mica and tourmaline further coexist in the selvages at the vein contacts with the wall rocks. Mica is abundant in the greisenized granite, while tourmaline is absent. Consequently, the former is a direct link to the tardi- to post-magmatic processes operating in the Panasqueira granite. Previous mica and tourmaline chemical data are limited to a regional study of the Variscan Sn-W deposits by Neiva (1987*b*) and Neiva et al. (2007), respectively; the boron isotopic compositions were never evaluated before.

(b) The second objective is to better constrain the temperature of the hydrothermal fluids. It is well established that the main ore stages from Panasqueira formed under relatively low- to moderate-temperature conditions (<360°C) (*e.g.*, Bussink, 1984; Jaques and Pascal, 2017; Kelly and Rye, 1979; Lecumberri-Sanchez et al., 2017). However, the deposit seems to be genetically linked to an S-type granite (*e.g.*, Bloot and de Wolf, 1953; Clark, 1964; Kelly and Rye, 1979; Neiva, 1987*b*), which raises several fundamental questions. If the fluids are magmatically-derived, why do we record a maximum of 360 °C in fluid inclusions (in quartz)? How did this hydrothermal system cool down? Several authors suggest that a non-magmatic fluid of meteoric origin interacted to variable degrees with the rocks they were flowing through (Burnard and Polya, 2004; Kelly and Rye, 1979; Noronha et al., 1992; Polya, 1989, 1988*b*). However, what would be the temperature of the early fluids that flowed through the alteration zones? To answer this question, we applied mineral geothermometers to mineral assemblages coexisting in the alteration halos, in particular, the Ti-in-quartz and boron-isotope muscovite-tourmaline geothermometers.

(c) The third objective is to compare the chemical compositions of tourmaline and white mica (major, minor and trace elements) with the composition of the host rocks, greisen, granite, and regional metasediments to investigate potential enrichments or depletion in some elements and to constrain the source of the metals. Whether the metals originate from the granite or the country rocks is not clear. Also, tourmaline is often regarded as a monitor for fluid composition and evolution in hydrothermal systems (van Hinsberg, 2011; van Hinsberg et al., 2017). Despite its great potential, white mica is barely used in such a way. Thus, coupling whole-rock chemistry and tourmaline and mica chemistry allows us to investigate the potential of those phases as fluid source and evolution monitors and pathfinder minerals.

(d) The fourth objective is the application of a numerical model that is capable of describing the evolution of the Panasqueira hydrological system. The model is able to simulate multi-phase flow of compressible high-temperature fluids, coupled with a dynamic permeability model, describing hydraulic fracturing and the transition from brittle to ductile rock behavior (*e.g.*, Weis et al., 2012, 2014; Weis, 2015). The unusual subhorizontal orientation of the ore veins crosscutting the subvertical bedding and the tectonic foliations, as well as the processes involved in the opening of the veins, have been the focus of several studies (Derré, 1982; Foxford et al., 1991, 2000; Jacques et al., 2018; Kelly and Rye, 1979; Marignac, 1973; Noronha et al., 1992; Ribeiro and Pereira, 1982). According to Kelly and Rye (1979), the joint opening is related to the decrease of lithostatic pressure due to erosion and the jointing is syn- to post-granitic. Other authors suggest that the vein-network is controlled by preexisting jointing developed during the Variscan Orogeny (Derré, 1982; Jacques et al., 2018; Noronha et al., 1992; Ribeiro and Pereira, 1982) and by the local stress field as a consequence of the granitic emplacement (Derré, 1982; Noronha et al., 1992; Ribeiro and Pereira, 1982). Foxford et al. (2000); Kelly and Rye (1979) further suggest horizontal compression and fault valving as main mechanisms for the vein formation. Building on previous simulation results (Weis et al., 2014; Weis, 2015), we investigate the effect of permeability and salinity in the fluid flow pattern in multiple connected fractures and faults and discuss its applicability to the Panasqueira vein-type ore deposit.

We used a multidisciplinary approach combining fieldwork, petrography, detailed mineralogy, mineral and isotope geochemistry, whole rock geochemistry of granite, greisen, altered and unaltered metasediments from the deposit and surface drill-cores and finally, numerical modeling to reach these objectives. Details concerning the sampling strategy are described in the Appendix A. The final goal of this project is to propose a numerical simulation of the evolution of the Panasqueira hydrothermal system and expand its applicability to other deposits in the same geologic context.

1.6 Structure of this thesis

This doctoral thesis is organized in seven chapters, starting with the general introduction presented here. The various chapters contain separate introduction and conclusion sections and should, therefore, stand alone. They are published, submitted or planned to be published as independent peer-reviewed articles.

This introduction (**Chapter 1**) provides a general overview of the economic importance of tungsten and tin, W-Sn deposits, numerical modeling, and identifies the overall aims and significance of this study.

Chapter 2 is dedicated to the Variscan, regional geology of the Panasqueira deposit, state of the art, and the historical background of the mine. This chapter is not intended to be a complete review of the geology of the Central Iberian Zone, but to give important background information for the following chapters. For more detailed descriptions, the interested readers are referred to the literature.

The main results of this doctoral thesis are presented in **Chapters 3, 4, 5 and 6**. **Chapter 3** focus on the chemical and B-isotopic compositions of tourmaline and presents a detailed in-situ study by microprobe and ion probe (SIMS). Tourmaline has significant chemical and boron-isotope variations at the sample scale, but are homogeneous on the deposit scale. The variations in chemical and boron isotopes of tourmaline were further combined with estimates from Ti-in-quartz thermometry. The results suggest that the hydrothermal alteration is associated with fluid cooling and extensive fluid-rock interaction in an evolving, dynamic system characterized by the injection of multiple fluid pulses. This chapter has been published in *Chemical Geology.*

Chapter 4 presents the first extensive case study of B-isotopes in coexisting muscovite and tourmaline by SIMS. The study combines the tourmaline data documented in chapter 3 and with new chemical and boron isotopic compositions of white mica. Both chemical and B-isotopic compositions of white mica show variations from more rock-dominated to fluid-dominated compositions. The median temperatures obtained with muscovite-tourmaline geothermometer record fluid cooling from ca. 500° to 250 °C. The results also confirm that Panasqueira is a dynamic hydrothermal system with recurrent fluid pulses with an uniform composition and magmatic-hydrothermal origin.This chapter has been published in *Economic Geology.*

Chapter 5 is dedicated to the major, minor and trace element compositions of white mica and tourmaline, and whole-rock chemistry of altered and unaltered rocks. The results show an enrichment in the ore metals (W, Sn, Cu, and Zn), as well as As, F, Li, Rb, and Cs in the alteration halos around the quartz-veins, relatively to the unaltered metasediments. Most of these trace elements and ore metals are preferentially incorporated into white mica over tourmaline, which makes mica a better tracer for fluid compositions at Panasqueira. Chapter 5 is written as a manuscript and has been submitted to *Geochimica et Cosmochimica Acta* in early March 2019. The readers must be aware of potential differences between the future publication and the current version. The research dataset used in this manuscript has been published in the Data Repository of GFZ Data Services.

Chapter 6 is devoted to the numerical simulation of fluid flow patterns in fractured media and its application to the Panasqueira hydrothermal system. The chapter presents the first results of the application of the numerical simulations. The main focus of this chapter is to test different methodologies to describe fluid flow through fractures. The first step was to implement a simple setup with a single fracture and compare two different approaches of fracture discretization and from there build a model that couples the magma chamber with fractures and faults in order to describe the flow processes at Panasqueira.

Chapter 7 presents the overall conclusions and final remarks of this study and future directions of work.

The **Appendixes A, B and C** include the description of the sampling strategy, a brief description of the normalization of microprobe mica data and finally, supplementary tables and figures to Chapter 5.

All geochemical data acquired during the course of this project were published as supplementary material to the articles (Chapters 3 and 4) or as a data publication (Chapter 5). Links for download are available at the end of each chapter. For the printed version all data are provided in the enclosed CD-ROM.

”The greatest challenge to any thinker is stating the problem in a way that will allow a solution.”

–Bertrand Russell

2

Background

2.1 Geological and Metallogenic Setting

2.1.1 The Variscan Orogeny and the European Variscides

The most important occurrences Sn and/or W mineralization in Central and Western Europe are associated with the Acadian-Variscan-Appalachian orogen (Romer and Kroner, 2016). The Variscan orogeny was a major event in the tectonic evolution of Western Europe resulting from the South Baltica–Gondwana collision through the late Devonian and most of the Carboniferous (Kroner et al., 2007; Martínez Catalán et al., 2009; Ribeiro, 1990). The diachronous final closure of the Rheic Ocean (Devonian-Carboniferous) in Europe involved oblique, north-directed subduction of the Gondwanan continental crust, followed by SE-directed exhumation, regional dextral transpression and voluminous granitic magmatism (*e.g.,* Kroner et al., 2007). Arenas et al. (2014) suggested two-stage successive collisional events separated by the generation of an ephemeral oceanic basin. The first occurred in the Devonian (*i.e.,* before ca. 400-390 Ma), whereas the second is likely to have occurred at ca. 370 Ma.

The configuration of the European Variscan Belt results from the continental convergence and collision of Gondwana and Gondwana-derived microplates with Laurussia (Laurentia + Baltica) (Figure 2.1). The European Variscides are typically described as a fan-like geometry orogen divided by sutures presenting opposite vergence nappes and migration of the recumbent folds towards external, Carboniferous basins (Matte, 1991). The eastern/northern limit of the orogen (Great Britain to Bohemian Massif) is marked by north to northwest vergence, whereas the southern flank is characterized by southerly vergences (Matte, 1991) (see Figure 2.1). The agreement that the opposed vergences on each side of an oceanic suture are linked to continental collisional settings. However, long-standing discussions debate their precise boundaries, the timing of separation or even their proper existence (see discussions by Fortey and Cocks, 2003; Landing, 2005; Matte, 1991; Robardet, 2003). The correlations between the different domains of the Variscan belt are difficult (see Figure 2.1) because: (i) the Cantabrian arc (late Variscan suture) is cut along its northern branch by a transcurrent fault with a long history (left lateral displacement – Permian; oceanic spreading of Biscay Gulf – Cretaceous; shortening during Pyrenean orogeny) and (ii) the sections in the Armorican Massif and in the Ardenne-Vosges-Schwarzwald have few things in common (*e.g.* presence vs. lack of a domain with undeformed or slightly deformed Proterozoic basement) (Ballèvre et al., 2009). This is especially noteworthy in the Iberian Massif (IM), where some authors consider that the IM possesses a single suture located between the South Portuguese Zone (SPZ) and Ossa-Morena Zone (OMZ) (*e.g.,* Quesada, 1991; Quesada et al., 1994; Ribeiro, 1990). Other authors suggest a Galicia-Southern Britany suture running through the Coimbra-Cordoba Shear Zone and separating the Armorica microplate into North and South Armorica (Matte, 1991).

Despite these uncertainties, it is broadly accepted that the separation of peri-Gondwanan terranes has favored the rifting of the Rheic Ocean. Evidence of continental rifting that resulted in the opening of Rheic are found in OMZ and SPZ, where massive igneous activity, evolving locally to peralkaline felsic volcanics is linked to this event (Díez Fernández et al., 2016, 2015, 2012; Montero et al., 2009; Sánchez-García et al., 2010). The continental collision is evidenced by widespread (Variscan) plutonism, strike-slip tectonics as

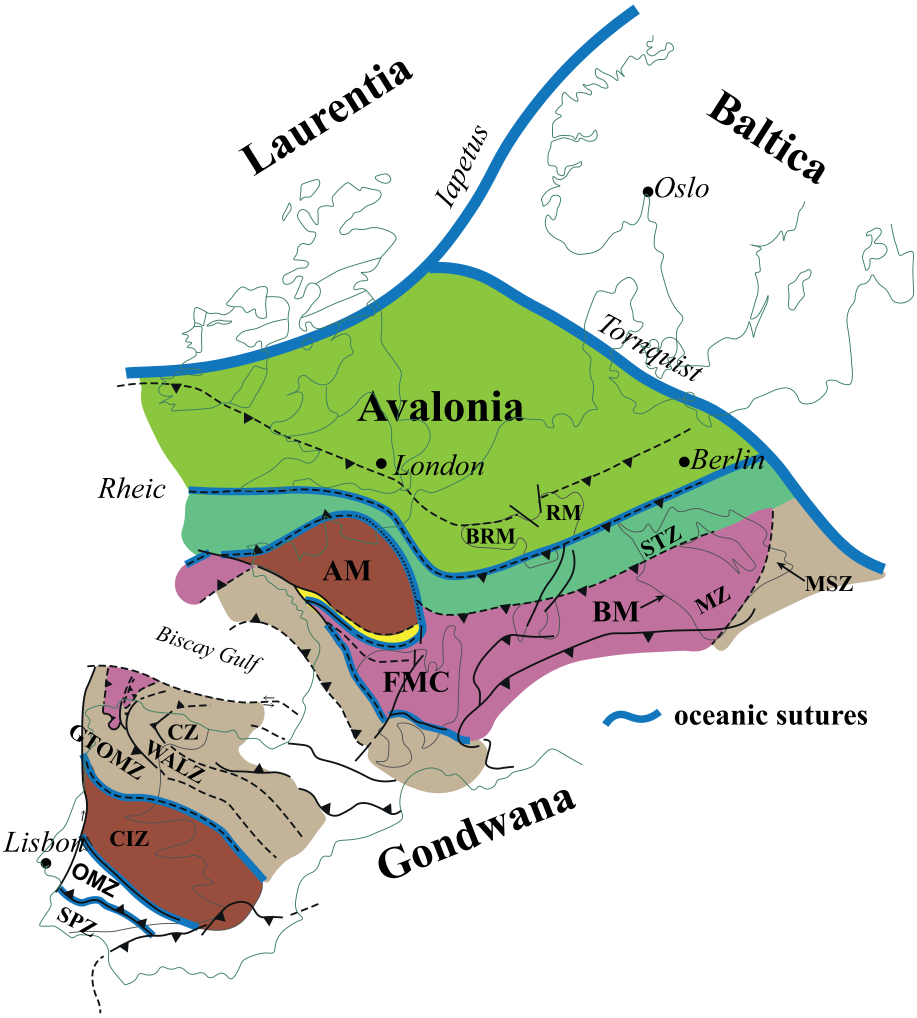

Figure 2.1: Configuration of the Variscan Belt. Different colors are used to overcome highlight potential correlations within the Variscan belt; inferred positions of the Rheic ocean suture and other second-order sutures are also shown (modified from Ballèvre et al., 2009). Abbreviations: AM – Armorican Massif, BM – Bohemian Massif, BRM – Brabant Massif, CZ – Cantabrian Zone, CIZ – Central Iberian Zone, FMC – French Massif Central, GTOMZ – Galicia-Trás-os-Montes Zone, MZ – Moldanubian Zone, OMZ – Ossa-Morena Zone, RM – Rhenish Massif, SMZ – Moravo-Silesian Zone, SPZ – South Portuguese Zone, STZ – Saxo-Thuringian Zone, WALZ – West Asturian-Leonese Zone.

well as by the exhumation of Gondwana high-pressure rocks (*e.g.,* Kroner et al., 2007; Nance et al., 2012; Rubio Pascual et al., 2013). In fact, a large number of granitoid intrusions are recognized throughout Variscan Belt of Western Europe, emplaced syn- to post-kinematically relatively to the Variscan orogeny. The Variscan magmatism represents the recycling of thickened peri-Gondwanan crust, with subordinate contribution of juvenile material (*e.g.,* Kroner and Romer, 2013, and references therein).

2.1.2 The Iberian Massif

The Iberian Massif (IM), one of the belts forming the pre-Mesozoic basement of the European Variscides, comprises six tectonostratigraphic units which include, from North to South: (i) the Cantabrian Zone (CZ), (ii) the West Asturian-Leonese Zone (WALZ), (iii) the Galicia-Trás-os-Montes Zone (GTOMZ); (iv) the Central Iberian Zone (CIZ), (v) the Ossa-Morena Zone (OMZ) and (vi) the South Portuguese Zone (SPZ) (*e.g.,* Martínez Catalán, 2012, and references therein). In addition, Arenas et al. (2016) proposed a new geotectonic zone – the Galicia-Ossa-Morena Zone – based on the correlation between allochthonous complexes. The CZ and SPZ are considered external, while the remnants are regarded as internal zones of the IM. These units are usually continuous in the Iberian Peninsula, with roughly parallel boundaries and separated by low- or high-angle crustal-scale shear zones (*e.g.,* Martínez Catalán et al., 2007; Ribeiro et al., 1990; Simancas et al., 2009). In general, the aforementioned zones consist of Neoproterozoic to Paleozoic sequences lying above a more or less reworked Cadomian basement, which formed part of the Gondwanan continental crust (*e.g.,* Martínez Catalán, 2012; Martínez Catalán et al., 2004). The CZ, WALZ, and CIZ represent continental fragments of the Iberian autochthon (Neoproterozoic Gondwanan), where the differences in their tectonic-thermal evolution can be related to their respective positions during the Variscan orogeny (López-Plaza et al., 2007). Contrarily, the GTOMZ is not continuous, only cropping out in the northern part of the Iberian Peninsula as a giant klippe[1] of allochthonous and parautochthonous terranes (Martínez Catalán, 2012).

2.1.3 Central Iberian Zone

The Central Iberian Zone is characterized by an extensive exposure of granitic rocks of Variscan age and an allochthonous, thick (up to 11,000 m) and monotonous Neoproterozoic-Cambrian siliciclastic succession (Figure 2.2). This succession consists of a turbiditic sequence comprising mostly pelitic and psammitic beds unconformably overlain by the Armorican Quartzite (*e.g.,* Ribeiro et al., 1990; Villaseca et al., 2014). The generation and emplacement of the granitic melts took place mostly between 320-290 Ma and sustained

---

[1] Remnant portion of a nappe after the erosion of the connecting parts of the original nappe.

several ore-forming systems with metallogenetic significance (Derré et al., 1986; Mateus and Noronha, 2010; Noronha et al., 2000).

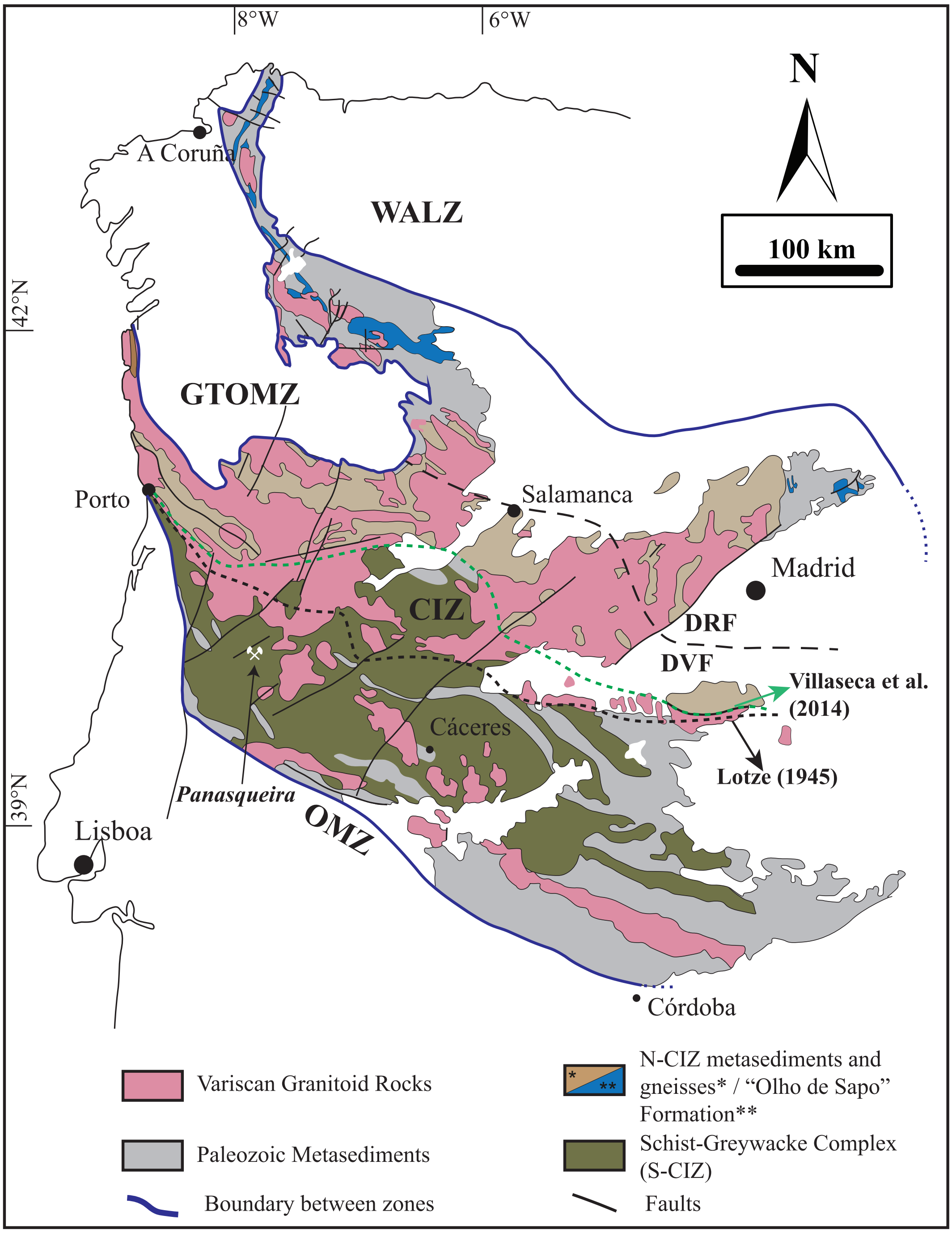

Figure 2.2: Geological sketch map of the Central Iberian Zone (CIZ) showing the Variscan granitoid intrusions and the metasediments distribution (modified from Pesquera et al., 2013; Villaseca et al., 2014). Also, the subdivision of CIZ from Villaseca et al. (2014) and (Lötze (1945) are shown for reference. CIZ – Central Iberian Zone, GTOMZ – Galicia-Trás-os-Montes Zone, N-CIZ – Northern Central Iberian Zone, S-CIZ – Southern Central Iberian Zone, OMZ – Ossa-Morena Zone, WALZ – West Asturian-Leonese Zone; DRF – Domain of the Recumbent Folds, DVF – Domain of the Vertical Faults.

The classical subdivision of the CIZ by Lötze (1945) has been recently revisited by Villaseca et al. (2014) (see Figure 2.2) on the basis of geochemical signatures, both of these authors agree that the CIZ is divided into two main domains, both they suggest different boundaries (see Figure 2.2). According to Villaseca et al. (2014), the southern domain of the CIZ (S-CIZ) comprises low-grade metasedimentary rocks (Schist Greywacke Complex, SGC) and the northern domain (N-CIZ) consists of higher grade metasedimentary rocks with more mature metapelitic protoliths with marked isotopic differences. The SGC was deposited in horst-graben structured basins and consists of shales and quartzites with minor meta-conglomerates, meta-carbonates and scarce meta-volcanoclastic layers of calc-alkaline affinity (Rodríguez-Alonso et al., 2004). The meta-carbonate beds are predominantly meta-dolostones, locally preserving remains of an Ediacaran fauna with ages ranging from 635 to 542 Ma (Herrero et al., 2011). The SCG is unconformably overlain by Ordovician to Silurian metasediments. The N-CIZ sector is dominated by paragneisses and migmatites (originally pelites) with minor amphibolite, calc-silicate, marble or psammitic interlayers. The carbonates are scarce and mainly consist of calcitic marble, with occasional dolomitic bands (Villaseca et al., 2014, and references therein).

The juvenile magmatic signature of the metasediments from the S-CIZ suggests that these formed in the proximity to a magmatic arc (Late Neoproterozoic), whereas the N-CIZ metasediments, which may derive from older and crustal-like sources, formed in a foreland-type scenario. Villaseca et al. (2014) proposed a geodynamic setting comprising (from S to N) a magmatic arc, a back-arc basin and a much older foreland at the end of the Ediacaran (Figure 2.3). This setting evolved from mainly compressive towards extensional tectonics at the end of the Early Ordovician. The evolution of a passive margin with sporadic basic magmatism of rifting affinity (*e.g.,* tholeiitic or alkaline) occurred later than previously estimated (ca. 477 Ma: Gutiérrez-Alonso et al. 2007), which represents the minimum age of deposition of the Armorican Quartzite (Villaseca et al., 2016). The sedimentation of the Armorican Quartzite marks the transition from a progressively exhumed orogenic area to a passive margin setting linked to the opening of the Rheic Ocean (*e.g.,* Ballèvre et al., 2012; Murphy and Nance, 2008).

In the CIZ, three main phases of ductile deformation (D1, D2, and D3) have been recognized (*e.g.,* Dias et al., 1998; Noronha et al., 1979; Ribeiro, 1990, 1974). The early

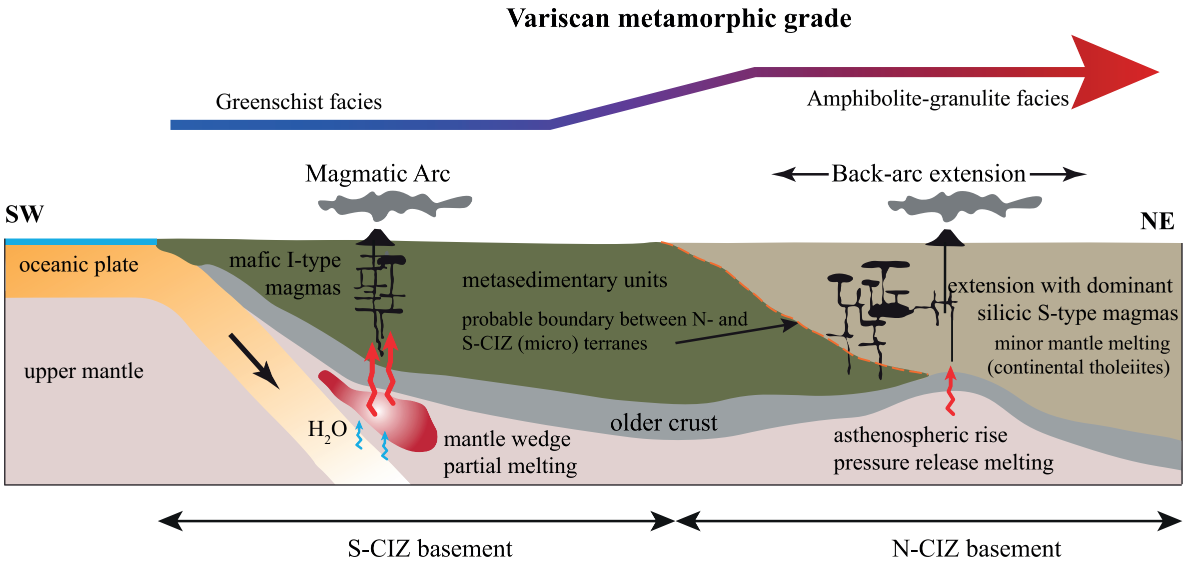

Figure 2.3: Schematic section (not at scale) for the geological setting of the CIZ during Early Ordovician time. The figure shows the variations in the metamorphic facies from SW to NE and the relative position of the tectonosedimentary units (S-CIZ and N-CIZ) (adapted from Villaseca et al., 2014). Main tectonic elements (arc and back-arc, Rubio-Ordóñez et al. (after 2012); magmatism at the back-arc setting after models from Martínez Catalán et al. (2007) and Wernicke et al. (1987). Crustal older basement (ensialic system) has been shortened in the vertical for simplicity, whereas the thickness of the N-CIZ and S-CIZ are vertically exaggerated. Metabasites in the N-CIZ described by Barbero and Villaseca (2000) and Villaseca et al. (2015).

phases D1 and D2 are thought to be continuous and span from 365-345 Ma (upper Devonian to early Carboniferous) to 345-320 Ma (early to mid-Carboniferous), respectively, corresponding to the collisional stage of the Variscan orogeny (*e.g.,* Dallmeyer et al., 1997; Martínez Catalán et al., 2004; Rubio Pascual et al., 2013). The generation of subvertical D1 folds with a steep slaty cleavage and, particularly in the allochthonous terrains of the Galicia Trás-os-Montes Zone, D2 recumbent folds with axial plane crenulation cleavage or schistosity associated to large thrust units or sub-horizontal extensional shear zones are characteristic of the ductile phases within the CIZ. The resultant crustal thickening is related to partial melting and limited production of granitoids of peraluminous affinity (*e.g.,* Dias et al., 1998; Valle Aguado et al., 2005). Nonetheless, most of the CIZ granitoids post-date the syn-collisional stage of the Variscan orogeny and were emplaced under extensional conditions (D3). Late stage D3 ductile deformation (ca. 320-300 Ma: e.g. Pereira et al. 2012) is related to transpressional tectonics with associated wrenching and strong uplift and it is responsible for oroclinal bending of the Ibero-Armorican arc (*e.g.,* Pastor-Galán et al., 2015; Shaw et al., 2012). This stage produced vertical folds with subhorizontal axes and subvertical strike-slip shear zones, both right and left lateral (*e.g.,* Martínez Catalán et al., 2014). The D3 ductile phase is followed by a fragile deformation phase (D4) during the Permian, giving rise to NE-SW, NNE-SSW and NW-SE fracture systems (Pereira et al., 1993).

2.1.4 Variscan Magmatism

The Iberian Massif contains one of the largest and best outcropping domains of the granites in the European Variscides, comprising ca. 70% of granitic intrusions and migmatitic complexes (Figure 2.2). The compositional range is wide and most granitic rocks are S-type peraluminous bodies, sometimes with abundant Al-rich minerals. Granitic rocks with transitional features between S- and I-type, I-type and hybrid granites, including rare metaluminous varieties, are also found (Pereira et al., 2017, and references therein).

The granitic suite emplacement occurred about 30-50 Ma after the Variscan collision phase (ca. 335-306 Ma; Bea et al. 2003; Dias et al. 1998; Ferreira et al. 1987; Neiva et al. 2009; Orejana et al. 2012; Pereira et al. 2017; Teixeira et al. 2011). The Permo-Carboniferous granitic rocks of calk-alkaline affinity (ca. 306-287 Ma Dias et al. 1998; Neiva et al. 2012; Orejana et al. 2012; Pereira et al. 2017; Villaseca et al. 2012) crosscut Variscan sutures, being therefore unrelated to the continental collision (Pereira et al., 2015).

The Variscan granites of the CIZ have variable and complex spatial and temporal relationships between them (Julivert et al., 1974) and with Variscan structures (Ferreira et al., 1987; Noronha et al., 1979; Oen, 1970). Many authors (Capdevila et al., 1973; Corretgé et al., 1977; Ferreira et al., 1987; López-Plaza and Martínez Catalán, 1987; Noronha et al., 1979; Oen, 1970) attempted to classify the Iberian granites distinguishing several groups or families combining compositional, mineralogical, geochronological and tectonic criteria. However, these classifications are still controversial and different classifications can be found on both sides of the Portuguese-Spanish border, mainly due to the lack of applicability and generalization of the classification from the Spanish to the Portuguese sector. The first attempts to classify the Variscan granites were done by (i)

Capdevila et al. (1973) and Capdevila and Floor (1970), and (ii) Oen (1970), Oen (1958), and Schermerhorn (1956) based on petrological-mineralogical and tectonic-metamorphic criteria, respectively. This initial subdivision was later refined by other authors (*e.g.,* Ferreira et al., 1987; López-Plaza and Martínez Catalán, 1987; Noronha et al., 1981) who distinguished three to four groups of intrusion: pre-D3, syn-D3, tardi-D3, and post-D3 granitoids. Granitic intrusions of Upper Proterozoic to Lower Paleozoic age are referred to as Pre-Variscan. Pre-D3 and syn-D3 granitoids have similar characteristics. However, the abundance of the Pre-D3 is reduced in Portugal when compared with Spain. Syn-D3 granitoids are typically extensive batholiths of two-mica, peraluminous granites and leucogranites. The late-post-D3 granitoids frequently form zoned complexes, within metamorphic aureoles and are predominantly undeformed, weekly to moderately peraluminous granodiorites and biotite granites (Azevedo and Valle Aguado, 2013).

Different types of sources have been widely discussed for the Variscan granitoids. These include crustal recycling of (i) metasedimentary and meta-igneous upper crustal sources, (ii) metasedimentary mid-crustal sources, (iii) meta-igneous lower crustal sources or (iv) mantle sources that interacted with distinct crustal melts (*e.g.,* Bea et al., 1999; Costa et al., 2014; Martins et al., 2013, 2014; Neiva and Gomes, 2001; Teixeira et al., 2011; Villaseca et al., 2012).

A large number of CIZ granitic bodies are highly evolved and can be the host of several occurences of Sn-W-Li-F-Nb-Ta-P-U mineralization (*e.g.,* Chicharro et al., 2016; López-Moro et al., 2017; Neiva et al., 2012; Noronha et al., 2013; Roda-Robles et al., 2016, 2012).

2.1.5 Metallogeny

The Western European Variscan belt is widely known for hosting numerous Sn-W ore deposits, especially important in Portugal (*e.g.,* Kelly and Rye, 1979; Moura et al., 2014; Neiva, 2008; Noronha, 1983), Spain (*e.g.,* Chicharro et al., 2016; Llorens and Moro, 2012*a*,*b*; Llorens González et al., 2017; Mangas and Arribas, 1988; Tornos et al., 2008), France (*e.g.,* Cuney et al., 2002; Marignac and Cuney, 1999; Vallance et al., 2001), SW England (*e.g.,* Jackson et al., 1989), Germany and the Czech Republic (*e.g.,* Štemprok, 1980; Štemprok and Steltmann, 1994). These consist of veins, stocks, skarns, breccia pipes and greisen type-deposits that belong to a metallogenic province, related to post-collision tectonics and magmatism (Štemprok, 1980). According to Derré (1982), the W-Sn mineralization in the Western Variscan European belt shows a spatial distribution with Sn<W and W>Sn bands that define W-E trend in the Iberian Massif (Figure 2.4).

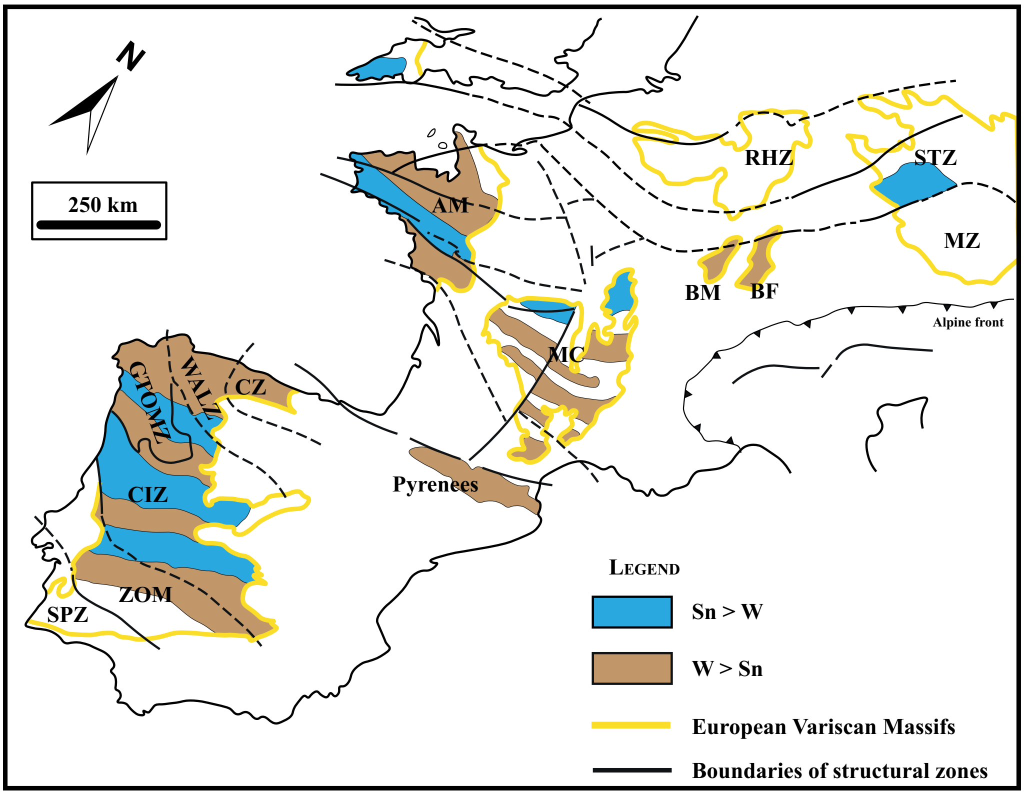

Figure 2.4: Sketch map of Sn-W metallogenic province of the Western European Variscan Belt showing the Sn and W dominant bands in the different Variscan massifs (adapted after Derré, 1982).

The Iberian Massif has been one of the leading tin-tungsten producers in Europe. The deposits extend from Galicia, through the N of Portugal to the SW of Spain (see Figure 2.5). These deposits are typically related to syn- to late-Variscan granites and developed in high-level apical portions of the granitic intrusions and/or are hosted by the surrounding metasedimentary rocks. In general, the W-Sn deposits are linked to outcropping granites or pegmatites, nonetheless, the associated granite may be a hidden intrusive body (*e.g.* Panasqueira: Kelly and Rye, 1979). Moreover, given the presence of some carbonate layers within the host metasedimentary units, some skarns may also appear (*e.g.,* Tabuaço: Gomes, 2016; Ramos et al., 2017; Spruzeniece et al., 2018; Los Santos: Tornos et al., 2008).

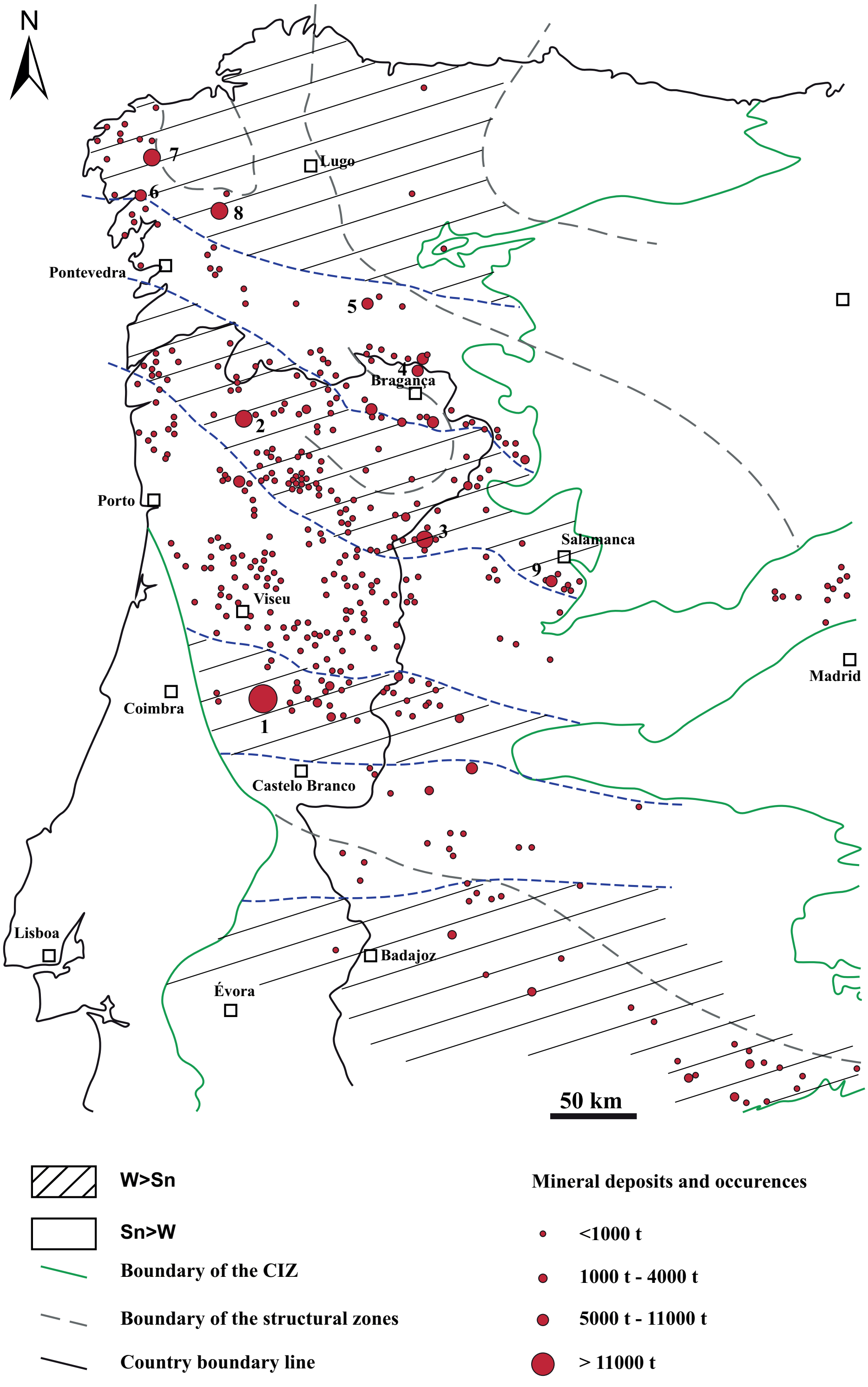

Figure 2.5: Distribution of the mineral deposits and occurrences of W and Sn deposits in the Central Iberian Zone (adapted after Derré, 1982). Numbers indicate the greatest deposits in the CIZ as follows: 1 – Panasqueira; 2 – Borralha; 3 – Barruecopardo; 4 – Montesinho; 5 – Penouta; 6 – San Finx; 7 – Santa Comba; 8 – Fontao; 9 – Los Santos.

The Panasqueira W-Sn-Cu ore deposit consists of an extensive swarm of subhorizontal veins peripheral to a late-Variscan granite. The veins consist of a quartz-mica-wolframite-cassiterite-chalcopyrite assemblage with an accessory content of many other oxides, sulfides, phosphates, silicates, and so forth. The state of the art, mining history, geology, mineralogy, and geochemistry will be further discussed in Section 2.2 and Chapters 3, 4 and 5. The local geology of the Panasqueira W-Sn-Cu ore deposit will be discussed in detail exclusively in Chapters 3, 4, 5 and 6.

2.2 Minas da Panasqueira

The Panasqueira ore deposit is located in the Castelo Branco district (Beira Baixa) in central Portugal (see Figure 2.6). The name "Panasqueira" is derived from an herbaceous plant belonging to the Gramineae family, a frequent plant in the region where the mine is located. In the following subsections, a short historical background is provided as well as state of the art.

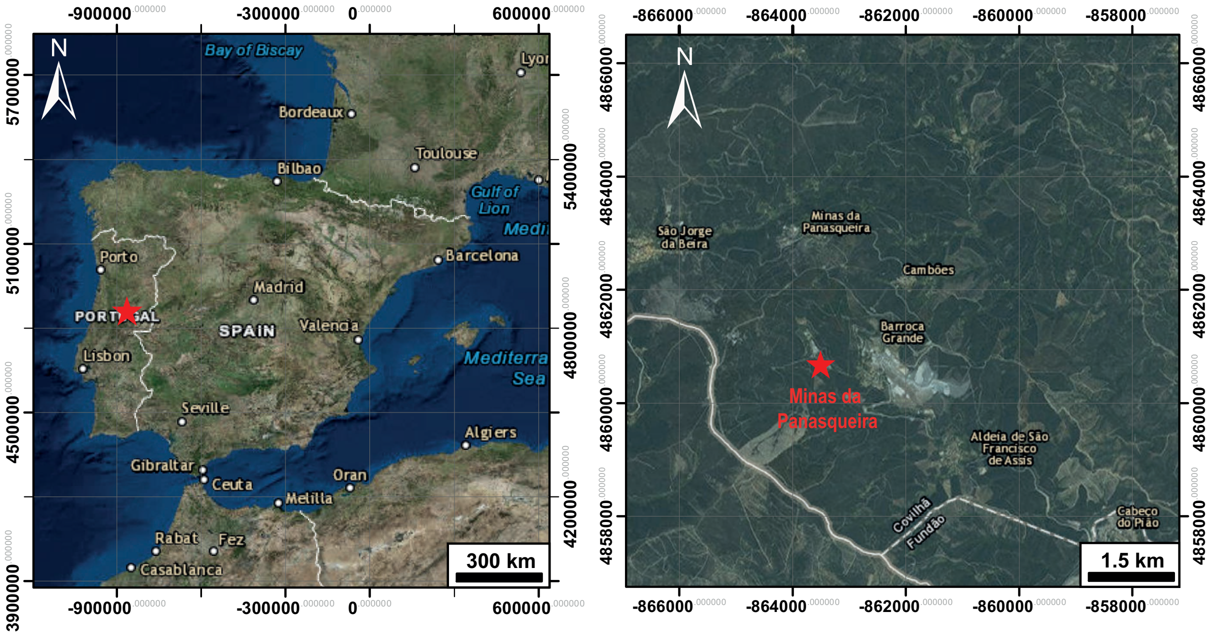

Figure 2.6: Location of the Panasqueira W-Sn-Cu deposit. Adapted from ESRI; WGS 1984 World Mercator projected coordinates.

2.2.1 Historical Background

Wolframite ore at Panasqueira was first discovered at the end of the XIX century by a woodchopper. The first exploration permit was granted in 1886 and the first mining concession in 1896 to the "Sociedade de Minas de Wolfram em Portugal-Lisboa". The mine concession for the "Couto Mineiro da Panasqueira" had an extension of ca. 21 km^2, with the main exploration area centered at Barroca Grande village (Figure 2.7). During its long mining history, Panasqueira had many owners and was closed twice in 1944 and 1994 (Figure 2.8). Wolfram Mining and Smelting bought the concession in 1911 and changed the name first to Beralt Tin & Wolfram (BTW) in 1928 after reorganization and inclusion of new shareholders and then to Beralt Tin & Tungsten Portugal S.A. in 1973 after the involvement of the Banco Nacional Ultramarino (BNU), who obtained 20% of the shares. Due to high fluctuations in tungsten prices (Figure 2.9), the remaining 80% of the shares were first sold from Charter Consolidated to Minorco S.A. in 1980, then to AVOCET in 1994/1995 after the mine's closure in 1994 (Corrêa de Sá et al., 1999), and finally to Primary Metals in 2003. Sojitz Corporation bought 100% of the shares in 2007 and eventually sold them to Almonty Industries in 2016 (Wheeler, 2016).

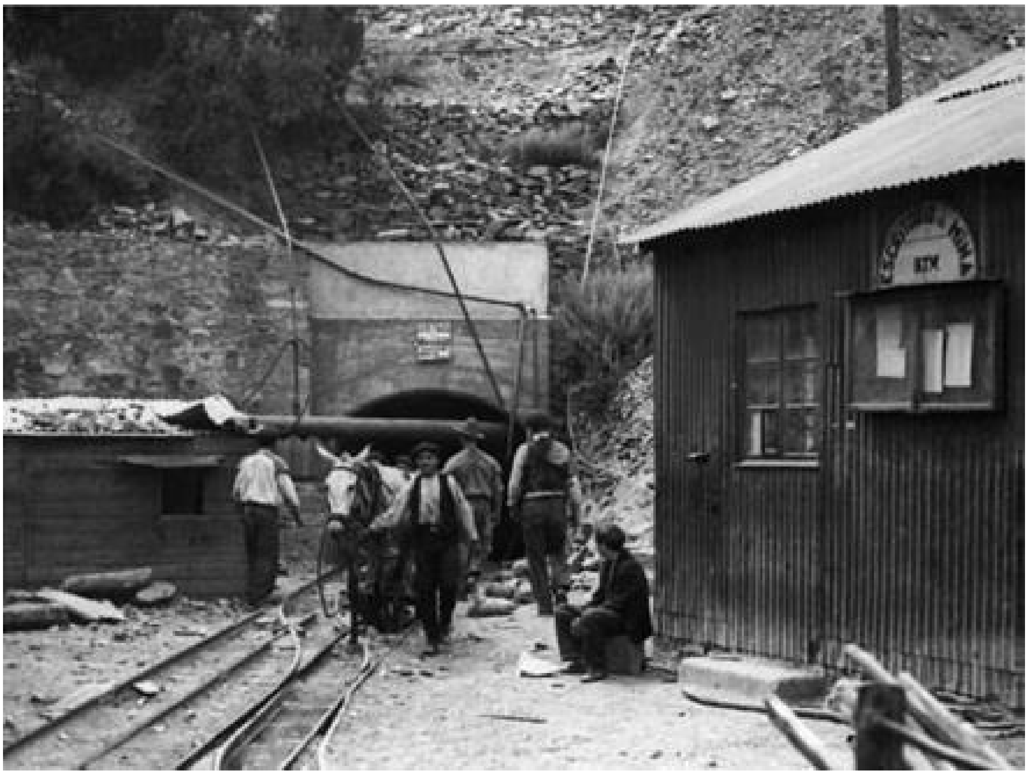

Figure 2.7: Entrance of the Barroca Grande Gallery (source: Pinto et al., 2014).

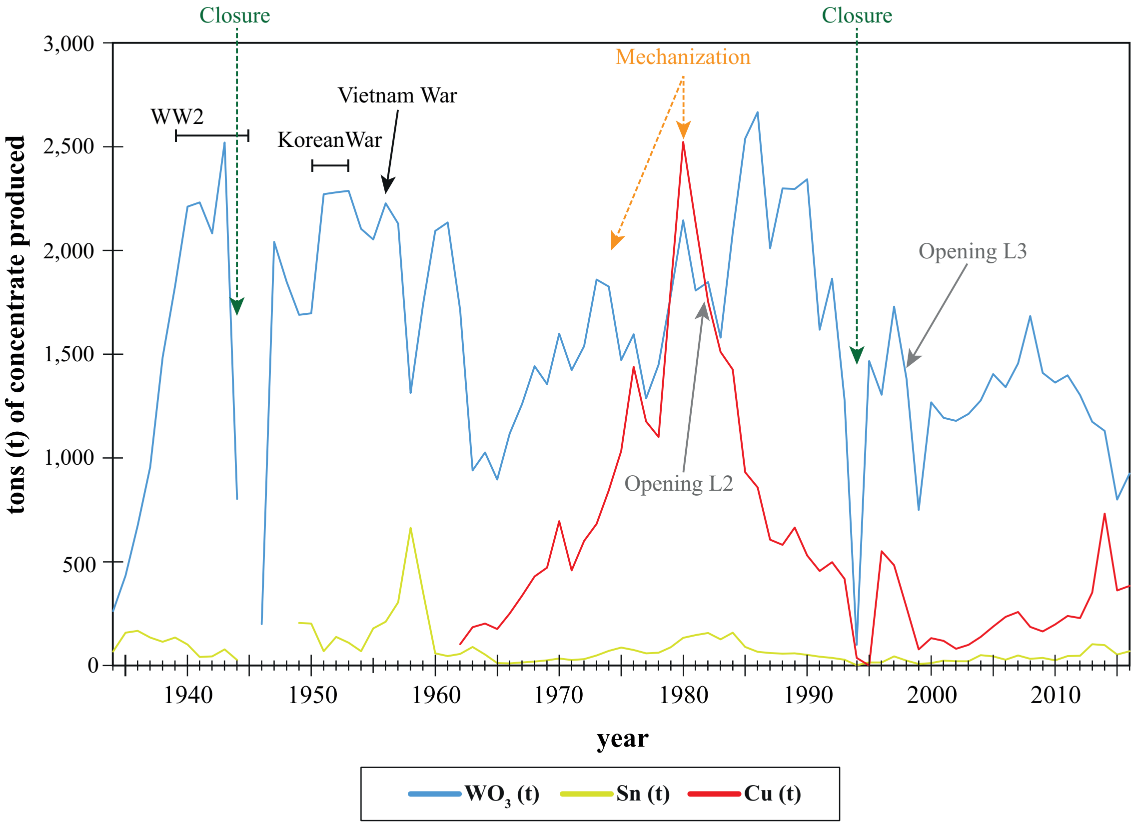

Figure 2.8: Historical production of tungsten (WO_3), tin and copper concentrates at Minas da Panasqueira. Data source: Wheeler (2016). L2 and L3 stand for level 2 and level 3 (underground galleries), respectively.

The evolution of the Panasqueira mine is intimately linked with historical and economic events (Figure 2.8). The opening of the mine followed the first industrial applications of tungsten to harden steel, which revolutionized engineering during the XX century (Lassner and Schubert, 2005). Market demands strongly control the fluctuations in tungsten prices and their peaks can be linked to major conflicts during the XX century (Figure 2.8). The two world wars were periods of strong increase in mining operations at Panasqueira in terms of machinery/mechanization, increase of workers and production rates (Figures 2.8) (Corrêa de Sá et al., 1999; Wheeler, 2016). Tungsten prices during the second world war were not as extreme as compared to first world war, probably due to overall higher supply rates (Figure 2.9). World production of tungsten concentrate increased from about 11,600 t in 1928 (Hess, 1933) to 61,000 t in 1943 (Davis, 1946). Between 1936 and 1945, China produced 25% of the world's tungsten ore, while Portugal was the leading producer in Europe with about 38,000 t of tungsten (WO_3) (Davis, 1946). Because tungsten prices decreased between the world wars (Figure 2.9), the company started to improve the recovery of tin ores. When tungsten prices increased again from 1936 to 1943 (Figure 2.9), mine production reached its peak and the number of miners increased from 750 in 1933 to 5,790 in 1943 and an additional 4,780 self-employed workers at the surface workings (Corrêa de Sá et al., 1999; Wheeler, 2016). From 1944 to 1946, the Portuguese government closed all operating tungsten mines (Corrêa de Sá et al., 1999).

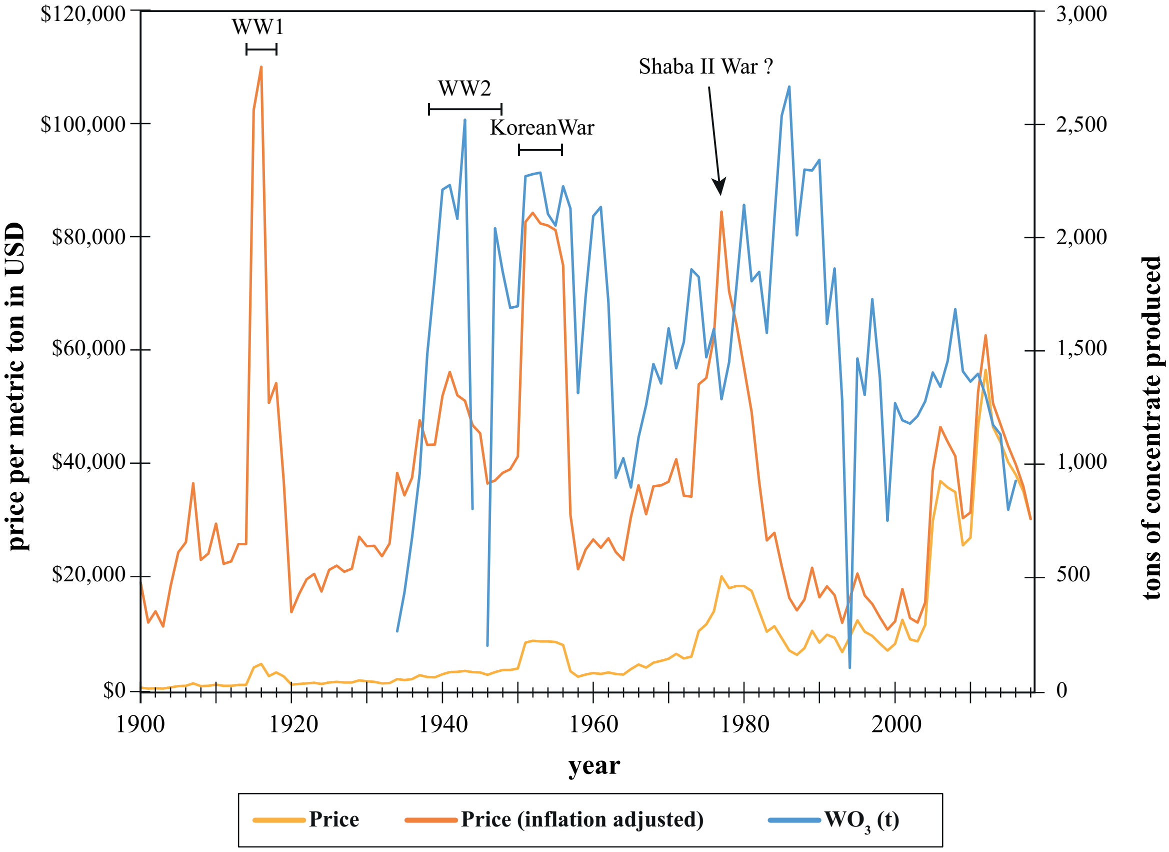

Figure 2.9: Historical tungsten price per metric ton in USD (left y-axis) and production of tungsten concentrate at Panasqueira (right y-axis). Tungsten prices retrieved from `https://www.metalary.com/tungsten-price/` on May 28, 2019.

After reopening, tungsten prices increased again in 1950 during the Korean War (Figure 2.9), but the mine operations focused more on tin recovery (Figure 2.8). From the late ’50s to early ’90s, tungsten prices fluctuated but stayed relatively low, which ultimately led to the second closure of the mine in 1993 (Figures 2.8 and 2.9) (Corrêa de Sá et al., 1999; Wheeler, 2016). During this period, production peaks coincide with events of improved mechanization and openings of new deeper levels (Figure 2.8). Since reopening in

1995, tungsten prices have continued to fluctuate with peaks in 2006 (1,342 t produced) and 2012 (1,303 t produced) (Figure 2.9). Production started to increase slightly in 2016 (Figure 2.8) under the new owner Almonty Industries, who expects to further increase the concentrate output by 10% by improving recovery rates from the tailings (Almonty Industries, 2018).

The Panasqueira deposit has already produced 130,000 t of WO_3 within the last 82 years and still has proven reserves of 775,000 t (1,694 t of WO_3), probable reserves of 1,176,000 t (3,928 t of WO_3) and total resources (incl. reserves) of 10,027,000 t (23,127 t of WO_3) (Almonty Industries, 2016) which may mean at least another 20 years of mining activity at the current production rate for tungsten.

2.2.2 State of the Art

The unique nature of Panasqueira mineralization attracted many researchers over the years. The studies are extensive and diverse covering several fields that accompanied the scientific and technological evolution. These include general and local geology, tectonics, whole rock geochemistry of metasediments and granitoids, mineralogy and paragenesis, fluid inclusions and stable isotopic studies, geochronology of the mineralization and related granites. In this section, the most relevant studies will be referred and synthesized, following roughly a chronological order.

The first work at Panasqueira focused on the crystallographic study of cassiterite and was undertaken by Cadel Vila in 1926 (in Thadeu, 1951*a*). This work was followed by studies giving particular emphasis to the geology and genesis of the W-Sn-Cu mineralized veins (Barbosa, 1944; Fonseca, 1943). Thadeu (1951*a*) is accountable for the first detailed work that describes the local and regional geology, as well as the occurrence of spotted schists and non-spotted schists and established the first paragenetic sequence for the mineralization. Some considerations concerning the granitic cupola and its genetic relation with the mineralization as well as the possible zonation within the deposit are also made. During the same year, the same author presented a synthesis of the Pb-Zn mineralization of Beira Baixa region (Thadeu, 1951*b*), including the mineralization associated with faults belonging to "Couto Mineiro da Panasqueira" (*e.g.,* Cebola, West and Main faults). Two years later a study (Bloot and de Wolf, 1953) based on petrographic observations establishes the relationship between the Panasqueira granite, the W-Sn-(Cu) mineralization and the hydrothermal alteration at the contact between the mineralized veins and the host rocks. In 1967, D'Orey presented a detailed work comparing the vein mineralogy and paragenesis at Barroca Grande, Panasqueira and Vale da Ermida, suggesting that the latter is an independent mineralized mass. He also identified stannite for the first time and pointed out two generations of cassiterite (primary and secondary) resulting from stannite alteration at Barroca Grande sector.

Conde et al. (1971) contributed a general description of the deposit, including geological and structural features, deuteric alteration and, most importantly, describes three different zones for the distribution of the mineralization around the cupola. The most distal zone presents cassiterite, which is probably corresponding to a second generation. Marignac (1982, 1973) proposed an alternative model based on the relationships between deformation, magmatic intrusion, and mineralization. According to this author, the thermal metamorphic aureole at Panasqueira is not related to the known cupola, but instead reflects the presence of a large granitic mass beneath or nearby the deposit. Based on geologic, geomorphologic and photogeologic criteria, Carvalho (1974) defined the link between the tectonic alignments and the hypogene deposits, in particular, the "Sn-W Góis alignment" [Panasqueira (W-Sn-Cu) – Argemela (Sn) – Ceife (Pb)]. By the end of the '70s, Kelly and Rye (1979) presented an extensive work including a synthesis of the regional geology and history of the deposit, as well as a model to explain the morphology and genesis of the mineralized veins. These authors established a four-stage paragenetic sequence for the mineralization. The study also includes a fluid inclusion study (quartz, apatite, siderite, fluorite, calcite, topaz and cassiterite) to obtain pressure and temperature conditions of the mineralizing fluids. Also, stable isotopes (carbon, oxygen, hydrogen, and sulfur) allowed the authors to make remarks regarding the origin of mineralizing fluids. At last, they establish a model for the genesis of the mineralization and its relation with the non-outcropping cupola. In the same year, Thadeu published another synthesis study about both regional geology and the mineralization and its connection to the granitic cupola.

Ribeiro and Pereira (1982) studied the paleogeographic, petrological and structural controls on hypogene deposits genesis and proposed a model for the stress field related to the emplacement of a post-tectonic granitic cupola at Panasqueira. Oosterom et al. (1984) performed the first litogeochemical study of the metasediments and studied the distribution of F, Li, Rb, Sn, W, Cu, and P. Two years later, Bussink studied the “specialized granites” and metasediments in the Beira Baixa region. At Panasqueira, he focused on the composition of gases from fluid inclusions and stable isotopes (oxygen, hydrogen, and nitrogen), and presented a model for the genesis of the deposit and its relation to the cupola (Bussink, 1984). Based on wolframite solubility in hydrothermal fluids from the granite at Panasqueira, Polya (1987) studied the physic-chemical conditions of the fluids and established a new genetic model. One year later, he presented two further studies, one about the compositional variation of wolframites at Barroca Grande sector in order to understand the variation in Nb, mainly in the vicinity of N-S faults and another one about the efficiency of ore formation at Panasqueira deposit (Polya, 1988*a*,*b*). In 1989, he published a study about the source of mineralizing fluids, in particular for W and Sn, using results obtained through fluid inclusions studies and thermodynamic studies of the mineral assemblages (temperature, pressure, salinity, and concentration of the volatiles). Neiva (1987*b*) studied the muscovite composition of the Panasqueira granite, the metasomatized host rock, as well the muscovite within the mineralized veins. Neiva (1987*a*) focused on the chemistry of greisenized granites and metasomatic schists of W-Sn deposits of northern Portugal, taking in consideration the W-Sn-(Cu) deposit at Panasqueira. Snee et al. (1988) applied thermochronological techniques to the deposit, dating of the stages of mineralization using ^{40}Ar/^{39}Ar on muscovite. Noronha et al. (1992) characterized the different types of fluids present in the barren quartz and mineralized veins using microthermometry, Raman spectrometric data (volatiles) and ion analysis of the fluid phases to distinguish between metamorphic and hydrothermal quartz.

Polya et al. (2000) studied the evolution and paragenetic context of anomalous low δD hydrothermal fluids at Panasqueira, emphasizing the mixing of meteoric waters with metasedimentary sources. Lourenço (2002) studied the mineral assemblages and proposed a sequence of deposition distinguishing two different generations of cassiterite. In addition, he studied fluid inclusions in mineral phases contemporaneous with mineralization, determining the composition and pressure-temperature conditions at the time of trapping. Foxford et al. (2000, 1991) combined structural and textural approaches to the mineralized veins in order to determine the tectonic controls during its genesis. Burnard and Polya (2004) measured He and Ar isotopes in ore minerals at Panasqueira deposit, providing important conclusions about the long-lived hydrothermal activity at the Panasqueira and the timing of the hydrothermal activity, which mostly or completely post-dates the granitic intrusion. They also concluded that mineralization resulted from a later pulse or pulses of mantle-derived heat and volatiles. Neiva et al. (2007) realized an extensive study focusing on the crystal chemistry of tourmaline from Variscan granites (comparison between magmatic, hydrothermal and metasomatic tourmaline) including the Panasqueira deposit. In 2008, Neiva characterized the geochemistry of cassiterite and wolframite (mainly mineral chemistry) from Sn-W quartz veins in Portugal, including the Panasqueira deposit.

Pinto et al. (2014) studied the distribution of Sn at Minas da Panasqueira and concluded that there is no relationship between the Sn mineralization and the proximity to the known cupola, considering that another granitic cupola is required to explain the distal enrichments in cassiterite. More recently, Lecumberri-Sanchez et al. (2017) presented a fluid-rock interaction model to explain the wolframite precipitation at Panasqueira. These authors demonstrated that magmatic fluids provided W in solution, whereas the wall rocks contribute the iron required to precipitate wolframite. Jacques et al. (2018) presents a new structural and tectonic model and postulate that Panasqueira formed under low differential stress, exploiting the pre-existing cross-fold joint system. During the same year, Jaques and Pascal (2017) contributed a new determination of the paleopressure at Panasqueira, conducting an extensive fluid inclusion study in quartz to derive fluid isochores and deducing P-T conditions based on arsenopyrite and sphalerite geothermometry and geobarometry. Martins (2017) studied the Bi- and Ag-rich phases, defined a new paragenetic sequence and identified two main zones in the western and eastern parts of the deposit, which are enriched in Ba + F + Sn ± P and F ± P ± B, respectively. Based on the textural analysis of growth band of hydrothermal tourmaline, Launay et al. (2018) inferred the direction and velocity of fluid flow at Panasqueira. They also emphasize the role of the greisen cupola in fluid focusing and the role of fluid overpressure during vein opening. Based on tourmaline chemistry they argue that the magmatic fluids were enriched in Na, K, Li, Sr, and Sn. Finally, a new approach using multifractal modeling, singularity mapping and geochemical indices for targeting buried mineralization was published by Gonçalves et al. (2018b).

Further works conducted at Panasqueira include Blaettler (1985) and Derré et al. (1986) [tectonics]; Cotelo Neiva (1944), Saraiva (1971), Knutson et al. (1985), Mignardi et al. (1995*a*,*b*,*a*) [mineralogy and paragenesis of mineralization]; Clark (1964), Campbell et al. (1988, 1984), Lüders (1996), Noronha et al. (2000, 1999) [fluid inclusions studies and stable isotopes and its connection to the granitic cupola]; Clark (1970), Kelly and Wagner (1977) and Priem and den Tex (1984) [absolute dating of mineralization and associated granites].

"If the facts do not fit the theory, change the facts."

–Albert Einstein

3

Chemical and boron isotopic composition of hydrothermal tourmaline from the Panasqueira W-Sn-Cu deposit, Portugal

Marta S. Codeço[1], Philipp Weis[1], Robert B. Trumbull[1], Filipe Pinto[2,3], Pilar Lecumberri-Sanchez[4,5], Franziska D.H. Wilke[1]

---

[1]GFZ German Research Centre for Geosciences, Telegrafenberg, 14473 Potsdam, Germany

[2]Beralt Tin & Wolfram (Portugal) S.A., Barroca Grande, 6225-051, Castelo Branco, Portugal

[3]Institute of Earth Sciences (ICT), Rua do Campo Alegre 687, 4169-007 Porto, Portugal

[4]Department of Geosciences, University of Arizona, Tucson, Arizona 85721, USA

[5]Department of Earth and Atmospheric Sciences, University of Alberta, Edmonton T6G2E3, Canada

---

Article published in Chemical Geology (2017, vol. 468, 1-16, doi: 10.1016/j.chemgeo.2017.07.011)

Abstract — Tourmaline is a locally abundant hydrothermal mineral in the wall rocks surrounding the W-Sn-Cu mineralized veins in the Panasqueira deposit (Portugal) and a minor phase within the veins themselves. Tourmaline chemical and boron-isotope compositions have been determined from three settings: (1) pervasive fine-grained tourmalinization zones in wall rocks within 10 cm of the veins, (2) coarser tourmaline in wall rock-hosted fault zones, and (3) needle-shaped tourmaline from late-stage vugs in the quartz veins. All tourmalines from Panasqueira have ferromagnesian compositions with significant octahedral aluminum contents and variable X-site vacancies. Tourmaline compositions show significant chemical variations at the grain and sample scale but are homogeneous on the deposit scale. Tourmaline is typically optically and chemically zoned, showing significant increases in Fe and F and decrease in Mg, Ca and Al from core to rim. Moreover, as a general trend, Al increases and Mg decreases with proximity to the vein contact. The observed chemical variation seems to have been controlled mainly by the vectors: $FeMg_{-1}$; $^{X}\square AlNa_{-1}(R^{2+})_{-1}$; $^{X}\square Al(OH)Na_{-1}(R^{2+})F_{-1}$; $(R^{2+})(OH,F)Al_{-1}O_{-1}$ and $^{X}\square Al_2ONa_{-1}(R^{2+})_{-2}(OH,F)_{-1}$.

The total range in tourmaline $\delta^{11}B$ values from the Panasqueira W-Sn-Cu deposit is from –3.7 to –12.7 ‰, including tourmaline from the three settings. The calculated B-isotope composition of the hydrothermal fluid based on the average tourmaline composition of –9 ‰ and an estimated alteration temperature in the wall rocks, based on Ti-in-quartz thermometry, of 500°C is –7.1 ‰. This isotopic composition is permissive of a boron source from local metasediments or an S-type granite, but the high boron concentration in the wall rocks, with >50 vol% tourmaline, along with the typical element association of Panasqueira (W, Sn, F, Nb, Ta, Rb) makes a granitic source more likely. Late-stage tourmaline needles in vugs within the mineralized veins show the same patterns and ranges in both chemical and boron isotope composition, suggesting that exsolved magmatic fluids were injected in at least two pulses.

The variations in chemical and boron isotopic compositions of tourmaline combined with estimates from Ti-in-quartz thermometry suggest that hydrothermal ore formation is associated with fluid cooling and geochemical fluid-rock interactions.

Key-words: Tourmaline; Boron isotopes; SIMS; Ore deposits; Panasqueira; Magmatic-

hydrothermal systems

3.1 Introduction

The Panasqueira W-Sn-Cu deposit in Central Portugal (Figure 3.1A) is Europe's largest tungsten deposit (the 9th largest worldwide), with over 110,000 tons of wolframite concentrate produced since 1947 (Shedd, 2017). The deposit consists of a swarm of sub-horizontal, hydrothermal quartz veins in proximity to the greisenized cupola (greisen) of a Variscan S-type granite (Figure 3.1B). The veins crosscut the metasedimentary host rocks and contain a variety of ore minerals, the most important economically being wolframite [(Fe,Mn)WO_4], cassiterite (SnO_2) and chalcopyrite ($CuFeS_2$). The Panasqueira granite has been proposed to be the source of the metals (Bloot and de Wolf, 1953; Clark, 1970; Neiva, 2008) and the cupola has been interpreted to play a critical role for channeling magmatic-hydrothermal fluids (Kelly and Rye, 1979). However, underground exposures show that mineralized veins crosscut the cupola, and the origin of the mineralizing fluids is still debated, with some workers favoring non-magmatic fluids of meteoric origin, which may have interacted to variable degrees with the rocks they were flowing through (Burnard and Polya, 2004; Kelly and Rye, 1979; Noronha et al., 1992; Polya, 1989, 1988*a*).

The greenschist-facies pelitic to psammitic schists (Beiras Group in Figure 3.1B and C; undifferentiated metasediments in Figure 3.1A) hosting the Panasqueira ore veins contain large amounts of tourmaline (up to 70 vol%), which are interpreted as the result of hydrothermal alteration dominantly predating the ore-forming event (Foxford et al., 1991; Marignac, 1982; Polya et al., 2000). Tourmaline has further been described as a minor or accessory mineral from pre-ore to post-ore stages at the deposit. The value of tourmaline as a chemical and isotopic tracer of fluid-rock or fluid-melt interaction has been demonstrated in many previous studies (see reviews in Marschall and Jiang, 2011; Slack, 1996; Slack and Trumbull, 2011), including some from the Central Iberian Zone which the deposit is associated with (Pesquera et al., 2013, 2005; Ribeiro da Costa et al., 2014; Roda-Robles et al., 2011). However, the tourmaline at the Panasqueira deposit has so far been largely unstudied, the exception being a few analyses in the regional study of Variscan ore deposits in Portugal by Neiva et al. (2007).

In this paper we explore the chemical and B-isotope variations in tourmaline from the Panasqueira deposit based on a suite of new samples from both former and active mining areas covering the spatial extent of the vein system currently exposed in the underground mine, and the temporal range of tourmaline formation from early to late stages in the paragenetic sequence (Figure 3.1C). The results suggest that hydrothermal ore formation is associated with fluid cooling and geochemical fluid-rock interactions. We find that the boron isotopic composition of tourmaline is remarkably homogeneous across the deposit, with values consistent with crystallization from a magmatic-hydrothermal fluid derived from an S-type granite. In contrast, the chemical composition of tourmaline shows significant zoning that suggests several fluid pulses in a dynamic hydrothermal system.

3.2 Geological background and previous work

The Panasqueira deposit is located in the Beira Baixa region (central Portugal), about 34 km west of Fundão (Figure 3.1A).The deposit is hosted by the Beiras Group (Grupo das Beiras) of Late Ediacaran to Early Cambrian age (Figure 3.1A), which was regionally metamorphosed in greenschist facies during the early compressive stages of the Variscan Orogeny (Romão et al., 2013). The Beiras Group consists of biotite-chlorite schists, phyllites and dark, fine-grained quartzites whose protoliths were a sequence of argillaceous to arenaceous shales, greywackes and fine-grained sandstones (Bloot and de Wolf, 1953; Conde et al., 1971; Kelly and Rye, 1979; Thadeu, 1951*a*). The depositional environment has been described as a flysch-type setting in a continental basin, possibly with some marine influence (Thadeu, 1951*a*).

The Panasqueira Granite is part of the Variscan granitic complex of northern Portugal (Figure 3.1A). It is a peraluminous S-type, two-mica granite (muscovite < biotite) with fine- to medium-grained porphyritic texture (Kelly and Rye, 1979). The emplacement of the granite produced a contact metamorphic aureole of biotite-chlorite hornfels, with minor cordierite and chiastolite, the so-called spotted schist (Bussink, 1984; Conde et al., 1971). The upper part of the granitic batholith includes a cupola of a greisenized granite with a silica cap (Figure 3.1B) that is cut by some of the ore veins (Burnard and Polya,

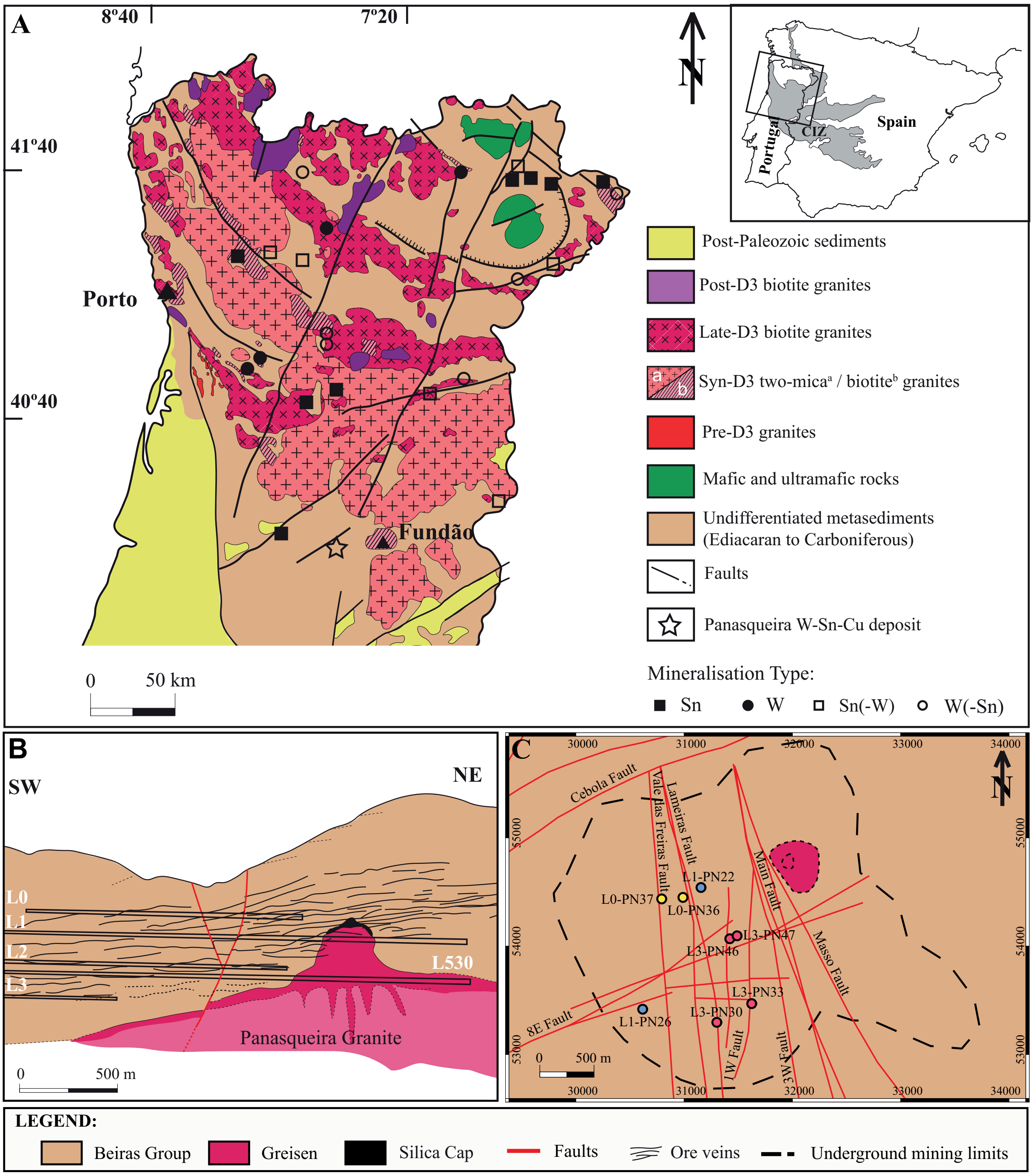

Figure 3.1: (A) Simplified geological map of northern and central Portugal with the representation of the main granite types and metasedimentary rocks. The undifferentiated metasediments include the Beiras Group hosting the Panasqueira deposit (modified after Derré, 1982; Mateus and Noronha, 2010; Noronha et al., 2013; Pereira et al., 1993; Sant'Ovaia et al., 2013). CIZ – Central Iberian Zone. **(B)** Schematic cross section (vertical exaggeration 3×) of the Panasqueira vein system, greisen (cupola) and Panasqueira granite (modified after Oosterom et al., 1984). L0 – Level 0 at 680 m; L1 – Level 1 at 620 m, L2 – Level 2 at 560 m, L530 – Level 530 (main water drainage level) at 530 m and L3 – Level 3 at 470 m above sea level. **(C)** Geological map showing the main geological elements and the sample location at Panasqueira Mines (map: courtesy of Beralt Tin and Wolfram (Portugal)).

2004; Bussink, 1984; Kelly and Rye, 1979; Polya, 1989, 1988*a*; Thadeu, 1951*a*). Neiva (1987*a*) described the mineralogical and chemical changes of the Panasqueira granite due to greisenization and found that neither the granite nor greisen rocks contain tourmaline. The deposit is cut by a number of subvertical faults with mostly NNW-SSE and ENE-WSW trends (Figure 3.1C). Although some studies emphasize the greisen cupola as the source of the magmatic-hydrothermal fluids, Polya (1989, 1988*a*) proposed that the subvertical faults acted as major pathways for hydrothermal fluid flow during ore precipitation noting that the Nb content in wolframite from the quartz veins increases towards these structures. However, the vertical faults crosscut the mineralized veins indicating that faulting either postdates mineralization or that several mineralization episodes have taken place.

Mineralization of wolframite, cassiterite, and chalcopyrite is predominantly hosted in the veins, with minor stringers and lenses of sulfide minerals in the altered metasedimentary wall rocks. The veins are mainly composed of gangue quartz, muscovite and minor carbonates, apatite, topaz, fluorite, tourmaline, rutile, ilmenite, arsenopyrite, sphalerite, pyrite, marcasite, stannite and pyrrhotite (*e.g.,* D'Orey, 1967; Kelly and Rye, 1979; Neiva, 2008; Polya, 1989; Polya et al., 2000; Thadeu, 1951*a*; Wimmers, 1985). The paragenetic sequence was subdivided by Kelly and Rye (1979) into four stages of mineralization: (1) oxide-silicate stage, (2) main-sulfide stage, (3) pyrrhotite alteration stage and (4) late carbonate stage, whereby (1) and (2) constitute the economically relevant ore stages for oxides (wolframite, cassiterite) and sulfides (chalcopyrite), respectively. Further studies proposed two preore stages with formation of a crack-seal quartz seam and muscovite selvages (*e.g.,* Polya et al., 2000). Tourmaline is reported to occur during all of these stages, with a predominance in the early stages (*e.g.,* Kelly and Rye, 1979; Polya et al., 2000). Lourenço (2002) describes a second stage of Sn-Cu mineralization, which he proposed was triggered by the emplacement of a second granite. This mineralization, with cassiterite and chalcopyrite as ore minerals but lacking wolframite, occurs in fractures cross-cutting the main veins. Associated minerals are tourmaline, apatite and siderite. There is a strong variation in the mineralogy of the vein selvages in the deposit although a clear spatial pattern in these variations is not apparent. Typically, the quartz fracture-filling is rimmed by a muscovite selvage up to 4 cm thick and commonly intergrown with arsenopyrite but in other parts of the deposit, especially in the southern part, the muscovite selvage is absent and a variably thick topaz-rich selvage forms instead. Less frequent are veins where both topaz and muscovite selvages are absent. Bussink (1984) distinguished three main alteration zones in the host rocks at progressively greater distance from the quartz veins: (1) an inner, tourmaline-rich zone 2 to 30 cm thick, (2) a muscovite-rich zone consisting mainly of muscovite, quartz, altered cordierite and minor tourmaline or topaz, whose extent depends strongly on the host rock composition and the presence of joints, and (3) a chlorite-muscovite-rich zone farthest from the veins.

Stable isotope studies of H, O, C, S and N in gangue and ore minerals from Panasqueira have been interpreted as evidence for interaction between fluids from more than one source and the host rock (*e.g.,* Bussink, 1984; Kelly and Rye, 1979; Noronha et al., 1992). The role of magmatic fluids derived from the Panasqueira granite in the early stages of mineralization is unclear; some interpretations suggest an exclusive magmatic influence (Clark, 1970; Kelly and Rye, 1979) and others suggest an early role of meteoric fluids (Kelly and Rye, 1979; Polya et al., 2000). Bussink (1984), Kelly and Rye (1979), Polya et al. (2000) and Lecumberri-Sanchez et al. (2017) reported that fluids at Panasqueira are dominantly low to moderate salinity fluids (5–10 wt% NaCl eq.) trapped at temperatures between 230 and 360 °C. Polya et al. (2000) attributed the progression from oxide-dominated to base-metal sulfide paragenesis to an increasing importance of reduced (presumably meteoric) fluids interacting with or derived from organic-rich metasediments.

Finally, helium isotopic data from wolframite and arsenopyrite were taken as evidence for a mantle component in the ore fluids (Burnard and Polya, 2004). Foxford et al. (2000) proposed a structural model for vein formation whereby sub-horizontal fractures that initially formed in a compressional stress regime underwent episodic dilation and vein-filling as lithostatically pressured (magmatic) fluids were injected into a hydrostatically pressured fluid regime. They showed that the observed pressure range of 100 to 20 MPa reported in fluid inclusion studies from the veins (Bussink, 1984; Kelly and Rye, 1979) is consistent with the difference between lithostatic and hydrostatic fluid pressure at about 3 km paleodepth (Foxford et al., 2000).

3.3 Tourmaline occurrence and sampling strategy

Tourmaline is ubiquitous in the altered metasedimentary wall rocks around mineralized veins. The current underground mine in Panasqueira extends about 2 km from the cupola to the west and southwest (Figure 3.1C) and is worked at four depth levels spaced 60 m (L0 to L2) and 90 m (L2 to L3) apart. Our sampling covers nearly the full spatial extent of the deposit both horizontally and vertically. We also sampled the different host rock lithologies involved (spotted schist and fine-grained schist) and, where possible, divided the samples into sections at variable distance from the vein contact. In addition, we collected tourmaline from the veins representing different stages in the temporal evolution of the mineralization (main-stage tourmalinization and late-vug fillings). The part of the greisen cupola exposed in the mine area contains no tourmaline and the Panasqueira granite has been described as tourmaline-free (Neiva, 1987*a*).

3.3.1 Tourmaline in the wall rock alteration zones

Two types of metasediments are distinguished in this study: spotted schists (SS) (Figure 3.2A) and fine-grained schists (FGS) (Figure 3.2B). The spotted schists were affected by contact metamorphism (*e.g.,* Bussink, 1984; Conde et al., 1971) and are coarser grained with porphyroblastic textures. The slightly flattened spots are sub-parallel to the main foliation. Far from the deposit, the spots contain a quartz-biotite-chlorite-

Figure 3.2 *(facing page)*: **(A)** and **(B)** Hand specimens of tourmaline-rich rocks from the contact with the mineralized veins: **(A)** corresponds to a spotted schist (SS) and **(B)** to a fine-grained schist (FGS). The stripes in the samples result from the saw cut. **(C)** and **(D)** Photomicrographs illustrating some petrographic features of tourmaline-rich rocks: detail **(C)** from a SS showing a quartz-rich spot surrounded by a tourmaline-rich matrix and **(D)** from FGS showing the transition from a quartz-rich layer to a tourmaline-muscovite-rich layer (plane-polarized light). **(E)** and **(F)** Back-scattered electron (BSE) images of: **(E)** oscillatory zoning in tourmaline, the dots correspond to the location of EPMA analyses and the values to the respective FeO (wt%) content and **(F)** prismatic subhedral tourmaline from metasediments showing oscillatory zoning and mineral inclusions. **(G)** and **(H)** Photomicrographs illustrating special features of tourmaline: **(G)** coarser-grained tourmaline from a fault-related setting and **(H)** contact between a SS and a muscovite selvage type vein; green-brownish tourmaline occurs within the wall rock and tourmaline slivers within the first millimeters of the vein (plane-polarized light). **(I)** Photograph of tourmaline needles associated with carbonates and quartz. Tur – tourmaline, Ms – muscovite, Qtz –quartz, Cb – carbonates, Py – pyrite, Mnz – monazite, Ap – apatite.

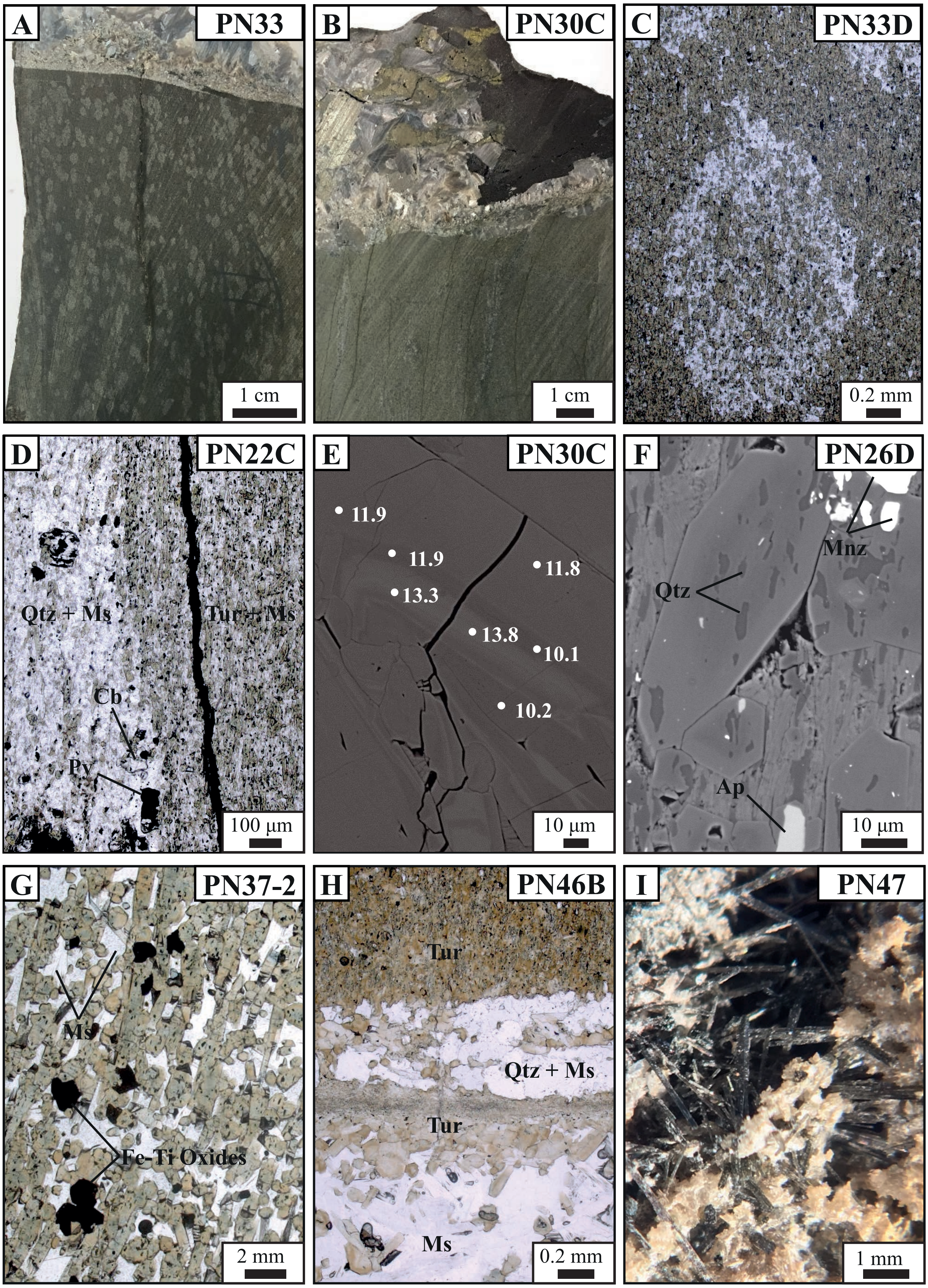
A
PN33
1 cm
B
PN30C
1 cm
C
PN33D
0.2 mm
D
PN22C
Qtz + Ms
Tur + Ms
Cb
Py
100 µm
E
PN30C
11.9
11.9
11.8
13.3
13.8
10.1
10.2
10 µm
F
PN26D
Mnz
Qtz
Ap
10 µm
G
PN37-2
Ms
Fe-Ti Oxides
2 mm
H
PN46B
Tur
Qtz + Ms
Tur
Ms
0.2 mm
I
PN47
1 mm

(cordierite) assemblage but in the vein contact zones they consist of quartz and tourmaline while the matrix is mainly comprised of tourmaline with accessory muscovite and quartz (see Figure 3.2C). The fine-grained schists typically display an alternation of quartz-rich and tourmaline-muscovite-rich layers (see Figure 3.2D), inheriting the layered pelitic-psammitic texture of the Beiras Group phyllites.

Tourmaline forms very fine (<0.1 to 0.3 mm diameter), prismatic subhedral to euhedral zoned crystals, with a pleochroism ranging from pale to deep green in the core to beige and brown in the rims (Figure 3.2D). The color zoning is less evident in the FGS than in the SS due to the smaller grains (<0.1 mm). Back-scatter electron (BSE) images (Figure 3.2E) show simple, concentric zonations with consistently darker cores and lighter rims for the majority of tourmaline crystals, while only few grains show fine-scale zonations, which can be oscillatory or patchy zoning in the cores. Exceptionally, several grains in sample PN30 show reverse zoning with darker rims in BSE images. Tourmaline in the fine-grained schist sample PN22 is unzoned. A common feature of all tourmalines is the presence of quartz, apatite and monazite inclusions, which are typically more abundant in the cores than rims (Figure 3.2F). Where the metasediments are cut by faults, there is a tendency to form assemblages of coarser grained tourmaline, muscovite, apatite, carbonates, chlorite, sulfides, and Fe-Ti oxides (Figure 3.2G). In the alteration zones of both spotted schists and fine-grained schists, tourmaline occurs together with quartz, muscovite, Fe-Ti oxides (locally containing Sn), rutile, zircon, apatite and siderite. Sulfide minerals, including arsenopyrite, pyrite, chalcopyrite and sphalerite, occur as disseminations and in thin quartz-sulfide-veinlets while wolframite is absent. The quartz-sulfide veinlets crosscut the alteration zones and are clearly later. The textural relations between tourmaline scale some samples show textural evidence for tourmaline recrystallization related to chalcopyrite and sphalerite precipitation and arsenopyrite is clearly coeval with early tourmaline. However, at the deposit scale the relations between tourmalinization of wall rocks and ore formation are not clear.

3.3.2 Tourmaline in the mineralized W-Sn-Cu veins

Tourmaline is rare in the veins themselves and, where present, typically develops at the wall rock contact or in slivers of wall rock subparallel to the vein contact (Figure

3.2H). The vein-hosted tourmaline is typically coarser (0.05–0.3 mm) than tourmaline from the host rock (e.g. Figure 3.2H) but still <5 mm in maximum dimension. Aside from a larger grain size and few mineral inclusions, tourmaline from the vein margins displays the same features described for tourmalines from the host rock. The paragenetic relation of vein-margin tourmaline and the ore minerals is typically hard to ascertain because they are rarely in contact. Vein-margin tourmalines appear to be coeval with wolframite, but the textural relationship with sulfides from the main sulfide stage is unclear. An important feature of tourmaline at Panasqueira is the occurrence of euhedral, radial clusters of tourmaline needles up to 1 cm long associated with euhedral apatite, quartz and carbonate crystals in vugs or pockets near the vein contacts (Figure 3.2I). Locally, the acicular tourmaline is overgrown by prismatic quartz crystals. The vugs are commonly related to late fractures, which may correlate with the pyrrhotite alteration stage proposed by Polya et al. (2000) and/or the late Sn-Cu mineralization recognized by Lourenço (2002). This, and the association with carbonates that are otherwise known to form late crosscutting veins, suggests that the acicular vug-filling tourmaline formed after the main mineralization event.

3.4 Analytical methods

3.4.1 Electron microprobe

The chemical compositions of tourmaline were determined on polished thin sections using a JEOL Superprobe JXA-8230 (EPMA) at GFZ Potsdam, equipped with a LaB6-cathode and 5 wavelength-dispersive spectrometers. We applied an accelerating voltage of 15 kV, a beam current of 10 nA with a beam diameter of 5 μm. The following standards were used: orthoclase (Si, Al, K), fluorite (F), rutile (Ti), diopside (Ca, Mg), tugtupite (Cl), BaSi2O5 (Ba), albite (Na), hematite (Fe) and rhodonite (Mn). Counting time on peaks were twice those on backgrounds, with 10 s for Si, K, and Na; 20 s for Al, F, Ti, Ca, Cl, Mg, Fe and Mn and 30 s for Ba. X-ray intensities of Si, K, and Na were acquired first and simultaneously. The structural formulae and site allocation of tourmalines were calculated from EPMA data by normalizing the sum of T + Z + Y cations to 15, assuming no vacancies (or deficiencies) in the T, Z, or Y sites as suggested by Henry et al. (2011) for Li-poor tourmaline. Estimates of the B_2O_3 and H_2O contents were obtained by stoichiometry, considering B= 3 apfu and OH +F =4 apfu. We obtained a total of 650 spot analyses from 15 samples.

The Ti concentrations in quartz were determined on 3 polished thin sections using a JEOL JXA-8500F Hyperprobe equipped with a field emission gun and five wavelength-dispersive spectrometers at GFZ Potsdam. Detection limits of 5 ppm for Ti were obtained with a 8 μm diameter beam at 20 kV and 100 nA in accordance to Donovan et al. (2011). Counting times were 500 s on peak, with additional 250 s for background measurements on both sides of the peak. Rutile was used to calibrate Ti. Si and O were calculated using a fixed ratio. We obtained a total of 209 spot analyses from 3 spotted schists samples. Analyses were discarded when a close association with Ti-phases was evident. In total, 174 analyses were considered for further calculations. All EPMA data are provided in Supplement 1.

3.4.2 Secondary ion mass spectrometry

The boron isotope compositions of tourmaline from a subset of 13 samples were determined by secondary ion mass spectrometry (SIMS) using the CAMECA 1280-HR instrument at GFZ Potsdam. This study involved two separate sessions of several days each in June and September 2016. The SIMS analyses employed a nominally 13 keV, 3 nA $^{16}O^-$ primary beam, focused to a ~10 μm diameter spot on larger tourmaline grains (June 2016 session) and 13 keV, 60 pA $^{16}O^-$ beam with a ~5 μm diameter in the smaller grains (Sept. 2016 session). A 3-min pre-sputter was conducted in order to remove the gold coat and establish equilibrium sputtering conditions, prior to each analysis. The mass spectrometer was operated in multi-collection mode (for 3 nA beam current) and mono-collection (for 60 pA beam current), both using faraday cup detectors. The mass resolution $M/\Delta M \approx 2000$ was sufficient to separate the isobaric interferences of $^{10}B^1H^+$ on the $^{11}B^+$ mass station and of $^9Be^1H^+$ and $^{30}Si_3^+$ on the $^{10}B^+$ mass station. A 400 μm diameter contrast aperture, a 4000 μm field aperture and a 50 V energy window were used without any voltage offset. These conditions resulted in a count rate of ~8 MHz for ^{11}B (3 nA) and 160 KHz (60 pA), to which a 46 ns deadtime correction was applied to our pulse counting system. A single analysis consisted of 20 integrations of the sequence $^{10}B^+$

(4 s) and $^{11}B^{+}$ (2 s), resulting in a total time of about 5 min for each analysis including pre-sputtering.

The instrumental mass fractionation (IMF) was determined using two tourmaline reference materials (RM) whose compositions are close to those of the Panasqueira tourmaline. The RMs used are dravite (Harvard mineral collection #108796) and schorl (#112566) described by Dyar et al. (2001), each measured several times during a given day of analyses. An overview of the daily RM results is given in Table 3.1. The within-run uncertainty for an individual analysis (1 sdmean for 20 cycles) was typically ± 0.1-0.2 ‰ and the repeatability of IMF values on each RM varied from day to day (Table 1) but was typically <1 ‰ (1sdmean). For each daily session, we used the mean IMF of all analyses on both schorl and dravite RMs to correct the sample data from that day. The 1 sd/mean value of the combined IMF data was typically less than ± 1.5‰, which is greater than the separate RM repeatabilities. This probably reflects a minor compositional matrix effect (see also Büttner et al., 2016) and is our best estimate for the overall the data were converted to $\delta^{11}B$ values relative to NIST SRM 951, using a $^{11}B/^{10}B$ ratio of 4.04362 (Catanzaro et al., 1970).

Wherever possible we measured rim and core compositions separately and placed SIMS analyses near previously determined microprobe analyses. A correspondence of SIMS and EPMA spot locations was achieved in 201 of 247 cases. However, the small grain size and abundance of mineral inclusions often prevented multiple SIMS analyses. The full dataset is reported in the Supplement 2.

3.5 Results

The sample coverage allows assessment of potential variations in the composition of tourmaline from the Panasqueira deposit related to (1) mineral zoning: core vs. rim; (2) location in alteration zones relative to the vein contact: proximal (<2 cm) vs. distal (>6 cm); (3) host-rock lithology: fine-grained (FGS) vs. spotted schist (SS); and (4) association with fault zones and late vugs.

The spread of sample locations within the Panasqueira mine (Figure 3.1C) also allowed assessment of spatial patterns on the scale of 10s to 100s of meters, resolving

Table 3.1: Summary of SIMS B-isotope analyses of reference tourmalines.

Date	^{11}B/^{10}B	IMF^{a}mean	Repeat. (‰)^{b}	n	^{11}B (‰)^{c}
Schorl (^{11}B/^{11}B = 3.9931 and δ^{11}B = –12.5 ‰)					
10/06/2016	3.825	0.9579	0.19	11	–11.7
13/06/2016	3.823	0.9575	0.26	12	–12.2
14/06/2016	3.931	0.9845	0.24	5	–11.7
08/09/2016	3.780	0.9468	0.80	10	–12.0
09/09/2016	3.793	0.9499	0.62	13	–11.9
12/09/2016	3.794	0.9502	0.67	14	–11.3
13/09/2016	3.794	0.9501	0.92	13	–11.9
14/09/2016	3.793	0.9498	1.10	13	–12.1
15/09/2016	3.793	0.9500	0.75	12	–11.9
Dravite (^{11}B/^{11}B = 4.0169 and δ^{11}B = –6.6 ‰)					
10/06/2016	3.845	0.9571	0.20	11	–6.7
13/06/2016	3.843	0.9567	0.23	21	–7.2
14/06/2016	3.947	0.9827	0.13	4	–7.6
08/09/2016	3.799	0.9456	0.52	8	–7.3
09/09/2016	3.812	0.9489	0.79	13	–7.1
12/09/2016	3.810	0.9485	0.71	15	–7.6
13/09/2016	3.811	0.9489	1.19	13	–7.2
14/09/2016	3.812	0.9491	1.32	14	–7.0
15/09/2016	3.811	0.9486	0.55	12	–7.4

[a] Instrumental Mass Fractionation (^{11}B/^{11}B measured / ^{11}B/^{11}B standard), mean of n analyses.

[b] Repeatability of IMF (standard deviation / mean) * 1000.

[c] Based on corrected ^{11}B/^{11}B ratios using the combined schorl-dravite IMF

different depth levels and variable horizontal distances from the cupola. However, the chemical and boron isotopic compositions showed no systematic variations on the deposit scale.

3.5.1 Chemical composition of tourmaline

3.5.1.1 General features of major element composition and classification.

Tourmaline variations and classifications depend on relative occupancies of major elements on crystallographic sites described by the general formula $XY_3Z_6(T_6O_{18})(BO_3)_3V_3W$ (*e.g.,* Henry et al., 2011). Variations of greatest petrologic interest occur on the X-site (*e.g.*, Na^+, K^+, Ca^{2+}, $\square$ = vacancy), the Y-site (e.g. Fe^{2+}, Mg^{2+}, Al^{3+}, Li^+) and the W-site (e.g. OH^-, O^{2-}, F^-, Cl^-), while the Z-, T- and V-sites are usually fully occupied by Al, Si, and (O, OH), respectively.

Panasqueira tourmalines show a wide range of major-element concentrations, in particular for Fe (0.72–2.25 apfu), Mg (0.14–1.55 apfu) and Al (5.88–6.83 apfu). The minor components Mn and Ti range from near 0 to 0.02 and 0 to 0.13 apfu, respectively. Based on the X- and Y-site proportions, most tourmalines belong to the alkali group and plot within the fields of tourmaline from Li-poor granitoids and metasedimentary rocks (Figure 3.3). The X-site from Panasqueira tourmaline has Na contents of 0.34 to 0.81 apfu (Figure 3.4A-C), and very low Ca (near 0 to 0.19 apfu), K (near 0 to 0.28 apfu) and Ba (near 0 to 0.01 apfu) contents. Exceptional cases with $^{X}\square$ values up to 0.64 pfu classify in the vacancy group and plot in the foitite field (Figure 3.3 A-C; Figure 3.4 D-F). F contents are highly variable (near 0 to 0.71 apfu) with many values between 0.50 and 0.71 apfu, indicative for fluor-variety tourmalines (Figure 3.4 A-C). Contents of Cl are negligible (<0.04 apfu). The average values of tourmaline analyses from each group are listed in Table 3.2.

The strongest variations relate to Fe/(Fe + Mg) ratios, which reflect the exchange vector $\mathrm{FeMg_{-1}}$. Given the low contents of Mn and Li, values of $\sum(\mathrm{Fe} + \mathrm{Mg}) < 3$ apfu indicate the presence of Al in the Y-site (Figure 3.5 D-F), which is further confirmed by Al contents in excess of the 6 apfu (atoms per formula unit) for ideal schorl-dravite (Figure 3.3 D-F; Figure 3.4 D-F). The amount of Al in the octahedral sites ($^{VI}\mathrm{Al} = {}^{Y}\mathrm{Al}$) varies from near zero to about 0.82 apfu (Figure 3.4 D-F and Figure 3.5 A-C). Its positive correlation with X-site vacancies ($^{X}\square$) suggests substantial amounts of Al being incorporated in the Y-site via the alkali-deficient exchange vector $[^{X}\square\mathrm{AlNa_{-1}(R^{2+}_{-1}}]$, deprotonation $[\mathrm{R^{2+}(OH^-,F^-)Al_{-1}O_{-1}}]$, where $\mathrm{R^{2+}}$=Mg + Fe + Mn (Figure 3.4 D-F) and to a minor extent, the vector $^{X}\square\mathrm{Al_2ONa_{-1}(R^{2+})_{-2}(OH,F)_{-1}}$.

Figure 3.3 ***(facing page)*****:** **(A-C)** Ca-X-site vacancy-Na(+K) ternary diagrams (after Hawthorne and Henry, 1999) and **(D-F)** Al-$\mathrm{Al_{50}Fe_{50}}$-$\mathrm{Al_{50}Mg_{50}}$ ternary diagrams (after Henry and Guidotti, 1985) showing the chemical variations of tourmaline. Crosses indicate analyses from the wall rocks proximal to the vein (up to 2 cm distance) and squares indicate analyses distal to the vein (within 6 to 8 cm distance). In plot D, numbers represent the rock types as defined by Henry and Guidotti (1985): (1) Li-rich granitoid pegmatites and aplites; (2) Li-poor granitoids and their associated pegmatites and aplites; (3) $\mathrm{Fe^{3+}}$-rich quartz-tourmaline rocks; (4) Metapelites and metapsammites coexisting with an Al-saturating phase; (5) Metapelites and metapsammites not coexisting with an Al-saturating phase; (6) $\mathrm{Fe^{3+}}$-rich quartz-tourmaline rocks, calc-silicate rocks and metapelites; (7) Low-Ca meta-ultramafics and Cr, V-rich metasediments and (8) Metacarbonates and meta-pyroxenites.

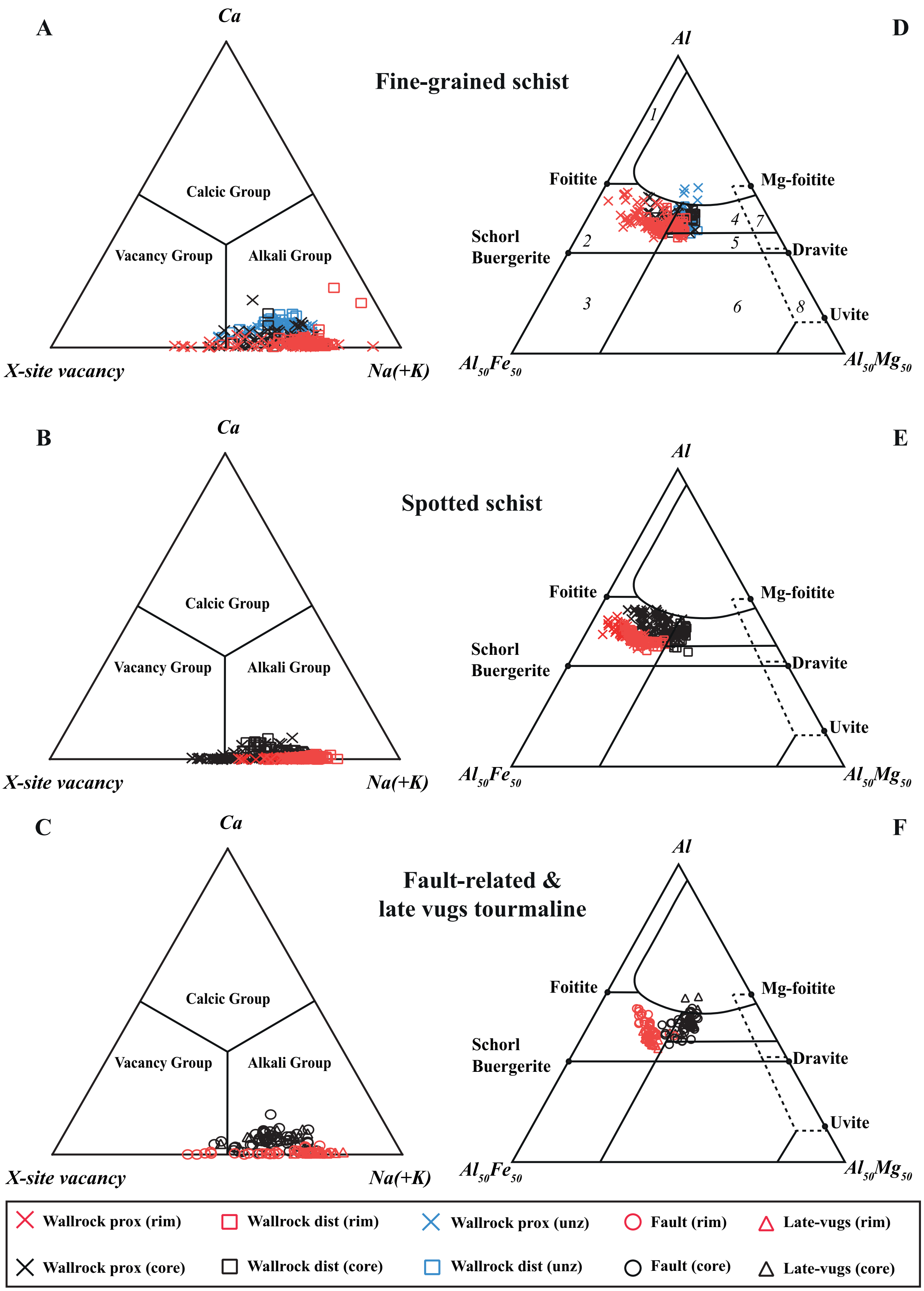
A
Ca
Calcic Group
Vacancy Group
Alkali Group
X-site vacancy
Na(+K)
Fine-grained schist
D
Al
1
Foitite
Mg-foitite
Schorl
Buergerite
2
3
4
5
6
7
8
Dravite
Uvite
Al50Fe50
Al50Mg50
B
Ca
Calcic Group
Vacancy Group
Alkali Group
X-site vacancy
Na(+K)
Spotted schist
E
Al
Foitite
Mg-foitite
Schorl
Buergerite
Dravite
Uvite
Al50Fe50
Al50Mg50
C
Ca
Calcic Group
Vacancy Group
Alkali Group
X-site vacancy
Na(+K)
Fault-related & late vugs tourmaline
F
Al
Foitite
Mg-foitite
Schorl
Buergerite
Dravite
Uvite
Al50Fe50
Al50Mg50
Wallrock prox (rim)
Wallrock dist (rim)
Wallrock prox (unz)
Fault (rim)
Late-vugs (rim)
Wallrock prox (core)
Wallrock dist (core)
Wallrock dist (unz)
Fault (core)
Late-vugs (core)

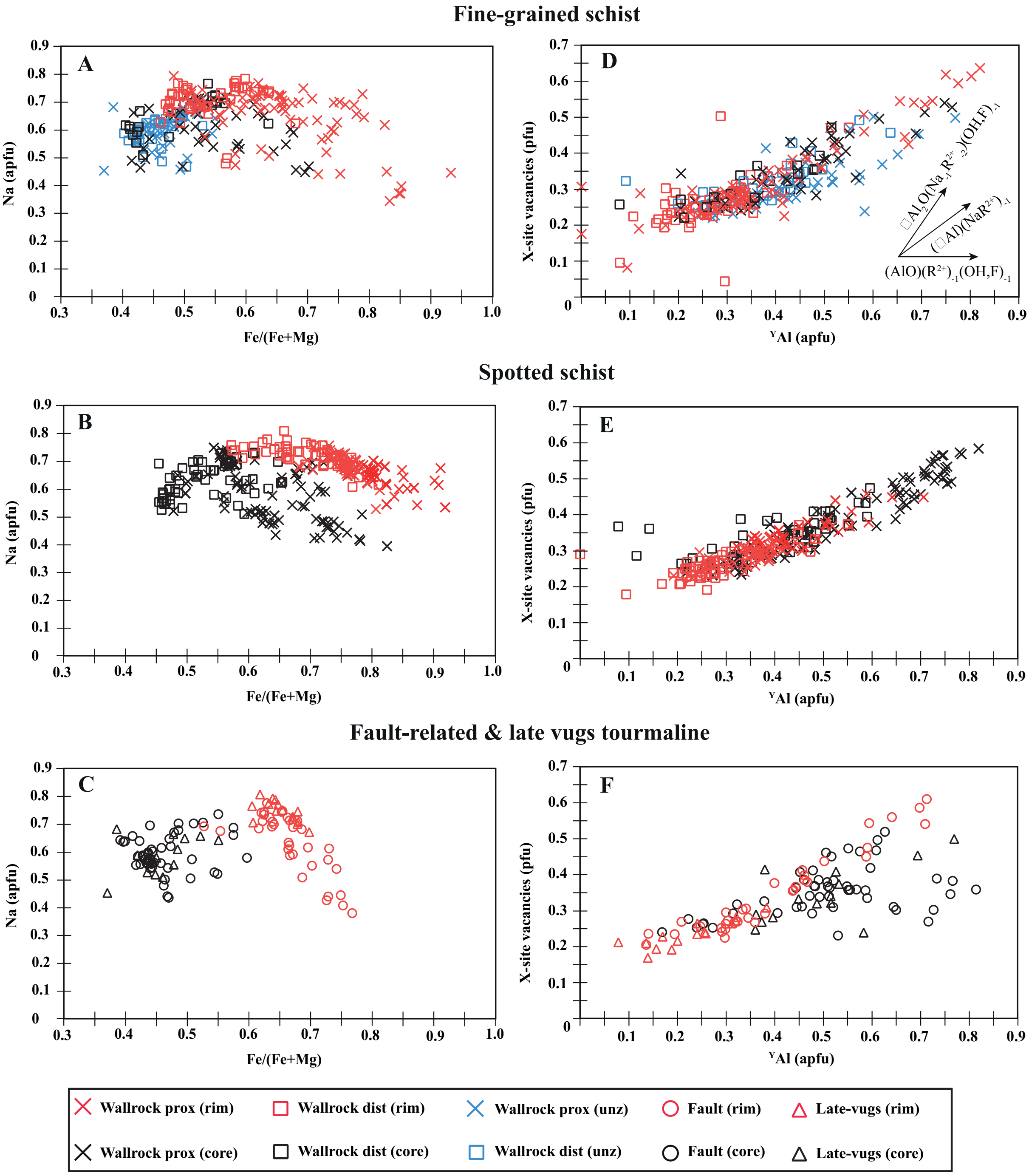

Figure 3.4: (A-C) Compositional variation diagrams showing the atomic ratios of Fe/(Fe + Mg) versus Na (in atoms per formula unit - apfu); and **(D-F)** octahedral Al (^{Y}Al) versus X-site vacancies $^{X}\square$ expressed in terms of atoms per formula unit (apfu) in tourmaline from the different host rocks. Crosses indicate analyses from the wall rocks proximal to the vein (up to 2 cm distance) and squares indicate analyses distal to the vein (within 6 to 8 cm distance). Exchange vectors are indicated by arrows.

Table 3.2: Mean tourmaline compositions and structural formulae.

	Fine grained schist						**Spotted schist**				**Fault zones**		**Late vugs**	
Dist. from vein	*Proximal*			*Distal*			*Proximal*		*Distal*					
Zoning	*Rim*	*Core*	*Unzoned*	*Rim*	*Core*	*Unzoned*	*Rim*	*Core*	*Rim*	*Core*	*Rim*	*Core*	*Rim*	*Core*
SiO_2	36.74	36.92	36.88	37.20	37.49	37.07	36.03	36.68	36.34	36.99	36.50	36.78	36.74	36.88
Al_2O_3	32.45	33.03	33.16	32.17	33.00	32.95	32.11	33.39	31.72	32.84	32.39	33.53	31.80	33.23
K_2O	0.05	0.03	0.04	0.05	0.03	0.04	0.04	0.02	0.04	0.03	0.03	0.04	0.05	0.03
TiO_2	0.40	0.33	0.42	0.40	0.41	0.52	0.53	0.29	0.57	0.47	0.38	0.28	0.49	0.42
CaO	0.05	0.18	0.34	0.13	0.14	0.41	0.02	0.07	0.03	0.14	0.04	0.25	0.03	0.33
BaO	0.09	0.08	0.08	0.08	0.08	0.08	0.08	0.08	0.08	0.08	0.08	0.08	0.08	0.09
Na_2O	2.00	1.88	1.87	2.20	2.02	1.86	2.02	1.81	2.20	1.98	1.94	1.85	2.31	1.82
MgO	3.46	4.49	5.10	4.7	5.14	5.50	2.06	3.53	3.07	4.61	3.24	5.23	3.67	5.09
FeO	11.27	9.48	8.20	9.92	8.74	8.23	13.48	10.49	12.44	9.48	11.51	8.03	12.18	7.77
MnO	0.06	0.06	0.03	0.05	0.03	0.03	0.08	0.05	0.07	0.04	0.07	0.04	0.07	0.03
F	0.85	0.62	0.52	1.01	0.53	0.47	0.85	0.55	1.00	0.61	0.83	0.51	1.05	0.47
Cl	0.00	0.00	0.00	0.00	0.00	0.00	0.00	0.00	0.00	0.00	0.00	0.00	0.00	0.00
Total	87.43	87.10	86.65	87.99	87.59	87.18	87.31	86.96	87.56	87.27	87.01	86.62	88.45	86.16
Structural formula on the basis of 15 Cations (T+ Z+Y)														
F	0.45	0.32	0.27	0.53	0.35	0.25	0.45	0.29	0.53	0.31	0.44	0.27	0.55	0.42

Continued on next page

Table 3.2 – *Continued from previous page*

	Fine grained schist						**Spotted schist**				**Fault zones**		**Late vugs**	
Dist. from vein	*Proximal*			*Distal*			*Proximal*		*Distal*					
Zoning	*Rim*	*Core*	*Unzoned*	*Rim*	*Core*	*Unzoned*	*Rim*	*Core*	*Rim*	*Core*	*Rim*	*Core*	*Rim*	*Core*
Cl	0.00	0.00	0.00	0.00	0.00	0.00	0.00	0.00	0.00	0.00	0.00	0.00	0.00	0.00
OH	3.55	3.68	3.73	3.46	3.65	3.75	3.55	3.71	3.47	3.69	3.56	3.73	3.45	3.58
B	3.00	3.00	3.00	3.00	3.00	3.00	3.00	3.00	3.00	3.00	3.00	3.00	3.00	3.00
Si	6.13	6.10	6.09	6.14	6.13	6.08	6.09	6.09	6.11	6.10	6.12	6.06	6.10	6.11
Al_T	0.00	0.00	0.00	0.00	0.00	0.00	0.00	0.00	0.00	0.00	0.00	0.00	0.00	0.00
Al_Z	6.00	6.00	6.00	6.00	6.00	6.00	6.00	6.00	6.00	6.00	6.00	6.00	6.00	6.00
Mg_Z	0.00	0.00	0.00	0.00	0.00	0.00	0.00	0.00	0.00	0.00	0.00	0.00	0.00	0.00
Al_Y	0.38	0.43	0.46	0.26	0.33	0.37	0.40	0.53	0.28	0.40	0.40	0.51	0.23	0.34
Mg_Y	0.86	1.11	1.26	1.15	1.27	1.35	0.52	0.87	0.77	1.14	0.81	1.28	0.91	1.06
Fe^{2+}	1.57	1.31	1.13	1.39	1.22	1.13	1.91	1.46	1.75	1.30	1.61	1.11	1.69	1.43
Mn^{2+}	0.01	0.01	0.00	0.01	0.01	0.00	0.01	0.01	0.01	0.01	0.01	0.01	0.01	0.01
Ti^{4+}	0.05	0.04	0.05	0.05	0.05	0.06	0.07	0.04	0.07	0.06	0.05	0.04	0.06	0.06
Ca	0.01	0.03	0.06	0.02	0.02	0.07	0.00	0.01	0.01	0.02	0.01	0.04	0.01	0.03
Ba	0.01	0.00	0.01	0.00	0.01	0.00	0.01	0.01	0.01	0.01	0.01	0.01	0.01	0.01
Na	0.65	0.60	0.60	0.70	0.66	0.59	0.66	0.58	0.72	0.63	0.63	0.59	0.74	0.68

Continued on next page

Table 3.2 – *Continued from previous page*

	Fine grained schist						**Spotted schist**				**Fault zones**		**Late vugs**	
Dist. from vein	*Proximal*			*Distal*			*Proximal*		*Distal*					
Zoning	*Rim*	*Core*	*Unzoned*	*Rim*	*Core*	*Unzoned*	*Rim*	*Core*	*Rim*	*Core*	*Rim*	*Core*	*Rim*	*Core*
K	0.01	0.01	0.01	0.01	0.01	0.01	0.01	0.00	0.01	0.00	0.01	0.01	0.01	0.01
$^{X}\square$	0.32	0.35	0.33	0.26	0.31	0.32	0.32	0.39	0.26	0.34	0.35	0.35	0.24	0.28
Fe/(Fe+Mg)	0.65	0.54	0.47	0.55	0.49	0.46	0.79	0.63	0.70	0.53	0.67	0.46	0.65	0.57
$^{X}\square$/(**Na**+$^{X}\square$)	0.33	0.37	0.35	0.26	0.32	0.35	0.33	0.40	0.27	0.35	0.36	0.37	0.24	0.30
Charge	49.42	49.40	49.49	49.41	49.40	49.42	49.41	49.41	49.40	49.41	49.39	49.39	49.32	49.42

Removing the relative influence of the alkali-deficient exchange by projecting compositions onto an Al-R^{2+} compositional plane (Figure 3.6 A-C) after Medaris et al. (2003) results in a negative correlation, which implies that most of the residual Al variation is due to $R^{2+}(OH^-,F^-)Al_{-1}O_{-1}$ and $FeAl_{-1}$ exchanges. Plotting excess charge against $R^{2+}+^{X}\square$ provides a rough minimum estimate of the amount of Fe^{3+} (Figure 3.6 D-F) (Medaris et al., 2003), indicating that most of the variations can be explained by the deprotonation vector and that Fe^{3+} contents are negligible since all data have excess charge. The data deviate from the ideal schorl-foitite/"oxy-foitite" line, suggesting that the incorporation of F is further controlled by $^{X}\square Al(OH)Na_{-1}(R^{2+})_{-1}F_{-1}$(fluor-schorl exchange vector), which in combination with the deprotonation vector results in $^{X}\square Al_2ONa_{-1}(R^{2+})_{-2}(OH,F)_{-1}$.

In summary, the compositional variability of hydrothermal tourmaline from Panasqueira seems to be controlled by a combination of (1) $FeMg_{-1}$; (2) $^{X}\square AlNa_{-1}(R^{2+}_{-1}$; (3) $^{X}\square Al(OH)Na_{-1}(R^{2+})_{-1}F_{-1}$ (4) $R^{2+}(OH^-,F^-)$ $Al_{-1}O_{-1}$ and (5) $^{X}\square Al_2ONa_{-1}(R^{2+})_{-2}(OH,F)_{-1}$. The $FeAl_{-1}$ exchange vector has a small influence, implying that Fe^{3+}-rich species are not important.

3.5.1.2 Variations in tourmaline composition

The color zoning of tourmaline is reflected by systematic chemical variations (black vs. red symbols in Figure 3.3 to Figure 3.6, where the rims are depleted in Mg and enriched in Fe relative to the cores (Figure 3.5 D-F). Rims also generally show a relative depletion in octahedral Al (Figure 3.4 D-F) and Ca (Figure 3.3 A-C) and an increase in F (Figure 3.5 A-C) and Ti (not shown). However, these trends are less regular than the Mg-Fe variations and some rim compositions with the highest octahedral Al correspond with very low F (Figure 3.5 A-C). The FGS tourmaline displays a large overlap of core and rim compositions (*e.g.,* Figure 3.5D), which may reflect the oscillatory zoning and local reverse zoning trends visible in BSE images from this sample (Figure 3.2E). The unzoned tourmaline from sample PN22 more closely resembles the core compositions of the other samples than their rims, especially with respect to Fe, Mg, and Ca (Figure 3.3A; Figure 3.5D), which suggests that rim growth in this sample was insignificant.

Further systematic variations are related to the distance of samples from the vein contact with wall rock tourmaline (FGS and SS), showing lower Mg values near the vein

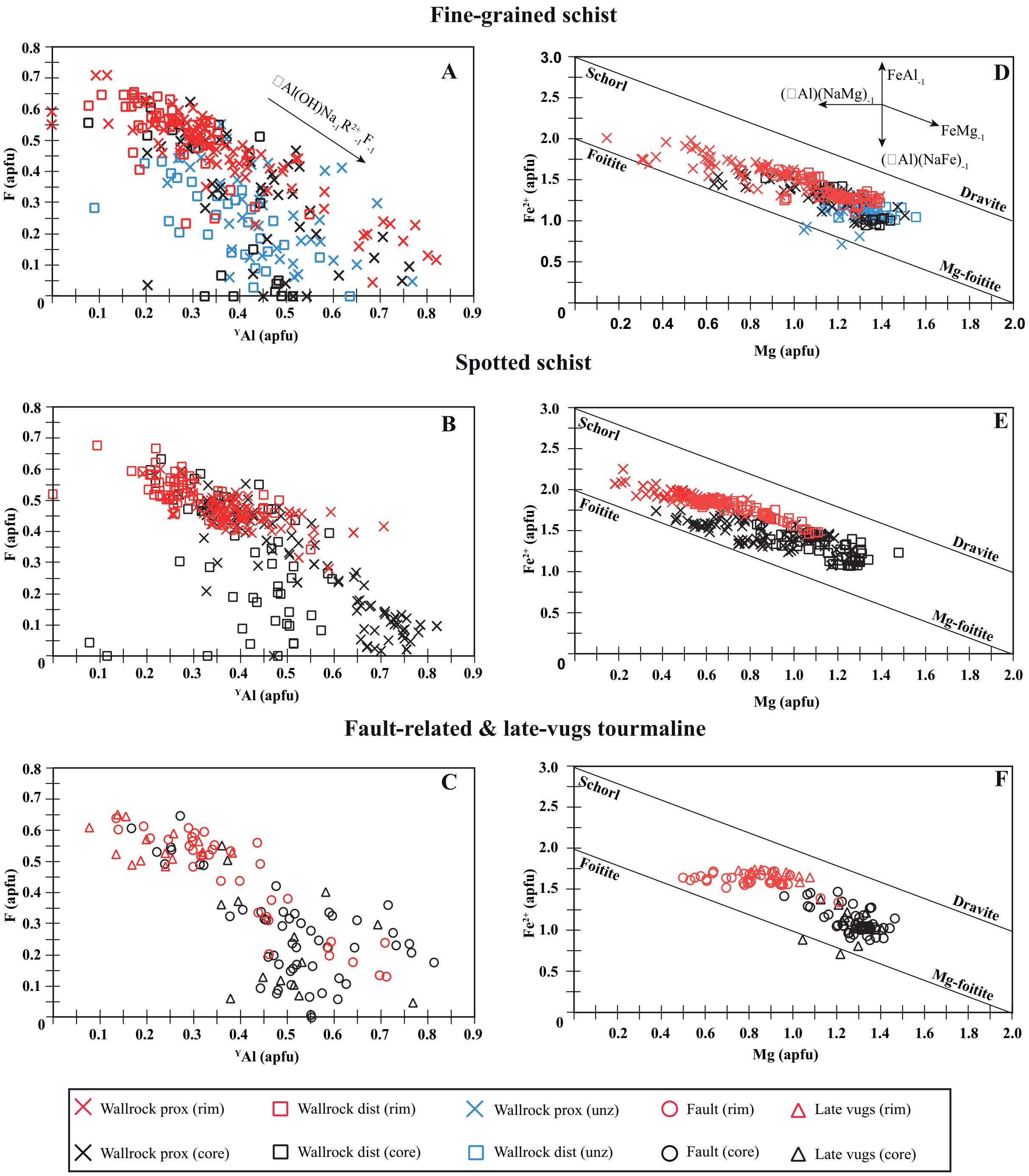

Figure 3.5: (A-C) Compositional variation diagrams showing octahedral Al (^{Y}Al) versus F; and **(D-F)** Mg versus Fe (in atoms per formula unit – apfu). Crosses indicate analyses from the wall rocks proximal to the vein (up to 2 cm distance) and squares indicate analyses distal to the vein (within 6 to 8 cm distance). Exchange vectors are indicated by arrows.

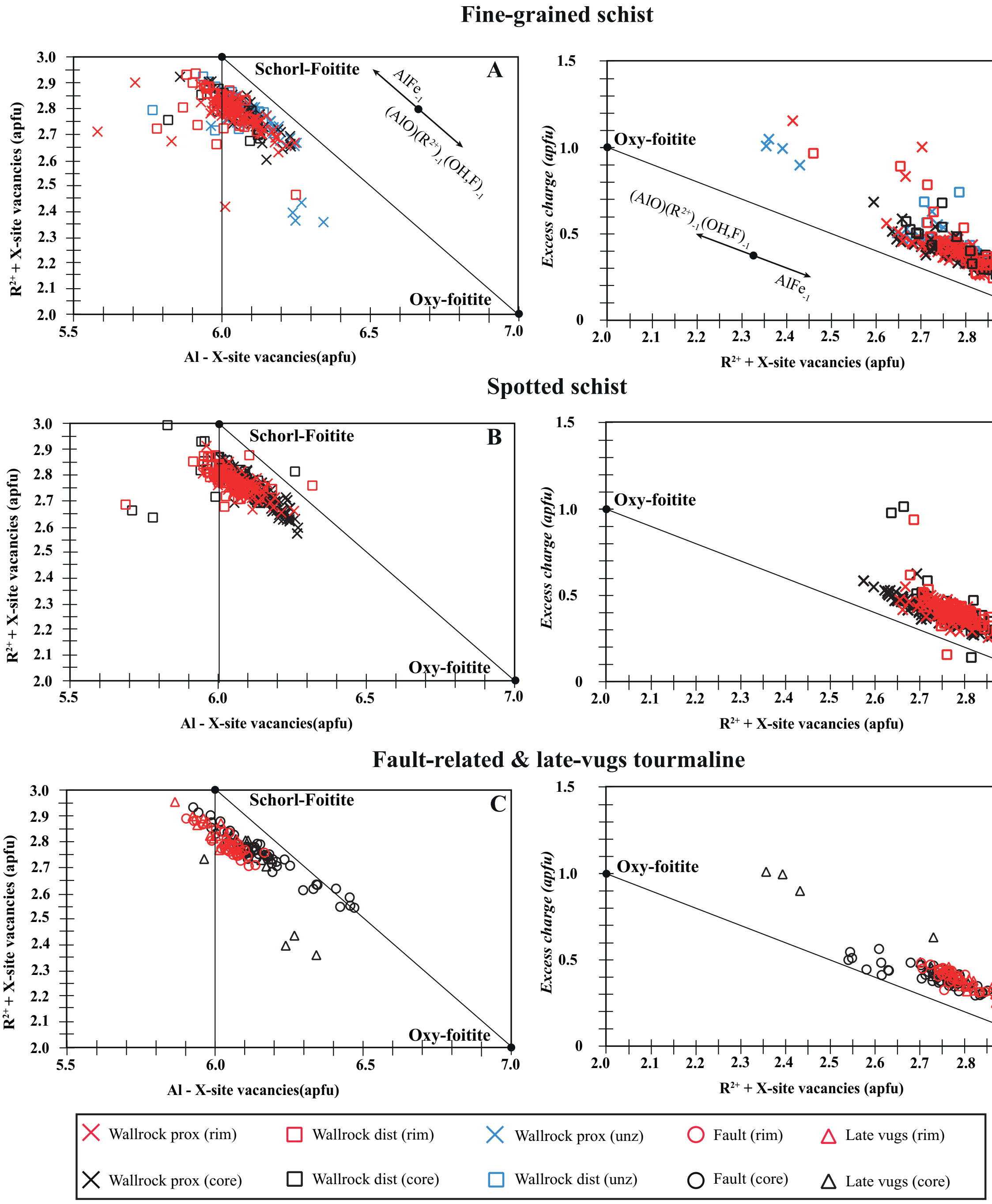

Figure 3.6: (A-C) Compositional variation diagrams showing (Al—X-site vacancies) versus (R^{2+}+X-site vacancies) and **(D-F)** (R^{2+}+X-site vacancies) versus (Excess Charge) (in atoms per formula unit – apfu) in tourmaline from wall rocks, late vugs and fault zone. R represents the sum of Fe (total), Mg and Mn (condensation of the data down the $FeMg_{-1}$ vector) (after Medaris et al., 2003). Exchange vectors are indicated by arrows; the location of the end-member schorl, foitite and "oxy-foitite" are designated by the filled circles. The excess charge is the sum of the total cation charge that is in excess of 49, assuming all Fe as Fe^{2+} (c.f. Henry and Dutrow, 1996). Crosses indicate analyses from the wall rocks proximal to the vein (up to 2 cm distance) and squares indicate analyses distal to the vein (within 6 to 8 cm distance). Exchange vectors are indicated by arrows.

(proximal, crosses) than farther away (distal, squares) (Figure 3.5D, E). This variation is most pronounced in rim compositions (red). Octahedral Al typically increases with proximity to the veins (Figure 3.4D, E). In some samples X-site vacancies show a slight tendency to increase from farther away towards the veins, especially in the cores (Figure 3.4D, E). F is highly variable, with no clear trend as a function of distance from the vein (Figure 3.5A, B). The host-rock lithology (FGS vs. SS) appears to have no systematic influence on tourmaline composition. The compositional range and variability trends of tourmaline from FGS and SS also show no systematic differences. Samples of the FGS tend to show more scatter in variation plots when compared with the SS samples, especially in terms of mineral zoning, which may simply reflect the finer grain size and resolvability of core and rim zones in the analyses. The compositional range of tourmalines from the fault zones and late-stage vugs is the same as the one for the wall rocks, showing the same sense of zoning (Figures 3.3-3.5). It is worth emphasis that the composition of late-stage tourmaline needles in vugs (PN47) is not the same as the rim composition of zoned tourmaline from the wall rock samples although they clearly formed later. Instead, the tourmaline needles show the same increase in Fe/(Fe + Mg) ratio and F contents from core to rim and the same decrease in Ca and Al (Figures 3.3-3.5), albeit generally within a smaller range and with less scatter.

3.5.2 Boron isotopic compositions of tourmaline

All host rock types at Panasqueira show a strong similarity in their δ^{11}B values, in total ranging from –3.7 to –12.7 ‰ with over 90% of the data between –7 and –11 ‰ (Table 3.3, Supplement 2) and a data distribution close to an ideal normal curve (Figure 3.7A), which is slightly skewed to higher δ^{11}B values (skewness =0.596). An important feature of these results is that the B-isotope composition of tourmalines from the wall rock samples varies considerably by more than the analytical uncertainty of 1.5 ‰ and commonly twice that much (Figure 3.7B). Examination of the SIMS analyses that resulted in extreme values on Figure 3.7 showed no irregularities and all data are therefore included in the total range.

The within-sample variations are not related to the core-rim zoning displayed in the chemical variations. The SIMS results show that even in strongly zoned grains that are large enough for separate core and rim analyses, the within-grain variation in δ^{11}B is <2 ‰ and therefore not meaningfully larger than the SIMS uncertainty.

The ranges of B-isotope composition of distal and proximal samples from the same locality are overlapping but not identical (Figure 3.7B). From the 5 sample pairs that can be compared, 4 show consistent trends towards lower δ^{11}B values in the proximal (P) relative to the distal (D) samples, highlighted schematically by red arrows, and one (PN26 AB and D) shows the opposite trend. The median B-isotope values in the sample pairs differ by less than the 1.5 ‰ uncertainty (Table 3.3), but the range of values is commonly offset by 2 or 3 ‰ and the consistency of the difference in 4 of 5 sample pairs suggests that this could be a significant feature.

There is no systematic difference between the two wall rock types FGS and SS. However, in contrast to the wide ranges of δ^{11}B–values of the wall rocks, the samples from the fault zone and the late-stage vugs only show a total range of about 2 ‰. The late-stage acicular tourmaline in vugs has the same B-isotopic composition as the earlier-formed and much more abundant tourmaline in wall-rock alteration zones. Comparing the normal distributions of the different host rock types and taking into account the respective distances from the vein contact, we see a large overlap of the distributions with a tendency of greater variations and a transition to higher δ^{11}B values with increasing distance from the late vugs vein fillings and fault-related tourmaline to the proximal and distal wall-rock samples (Figure 3.7C). However, all of these variations are close to the uncertainty of the measurements and should be treated with care.

3.5.3 Ti-in-quartz geothermometry

Quartz is a ubiquitous phase in the tourmaline alteration zone and textures show that quartz is co-genetic with tourmalinization and precipitated with micas as well as Ti (-Fe) oxides. The latter typically occur as inclusions in quartz and in tourmaline cores. The presence of quartz co-existing with Ti-bearing oxides allows application of the Ti-in-quartz geothermometer to constrain the temperature of tourmaline alteration in the wall rocks.

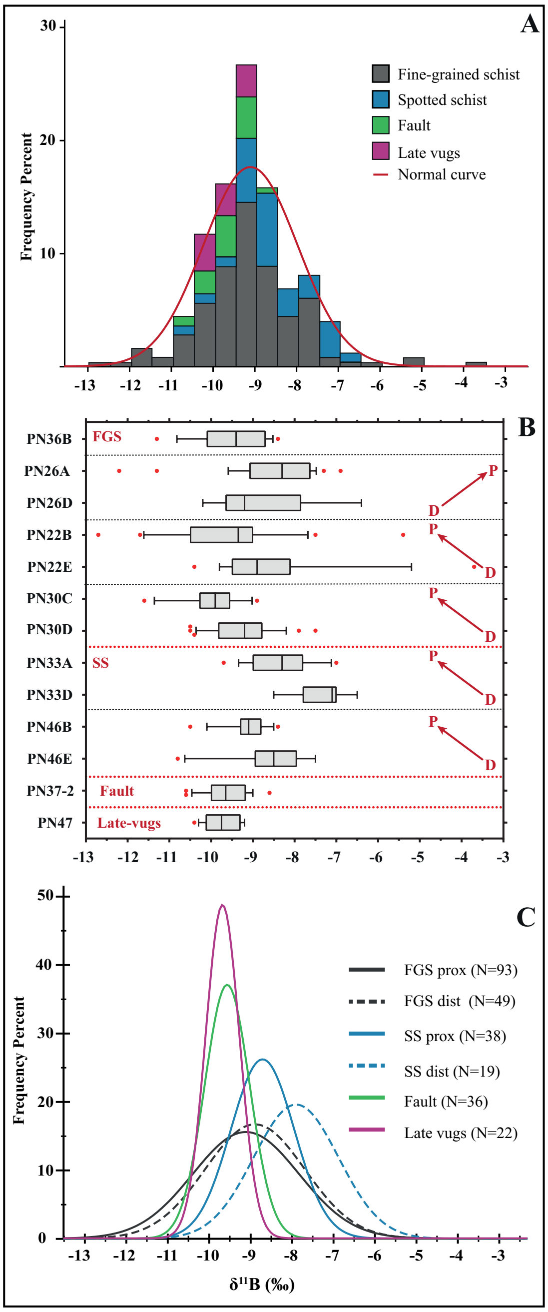

Figure 3.7: Statistic overview of the boron isotope results: **(A)** Frequency percent histogram of tourmalines from the fine-grained schists, spotted schist, fault zone and late vugs. **(B)** Box and whiskers plots; the grey box marks the 25th and 75th percentiles, the line in the box indicates the statistical median and the whiskers extend from the 10th to the 90th percentile; dots beyond the whiskers are individual extreme values. Proximal and distal sample pairs are labeled P and D, for locations <2 cm from veins (P) and 6–8 cm (D). (C) Comparison of the individual normal curves (frequency percent) for tourmaline from the late vugs, fault zone, fine-grained schists (FGS) and spotted schists (SS). The FGS and SS subgroups proximal prox.) and distal (dist.), show a tendency to higher values in the latter (see text).

Table 3.3: Boron isotope compositions of tourmaline.

Sample	*Host rock*	*Location*	*n*	$\delta^{11}B$ *mean*	*SD*	$\delta^{11}B$ *median*	$\delta^{11}B$ *Total Range*	
PN36B	FGS proximal	L0	15	–9.5	0.9	–9.4	–11.3	–8.4
PN22B	FGS proximal	L1	28	–9.5	1.4	–9.4	–12.7	–5.4
PN22E	FGS distal	L1	19	–8.6	1.6	–8.9	–10.4	–3.7
PN26AB	FGS proximal	L1	28	–8.5	1.2	–8.3	–12.2	–6.9
PN26D	FGS distal	L1	9	–8.8	1.2	–9.2	–10.2	–6.4
PN30C	FGS proximal	L3	13	–10.0	0.7	–10.0	–11.6	–8.9
PN30D	FGS distal	L3	30	–9.2	0.7	–9.2	–10.5	–7.5
PN46B	SS proximal	L3	23	–9.1	0.5	–9.1	–10.5	–8.4
PN46E	SS distal	L3	10	–8.6	0.9	–8.5	–10.8	–7.5
PN33A	SS proximal	L3	15	–8.3	0.8	–8.3	–9.7	–7.0
PN33D	SS distal	L3	9	–7.3	0.6	–7.1	–6.5	–8.5
PN37-2	Fault-related	L0	26	–9.6	0.5	–9.7	–10.6	–8.6
PN47	Late vugs	L3	22	–9.7	0.4	–9.8	–10.4	–9.2

FGS: fine-grained schist; SS: spotted schist; L0: level 0; L1: level 1; L3: level 3.

The results from three selected samples were calculated based on the calibration of Thomas et al. (2010) and Huang and Audétat (2012) (Table 3.4, Figure 3.8), which both require an input pressure to obtain the Ti solution in quartz. Following Foxford et al. (2000), we used the range from 100 MPa to 20 MPa. Depending on the pressure, temperatures calculated from Thomas et al. (2010) and Huang and Audétat (2012) differ by 60–100°C. The discrepancy between the two calibrations was evaluated by Thomas et al. (2015) with a third set of experiments and the authors concluded that the Thomas et al. (2010) calibration is more likely to represent equilibrium conditions. On that basis, the most plausible temperature range for quartz formation in the tourmalinized wall rocks at Panasqueira is 549–420°C assuming that alteration occurred at 100 MPa, and 530–404°C for 20 MPa.

Table 3.4: Temperature estimates (T, °C) from Ti-in-quartz geothermometry (N=174) for pressures of 20, 50 and 100 MPa.

	HA-100 *T (°C)*	*HA-50* *T (°C)*	*HA-20* *T (°C)*	*T-100* *T (°C)*	*T-50* *T (°C)*	*T-20* *T (°C)*
Mean	615	578	541	501	491	484
Standard deviation	30	29	27	24	24	23
Median	617	580	544	503	493	486
Minimum	514	481	449	420	410	404
Maximum	673	634	596	549	537	530

HA: Huang and Audétat (2012); T: Thomas et al. (2010)

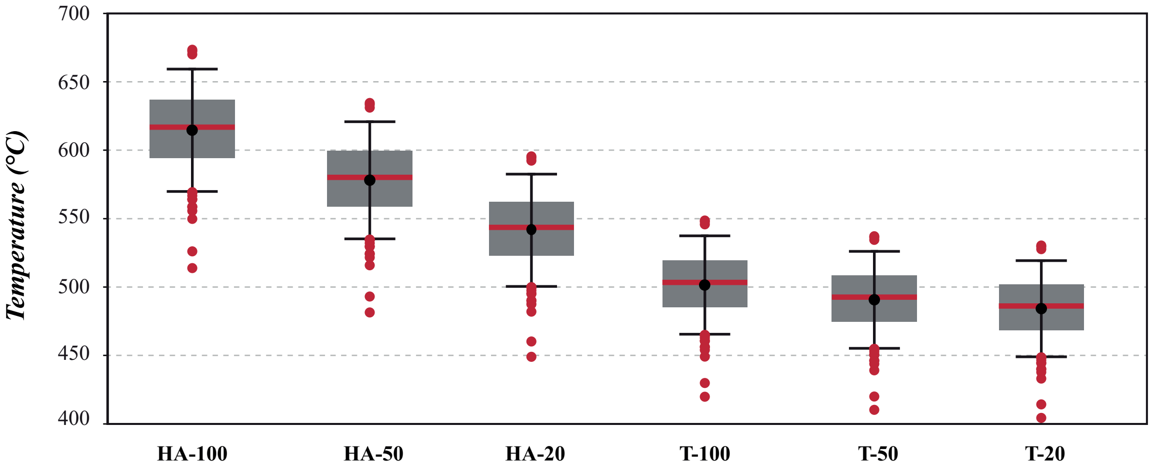

Figure 3.8: Box-whisker plots illustrating the distribution of temperature values for quartz formation (Ti-in-quartz) calculated from Thomas et al. (2010) (T) and Huang and Audétat (2012) (HA), for pressures of 20, 50 and 100 MPa, see text for details. The grey bands cover the 25th to 75th percentiles, the red lines and black dots indicate the median and mean values, resp., and the whiskers extend from the 10th to the 90th percentile; extreme values are shown as red dots.

3.6 Discussion

3.6.1 Tourmaline zoning and host rock vs. fluid controls on composition

This study documents considerable variations in tourmaline chemical compositions and systematic core-rim zoning trends that have implications for the evolution of the Panasqueira hydrothermal system. Variations in tourmaline composition can reflect several processes including changing fluid composition, element partitioning with coexisting minerals, variable wall-rock influence and temperature variations. To interpret the observations at Panasqueira we consider the following constraints on the host rock and fluid compositions, and on the degree of cooling during tourmaline growth. (1) the host rock is a chlorite-biotite schist with Al > Fe > Mg > K >> Ca (Table 3.5, columns 2 to 9); (2) quartz, muscovite, topaz and apatite are the co-precipitating hydrothermal minerals; (3) the hydrothermal fluids responsible for vein mineralization are B-Na-F-rich and Fe-Mg-Ca poor (Table 3.5, column 14); and (4) the likely range of temperatures for the hydrothermal system is ca. 500°C for early alteration to ca. 300°C for the main quartz vein formation.

The wall-rock schists likely contributed Ca, Fe, Mg and Al for the formation of tourmaline, in the main stage of hydrothermal alteration. The nearly complete depletion of Ca in tourmaline rims relative to cores (Figure 3.4 A-C) can be explained by consumption of all available Ca from the schist (0.06–0.4 wt% CaO, Table 3.5). A depletion of Mg and octahedral Al from core to rim could be explained in the same way. The depletion in octahedral Al in rims vs. cores can also reflect the co-precipitation of muscovite.

The behavior of Fe in the wall-rock alteration may have special significance for understanding the ore formation at Panasqueira, because Lecumberri-Sanchez et al. (2017) suggest that Fe from the wall rocks was necessary to allow precipitation of wolframite and Fe-sulfides in the vein. One of the most consistent features of tourmaline zoning is an increase in the Fe concentration and the Fe/(Fe + Mg) ratio from core to rim (Figure 3.4 A-C). Based on the work of Lecumberri-Sanchez et al. (2017), this increase in Fe in tourmaline rims is unlikely to be derived from the hydrothermal fluid, which was shown to be poor in Fe. A simple mass balance calculation based on the concentrations of Fe in the wall rocks (5.5–7.5 wt% Fe_2O_3: Table 3.5) and the modal abundance of tourmaline in alteration zones suggests that all Fe available in the unaltered schist could be used up in the formation of tourmaline cores, so the Fe-enrichment in the rims as a net increase in Fe concentrations in tourmaline rims would require some external addition. Iron could be added from the wall rocks beyond the tourmaline zone. In support of this, Bussink (1984) showed that the muscovite zone is depleted in Fe_2O_3 (and Na_2O) compared with the distal chlorite-muscovite zone, suggesting that Fe has been mobilized to the tourmaline zone.

Table 3.5: Selected compositional data from whole rock samples and quartz-hosted fluid inclusions.

	Unaltered regional schists			**Altered wall rocks at Panasqueira**					**Tourmaline zone**[f]				**Fluid inclusions**
Sample	*P-CG-U*[a]	*P-FG-U*[a]	*B-BG*[b]	*P-CG-A*[c]	*P-FG-A*[c]	*B-A*[d]	*LS-P*[e]	*LS-D*[e]	*Tur 100%*		*Tur 70%*		*MOSS*[g]
									Cores	Rims	Cores	Rims	
Al_2O_3	14.95	20.65	–	11.89	21.51	–	25	14.7	33.3	37	25.8	26	100 ppm Al)
													(highly variable
Fe_2O_3	6.16	7.27	5.83	5.42	7.31	6.37	3.7	5.6	10.4	13	7.3	9.3	<50 ppm Fe
			(3.43 – 7.95)			(3.89 – 9.41)							
MgO	2.17	2.27	2.08	2.02	2.51	2.19	1.7	1.7	4.4	3.3	3.1	2.2	<10 ppm Mg
			(1.29 -– 2.67)			(0.86 – 6.22)							
CaO	0.06	0.38	0.26	0.11	0.22	0.45	0.9	1.9	0.2	0.1	0.1	0	<200 ppm Ca
			(0.14 – 0.70)			(0.16 – 2.01)							
Na_2O	1.44	0.76	1.93	0.67	0.22	1.42	0.2	0.3	1.9	2.1	1.3	1.4	~30000 ppm Na
			(1.28 – 2.84)			(0.23 – 3.07)							
K_2O	2.04	3.92	2.08	3.21	5.92	4.38	9.4	4.3	0.03	0.1	0.02	0	~4000 ppm K
			(1.29 – 2.67)			(1.24 – 7.52)							
S	47	625	–	1455	2997	–	250	4496	–	–	–	–	–
As	6	20	–	42	20	–	5901	2681	–	–	–	–	~100
F	–	–	570	–	–	3800	10579	8762	–	–	–	–	–
			(340 – 970)			(1320 – 17400)							
B	–	–	100	–	–	1570	–	–	–	–	–	–	~2000
			(50 – 200)			(200 – 8000)							
W	3	<DL	<6	15	12	27	95	48	–	–	–	–	~20

Continued on next page

Table 3.5 – *Continued from previous page*

	Unaltered regional schists			Altered wall rocks at Panasqueira					Tourmaline zone[f]				Fluid inclusions
Sample	*P-CG-U*[a]	*P-FG-U*[a]	*B-BG*[b]	*P-CG-A*[c]	*P-FG-A*[c]	*B-A*[d]	*LS-P*[e]	*LS-D*[e]	*Tur 100%*		*Tur 70%*		*MOSS*[g]
									Cores	Rims	Cores	Rims	
			(1 – 10)			(10 – 55)							
Sn	<DL	<DL	2		33	90	50	78	41	–	–	–	–
			(1 – 6)			(23 – 135)							
Zn	77	79	140	102	170	190	99	243	–	–	–	–	~1
			(70 – 390)			(70 – 1160)							
Cu	13	25	23	31	50	55	292	152	–	–	–	–	~1

[a] P-CG-U and P-FG-U correspond to CG-U and FG-U from Polya (1989): unaltered coarse-grained schist and fine-grained schist, respectively.

[b] B-BG corresponds to Panasqueira background (N =18) in Bussink (1984).

[c] P-CG-A and P-FG-A correspond to CG-A and FG-A from Polya (1989): altered coarse-grained and fine-grained schist, respectively.

[d] B-A corresponds to Panasqueira anomalous (N =64) in Bussink (1984).

[e] LS-P and LS-D correspond to proximal and distal from the known cupola, respectively (see Appendix DR3 in Lecumberri-Sanchez et al., 2017).

[f] Tourmaline zone: the calculated composition of a bulk rock composed of 100% Tur and 70% tourmaline, assuming the remaining 30% is pure quartz (this study).

[g] MOSS: fluid inclusions data in quartz intergrown with wolframite from main oxide silicate stage (MOSS) (see Appendix DR3 in Lecumberri-Sanchez et al., 2017).

Fluorine contents increase strongly from core to rim and in the rims particularly, the F contents are inversely correlated with octahedral Al and X-site vacancies (red symbols on Figure 3.5 A-C). The background F concentrations in the host schists are low (Table 3.5), and the increase in tourmaline rims likely reflects a higher fluid-rock ratios during rim growth. Henry et al. (2011) point out that F uptake in tourmaline can also be limited by the crystal chemistry. Thus, a low charge on the X-site (< % vacancies) prevents high F contents in the W-site regardless of the fluid concentration and a high charge at the Y-site (>> charges per formula unit) can also limit F uptake. For the typical compositions of Panasqueira tourmaline with < 50% X-site vacancies and 6.3 charges on the Y-site, these limitations do not apply and the higher F contents in tourmaline rims can be attributed to F concentration in the hydrothermal fluid.

Another factor that can contribute to compositional zoning is cooling of the hydrothermal system and this can be important for Panasqueira because of the difference between the temperature of wall-rock alteration determined by Ti-in-quartz thermometry (ca. 500°C) and the 230–360°C fluid inclusion temperatures in the mineralized quartz veins (*e.g.,* Kelly and Rye, 1979; Lecumberri-Sanchez et al., 2017). Experiments on synthetic Mg tourmaline by von Goerne et al. (2001) showed that cooling from 700° to 500°C at constant fluid composition increased Na contents in tourmaline by 0.1 to 0.3 apfu, the exact amount being dependent on fluid salinity. These experiments are not strictly applicable to the natural system, but we note that typical core-rim increases in the Panasqueira tourmalines are 0.05 to 0.1 apfu (Table 3.2) and within the expected range of a cooling effect. Also, in their study of zoned tourmaline from the San Rafael Sn-Cu deposit in Peru, Mlynarczyk and Williams-Jones (2006) suggested that cooling was the most important factor for a core-to-rim increase in Fe/(Fe + Mg).

3.6.2 B-isotope constraints on the fluid source

The total range of δ^{11}B values in the tourmaline from Panasqueira is considerable (–4 to –13 ‰) but the important feature of this variation is a near-normal distribution of values with a single, strong frequency maximum around –9 ‰ (Figure 3.7A). The two samples where the fluid-rock ratio is expected to be highest (the fault-zone, PN37, and the vug-hosted needles, PN47) are the most homogeneous isotopically and their compositions coincide with the mean and median composition of all samples. Therefore, we use this value in the following discussion of the hydrothermal fluid source. The composition of a hydrous fluid in equilibrium with tourmaline having δ^{11}B = –9 ‰ depends on temperature. From the Ti-in-quartz temperatures of 500°C as a likely value for the temperature of early wall-rock alteration, application of fractionation factors from Meyer et al. (2008) results in a fluid composition of about –7 ‰.

We can then test the hypothesis of a granitic fluid source by estimating what the composition of a granitic melt would be that produces a fluid of –7 ‰. The fluid-melt partitioning of B-isotopes depends on the proportion of trigonal to tetrahedral coordination sites of boron in the melt phase, which is a complex function of alkali-alumina ratio and water content in natural silicate melts (*e.g.,* Dingwell et al., 1996). Empirical studies and spectroscopic measurements of natural melts show that boron is in mixed trigonal-tetrahedral coordination and for lack of better information we assume a ratio of 50:50, following Kaliwoda et al. (2011) and Trumbull et al. (2013). For these conditions and a temperature of 650°C as an estimate for the low-pressure solidus of hydrous, F-rich granitic melt, the B-isotope fractionation factors calculated from molecular dynamics (Kowalski et al., 2013) suggest an offset of about –5 ‰ between granitic melt and fluid. Experimental fluid-melt partitioning studies by Hervig et al. (2002) would suggest –7.2 ‰ but this is probably too high because it corresponds to 100% tetrahedral boron in the melt phase (see discussion in Trumbull et al., 2013). We conclude that the Panasqueira hydrothermal fluid could be derived from a granitic source with δ^{11}B near –12 ‰, which is a typical value for S-type granites worldwide (Trumbull and Slack, 2018).

The Panasqueira granite is not exposed in the mining district and drill-core intersections are hydrothermally altered and contain no tourmaline that might preserve the magmatic composition. However, B-isotope data from magmatic tourmaline in contemporary S-type granites from nearby regions of the Central Iberian Zone are in the same range as from Panasqueira (Figure 3.9, with references in the figure caption). The B-isotope data do not rule out the regional schists as a source of boron for Panasqueira tourmaline because the compositions are close to the crustal average and cannot distinguish a granitic and metasedimentary source (Figure 3.9). However, it is questionable whether the regional schists could supply the great volumes of tourmaline formed in the Panasqueira alteration zones given the low concentrations of B reported at Panasqueira (<200 ppm B, see Table 3.5) and from equivalent metasediments in the Penamacor-Monsanto region in Portugal (<280 ppm B_2O_3, Ribeiro da Costa et al. 2014). Considering the element association typical for evolved granites (W, Sn, F, Nb, Ta and Rb), we consider a boron source from the Panasqueira granite more likely. Finally, we note that the tourmaline from the Panasqueira B-isotope composition agrees well with the ones from of other granite-related W-Sn deposits (Figure 3.9) including Cligga Head W-Sn deposit (SW England) (Drivenes et al., 2015; Smith and Yardley, 1996), Baotan (China) (Zhang et al., 2014) and Baiganhu (China) (Zheng et al., 2016).

3.6.3 Chemical and B-isotope variations during fluid evolution

The shape of the B-isotope distribution curve (Figure 3.7A) suggests that a composition of –9 ‰ reflects the main hydrothermal fluid during formation of most Panasqueira tourmaline. Considering the lack of spatial patterns, the presence of gradual isotope variations rather than gaps in composition, and the fact that late-stage tourmaline in vugs has the same composition as early-formed tourmaline, suggests a uniform fluid composition and gives no indications for mixing of fluids with contrasting composition. The chemical variations from core to rim are not reflected in the B isotopes, because the within-grain δ^{11}B variations are within the uncertainty of the method. However, both the chemical and boron-isotope data show considerable within-sample variations and point towards systematic changes with distance to the vein contact. The interpretation of the chemical variations as fluid cooling and extensive fluid-rock reactions is also consistent with the δ^{11}B variations.

Hydrothermal tourmaline is isotopically lighter than the fluid by a temperature-dependent factor and thus, tourmaline crystallizing during a cooling event will show progressively lower δ^{11}B values. The contrast between Ti-in-quartz thermometry from the tourmaline alteration zone (ca. 500°C) and homogenization temperatures of fluid inclusions in vein quartz (360° to 230°C) suggests a likely range for cooling in the hydrothermal system by about 200°C. From the tourmaline-fluid fractionation factors of Meyer et al. (2008), this would cause a shift of isotopic composition to lower values by about 2 ‰, consistent with the lowest values of –11 to –13 ‰ given the uncertainty of the SIMS

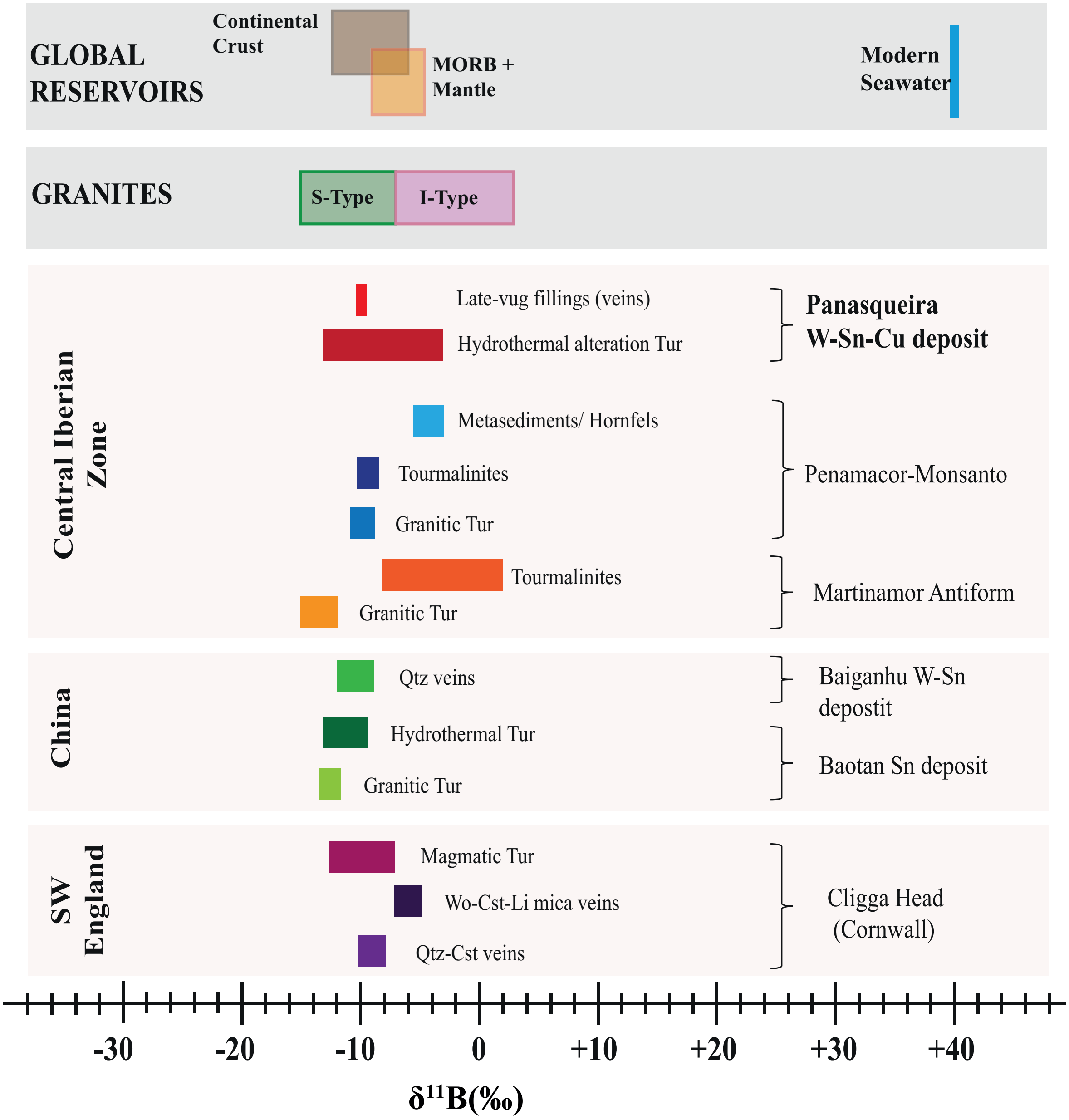

Figure 3.9: Comparison of δ^{11}B values measured in tourmaline samples from the Panasqueira W-Sn-Cu deposit with other related W-Sn deposits and settings from the Central Iberian Zone. S-type and I-type granite δ^{11}B values, as well the main global reservoirs (continental crust, MORB + mantle and seawater) are also shown. Data Sources: Drivenes et al. (2015), Marschall (2018), Palmer and Swihart (1996), Pesquera et al. (2005), Ribeiro da Costa et al. (2014), Smith and Yardley (1996), Trumbull and Slack (2018), Zhang et al. (2014), Zheng et al. (2016). Modified after van Hinsberg et al. (2011a).

measurements.

In contrast to this fluid-dominated scenario which may be appropriate for fluid transport in the open fractures (quartz veins), a rock-dominated scenario with a limited fluid reservoir may apply to the distal alteration zones with limited porosity and quartz veining. In this case, crystallization of abundant tourmaline can deplete the fluid in ^{10}B, meaning that boron in the fluid becomes isotopically heavier. Co-crystallization of muscovite will enhance this effect because the enrichment of ^{10}B in muscovite is stronger than in tourmaline. The shift in fluid composition by tourmaline and/or muscovite crystallization should be most effective farthest from the veins where the fluid-rock ratio is lowest, which can explain the systematic trend to higher δ^{11}B in tourmaline from the distal wall rock samples compared to those closer to the vein contact (Figure 3.7B, C).

In summary, we conclude that the spread in compositional variations of tourmaline can be caused by fractionation processes acting on a single hydrothermal fluid. The proposed processes of cooling and fluid-rock interaction have opposing effects on the δ^{11}B values and will operate at the same time in nature, explaining the near-normal distribution with a skew to higher values, which is also reflected by the larger spread and the shift of the mode of the distribution curves for the distal wall-rock samples as compared to the fault-related and late vugs tourmalines (Figure 3.7C).

3.6.4 Late-stage vug-filling needles and multiple fluid pulses

The similarity of chemical and B-isotopic compositions of the tourmaline needles from the vugs and the other samples is challenging to interpret, since geological observations show that they are separated in time and yet they record the same core-rim variations. Unless tourmaline in the wall rocks continued to grow until the latest stages, so that the shift from core to rim composition is coeval for wall-rock tourmaline and vug-filling needles, we must conclude at least two episodes of tourmaline growth, each showing the same starting composition and same evolution trend, and with the same B-isotope composition.

The structural analyses of the vein system scenario suggest a dynamic system with multiple fluid pulses caused by a repetition of the same processes and fluid compositions (Foxford et al., 2000). Field observations of cross-cutting veins and two or more generations of cassiterite mineralization and tourmaline alteration support the interpretation of more than one pulse of fluid release, potentially even to new magmatic intrusion events (Lourenço, 2002; Pinto, 2014; Pinto et al., 2015).

We have shown that both the chemical and boron isotope variations would be consistent with the scenario of an initial hot, magmatic fluid that cooled during progressive interaction with the wall rocks, resulting in tourmaline growth and zonation. Our data provide no constraints on whether cooling occurred due to conductive heat loss to the host rock or fluid mixing with cooler, convecting meteoric fluids as inferred for other magmatic-hydrothermal deposits (Audétat et al., 1998; Fekete et al., 2016; Mlynarczyk and Williams-Jones, 2006). Fine oscillatory zoning in some Panasqueira tourmaline is consistent with fluid mixing (London and Manning, 1995) but it is not common in the deposit.

Foxford et al. (2000) inferred that near-lithostatic fluid pressures prevailed during vein formation until the late pyrrhotite stage (possibly equivalent to the vug-hosted acicular tourmaline) but in a plausible scenario of multiple fluid pulses from a lithostatically pressurized magma source, there could be episodic incursion of meteoric fluid between pulses that would accelerate cooling and might be recorded in the tourmaline chemistry.

3.7 Conclusions

Tourmaline is a ubiquitous mineral in the alteration zone in wall rocks of the Panasqueira W-Sn-Cu vein-type deposit and an accessory phase within the mineralizing veins. Two stages of tourmaline growth are recognized: early tourmaline in the wall rocks and late tourmaline growing in vugs, suggesting a multi-stage system, where the exsolved magmatic fluids were injected in more than one pulse, considering a single dominant B-source and repetition of the processes in time. The fluid inclusions data indicates that the B-rich fluids are enriched in incompatible elements, such as B, W, Li, Cs and Rb, which is consistent with these components being derived from an evolved magma (Lecumberri-Sanchez et al., 2017). The high B contents in the fluid inclusions and the low B concentrations reported from Panasqueira metasediments (Bussink, 1984), support that a magmatic fluid source from the adjacent S-type Panasqueira granite is more likely than a source from the adjacent metasediments. However, the adjacent metasediments provided a local source of Al, Fe, Mg and Ca necessary to precipitate tourmaline from the boron-rich fluids. The data also suggests that the dravitic cores formed under rock-dominated conditions, from a hot magmatic fluid (500°C) during the early stages of vein opening, which is supported by the results from Ti-in-quartz thermometry. The continuous fluid-rock interaction may have contributed to the progressive cooling of the magmatic fluid and subsequent overgrowth of the cores by Fe-F-Na-rich rims.

We conclude that the chemical and B-isotopic ratios observed in the hydrothermal tourmaline from Panasqueira deposit are mainly controlled by the chemistry of the Mg-Fe-Al-Ca-rich host rocks, the B-Na-F-rich mineralizing fluids, co-precipitating minerals (mica, topaz, and apatite) and the cooling of the fluids in an evolving, dynamic hydrothermal system characterized by the injection of multiple fluid pulses.

Acknowledgments

We thank O. Appelt for help during the electron microprobe work, and M. Wiedenbeck, F. Couffignal and Z. Jin for assistance in the SIMS analyses. We also thank R. Vieira and A. Mateus for many inspiring discussions. We further would like to thank Beralt Tin & Wolfram (Portugal) S.A. for providing logistical support and access to the Panasqueira deposit over two field seasons. The project was funded by the German Federal Ministry of Education and Research (BMBF) within the project GRAMME (033R149). Reviews of Simone Kasemann, an anonymous reviewer and the Editor-in-Chief, Dr. Klaus Mezger, greatly improved the manuscript.

Supplementary data to this article can be found online at `http://dx.doi.org/10.1016/j.chemgeo.2017.07.011`.

Supplement 1:

`https://ars.els-cdn.com/content/image/1-s2.0-S0009254117304096-mmc1.xlsx`

Supplement 2:

`https://ars.els-cdn.com/content/image/1-s2.0-S0009254117304096-mmc2.xlsx`

For the printed copy of this thesis the supplementary material can be found in the enclosed CD-ROM.

"My definition of an expert in any field is a person who knows enough about what's really going on to be scared."

–PJ Plauger

4

Boron-isotope muscovite-tourmaline geothermometry indicates fluid cooling during magmatic-hydrothermal W-Sn-ore formation

Marta S. Codeço, Philipp Weis, Robert B. Trumbull, Johannes Glodny,
Michael Wiedenbeck, Rolf L. Romer

GFZ German Research Centre for Geosciences, Telegrafenberg, 14473 Potsdam, Germany

Article published in Economic Geology (2019, Vol.114, Issue 1, 153-163, doi: 10.5382/econgeo.2019.4625)

Abstract — Reconstructing the thermal evolution of hydrothermal ore deposits mainly relies on their fluid inclusion record, which is limited by favorable trapping conditions, calling for alternative temperature constraints. Muscovite and tourmaline coexist in many hydrothermal ore deposits and in the granites or pegmatites related with them. Whereas in-situ analyses of boron (B) isotopes in tourmaline are widely applied to constrain fluid sources and evolution, muscovite has seldom been used in this way, and the potential for isotope exchange thermometry with this mineral pair is unexplored. The different boron coordination in muscovite and tourmaline causes a significant, temperature-dependent isotopic fractionation between them, which has been determined experimentally. We used this relation to study mineralization conditions and fluid evolution at the Panasqueira W-Sn-Cu deposit in Portugal, where the source and evolution of the mineralizing fluids are still debated. The difference in $^{11}B/^{10}B$ ratios of coexisting muscovite and tourmaline, expressed as $\Delta^{11}B_{mica-tourmaline} = \delta^{11}B_{mica} - \delta^{11}B_{tourmaline}$, yields median temperatures for vein selvages from 400° to 460°C within a total range of 350° to 600°C, which agrees with published Ti-in-quartz temperatures. Mineral pairs from a late fault zone yield a lower median temperature of about 250°C (range 220° to 320°C), which fits with published homogenization temperatures of quartz-hosted fluid inclusions from the veins. Taking these temperatures into account, the calculated fluid composition of the early and late muscovite generations is about $\delta^{11}B_{fluid}$=–6 ± 2 ‰, which indicates that the recurrent fluid pulses had a uniform composition and a magmatic-hydrothermal origin.

4.1 Introduction

Magmatic-hydrothermal ore deposits are the prime sources for Cu, Mo, Sn, and W, and major suppliers for precious and critical metals like Au, Ag, In, Ge and Ga. All magmatic-hydrothermal deposits have in common that fluid flow leads to alteration of the country rock and that mineralization occurs at temperatures that are typically lower than the solidus of the intrusion by up to several hundred degrees (*e.g.*, Hedenquist and Lowenstern, 1994; Heinrich and Candela, 2014). However, the processes controlling the thermal evolution and timing of ore precipitation remain debated (*e.g.*, Fekete et al., 2016; Li et al., 2018). Fluid inclusion assemblages in gangue and ore minerals provide the best direct evidence to constrain mineralization temperatures and fluid source (*e.g.*, Bodnar et al., 2014; Roedder, 1986), inclusion record is generally incomplete, calling for independent constraints. Stable isotopes of oxygen, hydrogen, and carbon in quartz, micas and carbonate minerals have proven value both for thermometry and as fluid-source indicators. Boron (B) isotopes, particularly in tourmaline, have also been widely applied to constrain fluid sources, but their application for thermometry is underexplored (Klemme et al., 2011). Muscovite and tourmaline are common hydrous gangue minerals in a wide variety of hydrothermal ore deposits, and both minerals are important hosts for boron. Although oxygen and hydrogen isotope ratios in muscovite are commonly used to constrain fluid sources, very few studies included boron isotopes (Menold et al., 2016) and those were done on bulk mineral separates, which ignores the possibility of zoning and overgrowths.

Here, we present an extensive case study of B-isotopes in coexisting muscovite and tourmaline using in-situ microanalysis by secondary ion mass spectrometry (SIMS). The example chosen is from the world-class Panasqueira W-Sn-Cu deposit in Portugal and builds on a previous study of the chemical and B-isotope composition of tourmaline, which supported the prevailing magmatic-hydrothermal fluid model for this deposit (Codeço et al., 2017). However, the greisen body at Panasqueira, which should give the best estimate of a magmatic-hydrothermal fluid, contains no tourmaline and was not included in that study. Therefore, the goals of this study were (i) to test the validity of the tourmaline-muscovite B-isotope geothermometer in samples where both minerals coexist, and (ii) to further constrain the fluid source model for Panasqueira by analysis of muscovite from the greisen. The micas in all samples from this study are dioctahedral but many fall outside of the end-member muscovite composition, so the terms white mica and muscovite will be used interchangeably in this paper.

4.2 Boron isotopes systematics

Boron has two stable isotopes, ^{10}B and ^{11}B, with natural abundances of 19.9 atom% and 80.1 atom%, respectively (Palmer and Swihart, 1996). The isotopic composition of a natural sample with a measured ratio of $R_{sample} = {}^{11}B_{sample}/{}^{10}B_{sample}$ is commonly expressed by the delta notation as:

$$\delta^{11}B = \frac{R_{sample} - R_{RM}}{R_{RM}} \tag{4.1}$$

where RM indicates the reference material such as boric acid NBS-SRM951 with $B_{RM} = 4.043627$ (Catanzaro et al., 1970) as the most commonly used standard. Defined in this way, the delta values are very small, so they are typically given in ‰. During equilibrium fractionation, the isotopic compositions of two coexisting phases A and B can be described by the isotope fractionation factor α_{A-B} = R$_A$/R$_B$. In the boron system, the fractionation factor depends on the temperature and the coordination environment of boron in the phases in question (see reviews by Kowalski and Wunder, 2018). In the context of our study, the relevant phases are tourmaline, muscovite and an aqueous fluid. Boron is in trigonal coordination with oxygen in tourmaline and tetrahedral coordination in muscovite. Schmidt et al. (2005) used Raman spectroscopy to show that trigonal $B(OH)_3$ complexes are the predominant boron species in aqueous solution over a wide range of crustal P-T conditions in neutral to acidic pH, whereas tetrahedral boron complexes become important at pH $\geq$ 8 (see also Pokrovski et al., 1995). Kelly and Rye (1979) and Polya (1989) proposed neutral to slightly acid conditions for the mineralizing fluids at Panasqueira based on the muscovite-K-feldspar-quartz buffer, with salinities from fluid inclusion studies of 5-10 wt.% NaCl. For these conditions, the experimental studies of tourmaline-fluid by Meyer et al. (2008) and mica-fluid (neutral-acid) by Wunder et al. (2005)are applicable, giving the following temperature-dependent fractionation expressions:

$$\Delta^{11}B_{tourmaline-fluid} = \left(-4.2 \times \frac{1000}{T(K)}\right) + 3.52, \quad R^2 = 0.77, \quad SEE = 54°C, \quad \text{and} \tag{4.2}$$

$$\Delta^{11}B_{mica-fluid} = \left(-10.69 \times \frac{1000}{T(K)}\right) + 3.88, \quad R^2 = 0.992, \quad SEE = 67°C, \tag{4.3}$$

where R^2 describes the least-squared fit to the data, and SEE is the standard error of the estimate. Combining equations 4.2 and 4.3 gives this expression for the fractionation between mica and tourmaline:

$$\Delta^{11}B_{mica-tourmaline} = \left(-6.49 \times \frac{10^3}{T(K)}\right) + 0.36, \tag{4.4}$$

with $\Delta^{11}B_{A-B} = \delta^{11}B_A - \delta^{11}B_B$, which is the basis for the mica-tourmaline thermometry.

4.3 The Panasqueira W-Sn-Cu deposit

The Panasqueira mine is the largest W deposit in Europe and the 9th largest worldwide (Wheeler, 2016). The ore is hosted in sub-horizontal quartz veins within clastic metasediments (Figure 4.1A) (Thadeu, 1951*a*), containing wolframite, cassiterite, and chalcopyrite, with minor arsenopyrite, sphalerite, pyrite, pyrrhotite, galena and As-Sb-sulfosalts (Kelly and Rye, 1979; Polya, 1989; Polya et al., 2000; Martins et al., 2017). The deposit is crosscut by a number of subvertical faults and spatially associated with the Panasqueira Granite (289 ± 4 Ma; Priem and den Tex 1984), which is strongly greisenized in its upper parts (Figure 4.1A). The paragenetic sequence consists of a (i) pre-ore crack seal stage, (ii) pre- to syn-ore white mica selvage formation, (iii) oxide-silicate ore stage (OSS), (iv) main sulfide ore stage (MSS), (v) pyrrhotite alteration stage (PAS), and (vi) post-ore late carbonate stage (*e.g.*, Lourenço, 2002; Martins et al., 2017; Polya et al., 2000). An alteration halo over two meters wide is developed around the mineralized veins, typically displaying zonation from a vein-proximal tourmaline zone, followed by a muscovite zone and a distal chlorite-muscovite zone (Bussink, 1984). White mica is one of the most abundant and ubiquitous phases at Panasqueira, occurring in the greisen cupola, in all stages of the vein system from the pre-ore stage to the OSS, MSS, and PAS, and in the wall-rock alteration zones.

Mineralization at Panasqueira is still debated in terms of (i) the source of the fluids and metals (magmatic, meteoric, metamorphic or a mixture thereof), (ii) the fluid pathways involved [subhorizontal, emanating from the greisen cupola (Launay et al., 2018) or subvertically along the transverse fault zones (Polya, 1989)], and (iii) how the thermal state of the system evolved from magmatic temperatures of ca. 700°C (Neiva, 1987*a*) to the rather low temperatures for vein mineralization of 360° to 230°C indicated by fluid inclusion studies (Bussink, 1984; Jaques and Pascal, 2017; Kelly and Rye, 1979; Lecumberri-

Sanchez et al., 2017). Indeed, some workers (*e.g.*, Kelly and Rye, 1979) expressed surprise that W-Sn mineralization at Panasqueira took place at these low temperatures, pointing out the contrast to other magmatic-hydrothermal Sn-W deposits. Cathelineau et al. (2017) suggest that the low fluid inclusion temperatures might reflect decrepitation related to regional extension and exhumation. Codeço et al. (2017) obtained 503 ± 24°C (1 SD) for early wall-rock alteration on Ti-in quartz thermometry, and Jaques and Pascal (2017) also estimated high temperatures of 438 ± 44°C (1 SD) from arsenopyrite thermometry of the early oxide-silicate stage of mineralization.

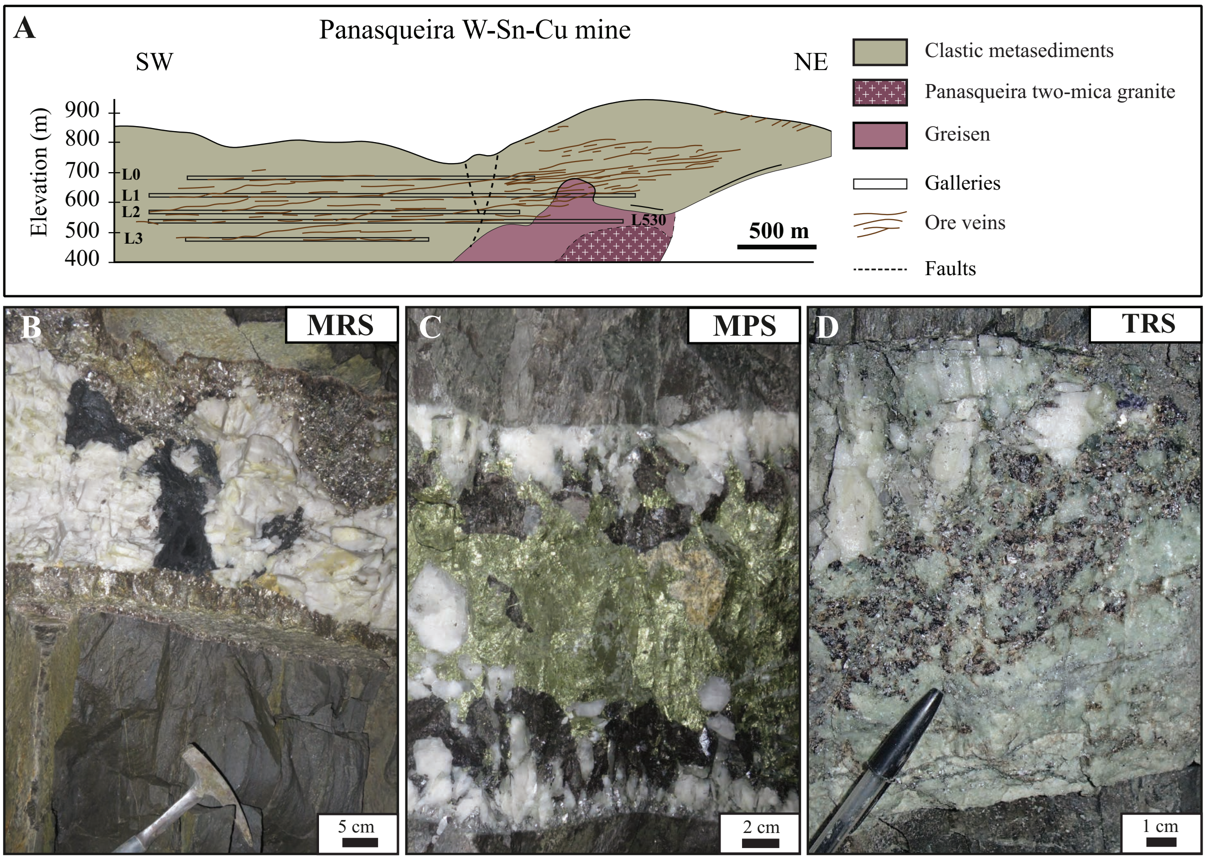

Figure 4.1: **(A)** Schematic cross section of the Panasqueira W-Sn-Cu deposit in Portugal modified (after Thadeu, 1951*a*). L0 = Level 0 at 680 m above sea level (a.s.l.); L1 = Level 1 at 620 m a.s.l., L2 = Level 2 at 560 m a.s.l., L530 = Level 530 (main water drainage level) at 530 m a.s.l.. and L3 = Level 3 at 470 m a.s.l. **(B)** Quartz-mica-wolframite vein with a mica-rich selvage (MRS); **(C)** Quartz-chalcopyrite-wolframite vein with a mica-poor selvage (MPS); the bright mineral at the contact is arsenopyrite; **(D)** Cassiterite-quartz vein with a topaz-rich selvage (TRS).

4.3.1 The composition of Panasqueira tourmaline

Tourmaline is a major mineral phase in the wall rock alteration zones, and it also occurs in some vein selvages but is absent from the greisen body. The chemical and B-isotopic compositions of tourmalines at Panasqueira have been described in detail by Codeço et al. (2017) and are only briefly summarized here. Tourmaline compositions classify as aluminum-rich intermediate schorl-dravite, with relatively high F contents (up to 1.4 wt.%). The grains are typically zoned, with increasing Fe, F, and Na from core to rim, and decreasing Mg, Ca, and Al. The total range in tourmaline $\delta^{11}B$ values is from –3.7 to –12.7 ‰, with no systematic differences between early formed tourmaline and late-vugs tourmaline. Codeço et al. (2017) interpreted the variations in chemical and boron isotopic compositions with a combination of (i) fluid cooling during mineralization and (ii) the growth of tourmaline and mica in alteration zones which depleted the fluid in ^{10}B. They concluded that the tourmaline compositions are consistent with, but not diagnostic of, a magmatic fluid source and record the injection of multiple fluid pulses in an evolving dynamic system, as shown by the homogeneity between tourmaline generations. Key evidence from the granite greisen body was missing in the earlier study because of the lack of tourmaline in the greisen, and this was one motivation for the B-isotope study of muscovite reported here.

4.4 Samples and Methods

4.4.1 Samples studied

Except for the greisen (sample PN6), all samples investigated here were previously studied for tourmaline composition by Codeço et al. (2017). Those samples represent selvages of the mineralized veins and the surrounding wall-rock alteration zones from several localities throughout the deposit (see Supplement: Figure S1 for sample locations). The vein-selvage samples are of three types. The most common are mica-rich selvages (MRS: samples PN22B, PN46B and PN33A; Figure 4.1B, 4.2A), some veins have mica-poor selvages (MPS: sample PN30C; Figure 4.1C, 4.2B), and the least-common type are topaz-rich selvages (TRS: samples PN26AB; Figure 4.1D, 4.2C). In the investigated samples, the

MRS vein assemblage includes wolframite, cassiterite, and chalcopyrite. One MRS sample (PN22B) contains two generations of mica: an early, fine-grained mica at the vein contact intergrown with quartz and tourmaline, and a late, coarser-grained mica intergrown with wolframite. The veins flanked by MPS are dominated by chalcopyrite and sphalerite ore minerals. Veins with TRS-type margins are rare, but the few observations suggest they are more cassiterite-rich. In the TRS sample investigated here, white mica is a secondary phase replacing topaz (sericite, Figure 4.2C), or forming flakes along micro-fractures in quartz. White mica in the wall rocks enclosing mineralized veins forms subhedral flakes, which are typically very fine-grained (< 1 mm diameter) and intergrown with tourmaline and quartz (Figure 4.2D). Locally, subvertical faults cut the veins and alteration zones. The fault zones show similar hydrothermal assemblages as the surrounding rocks but with tendentially coarser grain sizes (Figure 4.2E, sample PN37). The greisenized granite is mainly composed of fine- to medium-grained (up to 5 mm) quartz and white mica with minor topaz, chlorite, K-feldspar, albite, pyrite, arsenopyrite, and zircon (Figure 4.2F).

4.4.2 Electron microprobe analyses

The chemical compositions of white mica were determined on polished thin sections using a JEOL Superprobe JXA-8230 (EPMA) at GFZ Potsdam, equipped with a LaB6-cathode and five wavelength-dispersive spectrometers. This study involved two separate sessions, in April 2016 and in January 2018. The analyses were performed with an accelerating voltage of 15 kV, a beam current of 20 nA with a beam diameter of 5-μm for both sessions. The instrument was calibrated using natural and synthetic minerals: orthoclase (Si, Al, K), fluorite (F), rutile (Ti), diopside (Ca, Mg), tugtupite (Cl), $BaSi_2O_5$ (Ba), albite (Na), hematite (Fe) rhodonite (Mn) and, in the 2018 session, synthetic $RbAlSi_3O_8$ (Rb). Counting time on peaks were twice those on backgrounds and differed in the two sessions. The 2018 session used 10 s counting for Si, K, Al and Na and 20 s for F, Ti, Ca, Cl, Mg, Fe, Ba, Rb, and Mn, while counting times of 10 s for Na, F, Si, K and Ca and 20s for Mn, Fe, Ba, Al, Ti, Mg and Cl were applied during the 2016 session. X-ray intensities of Si, K, and Na were acquired first and simultaneously in both campaigns to minimize diffusion under the electron beam. The structural formulae and site allocations of mica were calculated from EPMA data based on 22 positive charges (Rieder et al., 1998).

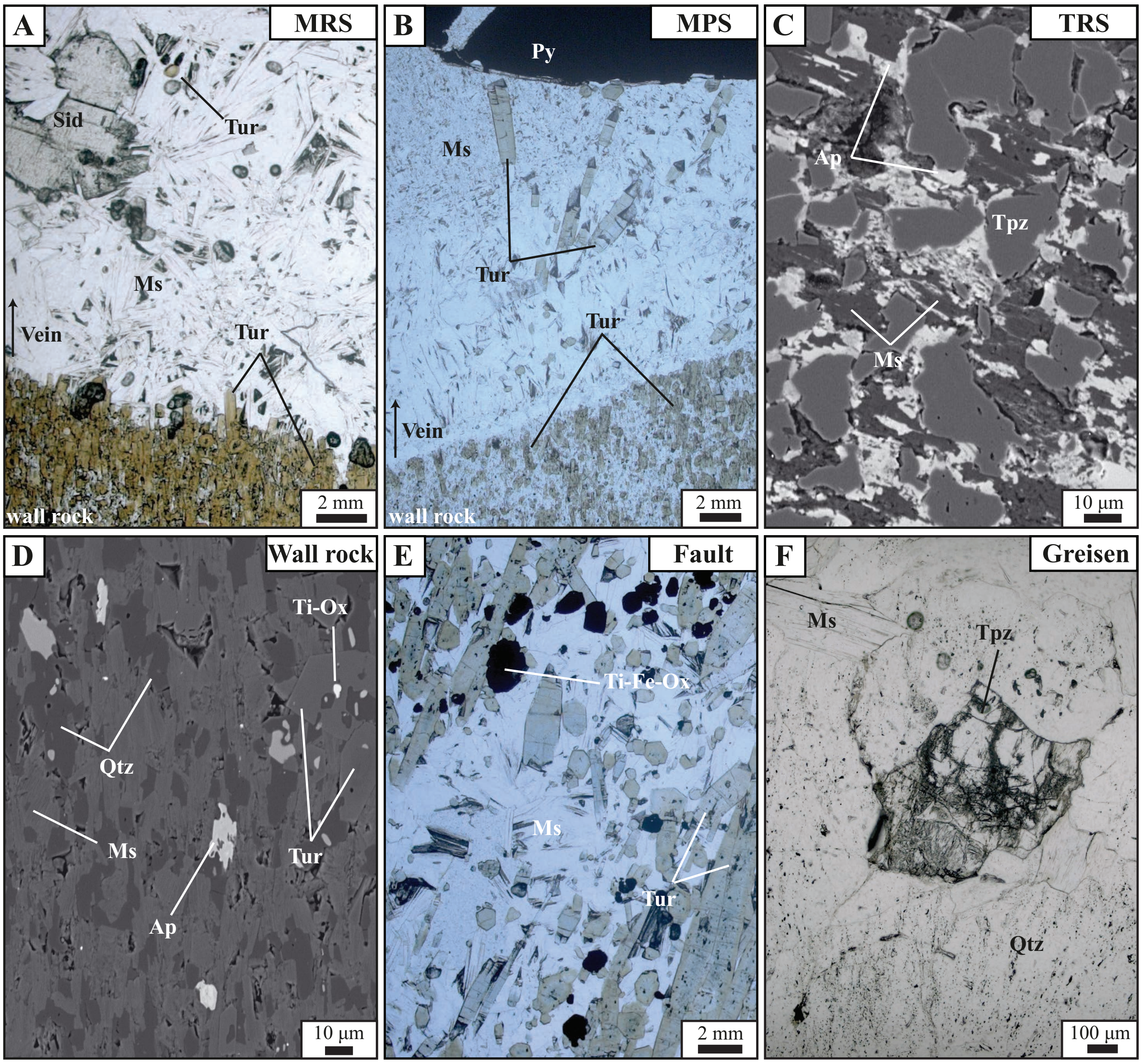

Figure 4.2: **(A)** Photomicrograph of the contact between tourmalinized wall rocks (below) and mica-rich vein selvage (MRS; plane-polarized light; sample PN33A); **(B)** Photomicrograph of the contact between the tourmalinized wall rocks and a mica-poor vein selvage (MPS) with fine-grained mica (plane-polarized light; sample PN30C); **(C)** Back-scatter electron (BSE) image of a topaz-rich vein selvage (TRS) showing alteration of topaz by white mica and apatite (sample PN26AB); **(E)** BSE image of white mica coexisting with tourmaline in the wall rocks (WR; sample PN30C); **(F)** Photomicrograph of coarse-grained tourmaline and white mica in a transverse fault zone (plane-polarized light; sample PN37-2);**(D)** Photomicrograph showing the main mineralogy and textural relationships in the greisen (plane-polarized light; sample PN6-1); Ap: apatite, Ms: muscovite/white mica, Qtz: quartz, Sid: siderite, Ti-Fe-Ox: Titanium-iron oxides, Ti-Ox: titanium oxides, Tpz: topaz, Tur: tourmaline.

4.4.3 Solution inductively coupled plasma-mass spectrometry

International reference materials for boron isotopic analysis of micas have not been established. The need of matrix-matched reference materials for SIMS analyses motivated us to use muscovite #98973 and muscovite #112791 described by Dyar et al. (2001) and McGuire et al. (1992) for this purpose. Their spatial homogeneity for use as microprobe references was established by Dyar et al. (2001). Sample homogeneity for B-isotopes was tested by SIMS analysis and found to be within 0.7 ‰ for #98973 (1 SD, n = 47) and 1.1 ‰ for #112791 (1 SD, n = 24). The two muscovites were then analyzed for their boron isotopic composition using the Thermo Element Neptune MC-ICP-MS at GFZ Potsdam. Analytical procedures for chemical separation of boron follow those of Romer et al. (2014). For analysis, the boron separated from the muscovite samples was taken up in a 2% HNO_3 solution, and B concentrations were determined from ^{11}B ion current intensities relative to intensities obtained from a 50 ng/g B calibration solution. For determination of isotopic compositions, B concentrations in sample solutions were adjusted to 50 ng/g B. Each sample was measured six times in two independent sessions using a reference material – sample – reference material bracketing procedure for accurate mass bias correction. The results yielded $\delta^{11}B$ values of –20.00 ± 0.36 ‰ (1 SD) for #98973 and $\delta^{11}B$ = –9.85 ± 0.12 ‰ (1 SD) for #112791.

4.4.4 Secondary ion mass spectrometry

The boron isotope compositions and boron concentrations of white mica were determined by secondary ion mass spectrometry (SIMS) using the CAMECA 1280-HR instrument at GFZ Potsdam. Prior to analyses, the samples were cleaned with ethanol in an ultrasonic bath and subsequently coated with 35 nm of high-purity gold in vacuum. The SIMS analyses employed a nominally 13 keV, $\sim$4 nA $^{16}O^{-}$ primary beam, focused to a $\sim$5-μm diameter spot on the sample surface. Each analysis was preceded by a 3-minute pre-sputter using a 10- $\times$ 10-μm raster, which was needed to remove the gold coating and any surface contamination and to establish equilibrium sputtering conditions. The mass spectrometer was operated in multi-collection mode using electron multipliers (EMs) set as follows: $^{39}K^{4+}$ (L2 position), $^{10}B^{+}$ (Center) and $^{11}B^{+}$ (H2). A 400-μm diameter contrast aperture, 5000-μm field aperture and 50 V energy window were used, with no voltage offset applied. The mass resolution for these conditions is M/ΔM ≈ 1800 (at 10 % peak height), which is sufficient to separate $^{10}B^{1}H^{+}$ and $^{11}B^{+}$ mass positions. These conditions resulted in a count rate for $^{11}B^{+}$ of about 1.5×10^{5} counts per second (cps) for reference muscovite #112791 (373 ppm boron) and 1.6×10^{3} cps for muscovite #98973 (44 ppm boron), which brackets the ^{11}B signal intensities from the Panasqueira micas (1.7 – 4.0×10^{3} cps). A single analysis consisted of 80 integrations of 4 seconds each, resulting in a total analysis time of ~12 minutes, including pre-burn. Fixed values used for the dead time correction were 65.6 ns (L2), 64.8 ns (C) and 64.4 ns (H2). The electron multiplier response was controlled by automatic HV voltage monitoring during the analytical sessions, and no drift was detected. The <1 ‰ repeatability of reference materials (see below) also indicates stable response of the EMs during this study.

Multiple daily analyses of reference muscovites #11271 and #98973 were used to determine the instrumental mass fractionation (IMF; Supplement Table S1) and to monitor analytical quality. Within-run uncertainty for an individual analysis of 80 cycles was typically 0.5 – 0.8 ‰ (1 SD/mean). The repeatability of reference materials was typically better that ±1 ‰ (1 SD/mean). The mean IMF values for the reference muscovites varied somewhat from day to day (Table S1), so we used the daily IMF value to correct the unknown values measured on that day. The overall 1 SD/mean value of combined IMF data for both muscovite references over the entire study was less than ± 1.5 ‰, which we suggest as a conservative estimate of total uncertainty. After correction for the IMF, the SIMS data were converted to $\delta^{11}B$ values relative to NIST SRM 951, using the $^{11}B/^{10}B$ ratio of 4.043627 (Catanzaro et al., 1970). The boron concentrations in mica were calculated using the K concentrations measured by EPMA and the K/B ratios measured by SIMS. The full dataset is reported in the Electronic Appendix (for the printed version of this thesis it can the found in the enclosed CD-ROM).

4.5 Results

4.5.1 Chemical compositions of white micas

The white micas from Panasqueira show a large range in compositions, in particular for SiO_2 (43.8 – 52.6 wt. %), Al_2O_3 (21.2 – 36.1 wt. %), MgO (0 – 5.4 wt. %), FeO (0.8 – 7.69 wt. %), and F (0 – 7.2 wt. % (see Electronic Appendix; for the printed version of this thesis it can the found in the enclosed CD-ROM). In terms of end-member compositions, the micas plot between the muscovite-celadonite and muscovite-phengite-Al-celadonite joins (Figure 4.3A, B). There are systematic variations in the Fe/Mg ratio (Figure 4.3C) depending on the sample setting (i.e., MRS, MPS, TRS, wall rocks, greisen or fault). Micas in the greisen have very high Fe/Mg ratios (>5), whereas the MRS micas vary in Fe/Mg from 7 to 0.4. Micas from wall-rock alteration zones plot at the low end of the Fe/Mg range, overlapping with most data from MPS mica and with the early-formed MRS muscovite. In contrast, mica from TRS and the fault zone have distinctly higher Si, Fe, and F contents (apart from Fe, which is as high in the greisen), and the lowest Al contents (Figure 4.3D). The B concentrations of white micas determined by SIMS range from 28 to 115 ppm (median = 66 ppm) and show no systematic variation according to the setting (Table 4.1).

4.5.2 B-isotope compositions of white micas

The $\delta^{11}B$ values of all samples range from –23.4 to –14.1 ‰ and are distributed into two main groups according to sample setting: (1) greisen, MRS, MPS and wall-rock alteration zones, and (2) TRS and fault zone (Figure 4.4, Table 4.1). Micas from the first group have overlapping compositions in the range of –20.3 to –14.1 ‰. The greisen and different types of vein selvage have equivalent median values (–17.3, –17.8 and –17.7 ‰ for MRS vs. –18.2 ‰ for MPS and –17.0 ‰ for the greisen). Unfortunately, white mica in the wall-rock alteration zones is very fine-grained, so only two SIMS analyses could be obtained. Both are from sample PN33A and yield –17.3 and –15.8 ‰ which are within the range of the vein selvage mica from the same sample (–19.7 to –15.2 ‰). For this example, and for the other MRS and MPS samples, there is no systematic difference in B-isotopic compositions of mica grains hosted in the vein vs. those at the wall-rock contact. Among the second group of samples (TRS and fault zone), the secondary mica altering topaz in TRS yielded similar $\delta^{11}B$ values to mica from group 1 (–18.1 to –17.7 ‰), but coarser-grained mica along fractures in quartz and next to sulfides gave lower values (–22.7 to –19.5 ‰). The $\delta^{11}B$ values of mica from the fault zone are also distinctly

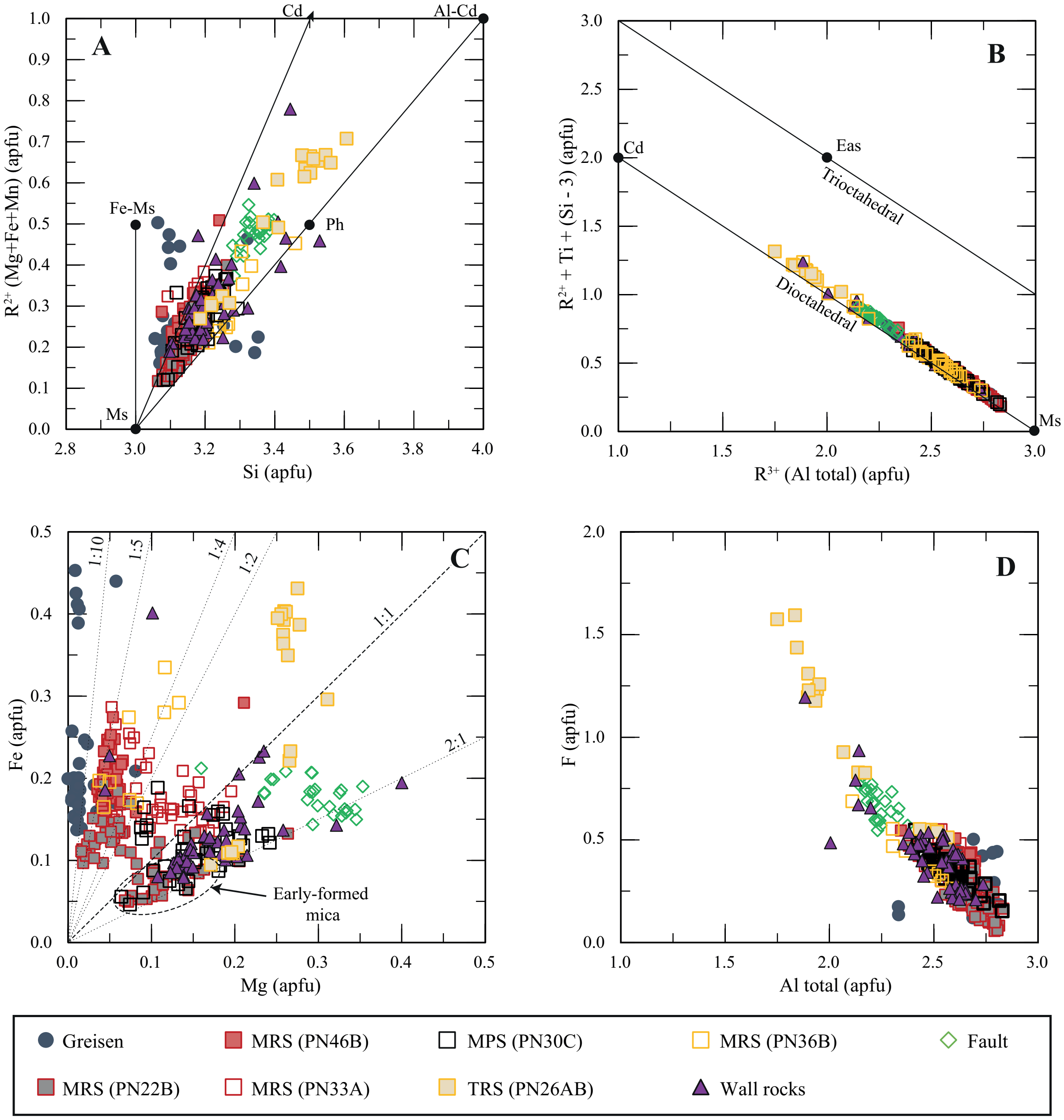

Figure 4.3: Classification diagrams of mica compositions in the Panasqueira deposit (after Guidotti, 1984; Tracy, 1987): **(A)** $R^{2+} = Fe + Mg + Mn$ vs. Si, **(B)** $R^{2+} + Ti + (Si - 3)$ vs. R^{3+} (total Al), **(C)** Fe vs. Mg, and **(D)** F vs. Al total (in atoms per formula unit – apfu). Lines in (A) and (B) represent the solid solution between the end-members muscovite (Ms), phengite (Ph), ferri-muscovite (Fe-Ms), aluminum-celadonite (Al-Cd), celadonite (Cd) and eastonite (Eas). MRS: mica-rich selvages; MPS: mica-poor selvages; TRS: topaz-rich selvages.

lower than for group 1 (–23.4 to –17.3 ‰, median = –21.6 ‰). The variation in $\delta^{11}B$ of multiple mica grains within the same sample and/or setting is about 5 ‰ which exceeds the analytical uncertainty of 1.5 ‰. Within-grain variations were tested in six cases where grain size permitted, and three of them showed significant internal variation (1.7, 3.2 and 3.5 ‰ offset between the extreme values).

Table 4.1: Boron isotope compositions of white mica from different settings in the Panasqueira deposit.

Sample	*Setting*[1]	*Location*[2]	*n*	$\delta^{11}B$ *mean* (‰)	$\delta^{11}B$ *median* (‰)	*SD* (‰)	*Range* (‰)		*B mean* ppm
PN6	Greisen	L1	19	–17.0	–17.0	1.1	–19.1	–15.5	73.5
PN22B	MRS	L1	16	–17.1	–17.3	1.5	–19.0	–14.1	59.3
PN46B	MRS	L3	24	–17.6	–17.8	1.4	–20.3	–14.4	76.1
PN33A	MRS	L3	26	–17.5	–17.7	1.2	–19.7	–15.2	60.2
PN30C	MPS	L3	15	–18.0	–18.8	1.6	–20.3	–14.1	–
PN26AB	TRS	L1	8	–19.9	–19.9	2.0	–22.7	–17.7	–
PN33A	Wall rocks	L3	2	–16.6	–16.6		–17.3	–15.8	50.1
PN37-2	Fault	L0	31	–21.3	–21.6	1.4	–23.4	–17.4	68.7

[1] Abbreviations: MRS (mica-rich selvages), MPS (mica-poor selvages), TRS (topaz-rich selvages).
[2] Sample location on mine levels L0, L1, L3 (see Figure S1).
Dash indicates concentration not determined.

4.6 Discussion

4.6.1 Variations in mica compositions

We interpret the systematic variations in Fe/Mg ratios of the first group of samples as a result of fluid-rock interactions, whereby the composition of wall-rock micas (lower Fe/Mg) is controlled by the rock composition, while vein-selvage and greisen micas reflect the compositions of the fluids. The chemical variations are not correlated with the B-isotopic compositions, which are in the same range for all samples in this group. Micas in the second group are distinctly different. The TRS micas are distinct in their chemical (higher Fe/Mg ratios and F and lower Al) compositions compatible with the mineralogy of these samples (e.g., topaz, apatite) and also lower $\delta^{11}B$ values, specifically for the coarse-grained mica. Similarly, the fault zone-hosted micas have higher Mg and F and lower Al concentrations, as well as distinctly lower $\delta^{11}B$ values compared to the greisen, MRS, MPS and wall-rock samples. The settings of the micas from group 2 suggest a later stage of growth than those in group 1, and it is likely that their composition reflects a later fluid pulse in the system.

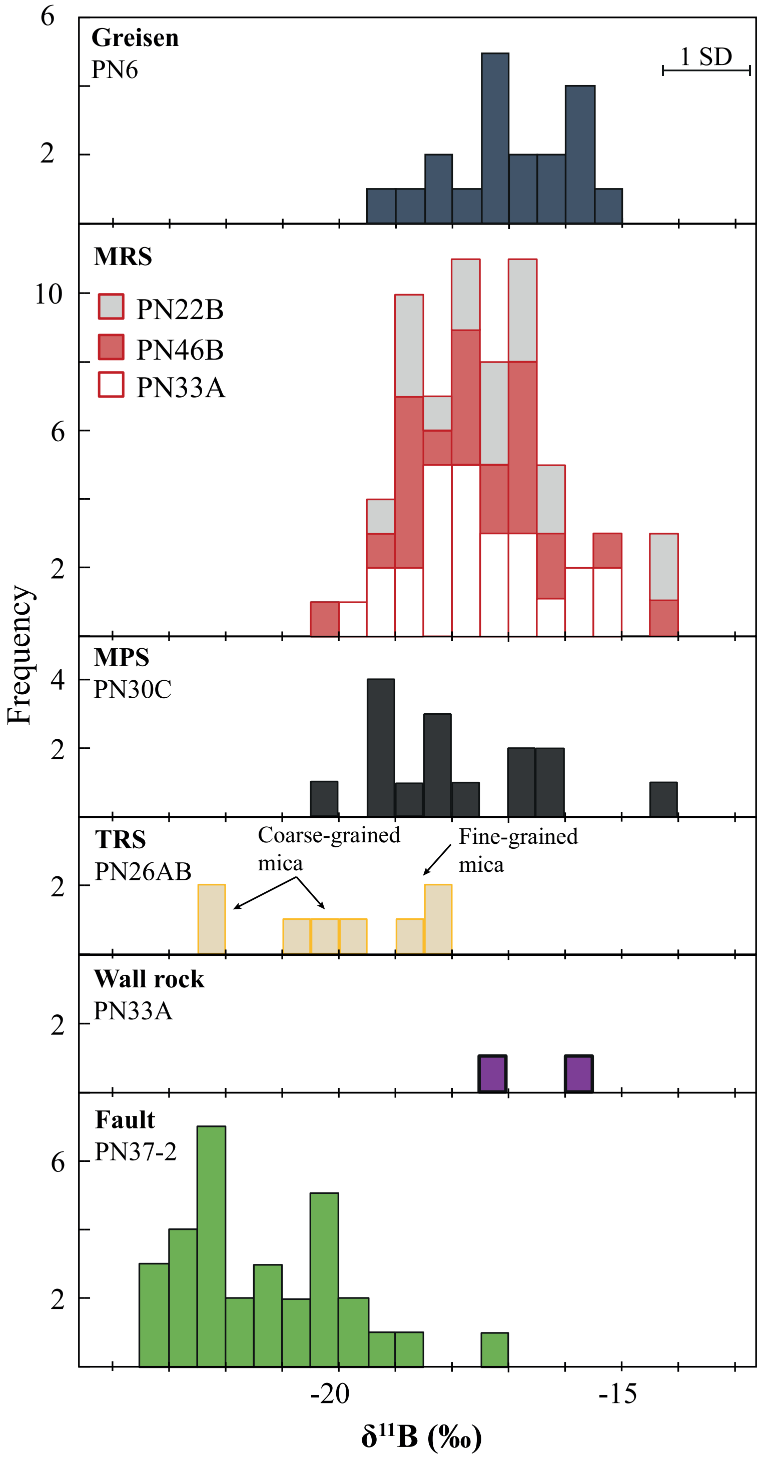

Figure 4.4: Frequency histograms showing δ^{11}B values of white micas from different settings in the Panasqueira deposit. The 1 SD uncertainty bar is 1.5‰ (see Table 1). MRS: mica-rich selvages; MPS: mica-poor selvages; TRS: topaz-rich selvages.

4.6.2 B-isotope geothermometry from tourmaline-mica pairs

Both white mica and tourmaline $\delta^{11}B$ compositions from the Panasqueira deposit show considerable variability (Figure 4.5). The variations in tourmaline were ascribed by Codeço et al. (2017) to a combination of Rayleigh fractionation related to depletion of the fluid in ^{10}B by tourmaline formation in the alteration zones, and a temperature effect on fluid-tourmaline isotope fractionation during cooling. The same processes will affect the composition of white mica in the samples, whereby the temperature effect for mica is expected to be stronger because of the larger fluid-mica fractionation factor. To estimate mineralization temperature with boron-isotope exchange geothermometry (Figure 4.6), we use the median values and the 25th–75th percentile ranges of all samples where both minerals are in direct contact (MRS-vein selvages PN33A, PN46B, PN30C; and fault zone PN37). In MRS sample PN22B, tourmaline does not occur in the vein selvage with mica but is abundant in the neighboring wall-rock alteration zone. Using equation (4), the three contact pairs in the MRS samples PN33A, PN46B and PN30C yielded median temperatures of about 400°, 430° and 460°C, respectively, within an overall range of 350° to 600°C (Figure 4.6). The MRS sample PN22B yielded a slightly higher median temperature (about 500°C), which may be unreliable because tourmaline and mica are not in contact. The fault-zone sample PN37 gave considerably lower temperatures (range: 220°–320°C, median 250°C). The analytical uncertainties of SIMS B-isotope ratios for tourmaline and mica in these samples are 0.6 ‰ and 1.5 ‰, respectively (1 SD), which correspond to a temperature uncertainty of 50° to 140°C after error propagation for the low- and high-temperature range, respectively. These errors are similar to, or larger than the uncertainties in the tourmaline-fluid and mica-fluid fractionation equations (54° and 67°C SEE, see above).

Independent temperature estimates from the Panasqueira veins and wall rocks show good agreement with the results from B-isotope thermometry. For example, the homogenization temperatures of fluid inclusions in quartz from several studies are in the range of 230° to 360°C, with the majority below 300°C (Bussink, 1984; Jaques and Pascal, 2017; Kelly and Rye, 1979; Lecumberri-Sanchez et al., 2017). It was noted that these temperatures are relatively low for a magmatic-hydrothermal system, and other methods yielded

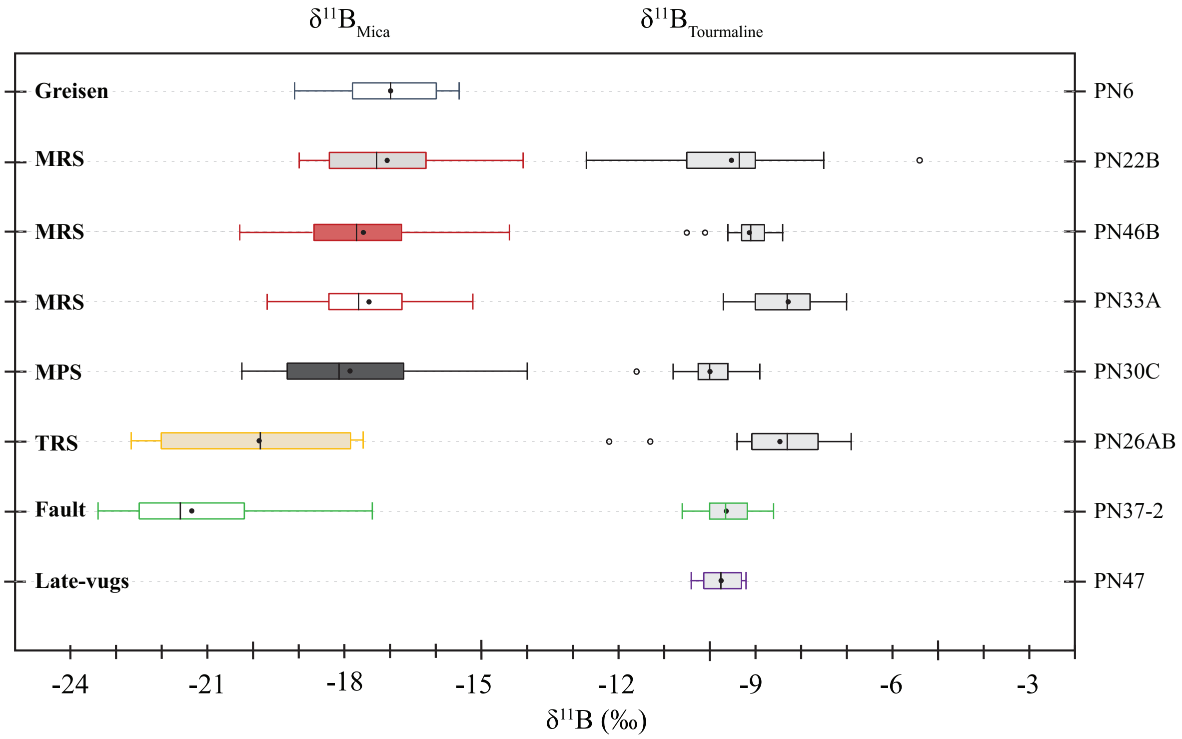

Figure 4.5: Boron-isotope composition of white mica and tourmaline from the Panasqueira deposit. Tourmaline data are from Codeço et al. (2017), mica data from this study. The grey boxes mark the 25th (P1) and 75th percentiles (P3), the black line and filled circles represent the median and average, respectively. The whiskers show the range, whereas open circles are outlier values (greater than $1.5 \times (P3 - P1)$ and $3 \times (P3 - P1)$, resp.).

higher temperatures (arsenopyrite: 438 ± 44°C; Ti-in-quartz: 503 ± 24°C, from Jaques and Pascal (2017), Codeço et al. (2017), respectively). The higher temperature range is in good agreement with the B-isotope temperatures for vein-selvage samples (median about 430°C), consistent with early stages of the hydrothermal system, whereas the lower B-isotope temperature of tourmaline-mica pairs in the cross-cutting fault sample PN37 (median 250°C) is similar to the low-temperature range found in vein-quartz fluid inclusion microthermometry. Taken together, these geothermometry estimates are consistent in showing a cooling by around 200°C from early to late-stages of hydrothermal activity at Panasqueira. Note that cooling from 500° to 300°C increases the $\Delta^{11}B_{tourmaline/fluid}$ by 2 ‰ (eq. 4.2), whereas the effect on mica-fluid fractionation is more than twice as much (5 ‰ from eq. 4.3). The weaker sensitivity of tourmaline to temperature changes explains why tourmaline $\delta^{11}B$ values in vein selvages and the fault zone overlap (Figure 4.5).

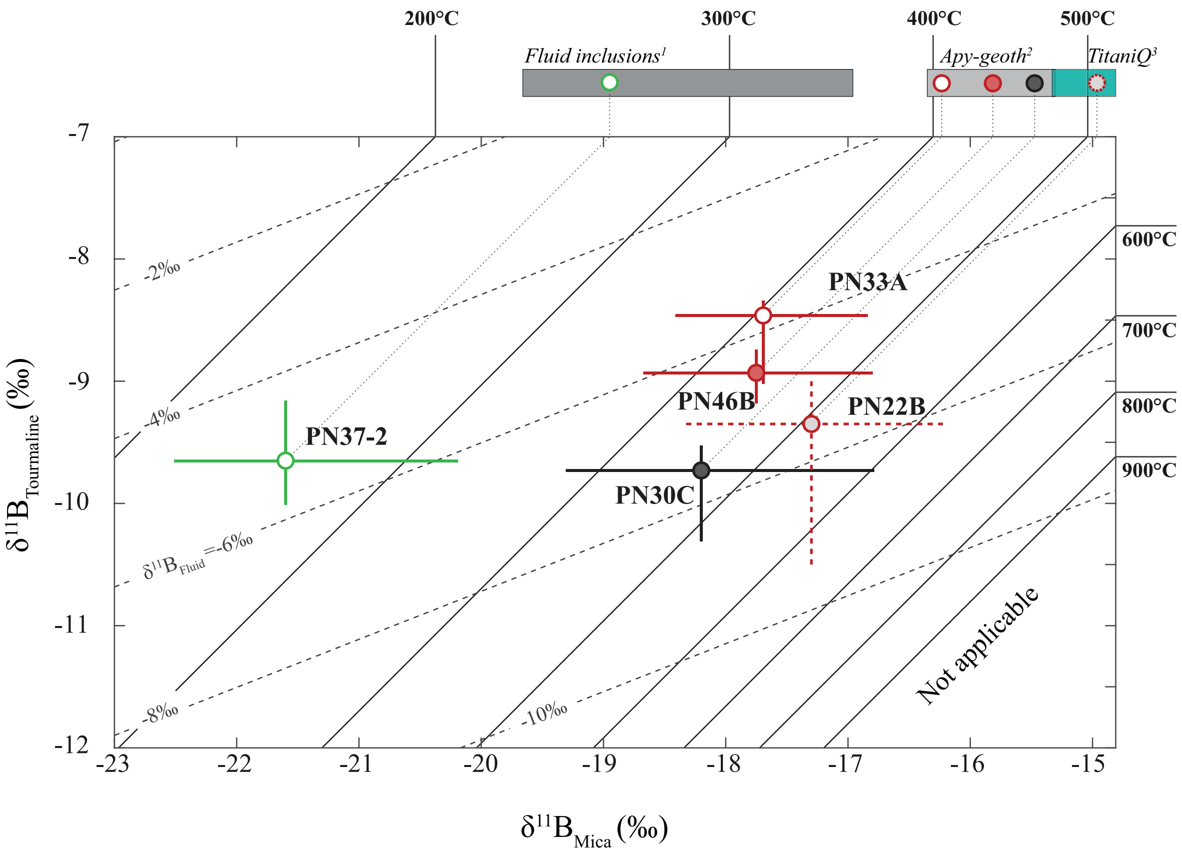

Figure 4.6: Temperature and $\delta^{11}B_{fluid}$ estimates calculated from Panasqueira mica-tourmaline pairs using fractionation factors of Wunder et al. 2005 (mica-fluid) and Meyer et al. 2008 (tourmaline-fluid). Solid lines are isotherms and dashed lines are isopleths of fluid B-isotope compositions ($\delta^{11}B_{fluid}$). The median compositions of tourmaline-mica pairs are indicated by open circles and the lines correspond to the 25th and 75th percentiles. The colors are as in Figure 4.5; sample PN22B is represented by dashed lines because the tourmaline and mica do not occur together (see text). Independent temperature estimates are shown on the upper right bars: ^{1}Fluid inclusions from Bussink (1984); Jaques and Pascal (2017); Kelly and Rye (1979); Lecumberri-Sanchez et al. (2017); ^{2}Arsenopyrite geothermometry (Apy-geoth) Jaques and Pascal (2017) and ^{3}Ti-in-quartz (TitaniQ) geothermometry from Codeço et al. (2017)

4.6.3 Fluid evolution at Panasqueira

The combined mica and tourmaline B-isotope data from Panasqueira provide information on all stages of fluid evolution from early greisen formation through the stages of mineralization and wall-rock alteration, and finally to late transverse faults and tourmaline vugs (Figure 4.5). Calculating fluid composition from these data requires knowledge of the respective formation temperatures. B-isotope thermometry from this study constrains the temperature of early vein formation and wall-rock alteration at 350° to 600 °C, and 220° to 320°C for late-stage faults. The temperature of greisen formation is unknown because only mica is present, but an estimate is possible from the 390° to 530°C range from arsenopyrite and Ti-in-quartz geothermometry at Panasqueira (see Figure 4.6), which is similar to the upper range of greisen formation in the classic Zinnwald Sn deposit in Germany (Korges et al., 2018). For the temperature of late vugs, which contain tourmaline but no mica, we assume the same range of 230° to 360°C as indicated by fluid inclusions in the quartz veins.

Figure 4.6 shows the calculated B-isotope compositions of the hydrothermal fluids (dashed lines) based on these temperature ranges and the 25th–75th percentile of mica and tourmaline B-isotope ratios. Mica and tourmaline compositions from vein selvages and alteration zones yield a $\delta^{11}B$ range of vein fluids from –7.5 to –5.8 ‰ (median values). These values are compatible with a fluid source from an S-type granite (Trumbull and Slack, 2018) as discussed by Codeço et al. (2017). The mica from the greisen (median value = –17.0 ‰) gives a fluid composition between –7.6 and –4.8 ‰ for the assumed temperatures of 530°C and 390°C respectively. This range is very similar to the range of (magmatic) fluid compositions estimated from mica-tourmaline pairs in the vein selvage (–7.5 to –5.8 ‰). The median fluid composition based on mica-tourmaline pairs in the fault zone is -5.2 ‰ (sample PN37-2). The predicted fluid composition of late vugs based on tourmaline $\delta^{11}B$ (median = –9.8 ‰) and a temperature range of 360° to 230°C is –6.7 to –5.0 ‰. Therefore, for all stages of hydrothermal activity represented by this study, the calculated B-isotopic compositions of the fluids are between about –4.8 and –7.6 ‰, which supports the interpretation of multiple injections of magmatic-hydrothermal fluid sourced from the Panasqueira granite (Bussink, 1984; Codeço et al., 2017; Kelly and Rye, 1979).

4.6.4 Applicability to other hydrothermal systems

White mica has some advantages over tourmaline, being (1) more widespread in hydrothermal ore deposits, and (2) having stronger temperature dependency on B-isotope fractionation and thus being a better monitor of temperature changes. Used alone, each mineral can help constrain fluid sources and where they occur together in isotopic equilibrium, the mica-tourmaline pair provides a useful geothermometer in cases where fluid inclusion microthermometry is difficult to apply or needs confirmation. White mica is among the most common hydrothermal minerals in all types of major hydrothermal ore deposits (including porphyry Cu-Mo, orogenic Au, iron-oxide-copper-gold, volcanogenic massive sulfide, and sediment-hosted Pb-Zn deposits), occurs over a large range of temperatures, and often coexists with tourmaline. Studies of stable isotope compositions of ore deposits should therefore also consider measuring B-isotopes in white mica to constrain the fluid source and thermal evolution of the hydrothermal system, especially in systems with multiple generations of fluid inclusions.

4.7 Conclusions

The chemical and boron isotopic compositions of white mica from the Panasqueira W-Sn-Cu deposit have been determined for samples representing the range of early to late hydrothermal fluid evolution (greisen, vein selvages, wall-rock alteration zones, cross-cutting fault zone). In most of these settings, mica coexists with tourmaline and one motivation of this study was to test the validity of B-isotope exchange geothermometry for tourmaline-muscovite pairs.

We distinguish two groups of samples by their setting. Group one (greisen, micaceous vein selvages and wall-rock alteration zones) and group two (secondary mica in topaz-bearing vein selvages and mica in the fault zone). Within group 1, micas from the greisen and the vein selvages have higher Fe/Mg ratios than those in the wall-rock alteration zones, which suggests a shift from fluid-dominated to rock-dominated conditions. The B-isotopic composition of all samples in this group overlap in the range of $\delta^{11}B$= –20.3 to –14.1 ‰. Micas of the second group are different. Those in the topaz-rich selvages (TRS) have higher Si and F contents and low Al, compatible with the distinctive mineralogy of the rocks (topaz, apatite). The TRS micas also range to low $\delta^{11}B$ values (–22.7 to –19.5 ‰ for coarse mica in fractures). The fault zone-hosted micas have lower Fe/Mg than TRS mica but also high F, low Al and low $\delta^{11}B$ values (–23.4 to –17.3 ‰, median = –21.6 ‰). The distinct composition of group 2 micas, and their setting, are compatible with later fluid pulses in the hydrothermal system.

The median temperatures obtained by B-isotope geothermometry of mica-tourmaline pairs in vein selvages vs. the late fault zone record cooling of the hydrothermal fluid from 460° to 250°C. The higher temperature agrees with published Ti-in-quartz and arsenopyrite thermometry for early vein formation and mineralization, and the lower temperature is compatible with the 230°to 360 °C indicated by fluid inclusions in quartz veins. The B-isotope composition of hydrothermal fluids calculated for these temperatures and the corresponding mica-tourmaline $\delta^{11}B$ values are –7.5 to –5.2 ‰, which is compatible with an origin from the S-type Panasqueira granite. Mica from the granite greisen (median $\delta^{11}B$ = –17.0 ‰) corresponds to a fluid of –7.6 and –4.8 ‰ at temperatures of greisenization between 530° and 390°C. Finally, a similar $\delta^{11}B$ range for late fluids (–6.7 to –5.0 ‰) is estimated from vug-filling tourmaline with median $\delta^{11}B$ = –9.8 ‰ at 230° to 360°C. Together, these results suggest that a similar magmatic-hydrothermal fluid was active in all stages of mineralization represented by our samples, supporting a multiple-injection model for Panasqueira.

More broadly, this work demonstrates that B-isotope studies of hydrothermal ore deposits should consider white mica in addition to tourmaline as a host mineral. Even though the B-concentrations in white mica are much lower than in tourmaline, white mica is equally useful to constrain fluid sources and it may be the better choice to record the thermal evolution of hydrothermal systems, because of its larger temperature-dependent B-isotopic fractionation.

Acknowledgments

We would like to thank Beralt Tin & Wolfram (Portugal) S.A. for providing logistical support and access to the Panasqueira deposit over two field seasons. For expert technical assistance in the laboratories, we thank F. Wilke, O. Appelt, F. Couffignal and B. Hübner (GFZ Potsdam) and U. Altenberger and M. Lorenz (Universität Potsdam). We further thank A. Gurenko and associate editor G. Pokrovski for their reviews, which helped to improve the manuscript. The project was founded by the German Federal Ministry of Education and Research (BMBF) within the project GRAMME (033R149).

Supplementary data to this article can be found online at: `https://pubs.geoscienceworld.org/segweb/economicgeology/article/114/1/153/569148/boron-isotope-muscovite-tourmaline-geothermometry`.

For the printed copy of this thesis the supplementary material can be found in the enclosed CD-ROM.

Supplement

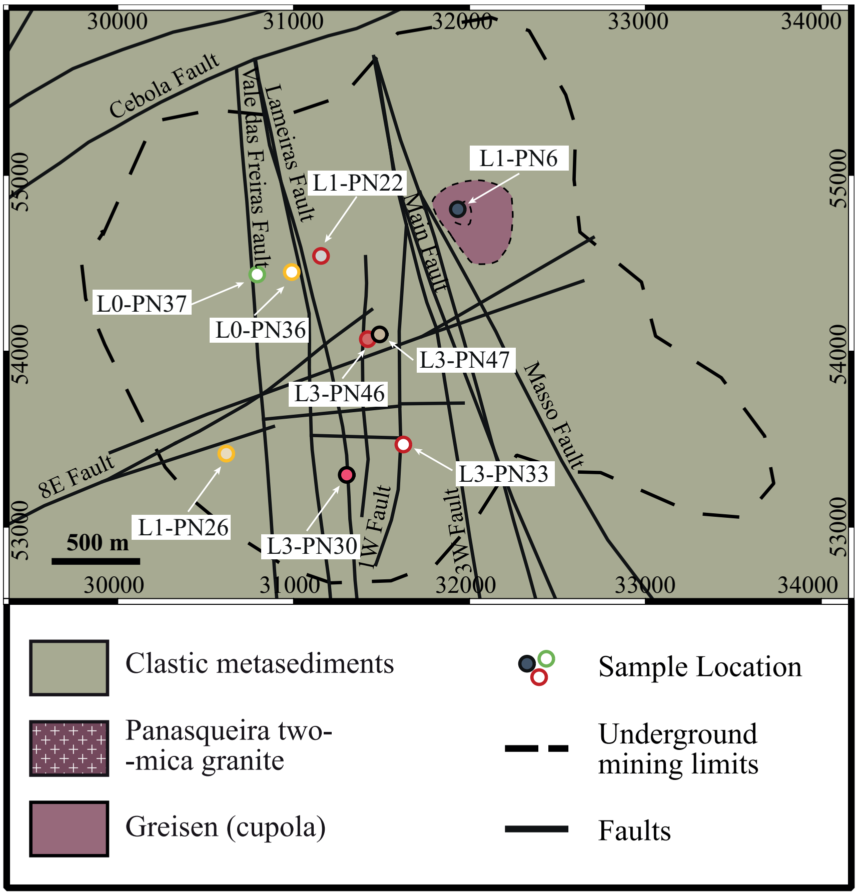

Figure S1: Geological map showing the main geological elements and the sample locations (map: Courtesy of Beralt Tin and Wolfram (Portugal). Samples from different galleries are labeled from top to bottom (Fig.4.1A) as L0 (Level 0 at 680m), L1 (Level 1 at 620 m), L2 (Level 2 at 560 m), L530 (Level 530 – main water drainage level at 530 m) and L3 (Level 3 at 470 m).

Table S1: Summary of SIMS B-isotope analyses of muscovite reference materials.

Date	$^{11}B/^{10}B$	IMF^{1}mean	Repeat. (‰)^{2}	n	^{11}B (‰)^{3}
98973 Muscovite ($^{11}B/^{11}B = 3.9627$ and $\delta^{11}B = –20.00$ ‰)^{4}					
10/11/2017	3.879	0.9790	0.68	6	–20.76
13/11/2017	3.882	0.9796	1.34	11	–20.33
14/11/2017	3.881	0.9794	0.70	12	–20.05
15/11/2017	3.891	0.9818	0.97	10	–20.20
16/11/2017	3.891	0.9819	1.49	10	–20.04
17/11/2017	3.890	0.9816	0.82	12	–19.96
05/04/2018	3.887	0.9783	1.26	8	–19.93
112791 Muscovite ($^{11}B/^{11}B = 4.0038$ and $\delta^{11}B = –9.85$ ‰)^{4}					
10/11/2017	3.924	0.9800	0.64	17	–9.85
13/11/2017	3.925	0.9803	0.44	10	–9.48
14/11/2017	3.922	0.9796	0.22	9	–9.77
15/11/2017	3.933	0.9822	0.56	13	–9.67
16/11/2017	3.932	0.9820	0.95	8	–9.80
17/11/2017	3.930	0.9815	0.46	9	–9.90
05/04/2018	3.914	0.9777	0.92	8	–10.19

[1] Instrumental Mass Fractionation ($^{11}B/^{11}B$ measured / $^{11}B/^{11}B$ reference materials), mean of *n* analyses.

[2] Repeatability of IMF (standard deviation / mean) * 1000.

[3] Based on corrected $^{11}B/^{11}B$ ratios, relative to NIST951 (after Catanzaro et al., 1970) using the combined mean IMF of both reference muscovites.

[4] Mean of the reference values measured by MC-ICP-MS.
For chemical analysis of 98973 and 112791 see Dyar et al. (2001) and McGuire et al. (1992), respectively.

"There are sadistic scientists who hurry to hunt down errors instead of establishing the truth."

–Marie Curie

5

Trace elements in white mica and tourmaline from the Panasqueira W-Sn-Cu deposit (Portugal), and their value as pathfinder minerals

Marta S. Codeço[1], Philipp Weis[1], Robert B. Trumbull[1], Vincent van Hinsberg[2], Filipe Pinto[3,4], Pilar Lecumberri-Sanchez[5], Anja M. Schleicher[1]

[1]GFZ German Research Centre for Geosciences, Telegrafenberg, 14473 Potsdam, Germany

[2] Department of Earth and Planetary Sciences, McGill University, Montreal H3A0E8, Canada

[3]Beralt Tin & Wolfram (Portugal) S.A., Barroca Grande, 6225-051, Castelo Branco, Portugal

[4]Institute of Earth Sciences (ICT), Rua do Campo Alegre 687, 4169-007 Porto, Portugal

[5]Department of Earth and Atmospheric Sciences, University of Alberta, Edmonton T6G2E3, Canada

---

Submitted to Geochimica et Cosmochimica Acta. Readers must be aware of possible differences between chapter 5 and the future publication

Abstract — Hydrothermal fluids flowing through the upper crust formed most of the earth's ore deposits. Thus, developing methods that help to trace the fluid origin, composition and evolution is essential to understand ore formation and to improve exploration strategies. Whole-rock chemistry and trace-element compositions of minerals can be used as fingerprints of these processes.

Whole-rock geochemistry of hydrothermally altered and unaltered metasediments was combined with results of a comprehensive set of in-situ LA-ICP-MS (trace elements) measurements of tourmaline and white mica from different settings within the Panasqueira mine to understand alteration patterns, fluid compositions and test the value of tourmaline and mica as pathfinders.

White mica has high concentrations in lithophile trace elements (Li, Rb, Cs, Tl, Nb, W, Sn and Ta) that may logically derive from granite-related fluids. Contrarily, tourmaline is comparatively richer in V, Sr, and Zn that were likely supplied by the country rocks. Moreover, whole-rock compositional trends probably reflect elements added or removed by the hydrothermal fluids, which suggest that those fluids were enriched predominantly in As, W, Sn, Cu, Zn, Li, F, Cs, Rb, and Tl. The combination of whole-rock geochemistry and in-situ mica measurements may indicate that the hydrothermal fluids were supplied by the Panasqueira granite. Mica generations also give constraints on the evolution of the hydrothermal system, with a progressive enrichment in Li, Mg, V, Sr, Sn, Cs, and Cu in the fluids over time. We suggest that mica is a good pathfinder for W-Sn deposits, and in combination with tourmaline gives valuable information regarding the fluid source, evolution and fluid-rock interaction processes.

5.1 Introduction

Alteration assemblages of hydrothermal ore deposits are important because they typically have much greater mineralogical and compositional variability than the mineralized parts that contain ore minerals at economic grades (*e.g.,* Large and McGoldrick, 1998; Lowell and Guilbert, 1970; Mathieu, 2018). Alteration halos, moreover, have a larger spatial footprint (Cooke et al., 2014; Eilu and Groves, 2001; Large and McGoldrick, 1998). Thus, the study of alteration minerals from ore deposits has great potential for use in exploration and for mineralogical vectoring towards undiscovered ore deposits (*e.g.,* Brzozowski et al., 2018; Cooke et al., 2014; Gaillard et al., 2018; Monnier et al., 2018; Wilkinson et al., 2015, 2017). However, this requires a detailed understanding of what controls the chemical composition of these alteration minerals, and to what extent they reflect the chemical signature of the mineralization they are associated with.

The Panasqueira deposit is a world-class W-Sn-Cu lode-type mineralization located in central Portugal (Figure 5.1A). It consists of a set of sub-horizontal mineralized quartz veins that are peripheral to a non-outcropping late-Variscan granite and are hosted by metasedimentary rocks (Figure 5.1B, C). The hydrothermal alteration around the veins forms a variably thick (typically up to 30 cm) tourmaline-rich (50-70 % vol. tourmaline) alteration halo. White mica and quartz are present in variable amounts with tourmaline, depending on the lithology of the host rocks (more abundant in schists compared to quartzites/greywackes). At the wall rock-vein contact, a thick mica selvage commonly occurs, containing minor tourmaline, quartz, and arsenopyrite. The abundance of white mica and tourmaline at Panasqueira, and their presence in different parts of the deposit, and associated with different stages of its formation, makes these minerals of prime interest as indicators of the composition and variability with time of the fluid from which they formed, and as potential exploration vectors.

Under equilibrium conditions, the composition of hydrothermal mica and tourmaline is controlled by the partition coefficients of the elements between the mineral and fluid phase. Partition coefficients are sensitive to pressure, temperature and element speciation in the fluid (van Hinsberg et al., 2010). Preliminary tourmaline-fluid element partition coefficients have been estimated for high-pressure subduction zone fluids (van Hinsberg et al., 2017) and tourmaline-melt partitioning between tourmaline and melt was studied by van Hinsberg (2011). Experimental studies related to mica-fluid partitioning are also limited (*e.g.,* Bos, 1990; Green and Adam, 2003; Melzer and Wunder, 2001; Zhu and Sverjensky, 1991), but it has been suggested that the main control on the incorporation of elements into mica is their abundance in the fluid, and that mica is not very selective (Legros et al., 2016, 2018).

In this paper, we first report the trace element compositions of altered and unaltered host-rock schists as well as the underlying greisenized granite from whole rock samples to identify the overall chemical changes related to the hydrothermal overprint. We then present the results of in-situ trace element analyses of white mica and tourmaline from alteration assemblages at Panasqueira by LA-ICP-MS and evaluate their potential as an indicator of (ore-)fluid composition and their respective value as pathfinder minerals for Sn-W deposit exploration. We also use principal component analysis (PCA) to better reveal geochemical patterns in bulk-rock, mica and tourmaline. We seek a better understanding of the nature of the hydrothermal alteration at Panasqueira, and to test the value of white mica and tourmaline as geochemical pathfinders for Sn-W mineralization. The study is based on a suite of samples previously analyzed for chemical and B-isotope variations of tourmaline and white mica by Codeço et al. (2017) and Codeço et al. (2019a), combined with bulk rock samples from underground exposures and exploration drill cores.

5.2 Mica and tourmaline crystal chemistry

The tourmaline group minerals consist of 33 currently accepted end-members (Henry and Dutrow, 2018) that exhibit a considerable variety of major and trace elements (Hawthorne and Henry, 1999; Henry et al., 2011). Given its broad P-T-stability and occurrence in diverse igneous, metamorphic and hydrothermal environments (Dutrow and Henry, 2011), tourmaline has been regarded as a key mineral to obtain geochemical information on the geological processes operating during its growth (Henry et al., 1999; Slack and Trumbull, 2011; van Hinsberg et al., 2011a,b). The general crystal-chemical formula of tourmaline-group minerals is $XY_3Z_6(T_6O_{18})(BO_3)_3V_3W$, where $X = Na^+$, Ca^{2+}, K^+, and (vacancy); $Y = Fe^{2+}$, Mg^{2+}, Mn^{2+}, Al^{3+}, Fe^{3+}, Li^+, Ti^{4+}, Zn^{2+}, Ni^{2+}, Co^{2+}, Cu^{2+}, Cr^{3+}, and V^{3+}; $Z = Al^{3+}$, Fe^{3+}, Mg^{2+}, Fe^{2+}, Cr^{3+}, and V^{3+}; $T = Si^{4+}$, Al^{3+}, and B^{3+}; $V = O^{2-}$ and OH^-, and $W = OH^-, F^-$, and O^{2-} (Bosi, 2018; Henry et al., 2011).

Although white mica is widespread in the same environments as tourmaline, its trace element compositions have not been exploited to the same extent, not even in hydrothermal systems and ore deposits where they are exceedingly common. Exceptions are the Li-rich micas, which are commonly used as indicators of magmatic evolution of evolved granites and pegmatites (*e.g.,* Lichtervelde et al., 2008; Johan et al., 2012; Roda-Robles et al., 2006; Vieira et al., 2011) and to a lesser extent, in W-Sn ore deposits (*e.g.,* Legros et al., 2016, 2018; Neiva, 1987*b*). Micas have the general crystal-chemical formula $IM_{2-3}\square_{1-0}T_4O_{12}A_2$. The dodecahedral-site ^{XII}I, also known as the interlayer site, is commonly occupied by K^+, Na^+, Ca^{2+}, Ba^{2+} and more rarely by Rb^+, Cs^+, Ba^{2+}, NH_4, Sr^{2+}, and vacancies ($\square$) as major components, whereas in the octahedral-site ^{VI}I, Mg^{2+}, Fe^{2+}, Al^{3+}, and Fe^{3+} are the most common components, and Li^+, Ti^{4+}, V^{3+}, Cr^{3+}, Mn^{2+}, Co^{2+}, Ni^{2+}, Cu^{2+}, and Zn^{2+} also occur. The tetrahedral-site ^{IV}T usually accommodates Si^{4+}, Al^{3+}, Fe^{3+} and, at lower concentrations, Be^{2+}, and B^{3+}) and A includes OH^-, Cl^-,F^-,O^{2-}, or S^{2-} (Brigatti and Guggenheim, 2002; Rieder et al., 1998).

5.3 Geology of Panasqueira deposit

5.3.1 Geological setting

The Panasqueira W-Sn-Cu deposit is part of the European Variscan Belt, which is widely known for hosting numerous Sn-W deposits (Cornwall, French Massif Central, Iberian Massif, Bohemian Massif, Armorican Massif) (*e.g.,* Cuney et al., 2002; Jackson et al., 1989; Kelly and Rye, 1979; Mangas and Arribas, 1988; Marignac and Cuney, 1999; Moura, 2005; Štemprok, 1980; Tornos et al., 2008). Those consist of veins, stocks, skarns, breccia pipes and greisen-type deposits that belong to a metallogenic province related to post-collision tectonics and magmatism (Romer and Kroner, 2015; Štemprok, 1980).

The granite at Panasqueira is typical for the Variscan granitic suite of northern Portugal (Figure 5.1A). It has an age of 290 ± 10 Ma (Clark, 1970) and is a peraluminous, S-type, two mica (muscovite > biotite) granite of fine- to medium-grained porphyritic texture and containing quartz, microcline, plagioclase, biotite, muscovite, apatite, ilmenite and zircon (Kelly and Rye, 1979; Neiva, 1987*a*).

The Panasqueira deposit takes the form of flat-lying quartz-wolframite ± chalcopyrite ± cassiterite veins hosted by greenschist-facies metaclastic rocks of the Almaceda Formation, part of the regional Schist Greywacke Complex – Beiras Group (SGC-BG) of Late Ediacaran to Early Cambrian age (Fig. 1). A contact metamorphic aureole of biotite-chlorite hornfels ("spotted schists") with minor cordierite and chiastolite porphyroblasts developed above the mostly unexposed Panasqueira granite (Bussink, 1984; Conde et al., 1971). A greisenized apex of the granite is exposed underground in the NE corner of the mine area (Figure 5.1C). The greisen is medium- to coarse-grained and composed mainly of quartz and white mica, with minor amounts of topaz, chlorite, K-feldspar, plagioclase, pyrite, arsenopyrite, and zircon (Bussink, 1984; Codeço et al., 2019a; Neiva, 1987*a*).

The quartz-W-Sn-Cu-bearing veins at Panasqueira are exposed by underground mining over an area of 2,500 m length, 400 m to 2,000 m width and at least 500 m in depth (Wheeler, 2016) (Figure 5.2). The deposit is delimited in the NE by the Cebola fault and cut by several sub-vertical faults, mostly trending NNW-SSE and ENE-WSW (Figure 5.2B). Hydrothermal alteration of the wall rocks around quartz veins is extensive, and took place before, during and possibly after ore formation (Bussink, 1984; Marignac, 1973). The alteration produced concentric zones with progressively greater distance from the veins, consisting of (1) a tourmaline-rich zone 2 to 30 cm thick, and (2) a muscovite-rich zone including minor quartz, tourmaline or topaz (Bussink, 1984). The unaltered schist of the Almaceda Formation contains a biotite-chlorite-quartz-feldspar assemblage, with local development of cordierite porphyroblasts (spotted schist) in a contact aureole around the buried granite. The geochemical variations in the alteration zones were described by Bussink (1984), who showed that the tourmaline zone is enriched in ore metals W, Sn, Cu and Zn, and in Sr, Mn and P, and depleted in Ba, Rb, Li, Cs and K relative to the adjacent muscovite zone. Tourmaline and muscovite, along with quartz, are the most abundant minerals in the alteration zones. In addition, coarse-grained white mica commonly forms centimeter-thick selvages at the vein contacts, along with locally abundant arsenopyrite, quartz and minor tourmaline.

The paragenetic sequence of the ore veins has been presented by several authors (*e.g.,* Foxford et al., 1991, 2000; Kelly and Rye, 1979; Polya, 1989; Polya et al., 2000) and divided into four to six stages of mineralization: (1) quartz-tourmaline, (2) muscovite selvage formation, (3) main oxide-silicate stage, (4) main sulfide stage, (5) pyrrhotite alteration stage and (6) late-carbonate stage. According to the available quartz-hosted fluid inclusion data, the main oxide stage and sulfide stage involved fluids at temperatures between 230–360 °C, low to moderate salinities (5-10 wt.% NaCl eq.), while inclusions from the late-carbonate stage involved much lower temperatures (<200°C) and salinities below 5 wt.% NaCl eq. (Bussink, 1984; Jaques and Pascal, 2017; Kelly and Rye, 1979;

Lecumberri-Sanchez et al., 2017; Polya et al., 2000). Based on muscovite-tourmaline boron-isotope exchange geothermometry, Codeço et al. (2019a) estimated temperatures

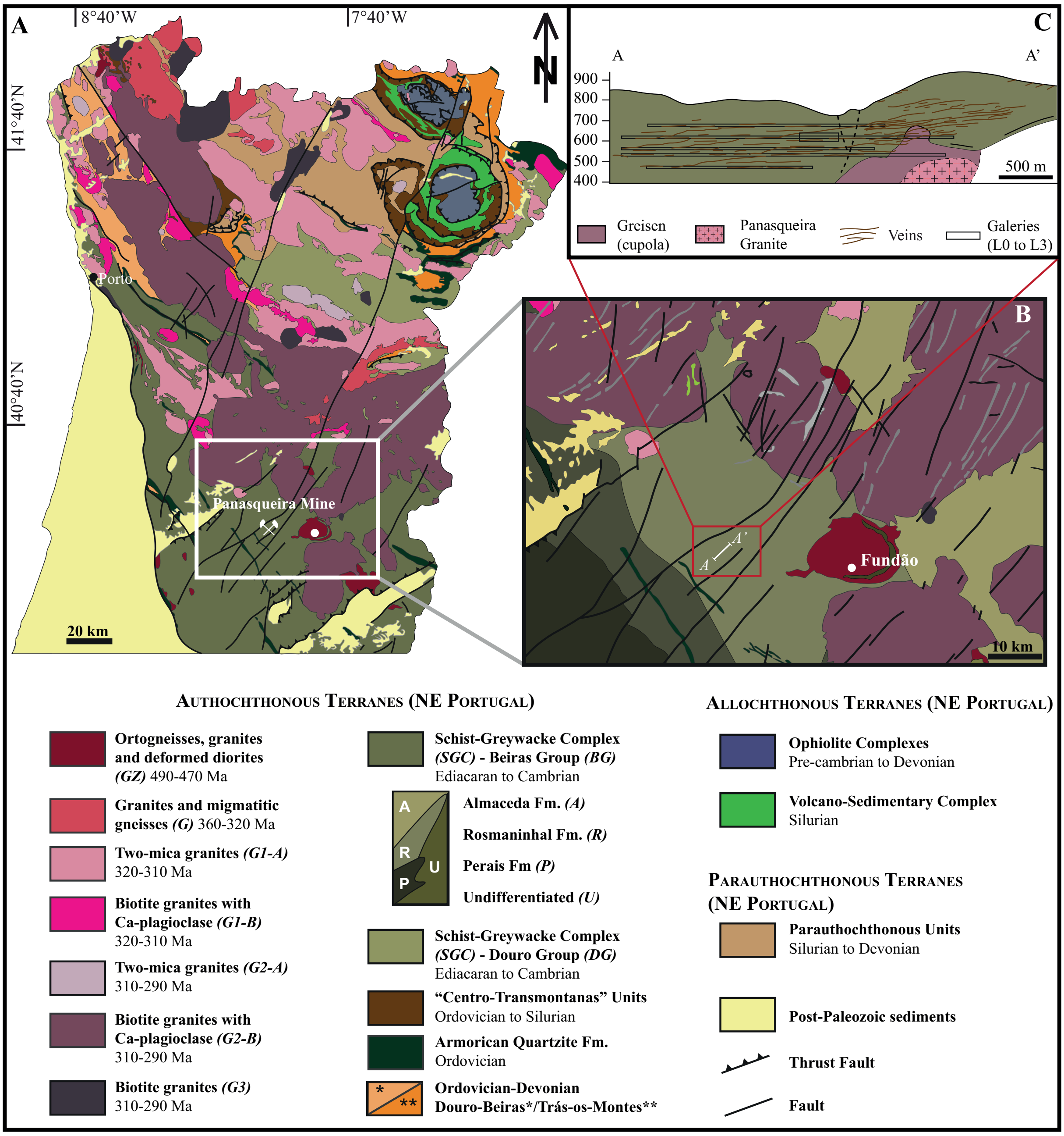

Figure 5.1: General setting of the studied area: **(A)** geological map of the northern and central Portugal with the representation of the different granitic suites and metasedimentary rocks [adapted from *Carta Geológica de Portugal à escala 1:1 000 000* (2010) and *Carta Geológica de Portugal à escala 1:500 000, Folha Norte* (1992)]; (B) geological map of the Panasqueira mine region [adapted *Carta Geológica de Portugal à escala 1:500 000, Folha Norte* (1992)], and (C) Schematic cross section of the Panasqueira vein system, greisen and Panasqueira granite (modified after Thadeu (1979). From top to bottom the galleries correspond to Level 0 at 680 m above sea level (a.s.l.), Level 1 at 620 m a.s.l., Level 2 at 560 m a.s.l., Level 530 – main water drainage level at 530 m a.s.l. and Level 3 at 470 m a.s.l..

ranging from ca. 420° to 490 °C for the early stages of vein formation and about 250 °C for post-ore stages.

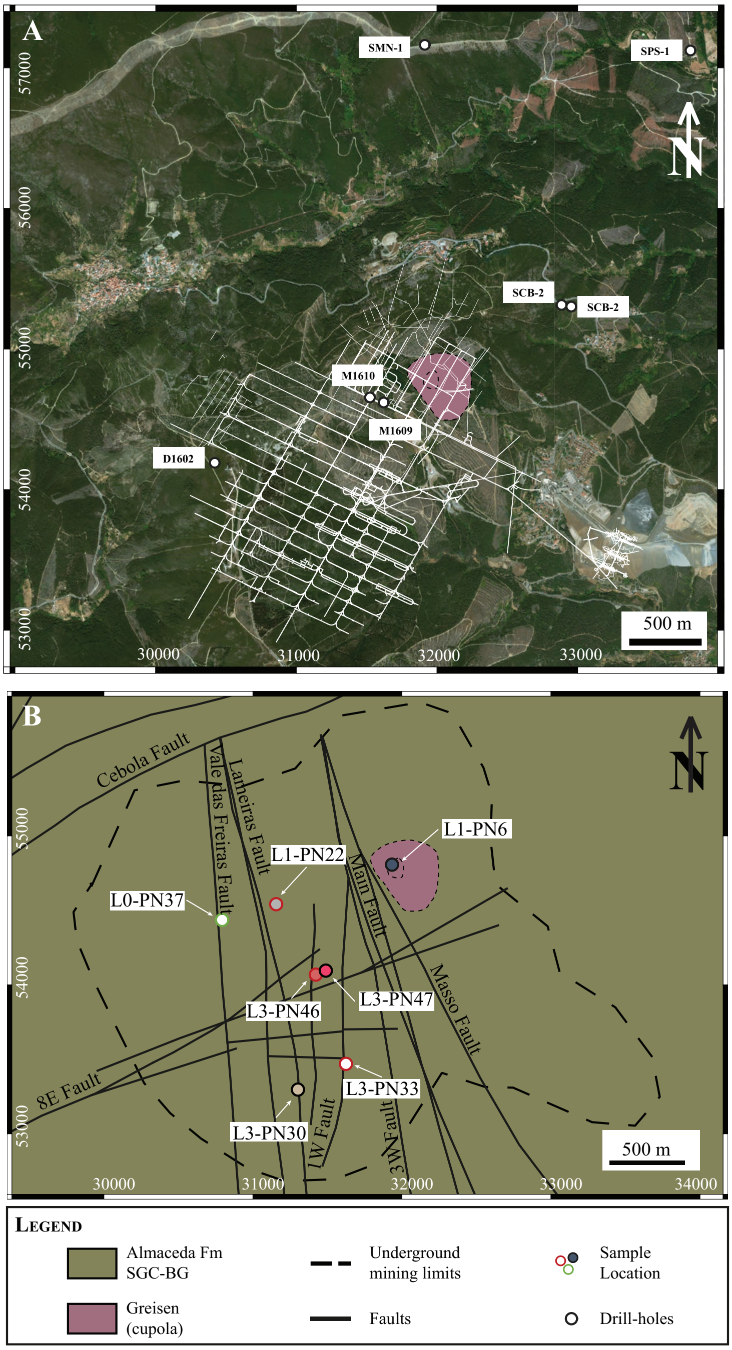

Figure 5.2: **(A)** Satellite map with the location of the different drill cores sampled in this study and **(B)** Geological map showing the main geological elements and the sample locations. The white lines in **A** represent the galleries. Maps: Courtesy of Beralt Tin and Wolfram (Portugal); coordinate system: ETRS89 / Portugal TM06 (EPSG:3763).

5.3.2 White mica and tourmaline in the deposit

Previous studies (*e.g.,* Bussink, 1984; Codeço et al., 2017; Kelly and Rye, 1979; Neiva et al., 2007) established that tourmaline occurs mainly in the wall-rock alteration zones and is dominantly related to the pre-ore stages. In contrast, white mica is more widespread, occurring in the granite and greisen as a magmatic and post-magmatic phase (respectively), and at the vein selvages and wall-rock alteration zone as a hydrothermal mineral both predating and synchronous with the mineralization.

White mica in the greisen is fine to medium grained (up to 2-3 mm) and shows a complex compositional zonation which seems to be more prominent along the cleavage planes and rims (Figure 5.3A). In vein selvages, white mica is, after quartz, the second most abundant silicate mineral. Despite considerable local variability in the mine area, three main vein types can be defined based on their selvage mineral assemblage (Codeço et al., 2019a):

(1) mica-rich selvages (MRS) are several centimeters thick along the wall-rock contacts where white mica coexists with quartz, arsenopyrite, topaz, apatite, and tourmaline (e.g., Figure 5.3B, C). In the veins, mica grains typically form coarse-grained (up to 5 cm) feather-like textures and coexist with wolframite ± chalcopyrite ± pyrite ± sphalerite (Figure 5.3D). Tourmaline generally forms aggregates or occurs in disrupted fragments of wall-rock (Figure 5.3C).

(2) mica-poor selvages (MPS) form a thin layer ($<< 1$ cm) at the edge of the veins together with quartz, topaz, tourmaline and variable amounts of sulfide minerals (*e.g.,* Figure 5.3E). In the sample studied (PN30), this layer is followed by altered host rock with fine-grained white mica pseudomorphs after an unidentified phase along with quartz (see Figure 5.3F), panasqueiraite: $CaMg(PO_4)(OH,F)$, and sulfides (pyrite, chalcopyrite, and sphalerite).

(3) topaz-rich selvages (TRS) are one to several cm-sized layers with light-green massive topaz aggregates with intense fracturing and sericitization. No mica selvage forms in these veins and the white mica is fine-grained, secondary after topaz.

White mica in the wall-rock alteration zones formed in response to hydrothermal alteration of the country rocks, co-genetic with tourmaline, quartz, and minor Ti-(Fe)-oxides, and occurs as fine-grained (<1 mm) flakes in schists (Figure 5.3F, G). In coarser-grained metasediments (i.e., spotted schists) mica is usually scarce and these are dominated by tourmaline with minor quartz (Figure 5.3G). Tourmaline displays optical zoning, is typically fine-grained and its size is mainly a function of the host-rock (Figure 5.3F, G) [*i.e.*, fine-grained shists vs. spotted schist (see Codeço et al., 2017, for further details)]. Places affected by syn- to post-mineralization faulting or fault reactivation develop coarser grained tourmaline, mica, and accessory, complex Ti-(Fe, W, Sn, Cr, Sr, V)-oxides. These often contain veinlets and "vugs" filled by apatite (Figure 5.3H) with variable amounts of chalcopyrite, sphalerite and pyrite.

In addition, tourmaline is present in late vugs (± carbonates ± quartz) within the veins, mainly associated with post-mineralization cracks or fractures (Figure 5.3I).

5.3.3 Chemical compositions of mica and tourmaline: previous work

The major-element composition of tourmaline and white mica are briefly addressed by Neiva (1987*b*) and Neiva et al. (2007) in regional studies of the Portuguese Variscan ore deposits and studied in detail by Codeço et al. (2017) and Codeço et al. (2019a). Tourmaline compositions from Panasqueira show significant variations at the grain scale, but are homogeneous on the deposit scale. The grains have ferromagnesian compositions (schorl-dravite), with significant octahedral Y-site aluminum contents (up to 0.9 apfu), variable X-site vacancies (0.1 to 0.6 apfu) and relatively high F contents (up to 0.7 apfu).

Figure 5.3 *(facing page)*: **(A)** Back-scatter electron (BSE) image of zoned mica in the greisen; **(B)** Photomicrograph of the contact between the tourmalinized wall rocks and a mica-rich selvage (MRS), with mica coexisting with quartz (plane-polarized light); **(C)** Photomicrograph of the contact between the tourmalinized wall rocks and a MRS showing additionally the tourmaline sleeves forming within the vein (plane-polarized light); **(D)** Feather-like mica intergrown with wolframite in MRS (plane-polarized light); **(E)** Photomicrograph of the contact between the tourmalinized wall-rocks and a mica-poor selvage (MPS), showing a layer of quartz and mica, which is followed by a domain formed by fine-grained mica pseudomorphs after an unknown phase (cross-polarized light); (**(F)** Photomicrograph of mica coexisting with tourmaline in the fine-grained schists (plane-polarized light); **(G)** BSE image of a spotted schist showing mica intergrown with tourmaline; **(H)** Photomicrograph of coarse-grained tourmaline, mica and apatite in a fault zone (plane-polarized light); **(I)** BSE image of tourmaline associated with quartz from the late-vugs. Ap, apatite; Ms, muscovite/white mica; Py, pyrite; Qtz, quartz; Ti(-Fe)Ox, titanium(-iron) oxides; Tur, tourmaline; Wo, wolframite.

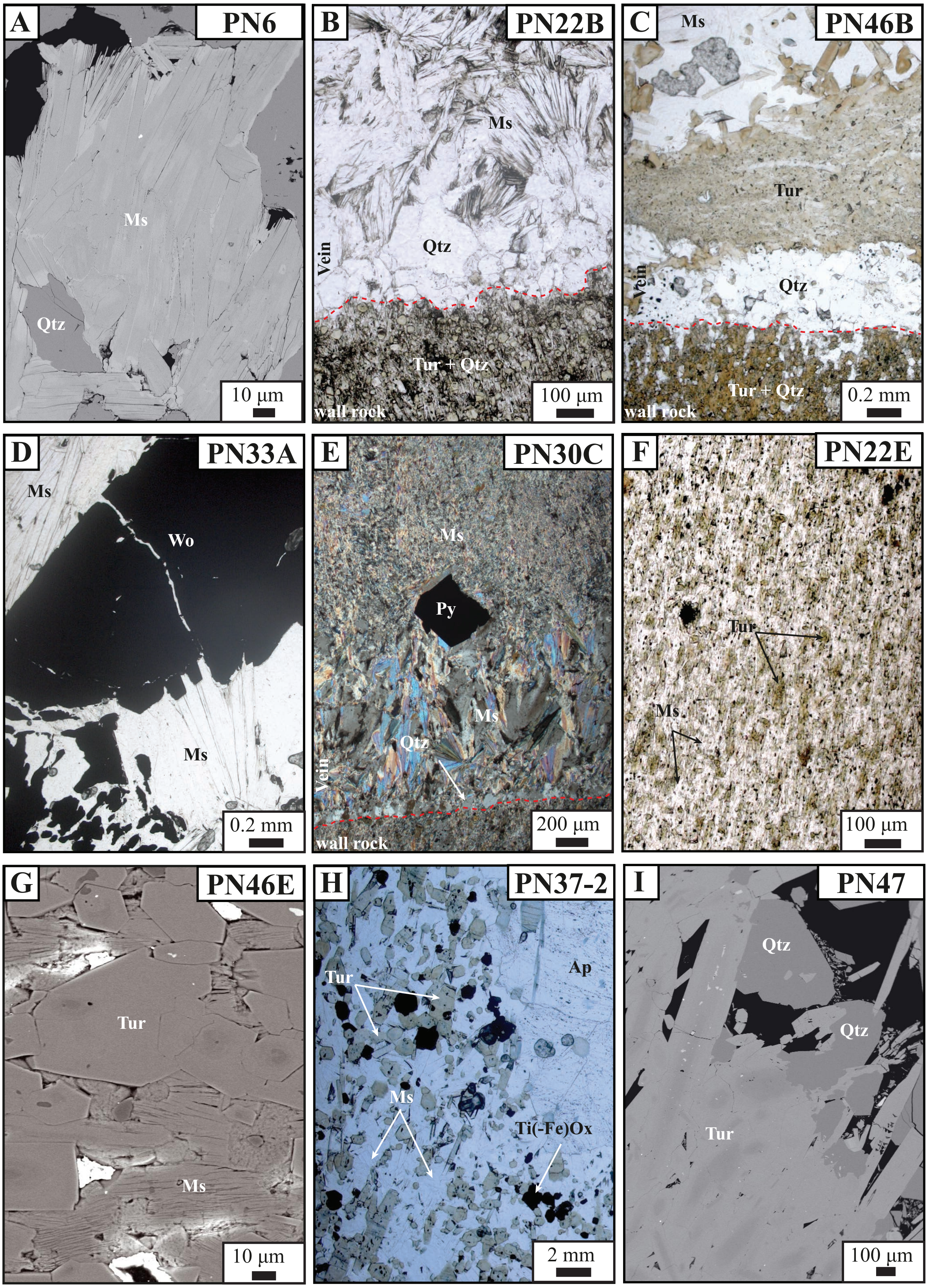
A
PN6
Ms
Qtz
10 µm
B
PN22B
Ms
Qtz
Vein
Tur + Qtz
wall rock
100 µm
C
PN46B
Ms
Tur
Qtz
Vein
Tur + Qtz
wall rock
0.2 mm
D
PN33A
Ms
Wo
Ms
0.2 mm
E
PN30C
Ms
Py
Ms
Qtz
Vein
wall rock
200 µm
F
PN22E
Tur
Ms
100 µm
G
PN46E
Tur
Ms
10 µm
H
PN37-2
Tur
Ap
Ms
Ti(-Fe)Ox
2 mm
I
PN47
Qtz
Qtz
Tur
100 µm

Tourmaline grains are typically zoned and show significant increases in Fe, F, and Na and decreases in Mg, Ca and Al from core to rim. Also, Al and Fe decrease and Mg increases with distance from the vein contact. Tourmaline compositions reflect the composition of the host schists and are interpreted to have formed at the expense of the chlorite-biotite-rich protoliths due to extensive fluid-rock interaction of a magmatic-hydrothermal B-Na-rich fluid during the early stages of Panasqueira hydrothermal system (Codeço et al., 2017).

The compositions of white mica range from muscovite towards the celadonite and alumino-celadonite end-members (Codeço et al., 2019a). The main variations in major elements include changes in the Fe/Mg ratio, Al, and F. The greisen shows the highest Fe/Mg ratios (up to 10), whereas mica from altered host rocks are the lowest (0.5 – 1), and the vein selvages have intermediate ratios. The greisen and most vein-selvage micas overlap in terms of Al and F with wall-rock mica, the exception being mica from the topaz-rich selvages, which has highest F and lowest Al contents (ca. 7 wt.% F and 21 wt.% Al_2O_3). Neiva (1987*b*) determined trace-element concentrations in mica from Panasqueira based on analyses of mineral separates. They reported high Rb (>2000 ppm) and relatively high Li (400 to 1000 ppm). Tungsten concentrations were mostly around 50 ppm, except for 2 analyses with more than 100 ppm that likely reflect inclusions. Tin concentrations ranged from 150 to 230 ppm, Cu below 40 ppm and Zn from 230 to 420 ppm. The Nb, Ta and Cs concentrations were typically around 40, 4 and 80 ppm, respectively, except for the greisen where Nb and Ta values reached 120 and 35 ppm, respectively. Based on these results, Neiva (1987*b*) suggested that Sn and Cs can be used in the hydrothermal micas from quartz-veins as an exploration tool for W and Sn deposits.

5.4 Samples and Methods

5.4.1 Samples

The samples used in this study are described in Codeço et al. (2017) and Codeço et al. (2019a), with major element compositions for mica and tourmaline reported in the latter study. The rock samples used for whole-rock chemistry were collected from three drill cores from underground galleries (D1602, M1609 and M1610) and four exploration drill-cores (SCB-1, SCB-2, SPS-1 and SMN-1) (Figure 5.2A). Samples representing the non-mineralized country rocks were taken from two outcrops at 5.5 and 10.5 km from the deposit [see the location in the Appendix A and sample detailed description in the Data Publication (Codeço et al., 2019b)].

The samples collected from underground drill cores show the hydrothermal variation in the host rock envelope. Petrographic observations corroborate that tourmalinization only occurs around the veins, be they mineralized or not. The amount of tourmaline increases towards veins and veinlets of quartz ± sulfides (often chalcopyrite and sphalerite) (Figure 5.4A) and the thickness of the tourmaline zone is a function of the vein size and vein density (Figure 5.4B). Away from the previously described zone, rocks are dominated by quartz, biotite, chlorite and white mica. Biotitization and chloritization result either from contact metamorphism or peak metamorphism under greenschists facies (chlorite zone) conditions, and these processes are indistinguishable in these samples (Figure 5.4C to E).

The samples from exploration drill cores are representative of the metasediments unaffected by the hydrothermal alteration. They consist of green-colored phyllites and schists typically intercalated with quartzite and greywackes (Figure 5.4D, E). The main minerals are muscovite, biotite, chlorite and quartz. Samples located close to the surface (< 50m) contain less biotite and more chlorite than those closer to the granitic body, which may reflect the contact metamorphism. The drill core SCB-2, located ca. 800 m NE of the limits of the current underground workings intersects the granitic body. The contact zone starts at ca. 315 m depth and consists of a pelitic hornfels with granoblastic

Figure 5.4 *(facing page)*: Photomicrographs of: **(A)** a tourmalinized fine-grained metasediment and a quartz-sulfide veinlet (plane-polarized light); **(B)** the contact between a sub-vertical quartz-sulfide veinlet and the metasediment increasingly tourmalinized at the contact (plane-polarized light); **(C)** a muscovite-quartz-biotite-chlorite-rich metasediment (plane-polarized light); **(D)** a unaltered greywacke (plane-polarized light); **(E)** the alternation of pelitic layers with greywacke layers slightly biotitized (plane-polarized light); **(E)** of a pelitic hornfels resulting from contact metamorphism with the granitic body (plane-polarized light); **(F)** the greisen in contact with the hornfels (plane-polarized light); **(H)** the coarse-grained two-mica granite (plane-polarized light); (I) the aplitic zone in the granitic body, showing sericitization of the feldspars (Fp*) and chloritization of biotite (?) (cross-polarized light). Bt, biotite; Cb, carbonates; Ccp, chalcopyrite; Chl, chlorite; Fp, feldspar; Fp*, sericitized feldspar; Ms, muscovite/white mica; Qtz, quartz; Po, pyrrhotite

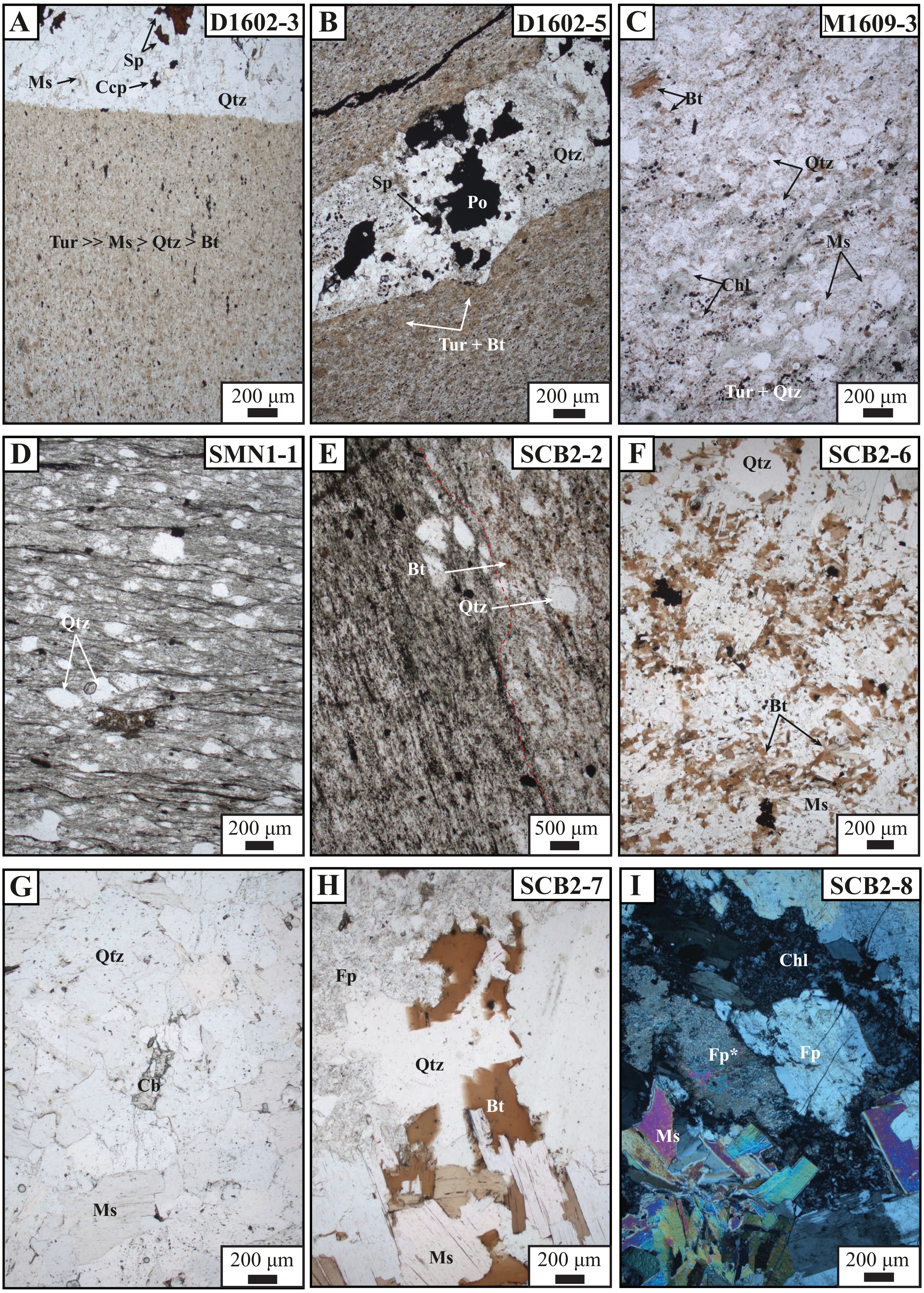
A
D1602-3
Sp
Ms
Ccp
Qtz
Tur >> Ms > Qtz > Bt
200 µm
B
D1602-5
Qtz
Sp
Po
Tur + Bt
200 µm
C
M1609-3
Bt
Qtz
Ms
Chl
Tur + Qtz
200 µm
D
SMN1-1
Qtz
200 µm
E
SCB2-2
Bt
Qtz
500 µm
F
SCB2-6
Qtz
Bt
Ms
200 µm
G
Qtz
Cb
Ms
200 µm
H
SCB2-7
Fp
Qtz
Bt
Ms
200 µm
I
SCB2-8
Chl
Fp*
Fp
Ms
200 µm

texture composed of quartz, muscovite, biotite and feldspars (Figure 5.4E). Accessory phases include tourmaline, cassiterite, sulfides and chlorite. The grain-size increases with depth and the hornfels gradually passes into greisen (ca. 316 m) (Figure 5.4F) and granite (at ca. 327 m). The granite is a coarse-grained two-mica granite, with muscovite >biotite (Figure 5.4G), commonly showing aplitic domains (Figure 5.4H). The main minerals are muscovite, biotite, albite, K-feldspar and quartz (Figure 5.4G). Zircon, sulfides and cassiterite occur as accessory phases. The aplitic domains commonly show advanced sericitization of the feldspars and chloritization of biotite (Figure 5.4H).

The samples collected in the outcrops consist of intercalations of greywacke, schist and quartzite layers displaying strong deformation, foliation and crenulation cleavage. The main minerals in these rocks are quartz, muscovite and minor biotite. Zircon and feldspar are accessory phases.

5.4.2 Whole-rock geochemistry

For whole-rock chemical analyses of major and trace elements, samples were crushed and subsequently powdered in an agate mill to a grain size of less than 62 micron at the University of Potsdam. Major element oxide (SiO_2, TiO_2, Al_2O_3, Fe_2O_3, MnO, MgO, CaO, Na_2O, K_2O, P_2O_5) and trace element (Ba, Cr, Ga, Nb, Ni, Rb, Sr, V, Y, Zn and Zr) analyses were carried out on fused disks, using a PANalytical Axios Advanced wavelength-dispersive x-ray fluorescence spectrometer (XRF) at the GeoForschungsZentrum (GFZ) Potsdam, Germany. Samples were quantified using calibration curves generated from 105 reference standards.

Sample digestion and measurement of selected trace elements including As, Be, Bi, Cd, Co, Cs, Cu, Ge, Mo, Pb, REE, Sb, Sc, Sn, Th, Tl, U, and W from 14 whole-rock samples (M1610-1, M1610-2, M1610-3, M1610-4, M1610-5, M1610-6, SCB1-1, SCB2-2, SCB2-4, SCB2-7, SCB2-8, SMN1-1, SMN1-4, SMN1-7) were performed by inductively coupled plasma mass-spectrometry (ICP-MS) at GFZ Potsdam, using a HR-ICP-MS Thermo Element 2XR. The samples (125 mg sample material) were digested in HF and aqua regia following the procedure explained in Pretorius et al. (2006) and Romer and Hahne (2010). The internal standard In (Indium) was added to the solutions to compensate for drift corrections. The reported analytical precision of the elements is better than ± 5% (Dulski, 2001).

In addition to the new samples from this study, we included whole rock data obtained at the University of Porto, which were previously published (Pinto et al., 2014)

5.4.3 Laser ablation-ICP-MS

For the LA-ICP-MS analyses, 120-μm-thick polished sections were prepared from the same sample billets as the thin sections used by Codeço et al. (2017) and Codeço et al. (2019a) for microprobe and SIMS analyses. Major, minor and trace element (^{7}Li, ^{11}B, ^{23}Na, ^{24}Mg, ^{27}Al, ^{29}Si, ^{39}K, ^{47}Ti, ^{51}V, ^{55}Mn, ^{57}Fe, ^{63}Cu, ^{66}Zn, ^{85}Rb, ^{88}Sr, ^{89}Y, ^{90}Zr, ^{93}Nb, ^{118}Sn, ^{133}Cs, ^{137}Ba, ^{153}Eu, ^{181}Ta, ^{182}W, ^{205}Tl, ^{208}Pb) concentrations in mica and tourmaline crystals were determined in 11 samples using a NewWave 213 nm Nd-YAG laser coupled to a Thermo-Finnegan iCAP Qc quadrupole ICP-MS in the Earth and Planetary Sciences department at McGill University. Except for grains <40 μm in size, line-scan mode was used to avoid the analysis of subsurface inclusions by minimizing the depth of ablation. We used the following analytical conditions: 9 to 10 J/cm^2 fluence, 10 Hz laser pulse frequency, 20-μm line width, 5-μm/sec linescan speed, 30 s warm-up, approximately 40 s ablation time and 20 s wash-out. Sample material was transported to the ICP-MS in an 800 mL/min He flow and mixed with Ar prior to injection into the plasma. Analyses were bracketed with NIST-SRM 610. In addition, Muscovite (#198973), Dravite (#1108796), Schorl (#1112566), an in-house tourmaline standard (UoB), as well as BGR-2G and GSD-1G reference materials were measured in the beginning and at the end of the session [tourmaline data from Dyar et al. (2001), others from the GEOREM database – Jochum et al. (2016)]. The raw data was processed using the Iolite data processing software. The limits of detection (LOD) and uncertainties of each element and each mineral are reported in Appendix C (Tables C.2 and C.1). The abundance of the major elements (Na, K, Mg, Fe, Ti, Al, Mn, Si) was used to normalize the collected data to 15 cations at the Y, Z and T sites (for tourmaline) and a 22 total charge (for white mica) and thereby correct for differences in ablation behavior between the samples and NIST-SRM-610. This method avoids the need for an internal reference element determined by another analytical technique. It was tested against direct normalization to major elements determined by electron microprobe from Codeço et al. (2017) and Codeço et al. (2019a), showing it to be robust and producing data of equivalent analytical uncertainty. It has the advantage over direct normalization that avoids a mismatch between laser and microprobe locations of analysis.

5.4.4 Principal Component Analysis

Principal component analysis (PCA) is a multivariate statistical technique that identifies compositional vectors in a dataset by transforming the initial variables (e.g., the elemental concentrations) into a new set of principal components (PCs). The principal components are defined as orthogonal linear combinations of the initial variables that align with the maximum variance in the dataset, with PC1 explaining most variance. Eigenvalues and eigenvectors are used to characterize each PC. The eigenvalues represent the contribution of each principal components to the overall variance of the original data, while the eigenvectors represent the correlations between the initial data and the principal components (Pawlowsky-Glahn et al., 2015, and references therein). It is commonly assumed that PCs with low eigenvalues are dominated by noise, and when these are subsequently discarded the dimensionality of the dataset is reduced, which facilitates interpretations of many-element datasets. The latter method is strictly speaking referred to as Factor Analysis (FA), although the terms are used interchangeably in common usage. Whereas PCA is a pure mathematical transformation, FA represents an interpretation of the data. PCA and FA have found many applications in evaluating geochemical data from studying compositional variations in volcanic rocks, to geochemical exploration, in detecting end-members compositions and chemical reactions in mineral solid-solutions, and for detecting mantle isotope end-members and their mixing relationships (see reviews by Belissont et al., 2014; Ueki and Iwamori, 2017). The statistical calculations and graphical results presented below were obtained using the ioGAS™ software (`https://reflexnow.com/iogas/`).

5.5 Results

5.5.1 Whole rock composition

The host-rock schist samples can be subdivided into unaltered and hydrothermally altered occurrences based on petrographic observations. We further distinguish between samples taken from the mine and from exploration drill cores at the NE continuation of the mine, which is barren. The samples from Pinto et al. (2014) are subdivided into samples proximal and distal to the cupola, while samples from this study are all proximal. The full data set of whole rock major, minor and trace element compositions are presented in the Data Publication (Codeço et al., 2019b) and the CD-ROM for the printed version. Both the altered and unaltered metasediments show a wide compositional range for most major elements, which reflects the varying proportion of sandstone-shale intervals in these units. The Rare Earth Element (REE) concentrations in altered and unaltered metasediments overlap completely (Appendix C, Figure C.1) and have relatively high middle- and heavy-REE contents (Sm, Eu, Gd, Yb and Lu) compared with the light REE. Thus, both major element and REE compositions are not useful indicators for the alteration and we focus on minor and trace element contents to identify and quantify the chemical overprint of hydrothermal fluid-rock interaction.

The minor and trace element concentrations from all analyzed samples were normalized to those of the average upper continental crust (Rudnick and Gao, 2014) and plotted with the elements ordered according to their normalized abundance in the altered rocks (Figure 5.5A). In decreasing order, the results show enrichments in As, Sn, Cd, Cs, Li, W, F, Bi, Cu, Rb, Zn, Tl, and Be in altered schists. The results from the greisen and granite samples analyzed in this study and in Pinto et al. (2014) show that these elements are also primarily enriched in the underlying, partially altered magmatic intrusion Figure 5.5B). The main exceptions from this pattern are Pb and Mo, which have elevated concentrations in greisen but variable concentrations in altered schists.

A factor analysis (FA) of all altered and unaltered schist samples using a set of 16 elements confirms the element systematics described above (Figure 5.6). We included two major elements of the rocks (Fe, Mg), ten elements that are most enriched during alteration (the ore elements W, Sn, Cu and Zn, as well as F, Rb, Cs, Li, As, and Tl), and

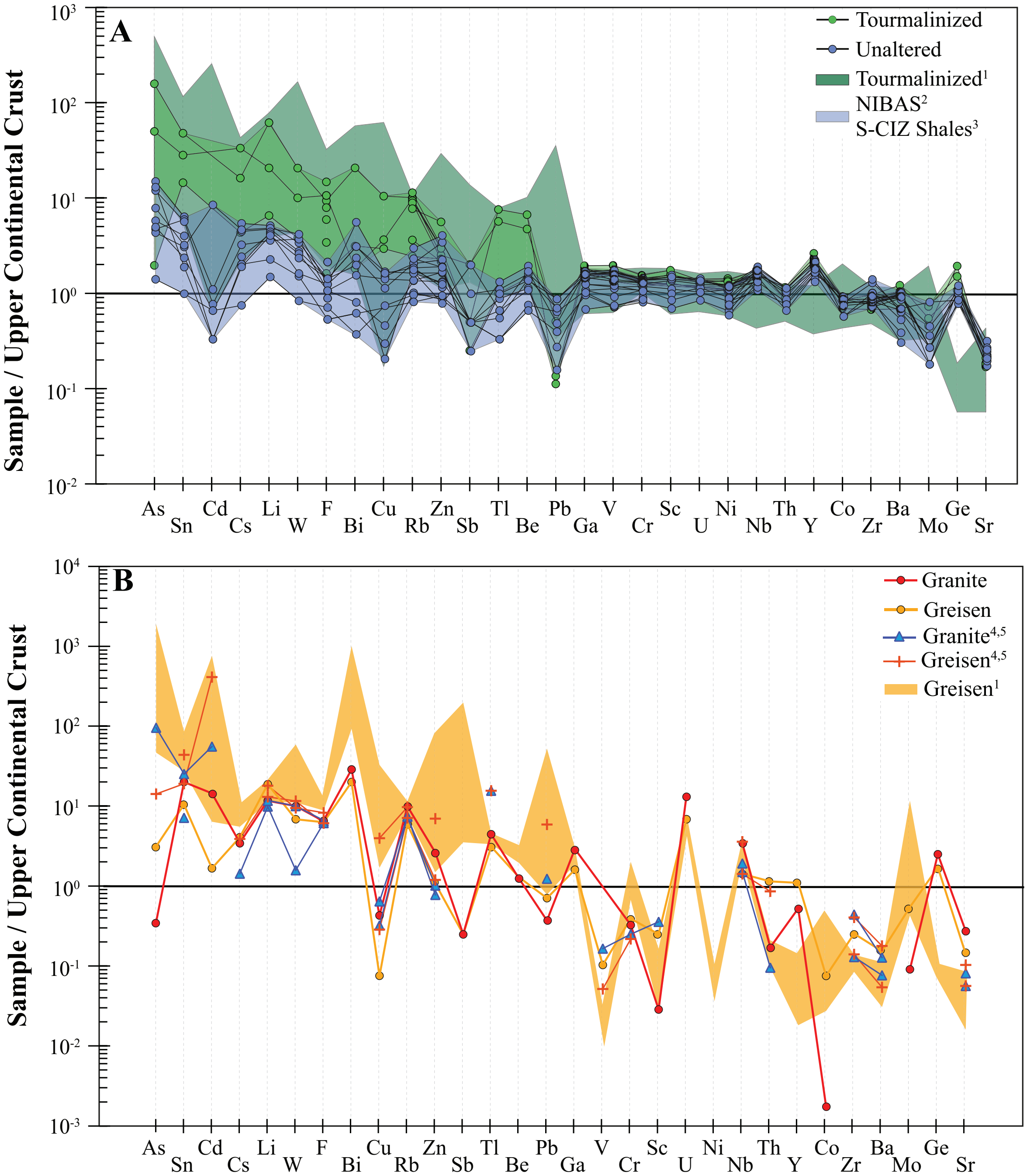

Figure 5.5: Distribution of trace elements **(A)** in the altered and unaltered metasediments and **(B)** in the granite and greisen. All data are normalized to the upper continental crust (Rudnick and Gao, 2014). Data sources: [1]Pinto et al. (2014), [2]Ugidos et al. (2010), [3]Villaseca et al. (2014), [4]Bussink (1984), and [5]Neiva (1987*a*).

four trace elements that are known to remain relatively unchanged during the alteration process (V, Sr, Ba, and Nb). The analysis shows that three principal components (PC) account for 81 % of the total variance with 45.4% for PC1, 24.4% for PC2 and 11.6% for PC3. PC1 separates unaltered and altered metasediment samples (Figure 5.6A) and most of the ten "alteration" elements load strongly on PC1, with weaker loadings for Zn, Cu and As (Fig 5.6B). PC2 reflects differences in the mineralogy with strong loadings for Mg, Ba, V and Fe. Nb also primarily loads on PC2, but is also the only element with a slightly negative correlation in PC1. PC2 may mainly reflect heterogeneities in the host rocks or different modal amounts of tourmaline and mica. PC3 seems to reflect the relative distance of samples from the greisen cupola, with more distal samples having higher Cu, Zn and As and proximal samples displaying higher Cs, Rb and Tl (Figure 5.6C and D). There is also a weak distinction in PC3 for F and Li (higher in proximal samples) and for Sn and W (higher in distal samples). Additionally, Sr loads relatively strong on PC3 but is uncorrelated with all other elements used for the analysis (Figure 5.6D).

5.5.2 Trace-element compositions of white mica and tourmaline

For the analyses of trace elements in white mica and tourmaline, we focus on the elements that have been investigated in the whole-rock data, namely Sn, W, Cu, Zn, Cs, Li, Rb, and Tl as the main elements representing enrichment by hydrothermal fluids (loading mainly on PC1 in Figure 5.6) and Fe, Mg, Ba, V, Nb, and Sr as elements that are not (or less) affected by the hydrothermal alteration (loading mainly on PC2 and PC3 in Figure 5.6). Other elements that show important variations in the whole-rock data, including As, Cd, F, Bi, and Sb, could not be analyzed or were not detected with LA-ICP-MS, and are not included here. Instead, we added Ta because Nb/Ta ratios are commonly used as markers of magmatic-hydrothermal processes. Tables with laser ablation analyses are provided in the Data Publication (Codeço et al., 2019a) and for the printed version of this thesis in the enclosed CD-ROM

5.5.2.1 White mica

The mica compositions show positive correlations of element pairs including Li-Mg (Figure 5.7A), Nb-Ta (Figure 5.7B) and Cs-Rb (Figure 5.7C). Sr and V show a negative correlation with highest V/Sr in the wall rock and lowest V/Sr in micas from the MPS within the same sample as well as generally low contents of both elements for several setting, including the fault zone and the greisen (Figure 5.7D). The Sn and W variations describe an overall negative correlation, with the highest W/Sn ratio in greisen mica and

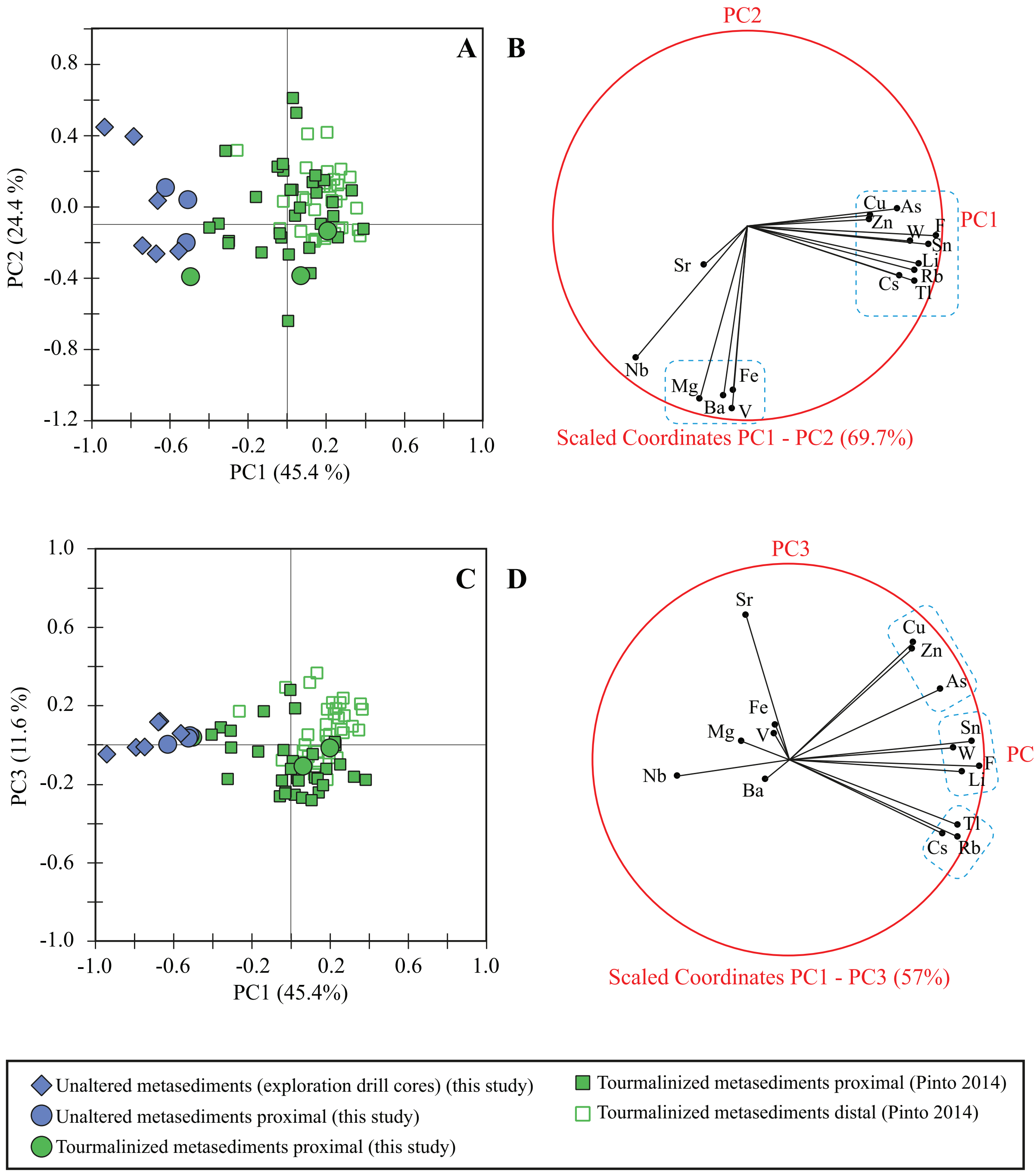

Figure 5.6: Results of principal components analysis (PCA) applied to major and trace element compositions of whole rock (log-transformed). **A** and **C** show analyses plotted in PC1 vs. PC2 and PC3 planes, resp., and **B** and **D** show element vectors (as variables) in the corresponding planes The terms proximal and distal in the legend refer to distance from the greisen cupola. Dashed outlines in **B** and **D** highlight element clusters.

the highest Sn/W in mica within the fault zone. The ore elements Cu and Zn are both highly variable and do not correlate with each other. In general, the data show strong clustering of data by setting and sample.

Mica compositions from the greisen sample show the most distinctive compositions with generally very low Mg contents. Compared to other settings, the greisen micas have very high Ta and Nb (up to 100 and 200 ppm, resp.), and high W and Zn (up to 120 and 150 ppm, resp.), but low Sn (70-170 ppm) contents. Their Li, Cs, Rb, and Cu contents are variable and overlap with the other settings. Some of this variability relates to compositional zoning with mica rims having higher Li and Sn, but lower Cu and W values relative to cores (see "rims" in Figures 5.7A, E, and F). In terms of Cs, Rb, Ta, and Nb, mica compositions form two distinctive clusters within individual grains (see "cl_2" in Figures 5.7B, C), but this clustering cannot be related to growth zones.

Mica compositions from the vein selvage type MRS (mica-rich) vary greatly among the three different samples, forming distinct clusters in some of the binary plots. Sample PN46 has high Nb and Ta contents that are comparable to the mica from the greisen. Sample PN22 has lower Li, Rb and Zn contents compared to PN33 and PN46. However, sample PN22 contains two mica generations, with early mica ("E_m" in Figure 5.7) having lower Mg, Li, Rb, W, and Zn contents but higher Sn, Nb, Ta, Sr and V than later mica generations and most other MRS samples. Mica from PN33 is distinctive for high V and low Sr contents. Micas from samples PN33, PN46 and PN22 (except the early micas) contain relatively high W and Zn, but low Sn concentrations. The mica from one sample of vein selvage type MPS (mica poor) have a compositional range intermediate between PN22 early micas and the remaining MRS micas. Their main distinction are high Sr concentrations and, in two cases, particularly low Sn and W contents.

Due to small grain sizes and intergrowths, only a few analyses of mica from only one sample of wall-rock alteration could be obtained. Mica in sample PN30 yielded high Li, V, and Mg contents compared with the vein selvages and greisen, but low W, Sn, and Zn contents. Wall-rock mica and the early generation of mica from MRS sample PN22 have similar Nb, Ta, Cs, and Rb contents. White mica from the fault zone (sample PN37-2) is distinctive from all others in terms of high Li, Mg, Sn, and low Nb, Ta, and

Figure 5.7 *(facing page)*: Main chemical variations of minor and trace elements in white mica. MRS: mica-rich selvages, MPS: mica-poor selvages, Wr-dist: wall-rock distal from the vein contact, E_m: Early formed mica in sample PN22, rim: *rims* or overgrowths in mica from the greisen.

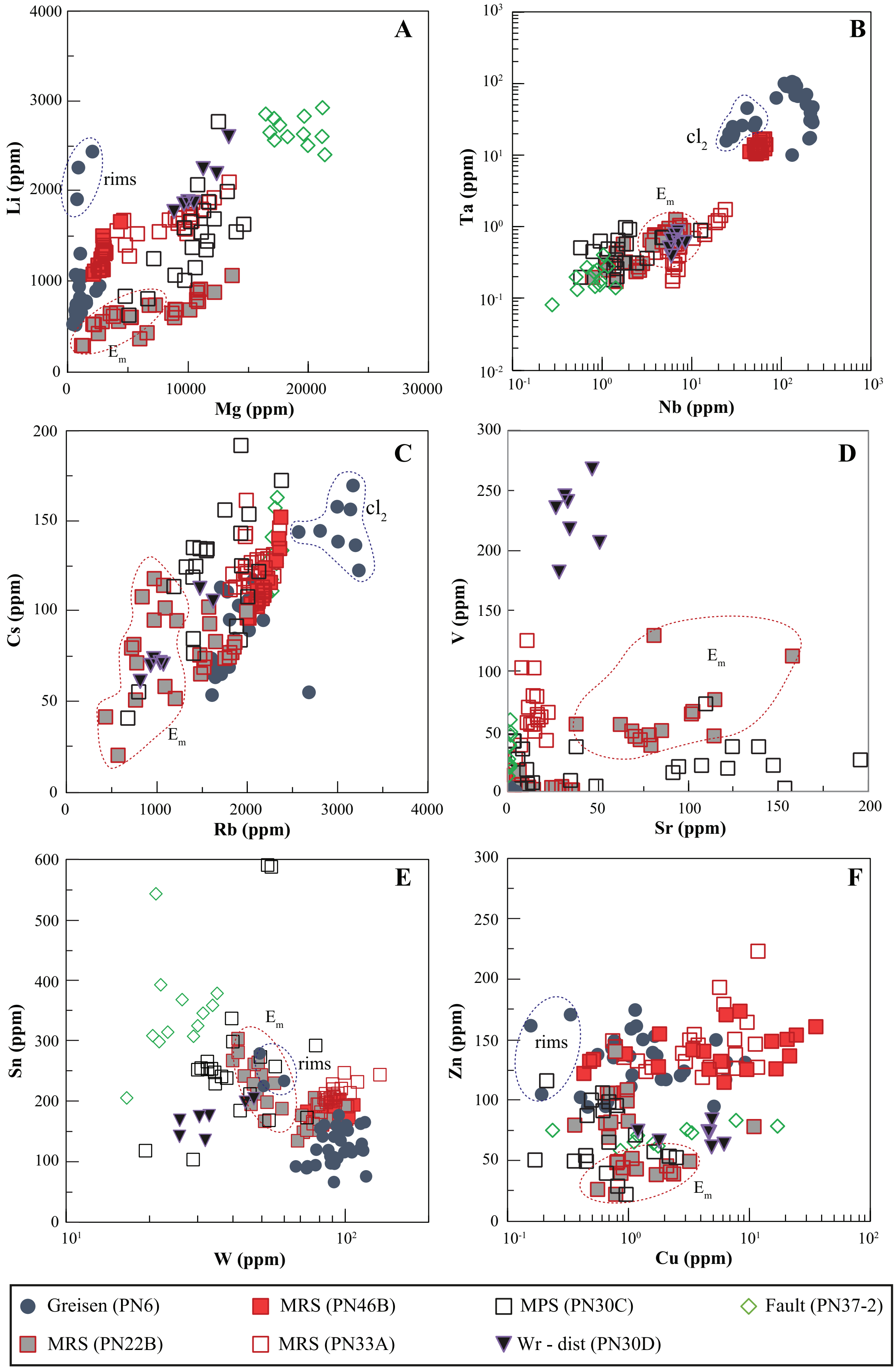
A
Li (ppm)
Mg (ppm)
0
1000
2000
3000
4000
10000
20000
30000
rims
E_m
B
Ta (ppm)
Nb (ppm)
10⁻²
10⁻¹
10⁰
10¹
10²
10³
cl₂
E_m
C
Cs (ppm)
Rb (ppm)
0
50
100
150
200
1000
2000
3000
4000
cl₂
E_m
D
V (ppm)
Sr (ppm)
0
50
100
150
200
250
300
E_m
E
Sn (ppm)
W (ppm)
0
100
200
300
400
500
600
10¹
10²
E_m
rims
F
Zn (ppm)
Cu (ppm)
0
50
100
150
200
250
300
10⁻¹
10⁰
10¹
10²
rims
E_m
● Greisen (PN6)
🟥 MRS (PN46B)
☐ MPS (PN30C)
◇ Fault (PN37-2)
▨ MRS (PN22B)
☐ MRS (PN33A)
▼ Wr - dist (PN30D)

W contents. For the other elements shown, the fault-zone mica overlaps with those from the vein selvages.

The clustering by setting and sample is also reflected by the PCA, where again three components account for 81% of the total variance, with 44.4% in PC1, 27.5% in PC2 and 8.7% in PC3 (Figure 5.8). High concentrations in W, Ta, and Nb distinguish the greisen from other settings. The early MRS is distinct in terms of Sr. The fault zone is distinguished by higher Sn and Mg, with low W, Ta, and Nb. In contrast to the whole-rock analysis (Figure 5.6B), the element vectors show less tendency to group together in the PC1-PC2 projection, i.e. some of their loadings contribute equally to both principal components (Figure 5.8B) and neither PCs dominates the mica variability. In contrast, the projection of PC1 and PC3 (Figure 5.8C, D) shows that the variation of most elements is controlled by PC1. Copper shows a different behavior, being strongly loading on PC3 (Figure 5.8D) but with little influence on PC1 and PC2 (i.e., short vector on Figure 5.8B).

5.5.2.2 Tourmaline

Tourmaline at Panasqueira is commonly zoned, with systematically higher Fe/Mg ratios from core to rim (Codeço et al., 2017). Wherever possible, core and rim compositions of tourmaline were acquired, but most of the analyses consist of mixtures between rim and core composition. The trace-element variations show this influence of the zoning, with tourmaline rims having higher Zn and Li and lower Sr and Mg contents than cores (Figure 5.9). Tourmalines from all settings typically show overlapping compositions and only occasionally clustering by sample or type. The only distinct compositions are noted in the cores of tourmaline from the fault zone and the late vugs (Figure 5.9), which show the highest Mg and Sr, and the lowest Li, and Zn contents in the dataset (see Figure 5.9A, D, F).

The lithophile element pairs Rb-Cs and Nb-Ta show the expected strong positive correlations with each other (Figure 5.9C, D) as was also found in mica, whereas the chalcophile Zn-Cu pair is not correlated. Indeed, Cu shows a large random variation with no relationship to other elements, to crystal zoning or to setting within the deposit. With scattered exceptions, both Sn and W concentrations are below 30 ppm, and the two elements show no correlation in the tourmaline, nor is there a systematic difference

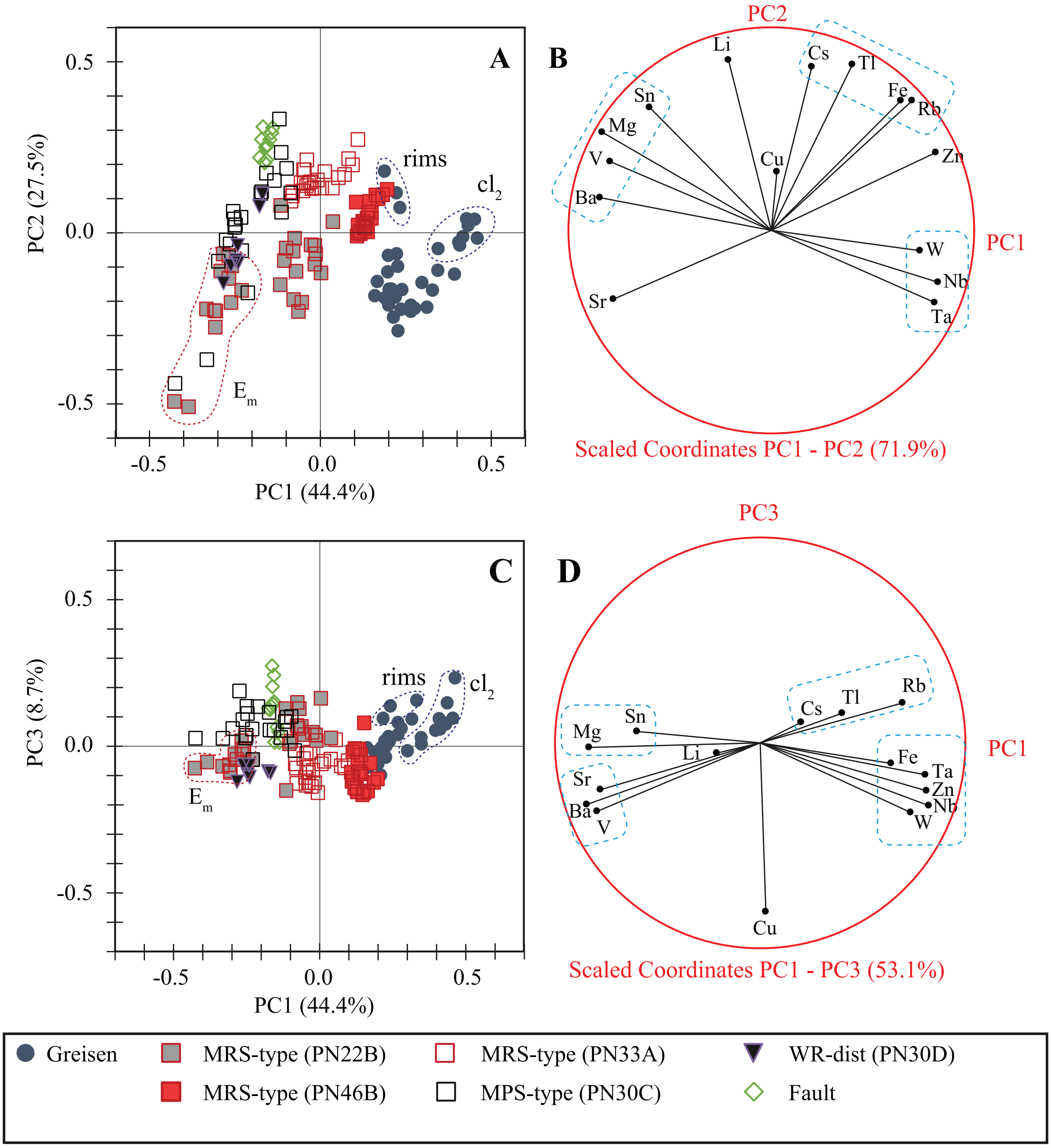

Figure 5.8: Principal components analysis (PCA) of the LA-ICP-MS log-transformed dataset of selected minor and trace elements in white mica from Panasqueira (see text for details). **A** and **C** show analyses plotted in PC1 vs. PC2 and PC3 planes, **B** and **D**show element vectors (as variables) in the corresponding planes. MRS: mica-rich selvages, MPS: mica-poor selvages, Wr-dist: wall-rock distal from the vein contact, E_m: Early formed mica in sample PN22, cl_2: distinctive cluster (see text for explanation), rim: *rims* or overgrowths in mica from the greisen. Dashed outlines in **B** and **D** highlight element clusters.

in concentrations relative to crystal zoning or to setting (Figure 5.9E).

The lack of clear correlations among the elements is reflected in the PCA results for tourmaline, whereby the first four PCs are needed to explain the most relevant variations (69.4% of the total variance), with 28.9% for PC1, 21.4% for PC2, 10.9% for PC3 and 8.3% PC4. From Figure 5.10A, C and E, the most noticeable trend is the separation between core and rim along PC1, where rims are enriched in Fe, Zn and Li and depleted in Sr and Mg relative to the cores. PC2 and PC3 are dominated by the variations in trace elements, and are mainly controlled by the two positive correlations in Cs-Rb and Nb-Ta with PC2 capturing a positive correlation of all four elements and PC3 showing opposing trends between these element pairs (Figure 5.10A to D). The PC4 component reflects the high Cu and V concentrations in the fault and wall rocks (Figure 5.10E, F).

5.6 Discussion

5.6.1 Constraining the composition of the hydrothermal fluid

The altered metasediments associated with mineralization show large scale enrichment in the ore metals W, Sn, Cu and Zn as well as in As, F, Li, Rb, Cs, and Tl relative to the unaltered metasediments (cf. green vs. blue symbols, Figures 5.5, 5.6). Contents of Mg, Ba, Fe, and V are not affected by alteration as indicated by PC2 in Figure 5.6A, while Nb and Sr tend to be more concentrated in the unaltered samples (Figures 5.5B, 5.6). The compositions of the unaltered schist and granite samples compare well with analyses from the literature (Bussink, 1984; Neiva, 1987*a*; Ugidos et al., 2010; Villaseca et al., 2014), showing that the metasediments and the magmatic intrusion at Panasqueira have typical compositions for this region.

The regional element systematics of altered and unaltered rocks are also seen in single drill-core profiles, which show a gradual transition from unaltered to strongly altered metasediments next to the vein. This is shown by data from drill core M1610 (Figure 5.11, see also filled circles in Figure 5.6). The proximity to a mineralized vein increases

Figure 5.9 *(facing page)*: Main chemical variations of minor and trace elements in tourmaline. MRS: mica-rich selvages, MPS: mica-poor selvages, Wr-dist: wall-rock distal from the vein contact.

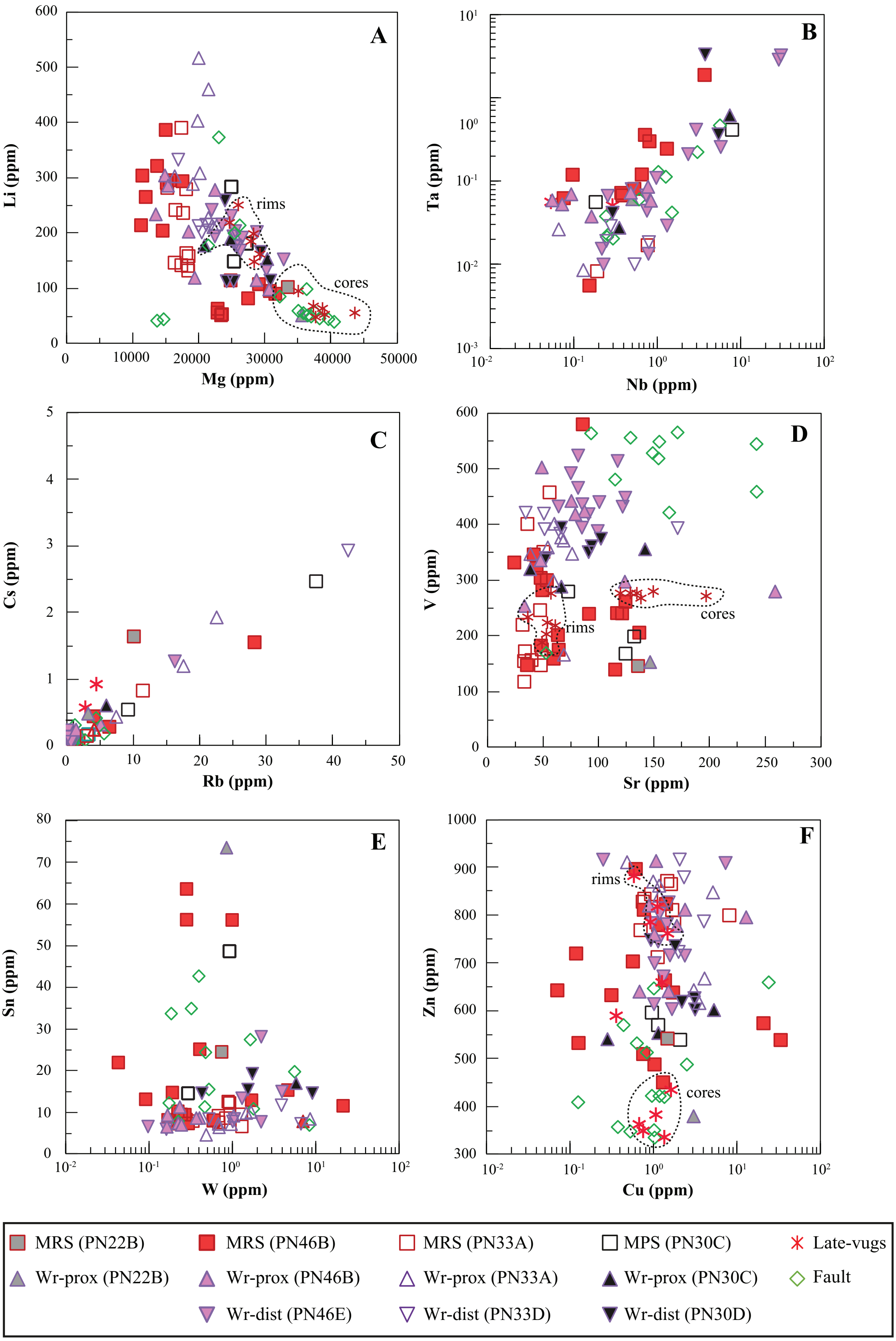
A
Li (ppm)
Mg (ppm)
0
100
200
300
400
500
600
0
10000
20000
30000
40000
50000
rims
cores
B
Ta (ppm)
Nb (ppm)
10^{-3}
10^{-2}
10^{-1}
10^{0}
10^{1}
10^{2}
C
Cs (ppm)
Rb (ppm)
0
1
2
3
4
5
0
10
20
30
40
50
D
V (ppm)
Sr (ppm)
0
100
200
300
400
500
600
0
50
100
150
200
250
300
rims
cores
E
Sn (ppm)
W (ppm)
0
10
20
30
40
50
60
70
80
10^{-2}
10^{-1}
10^{0}
10^{1}
10^{2}
F
Zn (ppm)
Cu (ppm)
300
400
500
600
700
800
900
1000
10^{-2}
10^{-1}
10^{0}
10^{1}
10^{2}
rims
cores
MRS (PN22B)
MRS (PN46B)
MRS (PN33A)
MPS (PN30C)
Late-vugs
Wr-prox (PN22B)
Wr-prox (PN46B)
Wr-prox (PN33A)
Wr-prox (PN30C)
Fault
Wr-dist (PN46E)
Wr-dist (PN33D)
Wr-dist (PN30D)

downward, and the lower samples show higher scores in PC1, reflecting an increase in the alteration overprint. This increase sets in abruptly at a distance of about 8 m from the bottom of the core (Figure 5.11), which we interpret as the vertical extent of the alteration front in this profile.

Another example of mineralogical control which is well reflected by the PCA analysis relates to the proximity of samples to the greisen cupola (Figure 5.6). This is best discriminated by PC3 (Figure 5.6C) where samples proximal to the cupola (filled green symbols) have mostly negative values, whereas the distal samples show predominantly positive values for PC3. Mineralogically, the samples close to the greisen are richer in mica, with selvages up to 3 cm thick, whereas the distal samples are associated with mineralized veins containing chalcopyrite, pyrite, arsenopyrite, cassiterite, wolframite, topaz and sphalerite. Thus, the negative values for PC3 (Figure 5.6D) reflect the higher Cs, Rb, and Tl in mica from proximal zones, whereas the distal samples have higher As, Zn and Cu contents related to vein mineralization, resulting in positive PC3 values. The Sn, W, Li and F variations are nearly independent of proximity to the cupola, but all are strongly enriched in the altered vs. unaltered samples (discriminated by PC1). We interpret these whole-rock compositional trends to reflect elements added or removed by the hydrothermal fluids, which suggests that the fluid was enriched predominantly in Cu, Zn, As, Sn, W, Li, F, Cs, Rb, and Tl. For comparison, direct measurements of quartz-hosted fluid inclusions from the mineralized veins at Panasqueira are available from the study of Lecumberri-Sanchez et al. (2017). They reported median concentrations above 100 ppm for Li, Cs, and Cu; from 10s to 100 ppm for As, Pb and W; variable but locally high values from tens to hundreds of ppm for Rb and Zn; and below detection limit for Sn. These fluid compositions are thus partly in agreement with observed enrichments in the altered relative to the unaltered rocks, with the notable exception of Sn. The lack of

Figure 5.10 ***(facing page)*****:** Principal components analysis (PCA) of the LA-ICP-MS log-transformed dataset of selected minor and trace elements (see text for further details) in tourmaline from Panasqueira. Plots on the left (**A**, **C**, and **E**) show analyses in the PC1 vs. PC2 and PC3 planes, and on the right (**B**, **D** and **F**) the elements (or variables) are plotted as vectors on the corresponding planes. MPS: mica-poor selvages, Wr-prox: wall-rock proximal to the vein-contact, Wr-dist: wall rock distal from the vein contact. Dashed outlines in **B**, **D** and **F** highlight element clusters.

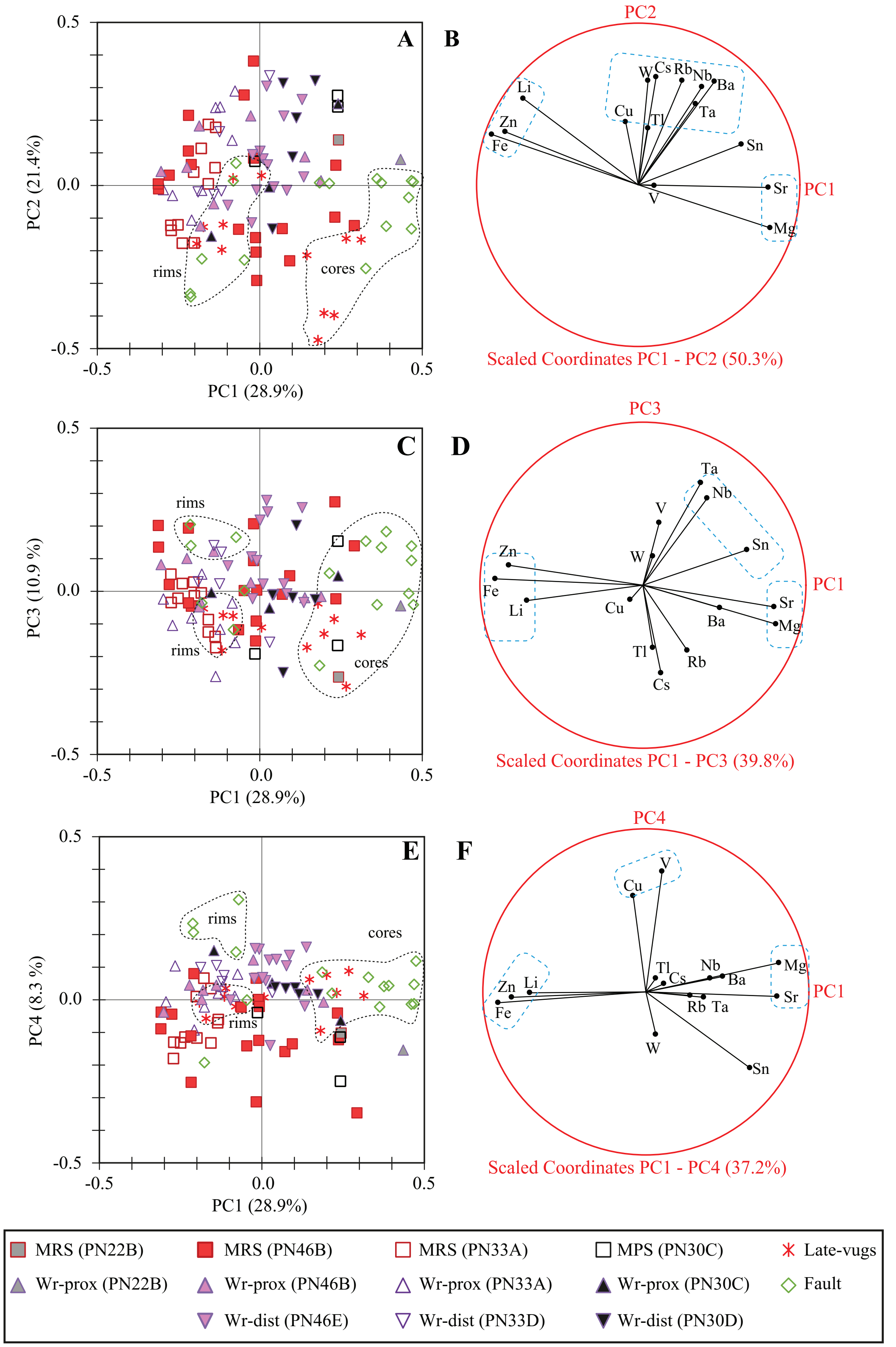
A
B
C
D
E
F
PC1 (28.9%)
PC2 (21.4%)
PC3 (10.9 %)
PC4 (8.3 %)
0.5
0.0
-0.5
rims
cores
PC1
PC2
PC3
PC4
W
Cs
Rb
Nb
Ba
Li
Zn
Fe
Cu
Tl
Ta
Sn
Sr
Mg
V
Scaled Coordinates PC1 - PC2 (50.3%)
Scaled Coordinates PC1 - PC3 (39.8%)
Scaled Coordinates PC1 - PC4 (37.2%)
MRS (PN22B)
MRS (PN46B)
MRS (PN33A)
MPS (PN30C)
Late-vugs
Wr-prox (PN22B)
Wr-prox (PN46B)
Wr-prox (PN33A)
Wr-prox (PN30C)
Fault
Wr-dist (PN46E)
Wr-dist (PN33D)
Wr-dist (PN30D)

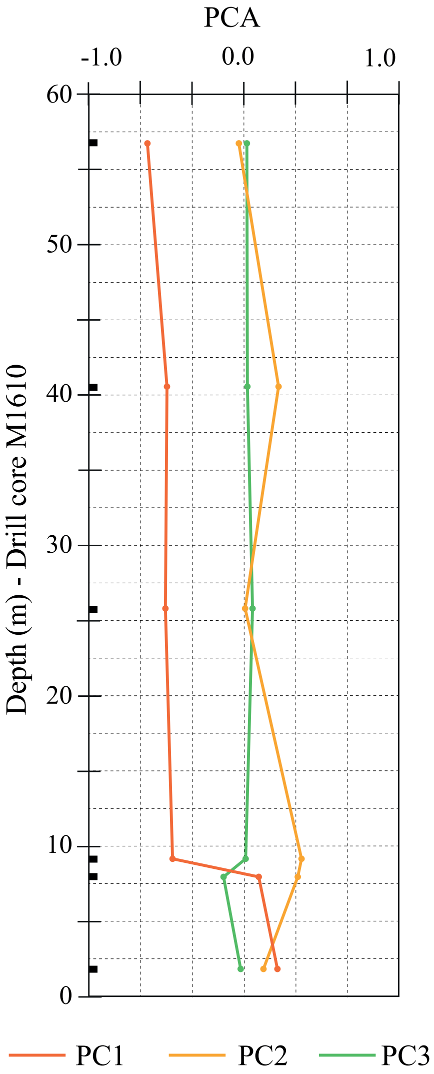

Figure 5.11: Variation of PC1, PC2 and PC3 along drill core M1610 (drilled upward from a mine stope). Black rectangles correspond to the position of the samples studied.

Sn in the fluid inclusions, especially for samples taken in the southern part of the mine where underground observations indicate the highest cassiterite grades, suggests that the trapped fluids analyzed by Lecumberri-Sanchez et al. (2017) may post-date Sn mineralization. This is consistent with the observations that Sn mineralization at Panasqueira predated W mineralization (Kelly and Rye, 1979; Martins et al., 2017), and it also agrees with our finding that Sn contents in early-formed MRS mica in sample PN22B are higher than in the later mica from that sample which is intergrown with arsenopyrite and wolframite (Figure 5.7E, Figure 5.8 8). Neiva (1987*b*) also explained large variations in Sn contents in mica (mineral separates) from Panasqueira by mica crystallization before and after cassiterite mineralization, although in that case there is a chance that the high Sn contents relate to unrecognized cassiterite inclusions. Audétat et al. (1998) found a sharp drop in metal contents (e.g. Sn, W, As) in fluid inclusions from mineralization in the Mole granite, which they related to the precipitation of cassiterite, wolframite and arsenopyrite.

Overall, there is agreement in the different approaches to estimate the element enrichments caused by hydrothermal fluid-rock interaction at Panasqueira. Furthermore, the element association of Li, Cs, Rb, F, W, Sn, F, As, and Cu indicated by hydrothermal mica, whole rock analyses and the chemical composition of fluid inclusions in Lecumberri-Sanchez et al. (2017) agree with the chemical signature of greisen alteration (Figure 5.5), so we conclude that fluids from the granitic intrusion were responsible for the hydrothermal alteration and mineralization at Panasqueira.

5.6.2 Element partitioning in tourmaline and mica and their value as pathfinders

It was shown above and in Codeço et al. (2019a) that white mica has distinct compositions in the different settings (e.g., greisen, vein selvages, wall rocks and fault zone) and in some cases also, within the vein-selvage (MRS) type we noted significant differences among individual samples (PN22, PN33, PN46) and of early- vs. late generations of mica within them (see Figure 5.7 and 5.8). In contrast, tourmaline from the different settings overlap in composition, although there is considerable local variation due to chemical zoning. Overall, the white mica is characterized by high concentrations of LILE (Rb, Cs, Ba), Li, Nb, Ta, W, and Sn (see Figures 5.7 and 5.9A, B, C, E), whereas tourmaline has generally high Zn, V, and Sr contents (Figures 5.7 and 5.9 D, F). To better understand the behavior of trace elements in mica and tourmaline and the partitioning between them, correlation plots are shown for selected trace elements in samples where the two phases coexist (Figure 5.12). The results show that Li, Rb, Cs, Tl, W, and Sn partition into mica over tourmaline ($D_{tur/mica}$ ranges from 0.0001 to 0.5); Cu, Ta, and Nb show considerable scatter, but are generally favored by mica ($D_{tur/mica} = 0.01$ to 30), whereas Sr, V, and Zn partition into tourmaline ($D_{tur/mica} = 0.6$ to 200). The only study known to the authors

Figure 5.12 *(facing page)*: Partitioning of trace elements between mica (horizontal axis) and tourmaline (vertical axis). MRS: mica-rich selvages, MPS: mica-poor selvages, Wr-dist: wall-rock distal from the vein contact.

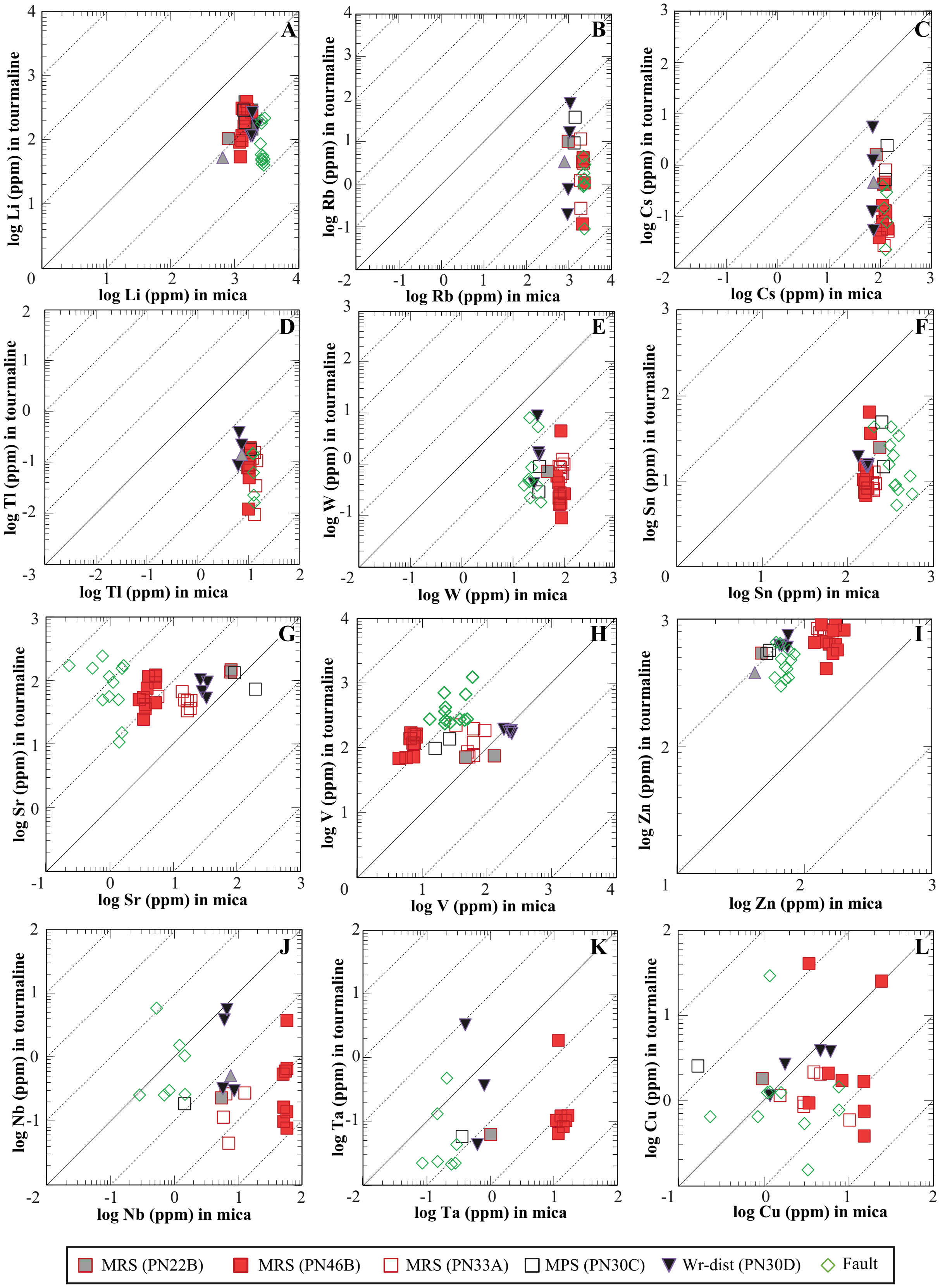
A
log Li (ppm) in tourmaline
log Li (ppm) in mica
B
log Rb (ppm) in tourmaline
log Rb (ppm) in mica
C
log Cs (ppm) in tourmaline
log Cs (ppm) in mica
D
log Tl (ppm) in tourmaline
log Tl (ppm) in mica
E
log W (ppm) in tourmaline
log W (ppm) in mica
F
log Sn (ppm) in tourmaline
log Sn (ppm) in mica
G
log Sr (ppm) in tourmaline
log Sr (ppm) in mica
H
log V (ppm) in tourmaline
log V (ppm) in mica
I
log Zn (ppm) in tourmaline
log Zn (ppm) in mica
J
log Nb (ppm) in tourmaline
log Nb (ppm) in mica
K
log Ta (ppm) in tourmaline
log Ta (ppm) in mica
L
log Cu (ppm) in tourmaline
log Cu (ppm) in mica
MRS (PN22B)
MRS (PN46B)
MRS (PN33A)
MPS (PN30C)
Wr-dist (PN30D)
Fault

where trace-element partitioning between tourmaline and mica was discussed is that of Klemme et al. (2011) who compared tourmaline and mica compositions in a single sample from Broken Hill, Australia, and with a range of four samples from Syros, Greece. That study also found variable apparent D-values between the two localities, but the overall pattern of partitioning is the same as in Panasqueira, i.e. D-values below 1 for Rb, W, Sn, Nb, and Ta, and above 1 for Sr, V, and Zn. However, the important point of the data from Panasqueira, is a general lack of correlation in the element concentrations between the two phases, which leads to a variation in tourmaline/mica D values of up to 3 orders of magnitude (e.g. Cs in Figure 5.12C). The D value between two minerals should be nearly constant if they reached and preserved chemical equilibrium with one another, so the lack of correlation in element concentrations in mica and tourmaline in our samples, is an important finding. There are several possible explanations for the lack of covariation in the two minerals. One is that the tourmaline and mica, although in direct contact, did not reach chemical equilibrium, or did not maintain it during the course of mineralization. The B-isotope ratios of coexisting white mica and tourmaline from these samples were found to be consistent with equilibrium partitioning (Codeço et al., 2019a), but this does not necessarily apply to the trace elements, since many studies showed a decoupling of chemical and B-isotope variations (*e.g.,* Codeço et al., 2017). Volume diffusion in tourmaline is known to be insignificant (van Hinsberg et al., 2011a), and we noted above that tourmaline tends to be more commonly zoned than mica. Mica compositions show stronger compositional dependency on the different settings in the deposit, suggesting it more readily adjusts to the local chemical environment.

It cannot be ruled out that the variable D-values reflect analytical problems related to unrecognized inclusions in the tourmaline and mica analyzed by LA-ICP-MS, but since care was taken to examine the time-spectra during data reduction and outlier values are readily seen in the results, this is not a likely explanation. We suggest instead that tourmaline and mica have not reached or maintained chemical equilibrium in the course of alteration and vein mineralization at Panasqueira. Furthermore, given that the white mica appears to more faithfully reflect the hydrothermal element enrichments shown by whole-rock compositions and by analysis of fluid inclusions than does tourmaline (e.g., Rb, Cs, Li, As, W, Cu), we suggest that mica is better pathfinder mineral for mineralization.

This is discussed more below where both minerals are compared using data from other deposits as well.

5.6.3 Mica as a pathfinder

Chemical variations in mica from different settings and generations reflect the evolution of the hydrothermal fluids. Early formed MRS micas (PN22B) have lower Rb, Li, W, and Zn, and higher Sr and V, when compared with the "normal" MRS micas (Figure 5.7); a lower Fe/Mg ratio in these early MRS micas was noted by (Codeço et al., 2019a). An increase in Li, Mg, V, Sr, Sn, Cs, and Cu is also detected in the vein-selvage micas compared to those from the greisen, suggesting a progressive relative enrichment in those elements in the fluid over time. We interpret that the early micas from PN22B record an early pulse of magmatic fluid.

Trace element concentrations in vein-selvage mica show a positive correlation between W, Sn, and Cu contents, and the relative abundance of the corresponding ore minerals (wolframite, cassiterite, and chalcopyrite) in the adjacent vein. In general, the higher W and Sn contents in mica are coincident with wolframite-cassiterite-rich veins. Although Cu is low in mica overall, the mica selvage with highest Cu contents coincides with chalcopyrite mineralization in the vein. Zn variations show the opposite behavior, possibly because Zn preferably partition into tourmaline over mica ($D_{tur/mica} = 5$ to 20) (see Figure 5.12).

To put these findings in a broader context, we compared our results from Panasqueira with available mica compositions from other tin-tungsten deposits as well as hydrothermal deposits with different metal associations (e.g. Cu-Au, Pb-Zn). Only a few studies determined mica trace-element compositions and most of the existing data are for trioctahedral micas (e.g., Maoping, Legros et al. 2016; Piotang, Legros et al. 2018; Cínovec/Zinnwald, Breiter et al. 2017a; Qiluling, Xie et al. 2015; Yashan, Li et al. 2015). Because micas at Panasqueira are exclusively dioctahedral, these comparisons must be carried with caution. Micas from the W-Sn association have higher Rb, Cs, Li, and Sn contents when compared with those from porphyry Cu and VMS base-metal deposits, whereas the range of W contents overlap for all (Figure 5.13A-C). Nevertheless, most mica from W-Sn deposits, including Panasqueira, have >10 ppm W, while the majority of porphyries have W

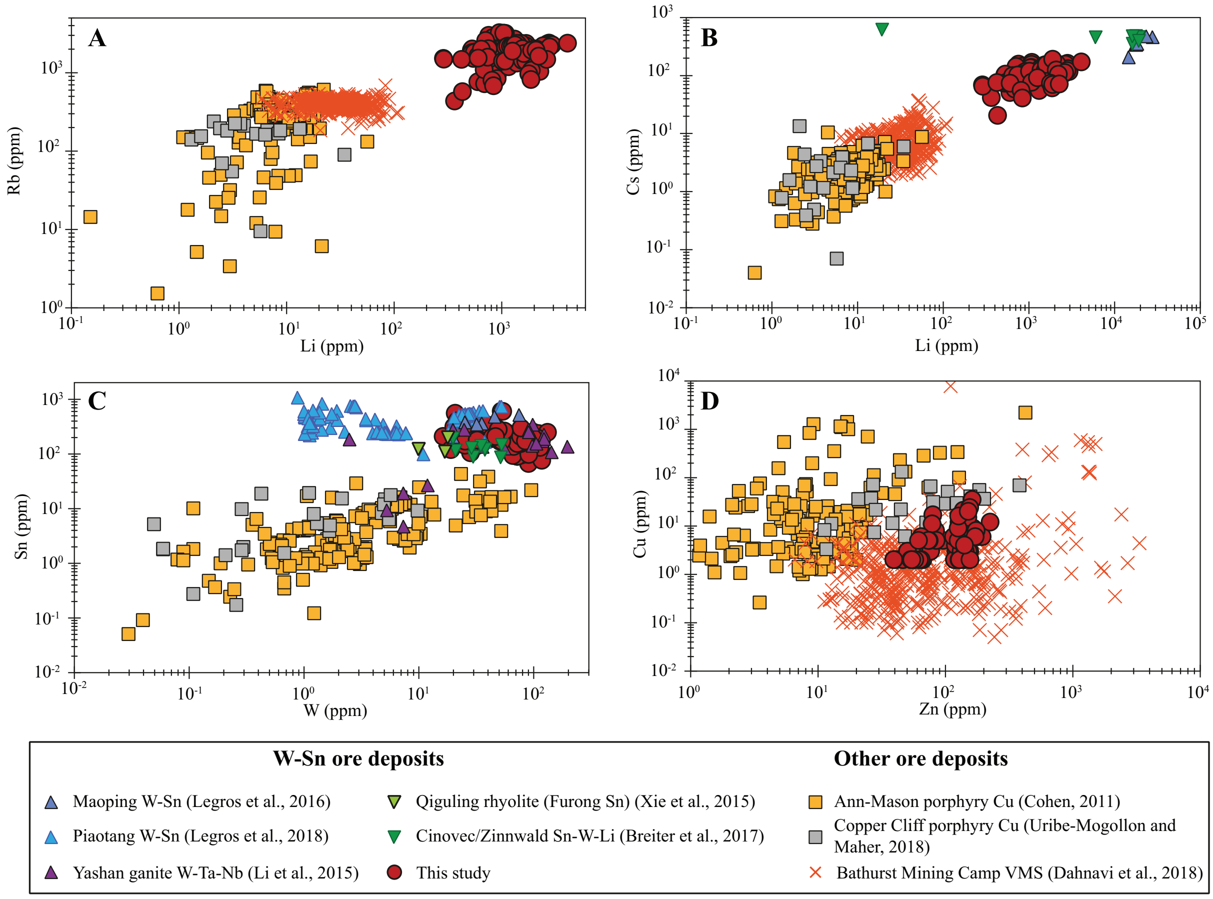

Figure 5.13: Comparison of trace element compositions in mica from ore deposits worldwide. Studies from Piaotang (Legros et al., 2018), Yashann(Li et al., 2015), and Qiguling (Xie et al., 2015) include trioctahedral and dioctahedral micas; Maoping (Legros et al., 2016) and Cinovec/Zinnwald (Breiter et al., 2017a) only comprise trioctahedral micas; data from other ore deposits are only dioctahedral micas (Cohen, 2011; Soltani Dehnavi et al., 2018; Uribe-Mogollon and Maher, 2018)

contents between 1 and 10 ppm. Early micas from the Piaotang deposit, which are coeval with cassiterite, yielded lower W contents than later mica from that deposit, confirming in this case that mica is a recorder of changing conditions (Legros et al., 2018). There are no comparative data for Zn and Cu from the W-Sn deposits other than Panasqueira, but comparing with data from VMS and Cu porphyries, we find that the range of Panasqueira overlaps completely (Figure 5.13D).

In summary, Panasqueira mica is characteristically enriched in the majority of the trace elements related to the mineralization, and, compared with other deposit types, shows a clear signature of granite-related fluids; for example there are higher Rb, Cs and Li contents when compared to VMS and porphyry examples. Micas from our study and those from the Piaotang Sn-W deposit have high Sn and W contents overall, and in both studies, a difference was observed between early and late micas that appears to reflect the early crystallization of cassiterite. In conclusion, white mica has a good potential as a pathfinder for ore deposits.

5.6.4 Tourmaline as a pathfinder

In contrast to white mica, tourmaline compositions do not show clear correlations with the sample setting. This may be partly because tourmaline is simply not as widespread as mica. It does not occur in the greisen and is only a minor phase in vein selvages. Most tourmaline forms in alteration zones in metasediments, where it replaced preexisting minerals rather than growing directly from the hydrothermal fluid, and thus to some extent incorporated trace elements from the host rocks. Another complexity is the common compositional zoning, and finally, many trace elements in tourmaline, including the REE, occur at very low concentrations so the geochemical palette is limited and analytical uncertainties are high. Several studies have attempted to distinguish a magmatic vs. metamorphic provenance of tourmaline in hydrothermal deposits by geochemical discrimination, including the classic Al-Fe-Mg discrimination of Henry and Guidotti (1985). Kalliomäki et al. (2017) reviewed this work in their study of Archean orogenic gold deposits in the Hattu schist belt of Finland, and concluded that the major and trace-element signature of hydrothermal tourmaline is largely controlled by the local host-rock composition and that relatively few elements are distinctive for the fluid source. Kalliomäki et al. (2017) found that Sr, V, and Li variations in tourmaline discriminate magmatic (high Li, low Sr and V) from metasediment-hosted tourmaline (higher Sr and V, low Li). The zoned tourmaline from Panasqueira wall-rock alteration has cores with higher Mg and Sr than the rims, reflecting wall-rock control, whereas the Li contents in tourmaline rims is higher (Figure 5.9A and D, Figure 5.10), suggesting that magmatic fluids made a stronger contribution as the hydrothermal system evolved and fluid/rock ratio increased. A change from rock-dominated to fluid-dominated conditions was invoked by Codeço et al. (2017) to explain tourmaline B-isotope variations in the wall rocks, and the increase in Li concentration from earlier to later white mica growth in the MRS selvages (see Figure 5.7) may relate to the same process.

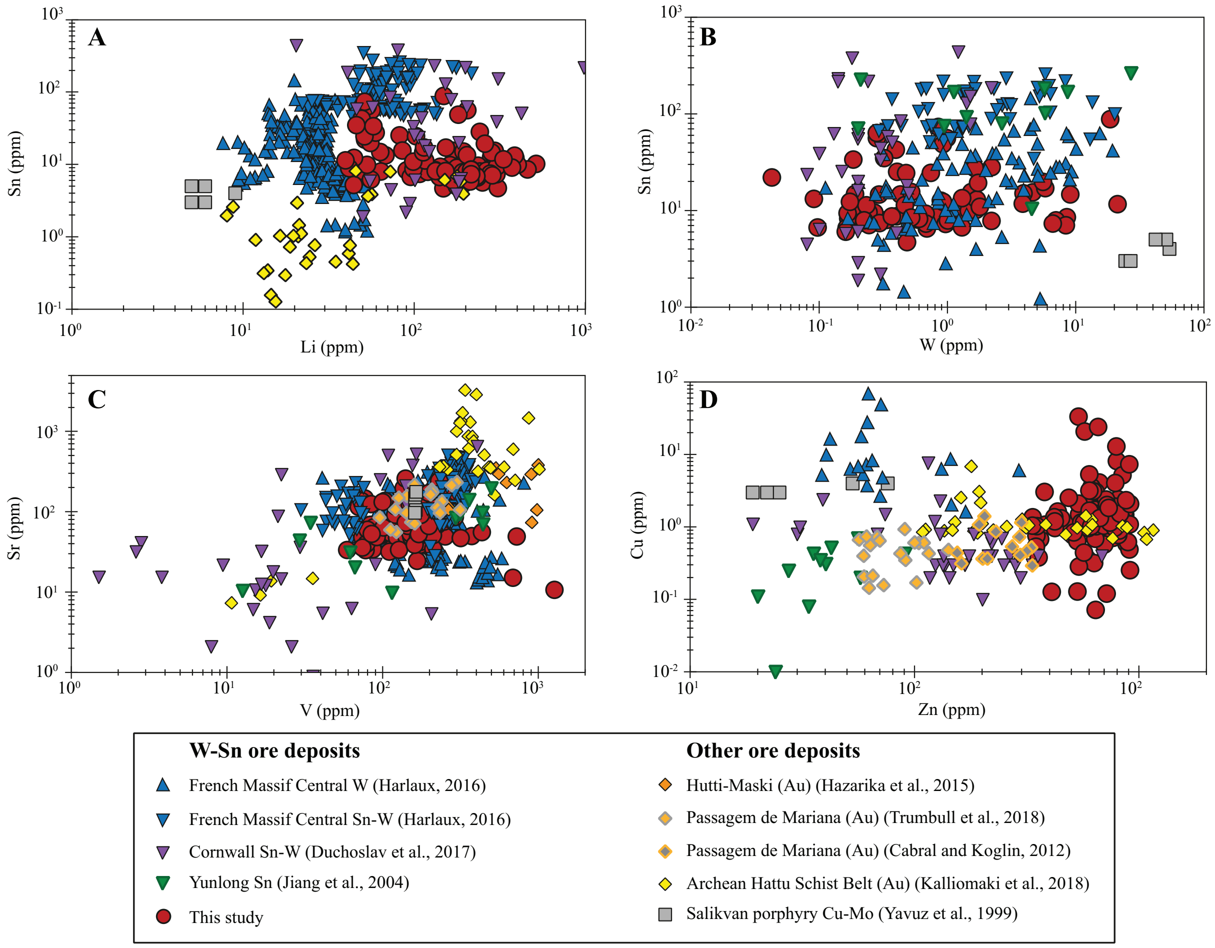

Figure 5.14: Comparison of trace element compositions in tourmaline from ore deposits worldwide. Data sources: (1) W-Sn ore deposits: Harlaux (2016), Duchoslav et al. (2017), and Jiang et al. (2004); (2) Gold deposits: Cabral et al. (2012), Hazarika et al. (2015), Kalliomäki et al. (2017), and Trumbull et al. (2019); and (3) Cu-Mo porphyry deposits: Yavuz et al. (1999)

Data from Panasqueira are compared with other studies on trace-element contents in tourmaline from Sn-W and other types of ore deposits in Figure 5.14(see caption for data sources). Tourmaline from the Sn-W deposits has relatively higher Sn and Li contents than tourmaline from the Salikvan Cu-Mo porphyry deposit and the orogenic gold associations (Figure 5.14A), but no significant difference was found for W (Figure 5.14B). The Sn-Li plot also discriminates between Sn-W deposits in the Massif Central (downward triangles, higher Sn) from deposits with W-only (upright triangles, lower Sn). The strong overlap of all deposits on the V and Sr plot (Figure 5.14C) underscores the suggestion by Kalliomäki et al. (2017) that these elements are host-rock controlled and depend on the local lithogeochemistry. The range of Cu concentrations in tourmaline is similar, and highly variable, in all deposits regardless of type, but Zn contents tend to be higher at Panasqueira than in all other Sn-W deposits plotted (Figure 5.14D). This may relate to the high sphalerite contents in the Panasqueira veins.

To summarize, we note an overall correlation of Sn and Li contents with mineralization type. Tin concentrations greater than 10 ppm are common in Sn-W deposits and rare in the Cu-porphyry and orogenic gold association. An interesting further distinction of Sn-rich and W-rich deposits can be seen in the Massif Central examples; i.e., higher Sn in cassiterite-dominated ones and lower Sn in wolframite-dominated deposits. There is no such difference in terms of W contents, and inexplicably, the W contents in tourmaline from Salikvan Cu-Mo porphyry are the highest of any in the comparison, but that deposit is not known for W mineralization. The Cu concentrations in tourmaline is non-diagnostic of source, showing overlaps in all deposits types. The Salikvan deposit is a major resource for Cu but its tourmaline is not particularly Cu-rich compared with the others. In fact, the highest Cu contents known (2 wt .% CuO; Beurlen et al. (2011)) are responsible for the blue color of “Paraíba” gem tourmaline, which occurs in granitic pegmatites. Clearly, the trace-element concentrations of tourmaline are affected by many factors and these can change with time in any one deposit as the hydrothermal system evolves, as shown by zoning at Panasqueira.

Compared with white mica, tourmaline seems less responsive to the composition of the hydrothermal fluid (cf. Figure 5.13, 5.14), but this study suggests that high Sn-Li contents in tourmaline (i.e. >10 ppm and 50 ppm, respectively) may distinguish magmatic-hydrothermal Sn deposits fairly well. In any case, since mica and tourmaline concentrate different sets of trace-elements and tend to occur together in hydrothermal systems, the best approach to geochemical discrimination is to combine information from both minerals.

5.7 Conclusions

At Panasqueira hydrothermal alteration zones show contrasting chemical signatures when compared with unaltered metasediments. These zones characterized by large-scale enrichments in W, Sn, Cu, Zn, As, F, Li, Rb, Cs, and Tl. Factor analysis results provide constraints of the alteration overprint but also suggest that the whole-rock chemistry varies as a function of distance from the greisen cupola. In this dataset the latter variation is, however, mainly mineralogically-controlled, with the proximal zones enriched in Rb, Cs, and Tl reflecting thick mica-selvages, and the distal zones richer in As, Zn, and Cu, reflecting vein mineralization.

White mica and tourmaline are the most abundant hydrothermal phases at Panasqueira, where mica forms thick vein-selvages at the contacts with the host rocks and tourmaline occur predominantly in the alteration haloes. In-situ LA-ICP-MS analysis performed in those phases showed that mica has higher Rb, Cs, Ba, Li, Nb, Ta, W and Sn, and lower Zn, V and Sr, comparatively to the tourmaline. Mica further reflects the evolution of the hydrothermal fluids; early micas have lower Fe/Mg ratios, Rb, Li, W and Zn, and higher Sr and V, compared to the "normal" micas from the selvages, likely recording an early pulse of the magmatic fluids. Moreover, the micas from the vein selvages show increases in Li, Mg, V, Sr, Sn, Cs, and Cu, relatively to mica from the greisen, suggesting a progressive enrichment in those elements in the fluid over time. We also found positive correlations between W, Sn, and Cu contents in mica from the vein-selvages and the abundance of ore minerals in the adjacent vein. White mica seems to reflect more the hydrothermal element enrichments revealed by whole-rock compositions and chemical composition of fluid inclusions than does tourmaline. In contrast, tourmaline forms at the expense of the host rocks and reflects extensive fluid-rock interaction.

The comparison of the results obtained based on whole-rock chemistry, mica in-situ chemistry and published chemical composition of fluid inclusions agree with the chemical signature of the greisen alteration and suggests that fluids released from the granitic intrusion were responsible for the hydrothermal alteration. The compositional trends indicate that the fluids were enriched predominantly in As, Li, F, Rb, W, Sn, Cu, Zn, Cs, and Tl. Finally, our results suggests that white mica is a good pathfinder for W-Sn mineralization.

Acknowledgments

We are particularly indebted to U. Altenberger (Universität Potsdam, Germany) and A. Jung (University McGill, Canada) for their support with the SEM and LA-ICP-MS analyses. We further thank F. Rosendahl for help with sample preparation and A. Gottsche and H. Rothe for performing the XRF and ICP-MS analyses at GFZ. We also thank M. Korges and A. Mateus for many inspiring discussions. The authors are grateful to Beralt Tin & Wolfram (Portugal) S.A. for providing logistical support and access to the Panasqueira deposit over two field seasons. The project was founded by the German Federal Ministry of Education and Research (BMBF) within the project GRAMME (033R149).

Supplementary (Data Publication) data to this manuscript can be found online at Codeço, Marta S.; Weis, Philipp; Trumbull, Robert B.; van Hinsberg, Vincent; Pinto, Filipe; Lecumberri-Sanchez, Pilar; Schleicher, Anja Maria (2019): Trace elements in of white mica and tourmaline from the Panasqueira W-Sn-Cu deposit (Portugal). GFZ Data Services. `http://doi.org/10.5880/GFZ.3.1.2019.001`
For the printed copy of this thesis the supplementary material can be found in the enclosed CD-ROM.

"Give a man a program, frustrate him for a day. Teach a man to program, frustrate him for a lifetime."

–Waseem Latif

6

Numerical simulations of fluid flow patterns at the Panasqueira W-Sn-Cu vein-type deposit

Marta S. Codeço, Philipp Weis, Christine Andersen

GFZ German Research Centre for Geosciences, Telegrafenberg, 14473 Potsdam, Germany

In preparation for submission to Geochemistry, Geophysics, Geosystems. Readers must be aware of possible differences between chapter 6 and the future publication.

Abstract — Numerical simulations were performed to study the first order geological and physical parameters controlling the fluid flow patterns at Panasqueira, where mineralization is structurally controlled and hosted by sub-horizontal veins. We present a first set of simulations comparing hydrothermal flow through a simple horizontal fracture either represented by two-dimensional elements or using a new method by applying lower-dimensional line elements in order to develop a method to resolve fractures and faults. Our results show that different mesh resolutions produce the same hydrothermal field. In a series of two-dimensional simulations we investigate the fluid flow patterns in faults and fractures in close association with a magmatic intrusion emplaced at crustal levels. The results show that the fluid flow has a strong lateral component in the presence of horizontal-structures and the subvertical faults play a critical role in the ascent of fluids and recharge of ambient meteoric waters. Moreover, the results further suggest that magmatic fluids dominate in the earlier stages, whereas mixing with meteoric fluids will only occur at later stages. These simulations are in good agreement with the field observations, at the Panasqueira W-Sn-Cu deposit, in particular, the physical processes leading to the formation of the subhorizontal veins and of low-temperature epigenetic Zn-Pb ore deposits associated to crustal subvertical faults.

Key-words: Numerical simulation, fluid flow, magmatic-hydrothermal ore deposits, faults, Panasqueira

6.1 Introduction

Many economic ore deposits have a hydrothermal origin and are majorly controlled by advective heat and solute transport with fluids flowing through permeable rocks, including porphyry, volcanogenic massive sulfide (VMS), sedimentary exhalative (SEDEX), Mississippi-Valley-type (MVT), and epithermal deposits (Ingebritsen and Appold, 2012). Focused fluid advection concentrates both metals and heat, leading to ore deposition at temperatures that can be significantly higher than the local background temperatures of the regular geothermal gradient. The genesis of hydrothermal ore deposits requires a favorable geodynamic setting where fluids can transport metals from a large source area along permeable fluid pathways to the deposition site (Cox, 2005; Heinrich and Candela, 2014; Kesler and Simon, 2015).

In many hydrothermal ore-forming systems, fractures and faults are interpreted to be high-permeability pathways for fluid, heat and solute transport (Berkowitz, 2002; Simms and Garven, 2004). This fracture-controlled fluid flow in initially low-permeability host rocks has been interpreted as the key to the generation of some magmatic-hydrothermal deposits, which are related to fluid release from magmatic intrusions (Černý et al., 2005; Cox, 2005; Polya et al., 2000). Fracture networks connected to the surface can also promote localized ore deposition by mixing of fluids from deeper and shallower reservoirs (*e.g.,* Ingebritsen and Appold, 2012; Matthäi and Belayneh, 2004). The Panasqueira W-Sn-Cu deposit in Portugal consists of mineralized sub-horizontal veins nearby a Variscan granitic intrusion, which is interpreted to have formed from focused flow of magmatic fluids with variable degrees of fluid mixing during later stages (Kelly and Rye, 1979; Polya et al., 2000). However, the physical hydrology and its interaction with the host-rocks remains poorly understood.

Numerical simulations with models that can handle high-temperature multi-phase flow of NaCl-H_2O fluids in porous media can help to quantify the dynamic behavior of and of mass and heat transfer in magmatic-hydrothermal systems (*e.g.,* Coumou et al., 2008*a*,*b*; Geiger et al., 2006*a*,*b*; Lewis and Lowell, 2009*a*,*b*; Weis et al., 2014). Previous studies focused on the physical hydrology of porphyry and epithermal deposits (Weis et al., 2012, 2014), active submarine hydrothermal systems (Coumou et al., 2008*b*; Gruen et al., 2012, 2014), VMS deposits (Schardt et al., 2005; Schardt and Large, 2009) and structure-controlled deposits (Liu et al., 2014, 2015; Micklethwaite et al., 2015; Zhang et al., 2011). Other studies investigated the patterns of fluid flow in fractured media focused on geothermal resources (*e.g.,* Bächler et al., 2003; Guillou-Frottier et al., 2013; Patterson et al., 2018a; Pribnow and Schellschmidt, 2000) and oil and gas reservoirs (*e.g.,* Azizmohammadi and Matthäi, 2017; Matthäi et al., 2007; Simms and Garven, 2004; Yapparova et al., 2017).

This study presents results from numerical simulations of the hydrology of vein-type magmatic-hydrothermal ore systems, constrained by observations from the Panasqueira deposit. We use two-dimensional transient numerical models of heat and mass transport to describe fluid flow in fractures and faults in close association with an upper crustal magmatic intrusion as the source for heat, fluids and metals. We investigate the effect of multiple connected fractures and fault zones on hydrothermal fluid flow patterns and discuss its applicability to the Panasqueira vein-type ore deposit.

6.2 Geological Setting

6.2.1 Regional Context

The Variscan orogeny was a major tectonic event in the evolution of Western Europe, resulting from the Laurussia-Gondwana collision through the late Devonian (370 Ma) and most of the Carboniferous, and culminating with the late closure of the Rheic Ocean (ca. 300 Ma) (Kroner et al., 2007, 2015; Matte, 1991; Romer and Kroner, 2016). The Variscan Iberian Massif is part of the Ibero-Armorican Arc, a curvilinear macrostructure stretching from Iberia into Britain (Pastor-Galán et al., 2015; Shaw et al., 2012)) and is traditionally subdivided into five tectonostratigraphic domains: Cantabrian Zone, West-Asturian Leonese Zone, Central Iberian Zone, Ossa-Morena Zone and the South Portuguese Zone (Julivert et al., 1974; Lötze, 1945) (Figure 6.1A). The Central Iberian Zone (CIZ) is characterized by an extensive exposure of granitic rocks of Variscan age and a thick (up to 11,000 m), monotonous Neo-Proterozoic-Cambrian siliciclastic succession, the so-called Schist-Greywacke Complex (SGC). The SGC was deposited in horst-graben structured basins that have evolved in different paleo-geographic scenarios and consists of shales and sandstones with minor conglomerates, limestones and scarce volcanoclastic layers (Rodríguez-Alonso et al., 2004). In the CIZ, three main phases of ductile deformation (D1, D2 and D3) have been recognized. The first stages (D1 and D2) correspond to the collisional phase of the Variscan Orogeny (365-320 Ma) and are associated to the generation of subvertical folds with penetrative slaty cleavage (S1) and D2 recumbent faults, which predominantly affected the NW part of the Iberian Massif. The latest transpressional stage (D3) culminated in the oroclinal bending of the Ibero-Armorican Arc and is characterized by upright folds, refolding the initial D1 folds (Martínez Catalán et al., 2014). The widespread intrusion of granitic rocks and associated high-temperature low-pressure metamorphism in the CIZ is syn- to post-genetic with D3, dated at 310-285 Ma (*e.g.,* Bea et al., 2003; Dias et al., 1998; Martínez Catalán et al., 2014; Villaseca et al., 2012). A large number of CIZ granitic bodies are highly evolved and locally host Sn-W-Li-F-Nb-Ta-P-U mineralization (*e.g.,* Chicharro, 2016; Llorens González et al., 2017; López-Moro et al., 2017; Neiva et al., 2012; Noronha et al., 2013; Roda-Robles et al., 2016; Sant'Ovaia et al., 2013).

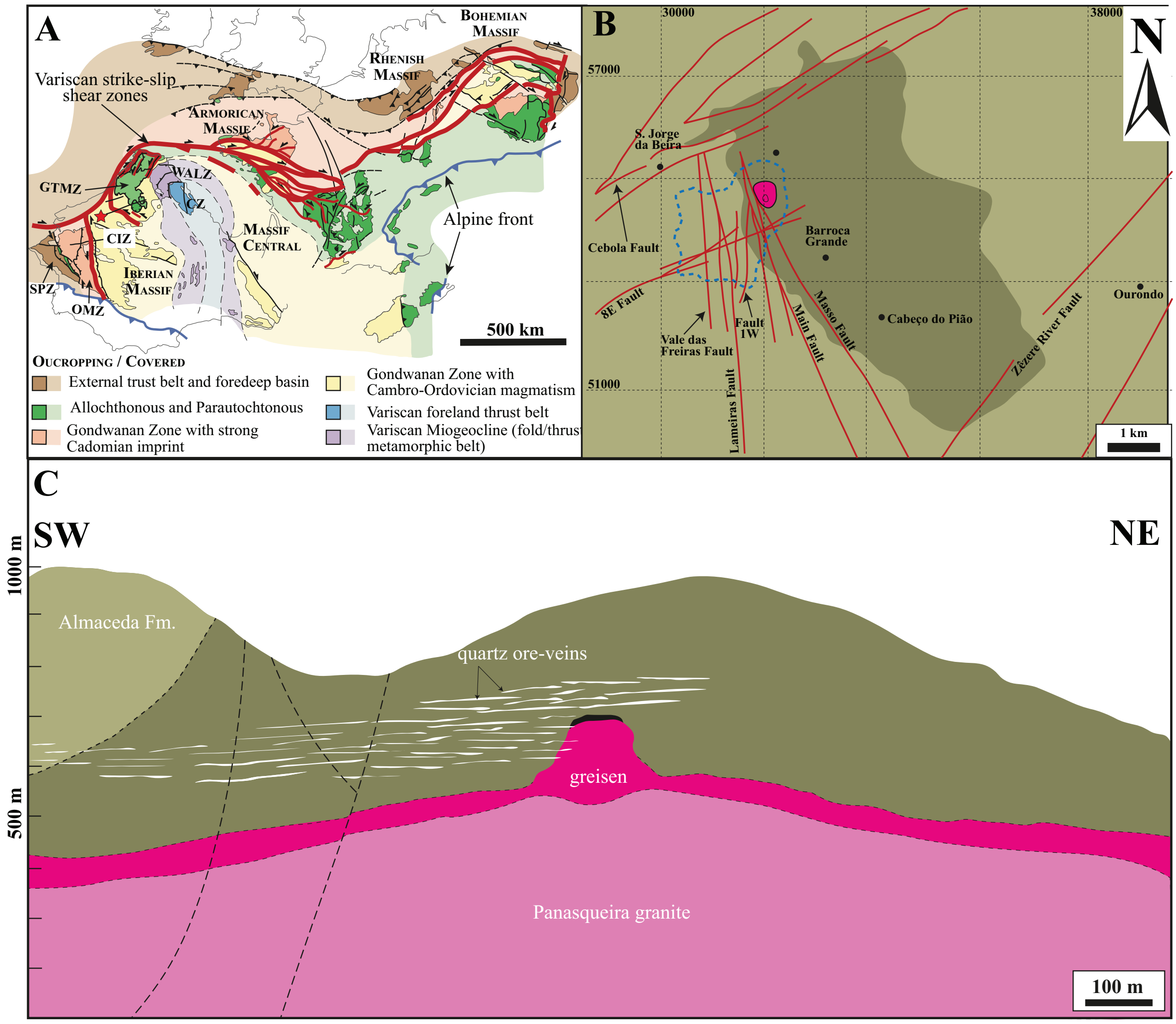

Figure 6.1: **A** Subdivision of the Variscan Belt showing the allochthonous terrains and the main transcurrent shear zones (adaptes from Martínez Catalán et al., 2007). **(B)** Regional geological map. The underground mine, whose extent is marked with blue dashed lines, is located in the vicinity of the contact metamorphism aureole (adpated from Jacques et al., 2018). **(C)** Schematic cross-section of the Panasqueira deposit (modified after Thadeu, 1951*a*), with a schematic representation of the mineralized veins and alteration halos. Abbreviations: CIZ – Central Iberian Zone, CZ – Cantabrian Zone, GTMZ – Galicia-Trás -os-Montes Zone, OMZ – Ossa Morena Zone, SPZ – South Portuguese Zone and WALZ – West Asturian-Leonese Zone.

6.2.2 The Panasqueira vein swarm

The Panasqueira Mine is located in the Castelo Branco district, in the center of Portugal. The deposit consists of a swarm of subhorizontal veins, dipping less than 20°, hosted by the Almaceda Formation (Schist Greywacke Complex) and is associated with a granitic body at depth (Figure 6.1B, C). Granite emplacement occurred at upper crustal levels (*e.g.,* Bussink, 1984; Kelly and Rye, 1979) and produced a metamorphic aureole of spotted schists with biotite-chlorite-cordierite porphyroblasts (Conde et al., 1971; Thadeu, 1951*a*) (Figure 6.1C). Recent gravimetric surveys showed that the Panasqueira granite consists of an irregular sheet intrusion with a maximum width of ca. 7 km and a depth of 2.5 km. The emplacement was limited by three NE-SW regional faults, the Cebola Fault located in the north, the Zêzere River Fault located in the SE and a third fault inferred from the gravimetry (Ribeiro, 2017), that may correspond to the 8E Fault (see Figure 6.1B). The Panasqueira granite consists of a porphyritic two-mica, peraluminous ($^{87}Sr/86^{S}r \approx$ 0.713) S-type granite of Variscan age (*e.g.,* Bussink, 1984; Kelly and Rye, 1979). In the deposit, the upper part of the granite is greisenized (cupola) and is cut by some of the ore veins (Burnard and Polya, 2004; Bussink, 1984; Kelly and Rye, 1979; Polya, 1989; Thadeu, 1951*a*). Some veins in the vicinity of the greisen consist of inclined veins (dip of ca. 40-50°), which are not parallel to the greisen-schists contact.

The mineralized zone is located to the SW of the outcropping cupola with only a very limited extension towards the NE (see Figure 6.1B, C). The quartz-W-Sn-Cu-bearing veins are exposed by underground mining over an area of 2,500m in length, 400 to 2,000 m in width and at least 500 m in depth (Wheeler, 2016) (Figure 6.1C). The mineralized veins are massive and tabular and range in thickness from <1 cm up to 1.5 m, with an average of 25 m and can be traced laterally over distances up to 100 m and overlap over large distances in a tridimensional manner (Jacques et al., 2018). The origin of the subhorizontal veins is still debated (Foxford et al., 1991, 2000; Jacques et al., 2018; Kelly and Rye, 1979; Marignac, 1973, 1982; Ribeiro and Pereira, 1982). According to Jacques et al. (2018), the vein system formed shortly after the tectonic inversion of the Variscan Orogeny, "under low differential stress exploiting pre-existing cross-fold-joint system". The vein dilatation was driven by fluid pressures, although the orientation was still dictated by the pre-existing (F2) fold geometry. Contrarily, Foxford et al. (2000) suggest that the vein system formed through extensional failure driven by hydraulic valving at moderate differential stress in a compressive crustal regime. Furthermore, based on fluid inclusion studies combined with geochemical analyses of coeval arsenopyrite and the sphalerite geobarometer, Jaques and Pascal (2017) constrained the P-T conditions, suggesting that the Panasqueira granite was emplaced at ca. 10 km depth and the vein system formed at similar depths under lithostatic pore pressures and a compressive stress regime. These depth estimates stand in contrast with the shallow depths of ca. 0.7-1.3 km and <1.8 km proposed by Bussink (1984); Kelly and Rye (1979), respectively.

The complex paragenetic sequence has been described by several authors (D'Orey, 1967; Foxford et al., 1991; Kelly and Rye, 1979; Lourenço, 2002; Martins, 2017; Polya, 1989; Polya et al., 2000). Kelly and Rye (1979) divided the paragenetic sequence into four stages of mineralization (1) oxide-silicate stage, (2) main-sulfide stage, (3) pyrrhotite alteration stage and (4) late carbonate stage, whereby (1) and (2) constitute the economically relevant ore stages for oxides (wolframite, cassiterite) and sulfides (chalcopyrite), respectively. More recent studies proposed two pre-ore stages with formation of a crack-seal quartz seam and muscovite selvages (Lourenço, 2002; Martins, 2017; Polya et al., 2000). The hydrothermal alteration produced an alteration halo over two meters wide around the quartz veins, typically displaying a zonation from proximal tourmalinization to distal muscovitization, that gradually passes to the chlorite-muscovite-biotite regional metasediments (Bussink, 1984)(see also Chapter 5). Constraints from mineral geothermometers (boron isotope muscovite-tourmaline, arsenopyrite, Ti-in-quartz) suggest that the wall-rock alteration and the early vein formation took place between 400° and 500°C (Codeço et al., 2017, 2019a; Jaques and Pascal, 2017). On the other hand, quartz-hosted fluid inclusions from the oxide-silicate and main-sulfide stage indicate temperatures ranging from 360° to 230°C and overlap the temperatures obtained from B-isotope geothermometry in a late-fault zone (Codeço et al., 2019a).

6.3 Methods

Conservation of mass, energy and momentum are the principal laws that describe fluid flow in hydrothermal systems (*e.g.,* Ingebritsen et al., 2010). The governing equations are solved with a Control Volume Finite Element (CVFEM) method implemented into the Complex Systems Modeling Platform CSMP++ (Figure 6.2), which can accommodate compressible flow of variably miscible, multiphase fluids (Weis et al., 2012, 2014). The saline fluid properties are calculated using the NaCl-H_2O system as described by Driesner (n.d.) and Driesner and Heinrich (2007).

6.3.1 Governing Equations

Two-phase fluid flow in fractured and porous media can be described by Darcy's law as:

$$v_i = -\mathbf{k}\frac{k_{ri}}{\mu_i}(\nabla p - \rho_i \mathbf{g}), \quad i = l, v \tag{6.1}$$

where v is the Darcy velocity of the mobile phases i (liquid l and vapor v), k is the intrinsic permeability, k_r is the relative permeability, μ is viscosity, p is pressure, ρ is density, and $\mathbf{g}$ is the acceleration due to gravity (Ingebritsen et al., 2006). Solid halite h is assumed to reduce the available permeability and block pore space. For the mobile phases, a linear relative permeability model is applied, ensuring that $k_{rv} + k_{rl} = 1 - S_h$, with S as the volumetric saturation of the indicated phase. The residual saturation R_l has been set to $0.3(1 - S_h)$ for the liquid phase and to 0.0 for the vapor phase (Weis et al., 2014).

The conservation of total fluid mass (eq. 6.2), energy (eq. 6.3) and salt mass (eq. 6.4) are given by the following expressions, respectively:

$$\frac{\partial[\phi(S_l\rho_l + S_v\rho_v + S_h\rho_h)]}{\partial t} = -\nabla\cdot(S_l\rho_l) - \nabla\cdot(S_v\rho_v) + Q_{H_2O+NaCl} \tag{6.2}$$

$$\frac{\partial[(1-\phi)\rho_r h_r + \phi(S_l\rho_l h_l + S_v\rho_v h_l + S_h\rho_h h_l)]}{\partial t} = \nabla\cdot(K\nabla T) - \nabla\cdot(S_l\rho_l h_l) - \nabla\cdot(S_v\rho_v h_v) + Q_e \tag{6.3}$$

$$\frac{\partial[\phi(S_l\rho_l X_l + S_v\rho_v X_v + S_h\rho_h X_h)]}{\partial t} = -\nabla \cdot (S_l\rho_l X_l) - \nabla \cdot (S_v\rho_v X_v) + Q_{NaCl} \qquad (6.4)$$

where ϕ is the porosity, S the volumetric saturation, h the specific enthalpy, X the mass fraction of NaCl in the respective phase, t the time, K the thermal conductivity, T the temperature and $Q_{H_2O+NaCl}$, Q_e, and Q_{NaCl} are the source terms; the superscript r stands for the rock matrix. In this approach, we assume that fluid and rock are in thermal equilibrium, requiring that the total enthalpy is distributed over the fluid and rock contained in a control volume. All fluid properties are updated at every time step (Weis et al., 2014).

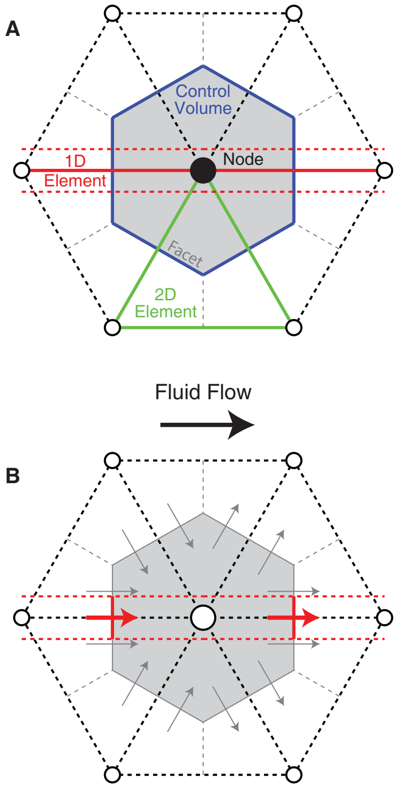

Figure 6.2: Construction of finite element and control volume capabilities. **(A)** The user-defined finite element mesh (green) is superimposed by a node-centered control volume mesh (blue) by the CSMP++ model. Facets are constructed from the mid-side point of the element's faces to the element's barycenter and define the segments of the control volume. The red line represents the one dimensional (1D) element. **(B)** Fluid flow is calculated across these facets between two neighboring node, exemplified by the gray arrows representing horizontal flow from left to right (black arrow). The red arrows show the additional flux across the facets of the 1D element representing higher-permeability faults and fractures. Modified after Weis et al. (2014).

6.3.2 Representation of fractures and faults

In two-dimensional (2D) modeling approaches, fractures and fault structures can be represented by high-resolution domains consisting of 2D elements (Figure 6.3, right hand side) with a thickness that corresponds to the width of the fracture or fault (e.g., 50 m, see Figure 6.3B). For this study, we used mixed-dimensional finite element meshes, where faults and fractures are included as lower-dimensional elements (Figure 6.3, left hand side), that is the fractures are discretely represented by one-dimensional line elements with a given thickness (Figure 6.3A). This mixed-dimensional approach enables us to use relatively coarse meshes and still resolve the influence of faults and fractures on hydrothermal circulation.

Fluid advection is calculated with the Finite Volume scheme (Figure 6.2) across facets between two neighboring nodes with the permeability k_b of the given element, representing the rock matrix (Weis et al., 2014). In the lower-dimensional element approach, the additional influence of fault permeability of each line element $k_{line-element}$ was calculated using the permeability $k_{fr,ft}$ and width of each fault and fracture $w_{fr,ft}$ as:

$$k_{line-element} = (k_{fr,ft} - k_b) \times w_{fr,ft} \tag{6.5}$$

In the case where the fault has the same permeability as the rock matrix ($k_{fr,ft} = k_b$) or if $w_{fr,ft} = 0$, the influence of the respective fault segment vanishes. Permeability can be regarded either as a static material property or as a dynamic parameter that changes in response to tectonism, fluid production, temperature, pressure, and geochemical reactions (Ingebritsen and Manning, 2011). For the simplified models with one horizontal fault zone, the permeability of the background matrix, k_b, is kept constant and isotropic. For the setups with the geometry of the Panasqueira system, we combined the new lower-dimensional element approach with the depth-, temperature- and pressure-dependent background permeability of Weis (2015) to describe the transition from brittle to ductile rock behavior and hydraulic fracturing.

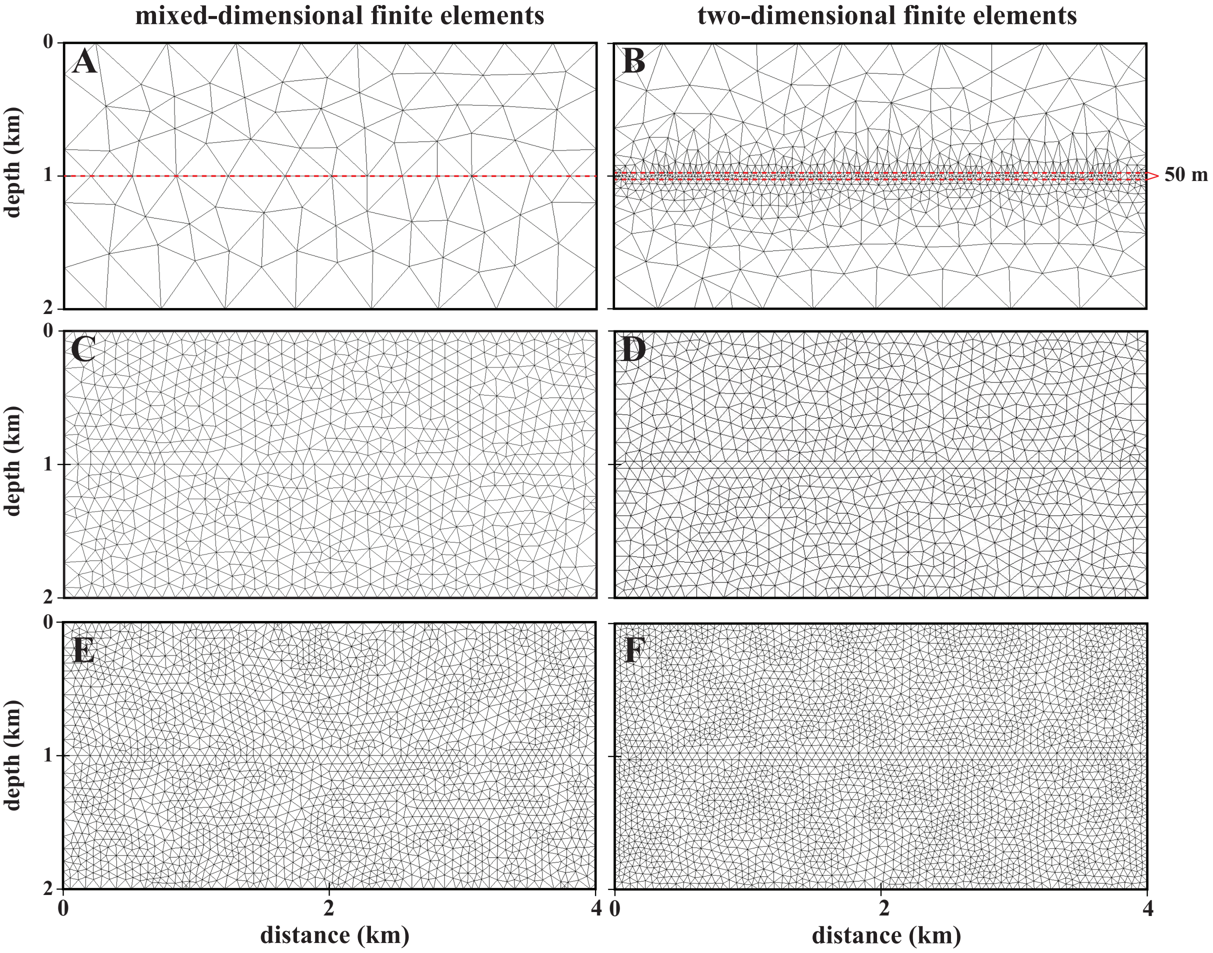

Figure 6.3: Model geometry and unstructured mesh for the mixed-dimensional (**A, C, E**) and two-dimensional finite elements methods (**B, D, F**) applied on the simple-fracture simulations. The red dashed lines in **A** and **B** show the position of the fracture, resolved by lower-dimensional elements and 2D elements, respectively.

6.3.3 Model configuration

The first simulations (simple horizontal fracture, subsection 6.4.1) were conducted with constant temperature and fluid pressure conditions on both ends of a rectangular domain of 4 km width and 2 km depth (Figure 6.3). The domain is oriented horizontally, that is without gravitational effects, with higher pressure (35 MPa) and temperature (350°C) values at the left boundary nodes, and lower pressure (25 MPa) and temperature (150°C) values at the right boundary, which leads to hot fluids flowing from left to right. We used two different general model geometries with a center line and a center zone, respectively, and created meshes with three different resolutions (see Figure 6.3A, B: coarse resolution; C, D: medium resolution and E, F: fine resolution). All model geometries were created using Rhinoceros 5 and the mesh generator ANSYS ICEM CFD. In order to represent the mixed-dimensional finite element domain, the fracture was placed at 1 km depth [Figure 6.3A (red dashed line), C, E]. The simulation domain representing the two-dimensional finite elements [Figure 6.3B (red dashed lines), D, F] is divided by a fracture zone of 50 meters between 1975 and 2025 m depth, which is resolved by a discretized mesh. In these simulations we assumed a constant permeability $k_{fr,ft}$ of $10^{-14}m^2$ and width $w_{fr,ft}$ of 50 m to the fracture. We further applied constant and uniform rock properties with an isotropic background matrix permeability k_b of $10^{-15}m^2$, a porosity ϕ of 0.1, a heat capacity c_{pr} of 880 J Kg^{-1} $°\mathrm{C}^{-2}$, a thermal conductivity K of 2 W $\mathrm{m}^{-2}°\mathrm{C}^{-2}$ and a rock density ρ_r of 2700 kg m^{-3}.

The second modeling set-up (Panasqueira hydrothermal system, subsection 6.4.2) represents a section of the upper continental crust with a magma chamber of initially 900 °C (2.5 × 7 km), with its roof emplaced at 5 km depth (Figure 6.4). The host rock porosity is kept constant with 0.05, the pore space is initially saturated with pure water under hydrostatic pressure and a thermal gradient of 22.5 °C km^{-1} is applied, which is maintained by a bottom heat flux of 45 mW m^{-2} and 20 °C at the top boundary, representing the Earth's surface. During the simulations, the top boundary is open to allow fluid outflow at atmospheric pressure and inflow of pure liquid water, the bottom, left and right boundaries are no-flow boundaries. To account for the fluid accumulation in the third dimension, the magma chamber is assumed to have half of the width in the dimension perpendicular to the modeling section as described by Weis (2015). The magma chamber uses the same rock property values but starts with a doubled heat capacity, which is gradually reduced during cooling of the magma chamber to account for the release of latent heat during crystallization (Weis, 2015). The permeabilities of the magma chamber and the surrounding host-rocks use the dynamic permeability model of Weis (2015) with a maximum permeability of $10^{-14}m^2$ at shallow levels down to 1 km depth and during intense hydraulic fracturing, and a minimum permeability of $10^{-22}m^2$ for rocks at temperatures above 550 °C, which are assumed to behave in a ductile way not allowing for any fluid flow. We assumed a salinity of 5 wt.% for the magmatic fluids in all simulations. In order to represent the hydrothermal veins at Panasqueira, we schematically placed three fractures above the magma chamber, ca. 3000 m wide, connected by a subvertical fracture that channelizes the fluids from the magma chamber to the fractured zone (Figure 6.4). We further added the two regional faults recognized by geophysical methods (Ribeiro, 2017) to play a role in the emplacement of the granites (Cebola and Zêzere River Fault). For this set-up we applied constant permeability $k_{fr,ft}$ of $10^{-14}m^2$ and a width $w_{fr,ft}$ of 10 m for the faults and fractures. By assigning this thickness to the structures, we account also for the vein and alteration zone (horizontal fractures) and provide an average permeability of fracture and surrounding matrix. In the setups, we only show the domain highlighted in Figure 6.4

6.4 Results

6.4.1 Simple horizontal fracture

We computed six examples of two-dimensional single-phase fluid flow with different mesh resolutions to test the validity of the new method introduced here (lower-dimensional elements). The first example (Figure 6.5A) shows the evolution of the thermal front [white dashed (two-dimensional dimensional) and solid line (lower-dimensional elements)] and fluid pressure (black dashed and solid lines, respectively) in a low-resolution mesh after 2000 years (Figure 6.5A, B). When the fracture is resolved by the mesh, the two-dimensional elements have a higher resolution of the fracture zone when compared with the lower-dimensional elements, consequently the isotherms of both methods diverge significantly (Figure 6.5A). Nevertheless, the two simulations roughly agree in the different positions and shapes of the thermal fronts, hence both capture the first-order flow pattern. In contrast, fluid pressures are only weekly affected by varying mesh type. Figure 6.5B shows the comparison between both methods in a medium resolution mesh, which has a similar discretization through the entire domain. In this case, both the isotherms and fluid pressure lines overlap in most of the domain. A similar scenario can be observed in Figure 6.5C where the two methods are compared in a high-resolution mesh. The results show that the representation of fault structures by lower-dimensional elements enables to use coarse- to intermediate-resolution meshes in order to save computational time and still capture the first-order fluid dynamics.

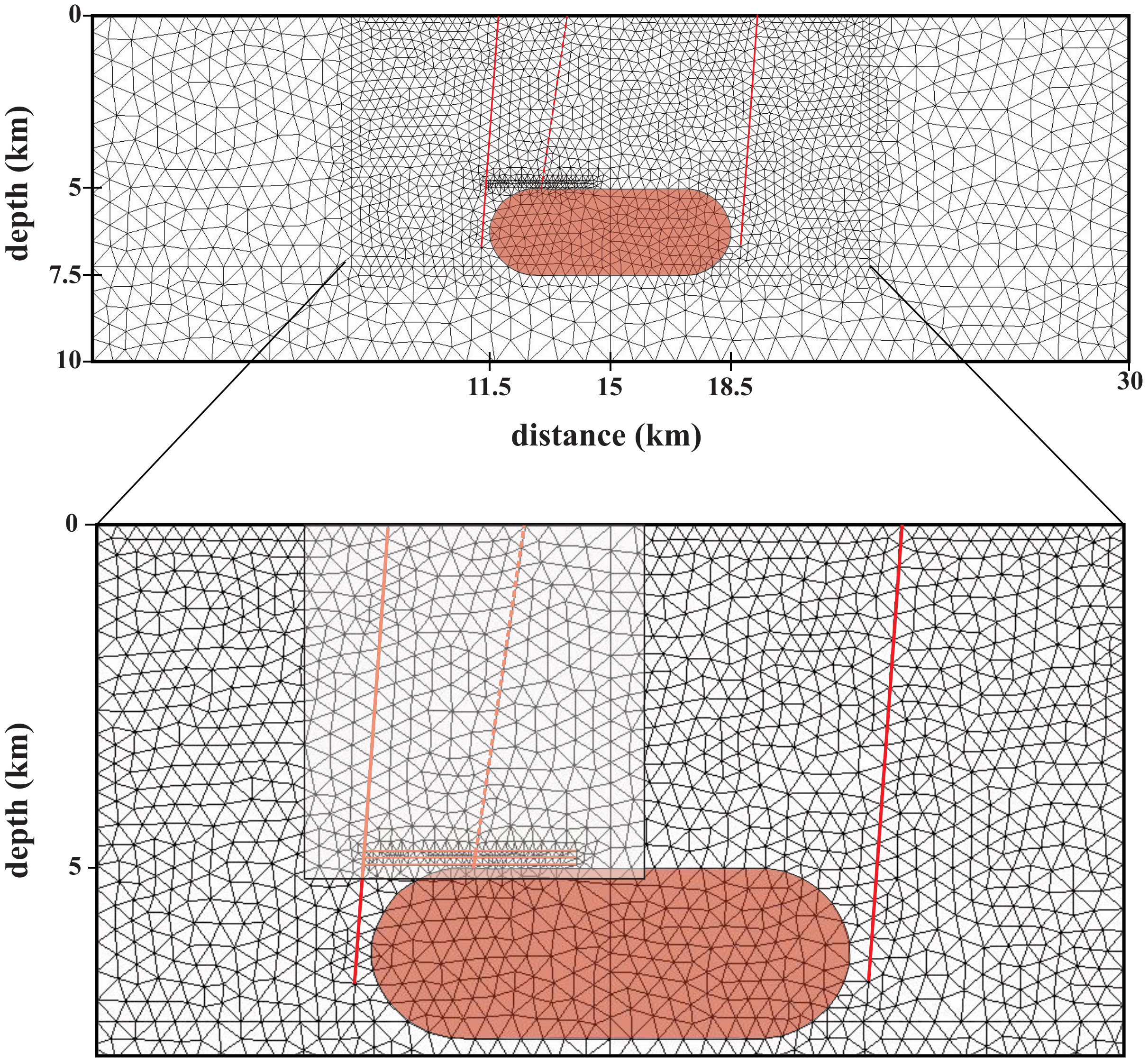

Figure 6.4: Unstructured mesh and model configuration with an elliptical magma chamber placed at 5 km depth (7km width and 2.5 km height). The magma chamber is controlled by two subvertical regional fault zones. Three fractures above the magma chamber schematically represent the mineralized vein system at Panasqueira. A third fracture/fault is placed at the discharge zone and works as a connection between the magma chamber and the veins. The dimensions are taken from gravimetry surveys and field observations (Ribeiro, 2017). The grey-shaded zone represents the domain that will be shown in Figures 6.6, 6.7, 6.8 and 6.9.

6.4.2 Panasqueira hydrothermal system

In order to understand the fault and fracture control on hydrothermal circulation pattern and the magmatic fluid release and from an underlying magma chamber associated to the Panasqueira deposit, we performed a series of simulations using preassigned fractures and faults in different combinations (Figure 6.4 and 6.6 6). Three different setups were

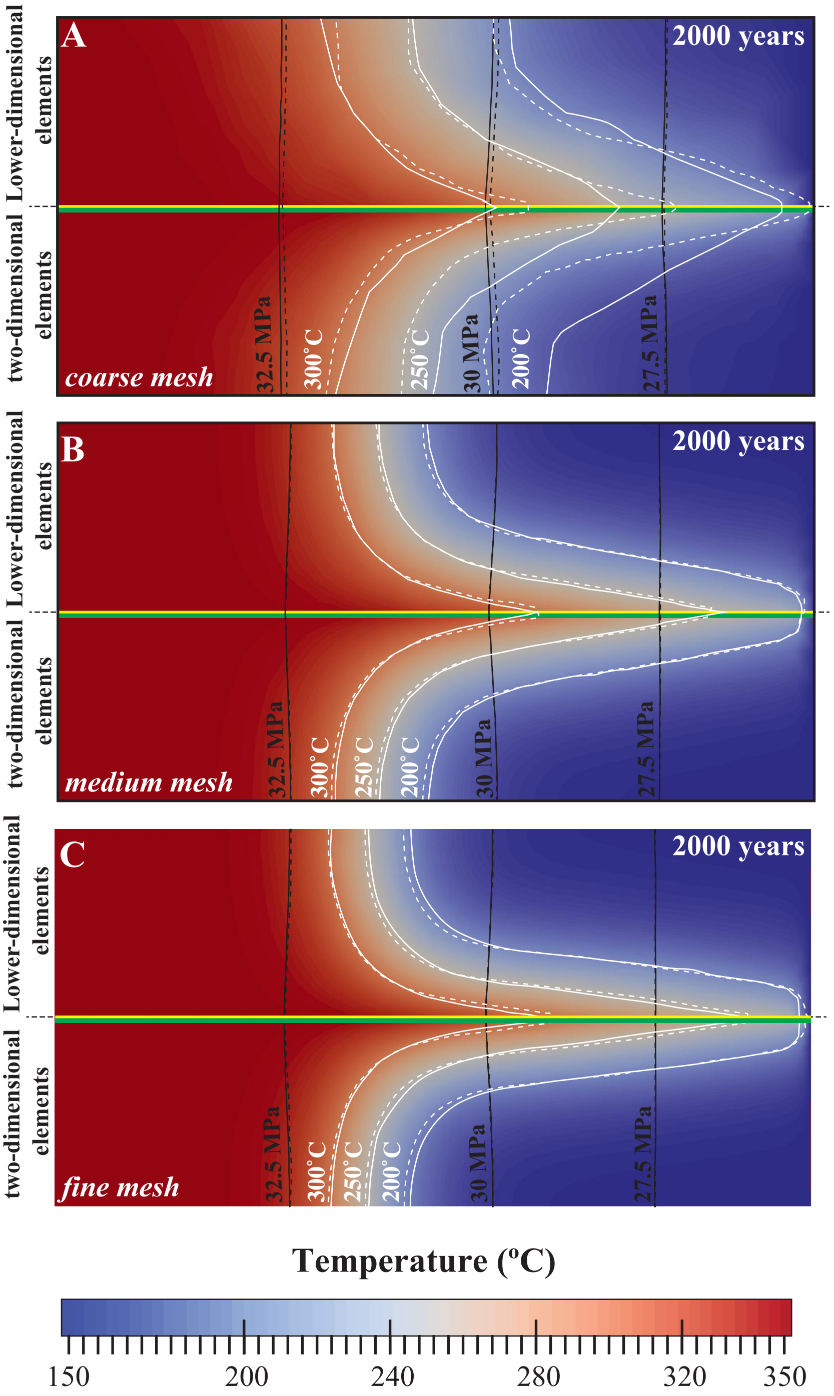

Figure 6.5: Snapshots of two-dimensional simulations of the propagation of a thermal front along a fault structure that is either resolved by two-dimensional or one-dimensional elements. Results for fluid pressure (black) and temperature (white) from lower dimensional simulations are plotted as solid lines, while results from two dimensional simulations as dashed lines. The lower dimension fracture is represented by the yellow line, whereas the green line represents the fault zone defined with 50m.

used to investigate the role of faults on fluid flow: (1) a crustal subvertical fault that connects the injection point of the magma chamber to the surface ("middle fault", 6.6C);

(2) the extend of this subvertical fault is limited to the connection between the fractures and the injection point, while the fault located at the left-hand side ("left fault") extends to the surface instead (Figure 6.6); (3) two crustal subvertical faults ("two faults", Figure 6.6E). We further carried out two simulations without any subvertical fault structures, including one with (Figure 6.6B)and one without (Figure 6.6A) horizontal fractures.

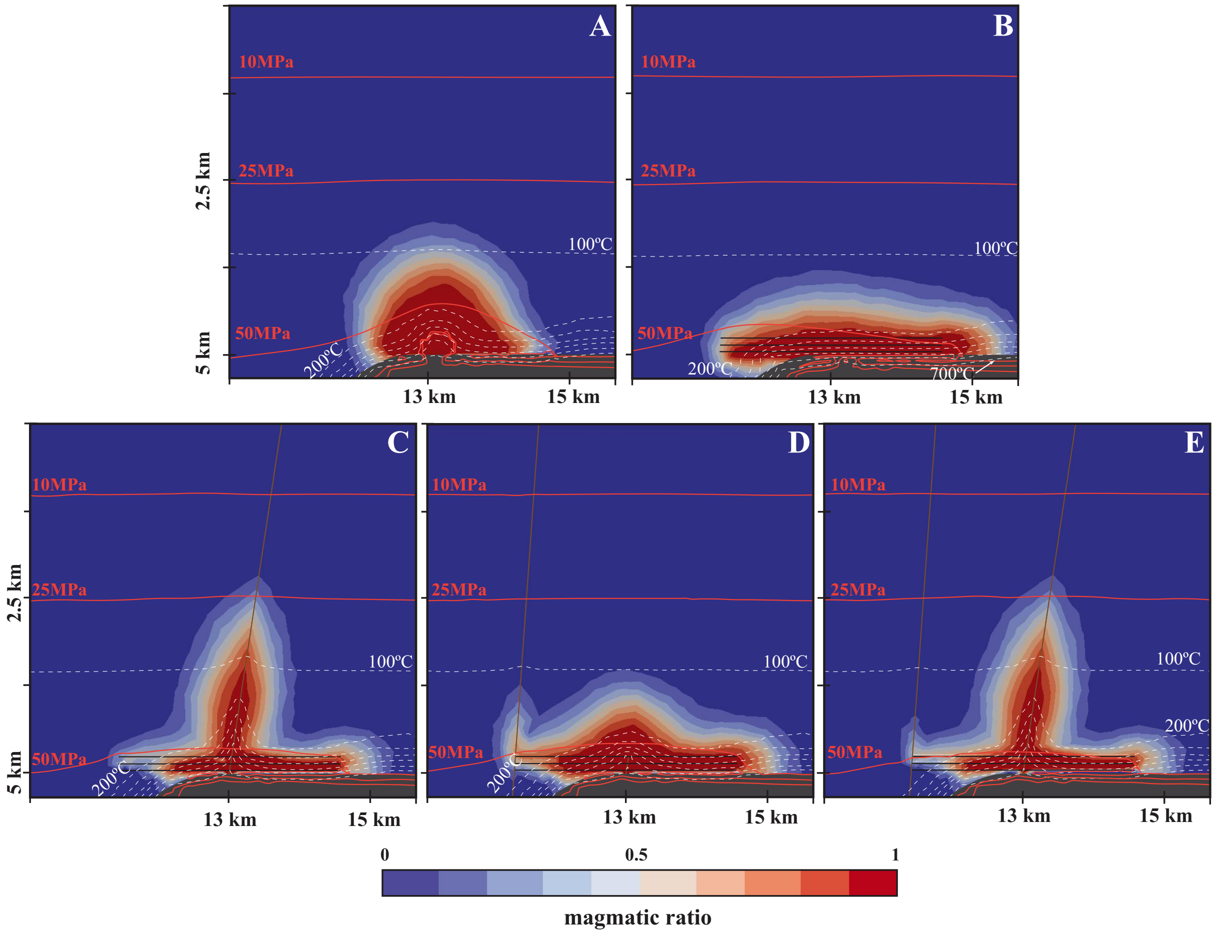

Figure 6.6: Simulation results for the initial stages (1,000 years) of fluid flow based on magmatic ratio (fraction of magmatic fluid in the respective pore volume from 0 to 1) **(A)** for a domain without structures, **(B)** for a domain with horizontal fractures, **(C)** to **(E)** for domains with horizontal fractures and one fault situated above the injection point **(C)**, one fault in the left side of the domain and a subvertical connecting fracture above the injection point **(D)** and two faults **(E)**. White lines represent the isotherms (from 0 to 700 °C) and the orange lines the fluid pressure (10 MPa to 100 MPa).

All performed simulations have in common that the magma chamber heats the surrounding host rocks by conduction and induces convection of ambient fluid. Because of the efficient cooling of the outer shell of the magma chamber, magmatic fluids are immediately produced and injected into the subvertical fracture or the host rocks in the absence of this structure. The initial expulsion event is accompanied by a locally pronounced fluid pressure anomaly to accommodate this fluid release. The fluid flow pattern after 1,000 years in the different simulations is shown in Figure 6.6. In the setup where the faults and fractures are not taken into account, the upward flow produces a radial front (Figure 6.6A). Conversely, in fractured media, fluid flow is subhorizontal with variable degrees of subvertical flow through faults (Figure 6.6B to E). In general, the magmatic and thermal fronts move faster upward in the presence of either two or one central subvertical fault ("middle fault" and "two faults" setups: Figure 6.6C, E). After 1,000 years of simulation time, the magmatic plume reached levels as shallow as 2.5 km for these simulations. With the continuous exsolution of magmatic fluids, the magmatic plume spreads to the surface at ca. 2,000 years for most of the simulations.

The thermal front has reached the surface at 6,000 years of simulation time and the ascending overpressured magmatic fluids have established a vertically extensive two-phase liquid-vapor (vapor-dominated) coexistence zone, with boiling taking place between ca. 2.5 km depth and the magma chamber, as well as near the surface (Figure 6.7, central panel). The temperature in the veins is in the range of 500° to 600 °C and in all cases, although spreading sideways, there is a tendency for higher temperatures in the left-hand side of the domain (Figure 6.7, left panel).

After 15,000 years of simulation time, the hydrothermal system is already declining due to reduced fluid production from a smaller magma chamber, which leads to increasing inflow meteoric waters and fluid mixing. However, the fracture system is still completely dominated by magmatic fluids (Figure 6.8). By this time, the temperature in the fractures is still dominantly above 600°C, except for the setup with the "middle fault", where the heat moves more efficiently upward (Figure 6.9A vs. B and C). The thermal fronts in the setup with the "two faults" are starting to merge into a single up flow zone centered between both faults (Figure 6.8C).

In these simulations, the fluids are injected mostly as two-phase fluids, as a response to the initial salinity of the magmatic fluid (5 wt.%), but with a vapor-dominated nature ($S_v > 0.6$). In most cases the fluid flow shows a pulsating behavior, with intermittent bursts of higher salinity fluids (see Figure 6.9 D and F). The high salinity fluids can also locally and temporarily saturate in solid halite, such as in the "middle fault" domain at

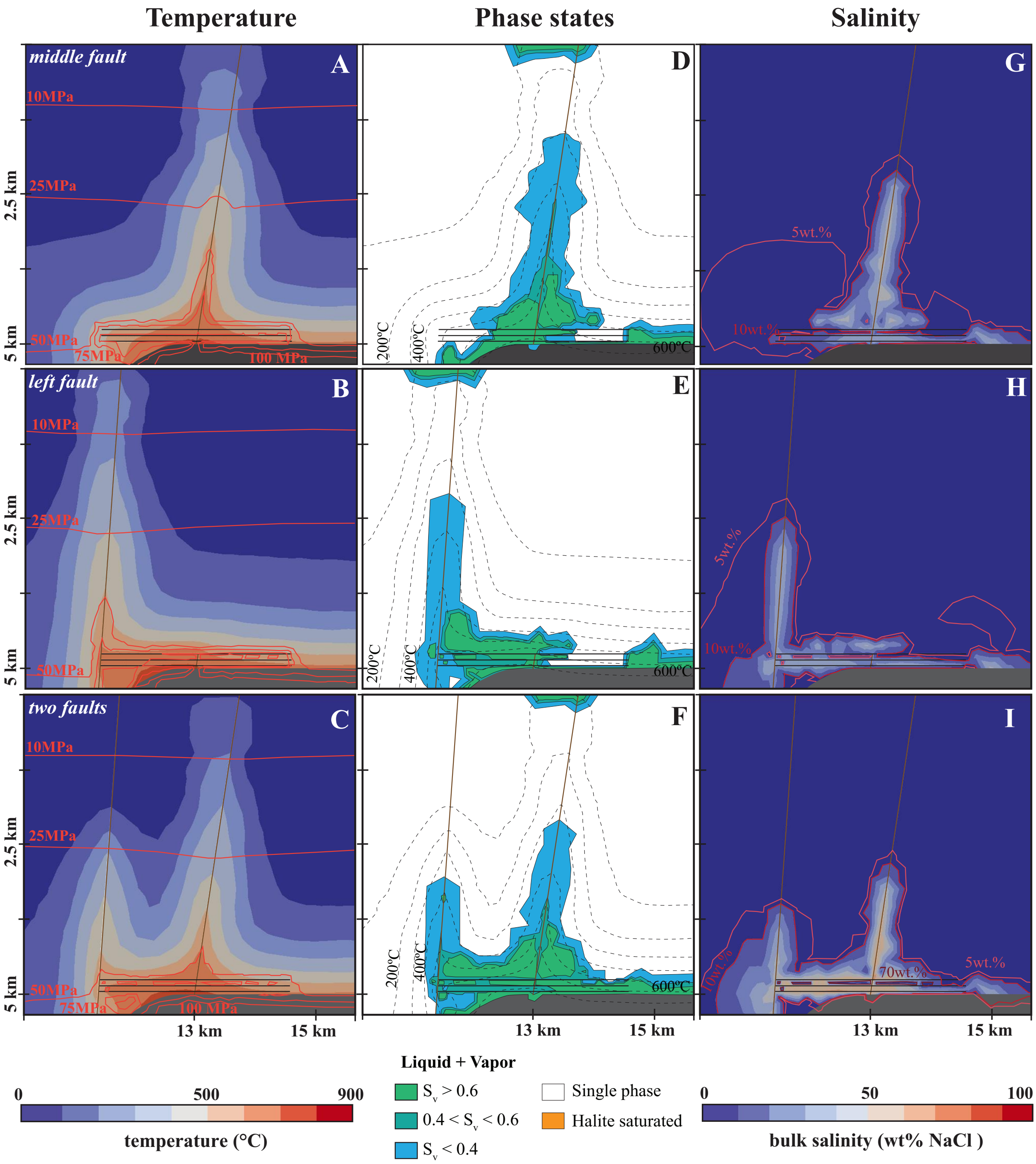

Figure 6.7: Simulation results showing magmatic-hydrothermal system at peak conditions (6,000 years).The left-hand side panels show the thermal evolution, the middle panels the phase states and the right-hand side panels the salinity. **A-C**: "middle fault"; **D-F**: "left fault" and **G-I**: "two faults". S_v: volumetric saturation in vapor

ca. 2.5. km, (Figure 6.9D).

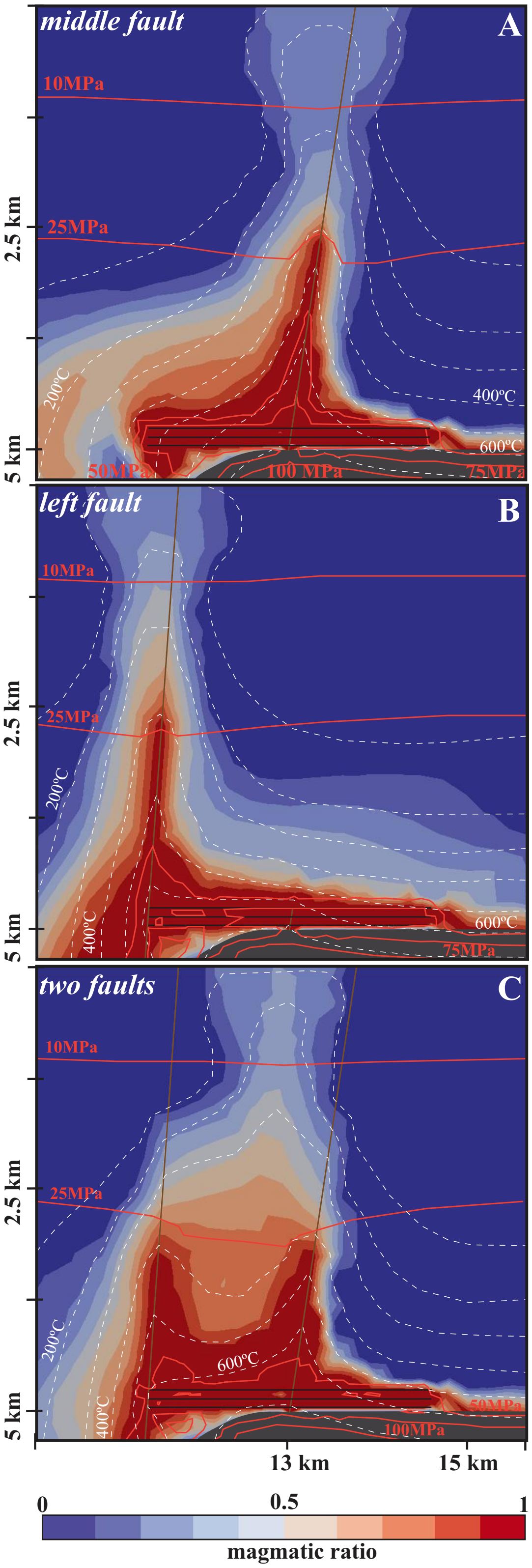

Figure 6.8: Simulation results showing the magmatic ratio for the waning stage (after 15,000 years) during incursion of meteoric waters. **A**: “middle fault”; **B**: “left fault” and **C**: “two faults”.

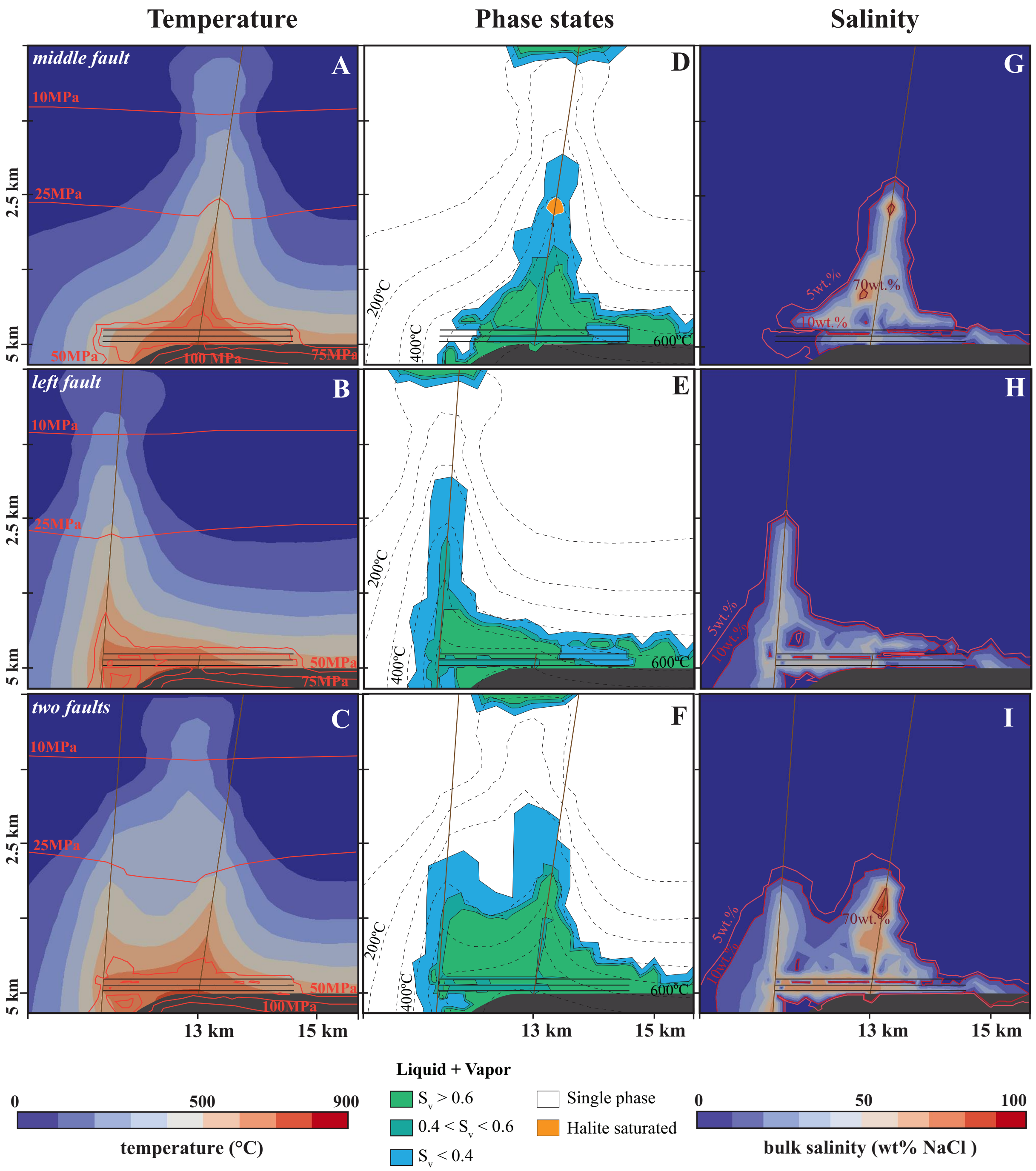

Figure 6.9: Simulation results for the waning stage of magmatic-hydrothermal system (15,000 years) during incursion of meteoric waters. The left-hand side panels show the thermal evolution, the middle panels the phase states and the right-hand side panels the salinity. **A-C**: "middle fault"; **D-F**: "left fault" and **G-I**: "two faults". S$_v$: volumetric saturation in vapor.

6.5 Discussion

Our simulations show that different hydrological regimes can occur in fractured geological media as a function of the structural arrangement. In the absence of fractures, the fluid flow is radial and fluids are overpressured right above the injection point of the magma chamber (e.g., Figure 6.6A), with pressures reaching 100 MPa after 1,000 years. Contrarily, in the presence of structural connectivities, especially to the surface, the fluid pressure remains lower (range of 50 MPa to 75MPa) in the region represented by the fractures (Figure 6.6B-E) and fluids rapidly ascend through the crust reaching the surface after ca. 2,000 years. With time, the fluid pressure seems to rise as vapor-dominated fluids move upwards (see Figures 6.7 and 6.9), with these zones reaching fluid pressures of 75MPa. In some simulations, a counteracting effect exerted by the downflow of meteoric waters, leads to further increase in fluid pressure (e.g., Figure 6.7A; Figure 6.9A, B and C). Another interesting outcome of these results is the heat and fluid distribution within the horizontal fractures. Figures 6.7 and 6.9 show that fluids have a preference to flow to the left hand-side of the fractured domain, even in the setup with a single fault in the middle. This behavior may relate to the inflow of meteoric waters, which seems to be faster on the right-hand-side of the domain, pushing the magmatic fluids to the opposite direction.

6.5.1 The hydrological evolution at Panasqueira

The physical processes modeled by our simulations can explain several specific observations at the Panasqueira W-Sn-Cu deposit. For the present setup we assumed that all fracture networks are fully open at the time of fluid expulsion. Several authors suggested that the vein system exploits the pre-existing joint system developed during the Variscan orogeny (*e.g.,* Derré et al., 1986; Jacques et al., 2018; Marignac, 1973, 1982) and the vein network is often connected by inclined veins which we represented as the fracture/fault in the middle. As shown in Figure 6.1B, the deposit is crosscut by numerous faults, some of them with regional expression. The Cebola Fault in the N controls the extent of the deposit and has been suggest as one of the controls on the emplacement of the Panasqueira granite and is represented in the model as the fault in the left-hand side. The Cebola fault is interpreted to be part of the system *Bragança-Vilariça-São Jorge da Beira-Figueiró dos Vinhos*, which consists of a, 250-km-long, NNE-striking-slip zone (Rockwell et al., 2009; da Silva, 2016). The NE-SW Late-Variscan faults have dextral kinematics, with sinistral reactivation during the Alpine (Marques et al., 2002).

The results from our simulations show that fluid flow always develops a horizontal component if the fractures are connected. In that respect, the Cebola fault may play a critical role in the ascent of the fluids to the surface. The presence of this fault coupled with a second fault (here represented in the middle) are efficient fluid conduits to the surface and can also be used as recharge channels for ambient meteoric waters in later stages of the hydrothermal system. The simulations shown after 15,000 years, already suggests the inflow of meteoric waters into the system. Mixing with meteoric has been suggested by several authors to occur either at early stages (Polya et al., 2000) or at the late stages of mineralization (Bussink, 1984; Kelly and Rye, 1979). The current model suggests that the mixing will only occur at later stages, given the dominance of magmatic fluids in the veins during the early stages.

The percolation of mineralizing fluids through subvertical structures such as the Cebola fault may lead to the precipitation of lower temperature mineralization, such as galena and sphalerite. In fact, there are occurrences of several small epigenetic Pb-Zn vein-type deposits (orientation N-S to ENE-WSW) along the segmented parts of the Cebola fault, consisting of galena ± sphalerite with variable amounts of Ag and Au (Ceiroco, Lamba das Vargens, Ribeira do Asno, Meas, Ceife) (*e.g.,* Thadeu, 1951*b*). In the deposit, some subvertical faults have been identified to host Pb-Zn mineralization as well as associated to N-S and NE-SW strike-slip faults Lourenço (*e.g.,* 2002), thus with the same geometry as the Cebola fault. Lourenço (2002) suggests that the Pb-Zn mineralization occurs associated with aqueous fluids of probable meteoric origin with high salinities (mainly $CaCl_2$) and minimum temperatures of 120°C. Also, Lecumberri-Sanchez et al. (2018) described the presence of high salinity fluids (20–35 wt.%) with higher Cu, Zn and Pb on fluid inclusions in quartz related to the sulfide stage. After chalcopyrite and sphalerite precipitation in the subhorizontal-veins, the Pb and Zn can be transported and deposited farther at lower temperatures, precipitating galena and sphalerite in the subvertical faults.

6.5.2 Model limitations and future objectives

We explicitly focused on simulations with a coarse mesh resolution using lower-dimensional line elements as faults and fractures to test the validity of the approach and to understand the first-order controls of fluid flow at Panasqueira, in particular fluid movement through the horizontal fracture system. While the simulations can capture the general dynamics of the hydrothermal systems, we can identify some important aspects that may be captured by future simulations:

(a) Some areas within the modelling domain seem to require a slightly higher resolution. In particular, increasing the resolution in the areas between the horizontal fractures may provide better insights into fluid flow within the deposit.

(b) While there is evidence for fluid boiling in the fluid inclusion record, the predominant type contains a single-phase fluid at lower temperatures. To avoid phase separation in the horizontal fractures, either the fluid pressures were higher or the temperatures lower – or both. Higher fluid pressures near lithostatic values might be obtained if we use a dynamic permeability model for the fractures similar to the one applied to the host rock, instead of assuming a preexisting constant permeability of the line elements.

(c) We currently prescribe three horizontal fractures with a constant width of 10 m, which also takes into account the alteration halo. Alternatively, the lower-dimensional element approach can be modified to only use the actual aperture of the fracture as described by (*e.g.,* Azizmohammadi and Matthäi, 2017; Matthäi and Belayneh, 2004; Patterson et al., 2018a,b). Again, aperture width could also be used as a dynamic parameter of the line elements to obtain near-lithostatic fluid pressures during fluid expulsion.

(d) Observations suggest that an extensive metamorphic aureole above the inferred granitic body develops before the hydrothermal alteration (see Figure 6.1B), which is constrained by geothermometry (Codeço et al., 2017, 2019a) and microthermometry (Jaques and Pascal, 2017; Kelly and Rye, 1979; Lecumberri-Sanchez et al., 2017) to start at temperatures below 500° – 600°C (Codeço et al., 2017, 2019a). Such an evolution could be related to an incremental growth of the magma chamber rather than an instantaneous emplacement of a large magmatic intrusion as prescribed in the current set-up.

(e) Fault structures can develop convection patterns within the fault planes itself (Patterson et al., 2018b), which may allow for the recharge of meteoric waters and consequently cooling and fluid mixing at much earlier stages than simulated here. Because computational time increases dramatically when changing from 2D to 3D simulations, the lower-dimensional element approach presented will become even more important. In that case, fractures and faults are represented as 2D planes in a 3D mesh.

6.6 Conclusions

In a first set of simulations we compare hydrothermal flow through a simple horizontal fracture represented by a discrete two-dimensional mesh versus a new approach applying lower dimensional line elements. We show that the same hydrothermal field can be produced by both methods with varying mesh resolutions.

We further apply the new lower-dimensional element approach and present simulation results of two-phase hydrothermal flow patterns in fractured media applied to the Panasqueira vein-type deposit. The simulations show that the fluid flow always develops a horizontal component if the fractures are available by fracture connectivity. Subvertical faults are efficient fluid conduits to the surface and can also be used as recharge channels for the inflow of meteoric waters. Our model results suggests that mixing with meteoric fluids will only occur at later stages during the evolution of the magmatic-hydrothermal system, while magmatic fluid in the veins are dominating in the earlier phases. The percolation of fluid through these subvertical structures may lead to the precipitation of low temperature Pb-Zn mineralization as observed along the Cebola fault to the NW and along subvertical faults within the deposit.

Acknowledgments

We are very grateful to the CSMP++ platform community of developers and users for code development. The project was founded by the German Federal Ministry of Education and Research (BMBF) within the project GRAMME (033R149).

"We live on an island surrounded by a sea of ignorance. As our island of knowledge grows, so does the shore of our ignorance"

–John Archibald Wheeler

7

Conclusions

There is an old saying that describes very well the study, detection, and discovery of ore deposits: *"mineral exploration is like finding a needle in a haystack"* (Carranza and Sadeghi, 2012). This recaps the importance of developing tools and techniques capable of detecting mineral deposits beneath the ground surface. Operating mines are extraordinary fossil laboratories with three-dimensional insights into the geochemical anomalies in the crust. Thus, by studying the primary geochemical characteristics of mineral deposits (e.g., alteration halos, hydrothermal and ore minerals, fluid inclusions), we can better constrain the mineralization processes since the chemical processes during mineralization are the ones to ultimately cause metal precipitation and mineral deposit formation. Geochemistry is, therefore, a suitable tool to deduce *"where in a needle-bearing haystack, is the needle located"* (Carranza and Sadeghi, 2012).

7.1 Overall conclusions and outlook

The formation of magmatic-hydrothermal ore deposits requires the conjunction of physic-chemical factors operating within and outside a magmatic intrusion that result in an extreme metal enrichment. By characterizing and understanding the physical and chemical processes operating in ore systems one can constrain their driving forces and provide answers to constrain ore formation. Hence, this project has aimed to explore, develop, and integrate the potentialities of geochemistry and numerical modeling on mineral exploration.

The study of underground samples of altered host-rocks, including a portion of the vein, as well as vertical profiles in drill cores that intersected the altered and unaltered metasediments, greisen, and granite, resulted in new insights onto the formation of the Panasqueira W-Sn-Cu deposit. The early stages of alteration occurred at temperatures ranging from ca. 400° to 550°C and are characterized by the replacement of the biotite-chlorite metasediments of the Almaceda Fm. by an association of tourmaline ± quartz ± white mica and formation of the mica selvages in the veins. Mineral chemistry (major and trace elements) suggests that tourmaline formed at the expense of the host rocks under extensive fluid rock-interaction conditions, yet with a substantial contribution from the magmatic fluid (e.g., B, Li, F). On the other hand, the white mica compositions record the evolution of the fluids, where an increase in Fe, Rb, Li, W, Zn and decrease in Sn, Sr, and V is observed from the early to main ore-stage micas, associated with wolframite precipitation. The compositions recorded by the white mica are compatible with the alteration overprint indicated by bulk-rock analysis, marked by enrichments in W, Sn, Cu, Zn, Li, F, Cs, Rb, and Tl, making mica a good pathfinder for Sn-W deposits like Panasqueira. In contrast, micas from a late fault zone present higher Li and Sn contents, which is possibly related to a different mineralizing event. Boron-isotope mica-tourmaline geothermometry provides a median temperature of 250°C from the fault zone sample, which is compatible with the temperature obtained from fluid inclusions in the quartz from the veins. Together, the whole-rock and mineral chemistry and boron isotopic compositions of both tourmaline and mica suggest that a similar magmatic-hydrothermal fluid was active at all stages of mineralization represented by these samples, supporting a multiple injection model for Panasqueira, and a transition from wall-rock to fluid-dominated conditions during the early stages of vein opening and mineralization.

The numerical modeling results confirm that the presence of fractures with enhanced permeability plays a crucial role in the lateral fluid flow and its ascent to the surface, as well as for the recharge of meteoric waters. Moreover, the studies show that the earlier stages are entirely dominated by magmatic fluids, whereas in later stages there are conditions that permit the entrainment of meteoric fluids and fluid mixing. The integration of all results suggests that Panasqueira is an extremely complex hydrothermal system, characterized by multiple injections of magmatic-hydrothermal fluids and possibly mixing with meteoric-derived fluids at later stages of mineralization. It is likely that during the later stages, high saline fluids flowing through N-S, NE-SW (e.g., Cebola Fault, Main Fault) strike-slip faults have lead to the formation of small epigenetic Pb-Zn vein-type deposits.

Overall, the results of this thesis have improved the understanding of the Panasqueira deposit and ore deposits in the following ways:

(i) the thermal evolution of highly complex hydrothermal systems where favorable trapping conditions for fluid inclusions were not attained or fluid inclusions decrepitated due to later deformation events or crustal uplift, can be successfully obtained by mineral thermometry (B-isotope thermometry, Ti-in-quartz thermometry);

(ii) the mineral chemistry of mica and tourmaline have great potential as exploration guides for W-Sn deposits and possibly for other ores, as they record not only the evolution of the hydrothermal system but as well fluid-rock interaction processes and give constraints on fluid composition and source;

(iii) the numerical simulations offer new constraints on the understanding of the physical processes that led to the formation of Panasqueira's unusual subhorizontal ore veins, as well as on the evolution of the hydrothermal system from early to later stages of mineralization and hydrothermal alteration.

7.2 Future work directions

This study here mainly focused in detail on the early stages of hydrothermal alteration at Panasqueira. Further constrains from a late sub-vertical fault and tourmaline needles from the late-vugs (syn-ore stage) provide valuable insights on the dynamic nature of Panasqueira system. However, up to the present time, the deposit lacks a detailed study to better understand the paragenetic sequence which is critical to grasp the overall evolution of the system, from the early vein opening to the late carbonate stage and possible reworking during the Alpine orogeny.

This work described the occurrence of different vein-selvages (mica-rich, topaz-rich and mica-poor), although our sampling coverage did not allow us to understand the reason for these differences. Thus, to better comprehend the coverage and formation of these contrasting types, a systematic mapping and characterization of these veins would be essential. Regarding the topaz-rich selvages, studies of fluid inclusions and trace element geochemistry could provide some answers regarding its formation.

Future research might apply dating of the ore minerals, e.g., wolframite, cassiterite by U-Pb and Sm-Nd: (*e.g.,* Guo et al., 2018; Harlaux et al., 2018; Li et al., 2016; Neymark et al., 2018), chalcopyrite by Re-Os: e.g., (*e.g.,* Deng et al., 2016; Zhimin and Yali, 2013), which offers the possibility for constraining the age of mineralization and perhaps to understand the relationship between oxide and sulfide stage. Furthermore, the study of in-situ trace element compositions of those ore minerals can provide key insights on the fluid compositions.

It will be important that future research investigates the Panasqueira granite, including mineral chemistry with particular emphasis on trace element contents of micas, isotopic studies, U-Pb dating of zircon, geothermometry (e.g., zircon saturation, Ti-in-zircon, Ti-in-quartz), and melt inclusions. This information would give valuable constraints to understand the processes and PTX conditions operating in such systems.

At last, but not least important is the need for the new experiments on boron isotope fractionation between silicate melts and hydrous fluids since current models are inadequate. Moreover, a better understanding of trace element partitioning between hydrothermal minerals (e.g., dioctahedral and trioctahedral micas, tourmaline, chlorite, epidote) and fluids, would be important in order to better understand the hydrothermal system and predict trace element behavior in hydrothermal systems.

Bibliography

Almonty Industries (2016), 'Panasqueira mine'.
URL: *http://www.almonty.com/projects/panasqueira/*

Almonty Industries (2018), 'Almonty industries: News releases'.
URL: *http://www.almonty.com/investors/news/*

Arenas, R., Díez Fernández, R., Sánchez Martínez, S., Gerdes, A., Fernández-Suárez, J. and Albert, R. (2014), 'Two-stage collision: Exploring the birth of Pangea in the Variscan terranes', *Gondwana Research* **25**(2), 756–763.
URL: *http://dx.doi.org/10.1016/j.gr.2013.08.009*

Arenas, R., Sánchez Martínez, S., Díez Fernández, R., Gerdes, A., Abati, J., Fernández-Suárez, J., Andonaegui, P., González Cuadra, P., López Carmona, A., Albert, R., Fuenlabrada, J. M. and Rubio Pascual, F. J. (2016), 'Allochthonous terranes involved in the Variscan suture of NW Iberia: A review of their origin and tectonothermal evolution', *Earth-Science Reviews* **161**, 140–178.
URL: *http://dx.doi.org/10.1016/j.earscirev.2016.08.010*

Audétat, A., Guenther, D. and Heinrich, C. A. (1998), 'Formation of a Magmatic-Hydrothermal Ore Deposit: Insights with LA-ICP-MS Analysis of Fluid Inclusions', *Science* **279**(5359), 2091–2094.
URL: *http://www.sciencemag.org/cgi/doi/10.1126/science.279.5359.2091*

Audétat, A., Guenther, D. and Heinrich, C. A. (2000), 'Magmatic-hydrothermal evolution in a fractionating granite: a microchemical study of the sn-w-f-mineralized mole granite (Australia)', *Geochimica et Cosmochimica Acta* **64**(19), 3373–3393.
URL: *http://linkinghub.elsevier.com/retrieve/pii/S0016703700004282*

Azevedo, M. R. and Valle Aguado, B. (2013), Origem e instalação de Granitóides Variscos na Zona Centro-Ibérica, *in* R. Dias, A. Araújo, P. Terrinha and J. C. Kullberg, eds, 'Geologia de Portugal, Vol. I: Geologia Pré-mesozóica de Portugal', Escolar Editora, Lisbon, pp. 375–401.

Azizmohammadi, S. and Matthäi, S. K. (2017), 'Is the permeability of naturally fractured rocks scale dependent?', *Water Resources Research* **53**(9), 8041–8063.

Bächler, D., Kohl, T. and Rybach, L. (2003), 'Impact of graben-parallel faults on hydrothermal convection—Rhine Graben case study', *Physics and Chemistry of the Earth, Parts A/B/C* **28**(9-11), 431–441.
URL: *http://linkinghub.elsevier.com/retrieve/pii/S1474706503000639*

Ballèvre, M., Bosse, V., Ducassou, C. and Pitra, P. (2009), 'Palaeozoic history of the Armorican Massif: Models for the tectonic evolution of the suture zones', *Comptes Rendus - Geoscience* **341**(2-3), 174–201.

Ballèvre, M., Fourcade, S., Capdevila, R., Peucat, J. J., Cocherie, A. and Fanning, C. M. (2012), 'Geochronology and geochemistry of Ordovician felsic volcanism in the Southern Armorican Massif (Variscan belt, France): Implications for the breakup of Gondwana', *Gondwana Research* **21**(4), 1019–1036.
URL: *http://dx.doi.org/10.1016/j.gr.2011.07.030*

Barbero, L. and Villaseca, C. (2000), 'Eclogite facies relics in metabasites Sierra de Guadarrama (Spanish Central System): P-T estimations and implications for from the the Hercynian evolution', *Mineralogical Magazine* **64**(5), 815–836.

Barbosa, A. A. (1944), 'Algumas notas sobre o campo filoniano da Panasqueira', *Técnica,* **150**, 11–19.

Bea, F., Montero, P. and Molina, J. F. (1999), 'Mafic Precursors, Peraluminous Granitoids, and Late Lamprophyres in the Avila Batholith: A Model for the Generation of Variscan Batholiths in Iberia', *The Journal of Geology* **107**(4), 399–419.
URL: *http://www.journals.uchicago.edu/doi/10.1086/314356*

Bea, F., Montero, P. and Zinger, T. (2003), 'The Nature, Origin, and Thermal Influence of the Granite Source Layer of Central Iberia', *The Journal of Geology* **111**(5), 579–595.

Belissont, R., Boiron, M. C., Luais, B. and Cathelineau, M. (2014), 'LA-ICP-MS analyses of minor and trace elements and bulk Ge isotopes in zoned Ge-rich sphalerites from the Noailhac - Saint-Salvy deposit (France): Insights into incorporation mechanisms and ore deposition processes', *Geochimica et Cosmochimica Acta* **126**, 518–540.

Berkowitz, B. (2002), 'Characterizing flow and transport in fractured geological media: A review', *Advances in Water Resources* **25**(8-12), 861–884.
URL: *http://linkinghub.elsevier.com/retrieve/pii/S0309170802000428*

Beurlen, H., de Moura, O. J. M., Soares, D. R., Da Silva, M. R. R. and Rhede, D. (2011), 'Geochemical and geological controls on the genesis of gem-quality "Paraiba Tourmaline" in granitic pegmatites from northeastern Brazil', *The Canadian Mineralogist* **49**(1), 277–300.
URL: *http://www.canmin.org/cgi/doi/10.3749/canmin.49.1.277*

Blaettler, A. (1985), Structural analysis of the fault pattern in the tungsten-tin mine of Panasqueira, Portugal, Unpublished phd thesis, University of Geneva.

Bloot, C. and de Wolf, L. C. M. (1953), 'Geological features of the Panasqueira tin-tungsten ore occurence (Portugal)', *Soc. Geol. Portugal Bol.* **11**(September 1953), 1–58.

Bodnar, R., Lecumberri-Sanchez, P., Moncada, D. and Steele-MacInnis, M. (2014), Fluid Inclusions in Hydrothermal Ore Deposits, *in* 'Treatise on Geochemistry', Vol. 13, Elsevier, pp. 119–142.
URL: *https://linkinghub.elsevier.com/retrieve/pii/B9780080959757011050*

Bos, A. (1990), Hydrothermal element distributions at high temperatures : an experimental study on the partitioning of major and trace elements between phlogopite, haplogranitic melt and vapour, Unpublished phd thesis, Utrecht University.

Bosi, F. (2018), 'Tourmaline crystal chemistry', *American Mineralogist* **103**(2), 298–306.

Bouchot, V., Ledru, P., Lerouge, C., Lescuyer, J.-L. and Milesi, J.-P. (2005), '5: Late Variscan mineralizing systems related to orogenic processes: The French Massif Central', *Ore Geology Reviews* **27**(1-4), 169–197.
URL: *http://linkinghub.elsevier.com/retrieve/pii/S0169136805000624*

Breiter, K., Förster, H. J. and Seltmann, R. (1999), 'Variscan silicic magmatism and related tin-tungsten mineralization in the Erzgebirge-Slavkovsky les metallogenic province', *Mineralium Deposita* **34**(5-6), 505–521.

Breiter, K., Müller, A., Leichmann, J. and Gabašová, A. (2005), 'Textural and chemical evolution of a fractionated granitic system: the Podlesí stock, Czech Republic', *Lithos* **80**(1-4), 323–345.
URL: *http://linkinghub.elsevier.com/retrieve/pii/S0024493704002968*

Breiter, K., Vaňková, M., Galiová, M. V., Korbelová, Z. and Kanický, V. (2017a), 'Lithium and trace-element concentrations in trioctahedral micas from granites of different geochemical types measured via laser ablation ICP-MS', *Mineralogical Magazine* **81**(1), 15–33.
URL: *http://www.ingentaconnect.com/content/10.1180/minmag.2016.080.137*

Brigatti, M. F. and Guggenheim, S. (2002), 'Mica Crystal Chemistry and the Influence of Pressure, Temperature, and Solid Solution on Atomistic Models', *Reviews in Mineralogy and Geochemistry* **46**(1), 1–97.

Brown, T. and Pitfield, P. (2013), Tungsten, *in* 'Critical Metals Handbook', John Wiley & Sons, Oxford, pp. 385–413.
URL: *http://doi.wiley.com/10.1002/9781118755341.ch16*

Brzozowski, M., Samson, I., Gagnon, J., Linnen, R., Good, D., Ames, D. and Flemming, R. (2018), 'Controls on the chemistry of minerals in late-stage veins and implications for exploration vectoring tools for mineral deposits: An example from the Marathon Cu-Pd deposit, Ontario, Canada', *Journal of Geochemical Exploration* **190**, 109–129.
URL: *https://linkinghub.elsevier.com/retrieve/pii/S0375674217305010*

Burnard, P. G. and Polya, D. A. (2004), ‘Importance of mantle derived fluids during granite associated hydrothermal circulation: He and Ar isotopes of ore minerals from Panasqueira’, *Geochimica et Cosmochimica Acta* **68**(7), 1607–1615.

Burnham, C. W. (1997), Magmas and hydrothermal fluids, *in* H. L. Barnes, ed., ‘Geochemistry of Hydrothermal Ore Deposits’, 3rd edition edn, John Wiley & Sons, New York, pp. 63–123.

Bussink, R. W. (1984), ‘Geochemistry of the Panasqueira Tungsten-tin deposit, Portugal’, *Geologica Ultraiectina* **33**, 170.

Büttner, S. H., Reid, W., Glodny, J., Wiedenbeck, M., Chuwa, G., Moloto, T. and Gucsik, A. (2016), ‘Fluid sources in the Twangiza–Namoya Gold Belt (Democratic Republic of Congo): Evidence from tourmaline and fluid compositions, and from boron and Rb–Sr isotope systematics’, *Precambrian Research* **280**, 161–178.
URL: *http://linkinghub.elsevier.com/retrieve/pii/S0301926816301280*

Cabral, A. R., Wiedenbeck, M., Koglin, N., Lehmann, B. and De Abreu, F. R. (2012), ‘Boron-isotopic constraints on the petrogenesis of hematitic phyllite in the southern Serra do Espinhaço, Minas Gerais, Brazil’, *Lithos* **140-141**, 224–233.
URL: *http://dx.doi.org/10.1016/j.lithos.2012.01.011*

Campbell, A., Robinson Cook, S. and Amindyas, C. (1988), ‘Observation of fluid inclusions in wolframite from Panasqueira, Portugal.’, *Bull. Mineral.* **111**(3-4), 251–256.

Campbell, A., Rye, D. M. and Peterson, U. (1984), ‘A hydrogen and oxygen isotope study of the San Cristobal mine, Peru: implications of the role of water to rock ratio for the genesis of wolframite deposits.’, *Economic Geology* **79**(8), 1818–1832.

Capdevila, R., Corretgé, G. and Floor, P. (1973), ‘Les granitoïdes varisques de la Meseta ibérique’, *Bulletin de la Société géologique de France* **15**(3), 209–228.

Capdevila, R. and Floor, P. (1970), ‘Les différents types de granites hercynniens et leur distribution dans le NW de l’Espagne’, *Bol. Geol. Min. España* **81**(2-3), 215–225.

Carranza, E. J. M. (2012), 'Geochemical characteristics of mineral deposits: Implications for ore genesis', *Geochemistry: Exploration, Environment, Analysis* **12**, 89–92.
URL: *https://doi.org/10.1144/1467-7873/12-MINDEP-122*

Carranza, E. J. M. and Sadeghi, M. (2012), 'Primary geochemical characteristics of mineral deposits — Implications for exploration', *Ore Geology Reviews* **45**, 1–4.
URL: *https://linkinghub.elsevier.com/retrieve/pii/S0169136812000248*

Carta Geológica de Portugal à escala 1:1 000 000 (2010).

Carta Geológica de Portugal à escala 1:500 000, Folha Norte (1992).

Carvalho, D. (1974), 'Lineament patterns and hypogene mineralization in Portugal', *Estud. Notas Trab. Serv. Fom. Min.* **23**(3-4), 91–106.

Catanzaro, E. J., Champion, C. E., Garner, E. L., Marinenko, G., Sappenfield, K. M. and Shilds, W. R. (1970), 'Boric Acid; Isotopic, and Assay Standard Reference Materials', *National Bureau of Standards Special publication* **260-17**, 70.

Cathelineau, M., Marignac, C., Rolland, J.-M., Boiron, M. C., Dejan, M. and Carocci, E. (2017), Are we sure to know the fluids responsible for W mineralization at Panasqueira (Portugal): the case for loss of information due to intense quartz recrystallization and FI natural decrepitation, *in* 'Ecrofi 2017 Biennial Meeting', Nancy, France, p. 98.

Černý, P., Blevin, P. L., Cuney, M. and London, D. (2005), 'Granite-related Ore Deposits', *Economic Geology 100th Anniversary Volume* pp. 337–370.

Cheilletz, A., Pelleter, E., Martin-Izard, A. and Tornos, F. (2005), 'World skarn deposits: skarns of Western Europe', *Economic Geology 100th Anniversary Volume* pp. 1–10.

Chicharro, E. (2016), Petrologic-metallogenic characterization of a specialized granite: the Logrosán stock (Cáceres), Unpublished phd thesis, Universidad Complutense de Madrid.

Chicharro, E., Boiron, M. C., López-García, J. Á., Barfod, D. N. and Villaseca, C. (2016), 'Origin, ore forming fluid evolution and timing of the Logrosán Sn-(W) ore deposits

(Central Iberian Zone, Spain)', *Ore Geology Reviews* **72**, 896–913.
URL: *http://dx.doi.org/10.1016/j.oregeorev.2015.09.020*

Clark, A. H. (1970), 'Potassium-argon ages and regional relationships of the Panasqueira tin-tungsten mineralization.', *Comunicações dos Serviços Geológicos de Portugal* **54**, 243–261.

Clark, C. (1964), 'Preliminary study of temperatures and confining pressures of granite emplacement and mineralization, Panasqueira, Portugal', *Inst. Min. Metall. Trans.* **73**, 813–824.

Codeço, M. S., Weis, P., Trumbull, R. B., Glodny, J., Wiedenbeck, M. and Romer, R. L. (2019a), 'Boron-isotope muscovite-tourmaline geothermometry indicates fluid cooling during magmatic-hydrothermal W-Sn-ore formation', *Economic Geology* **114**(1), 153–163.

Codeço, M. S., Weis, P., Trumbull, R. B., Pinto, F., Lecumberri-Sanchez, P. and Wilke, F. D. H. (2017), 'Chemical and boron isotopic composition of hydrothermal tourmaline from the Panasqueira W-Sn-Cu deposit, Portugal', *Chemical Geology* **468**, 1–16.
URL: *http://www.sciencedirect.com/science/article/pii/S0009254117304096*

Codeço, M. S., Weis, P., Trumbull, R. B., van Hinsberg, V. J., Pinto, F., Lecumberri-Sanchez, P. and Schleicher, A. M. (2019b), 'Data Supplement to: Trace element signatures of white mica and tourmaline from the Panasqueira W-Sn-Cu deposit, Portugal, and their value as pathfinder minerals. GFZ Data Services'.

Cohen, D. (2007), 'Earth's natural wealth: an audit', *New Scientist* **194**(2605), 34–41.

Cohen, J. F. (2011), Compositional Variations in Hydrothermal White Mica and Chlorite from Wall-Rock Alteration at the Ann-Mason Porphyry Copper Deposit, Nevada, Upublished master thesis, Oregon State University.

Conde, L. N., Pereira, V., Ribeiro, A. and Thadeu, D. (1971), 'Jazigos Hipogénicos de Estanho e Volfrâmio'.

Cooke, D. R., Baker, M., Hollings, P., Sweet, G., Zhaoshan, C., Danyushevsky, L., Gilbert, S., Zhou, T., White, N. C., Gemmell, J. B. and Inglis, S. (2014), 'New Advances in Detecting the Distal Geochemical Footprints of Porphyry Systems–Epidote Mineral Chemistry as a Tool for Vectoring and Fertility Assessments', *SEG Special Publication 18* pp. 127–152.

Corrêa de Sá, A., Naique, R. A. and Nobre, E. (1999), 'Minas da Panasqueira - 100 anos de história mineira', *Boletim de Minas* **36**, 3–22.

Corretgé, G., Ugidos, J. and Martínez, F. (1977), Les séries granitiques varisques du secteur centre-occidental Espagnol, *in* 'La Chaîne Varisque d'Europe Moyenne et Occidentale. Coll Internat C.N.R.S. Rennes 243', Vol. 1, pp. 453–461.

Costa, M. M., Neiva, A. M. R., Azevedo, M. R. and Corfu, F. (2014), 'Distinct sources for syntectonic Variscan granitoids: Insights from the Aguiar da Beira region, Central Portugal', *Lithos* **196-197**, 83–98.
URL: *http://dx.doi.org/10.1016/j.lithos.2014.02.023*

Cotelo Neiva, J. (1944), 'Jazigos portugueses de cassiterite e de volframite', *Comunicações dos Serviços Geológicos de Portugal* **25**, 1–251.

Coumou, D., Driesner, T. and Heinrich, C. A. (2008*a*), 'Heat transport at boiling, near-critical conditions', *Geofluids* **8**(3), 208–215.
URL: *http://doi.wiley.com/10.1111/j.1468-8123.2008.00218.x*

Coumou, D., Driesner, T. and Heinrich, C. A. (2008*b*), 'The Structure and Dynamics of Mid-Ocean Ridge Hydrothermal Systems', *Science* **321**(5897), 1825–1828.
URL: *http://www.sciencemag.org/cgi/doi/10.1126/science.1159582*

Cox, D. P. and Bagby, W. C. (1986), Descriptive model of W veins, *in* D. P. Cox and D. A. Singer, eds, 'Mineral deposit models', U.S. Geological Survey Bulletin 1693, p. 64.

Cox, S. F. (2005), Coupling between Deformation, Fluid Pressures, and Fluid Flow in Ore-Producing Hydrothermal Systems at Depth in the Crust, *in* J. W. Hedenquist, J. F. H. Thompson, R. J. Goldfarb and J. P. Richards, eds, 'One Hundredth Anniversary Volume', Society of Economic Geologists, pp. 39–75.

Cuney, M., Alexandrov, P., De Veslud, C. L. C., Cheilletz, A., Raimbault, L., Ruffet, G. and Scaillet, S. (2002), 'The timing of W-Sn-rare metals mineral deposit formation in the Western Variscan chain in their orogenic setting: The case of the Limousin area (Massif Central, France)', *Geological Society Special Publication* **204**, 213–228.
URL: *http://sp.lyellcollection.org/content/204/1/213.full.pdf*

da Silva, A. F. (2016), 'Enquadramento Geotectónico e a Relação Entre a Tectónica e os Traçados Fluviais da Região Centro-Nordeste de Portugal', *Boletim de Minas* **51**(2), 43–61.

Dallmeyer, R. D., Catalán, J., Arenas, R., Gil Ibarguchi, J. I., Gutiérrez^Alonso, G., Farias, P., Bastida, F. and Aller, J. (1997), 'Diachronous Variscan tectonothermal activity in the NW Iberian Massif: Evidence from 40Ar/39Ar dating of regional fabrics', *Tectonophysics* **277**(4), 307–337.
URL: *http://www.sciencedirect.com/science/article/pii/S0040195197000358*

Davis, H. W. (1946), Tungsten, *in* E. W. Pehrson and A. F. Matthews, eds, 'Minerals yearbook 1946', US Department of Commerce, Washington: United States Government Printing Office, pp. 1192–1204.
URL: *http://digital.library.wisc.edu/1711.dl/EcoNatRes.MinYB1946*

Deng, X.-H., Wang, J.-B., Pirajno, F., Wang, Y.-W., Li, Y.-C., Li, C., Zhou, L.-M. and Chen, Y.-J. (2016), 'Re–Os dating of chalcopyrite from selected mineral deposits in the Kalatag district in the eastern Tianshan Orogen, China', *Ore Geology Reviews* **77**, 72–81.
URL: *https://linkinghub.elsevier.com/retrieve/pii/S0169136815302900*

Derré, C. (1982), 'Caracteristiques de la Distribution des Gisements à Etain et Tungstene Dans L'Ouest de L'Europe', *Mineralium Deposita* **17**(1), 55–77.

Derré, C., Lecolle, M., Roger, G. and Tavares de Freitas Carvalho, J. (1986), 'Tectonics, magmatism, hydrothermalism and sets of flat joints locally filled by Sn-W aplite-pegmatite and quartz veins; southeastern border of the Serra de Estrela granitic massif (Beira Baixa, Portugal)', *Ore Geology Reviews* **1**(1), 43–56.
URL: *http://linkinghub.elsevier.com/retrieve/pii/0169136886900041*

Dias, G., Leterrier, J., Mendes, A., Simões, P. P. and Bertrand, J. M. (1998), 'U-Pb zircon and monazite geochronology of post-collisional Hercynian granitoids from the Central Iberian Zone (Northern Portugal)', *Lithos* **45**(1-4), 349–369.

Díez Fernández, R., Arenas, R., Pereira, M. F., Sánchez-Martínez, S., Albert, R., Martín Parra, L. M., Rubio Pascual, F. J. and Matas, J. (2016), 'Tectonic evolution of Variscan Iberia: Gondwana–Laurussia collision revisited', *Earth-Science Reviews* **162**(2), 269–292.

URL: *http://dx.doi.org/10.1016/j.earscirev.2016.08.002*

Díez Fernández, R., Castiñeiras, P. and Gómez Barreiro, J. (2012), 'Age constraints on Lower Paleozoic convection system: Magmatic events in the NW Iberian Gondwana margin', *Gondwana Research* **21**(4), 1066–1079.

URL: *http://linkinghub.elsevier.com/retrieve/pii/S1342937X1100222X*

Díez Fernández, R., Pereira, M. F. and Foster, D. A. (2015), 'Peralkaline and alkaline magmatism of the Ossa-Morena zone (SW Iberia): Age, source, and implications for the Paleozoic evolution of Gondwanan lithosphere', *Lithosphere* **7**(1), 73–90.

URL: *http://lithosphere.gsapubs.org/content/early/2014/12/11/L379.1.abstract http://pubs.geoscienceworld.org/lithosphere/article/7/1/73/145736/Peralkaline-and-alkaline-magmatism-of-the*

Dingwell, D., Pichavant, M. and HoltzF. (1996), Experimental studies of boron in granitic melts, *in* E. Grew and L. Anovitz, eds, 'Boron: Mineralogy, Petrology and Geochemistry', 33 edn, Reviews in Mineralogy and Geochemistry, Mineralogical Society of America, pp. 331–385.

DonkeyStock (2017), 'Tin Market'.

Donovan, J. J., Lowers, H. A. and Rusk, B. G. (2011), 'Improved electron probe microanalysis of trace elements in quartz', *American Mineralogist* **96**(2-3), 274–282.

D'Orey, F. (1967), 'Tungsten-tin mineralization and paragenesis in the Panasqueira and Vale da Ermida mining districts, Portugal', *Comunicações Geológicas* **52**, 117–167.

Driesner, T. (n.d.), ‘The system H2O-NaCl. Part II: Correlations for molar volume, enthalpy, and isobaric heat capacity from 0 to 1000°c, 1 to 5000 bar, and 0 to 1 xnacl’, *Geochimica et Cosmochimica Acta* **71**(20), 4902–4919.

Driesner, T. and Heinrich, C. A. (2007), ‘The system H2O-NaCl. Part I: Correlation formulae for phase relations in temperature-pressure-composition space from 0 to 1000 , 0 to 5000 bar, and 0 to 1 XNaCl’, *Geochimica et Cosmochimica Acta* **71**(20), 4880–4901.

Drivenes, K., Larsen, R. B., Müller, A., Sørensen, B. E., Wiedenbeck, M. and Raanes, M. P. (2015), ‘Late-magmatic immiscibility during batholith formation: assessment of B isotopes and trace elements in tourmaline from the Land’s End granite, SW England’, *Contributions to Mineralogy and Petrology* **169**(6), 1–27.

Duchoslav, M., Marks, M. A. W., Drost, K., McCammon, C., Marschall, H. R., Wenzel, T. and Markl, G. (2017), ‘Changes in tourmaline composition during magmatic and hydrothermal processes leading to tin-ore deposition: The Cornubian Batholith, SW England’, *Ore Geology Reviews* **83**, 215–234.
URL: *http://dx.doi.org/10.1016/j.oregeorev.2016.11.012*

Dulski, P. (2001), ‘Reference materials for geochemical studies: New analytical data by ICP-MS and critical discussion of reference values’, *Geostandards Newsletter* **25**(1), 87–125.

Dutrow, B. L. and Henry, D. J. (2011), ‘Tourmaline: A geologic DVD’, *Elements* **7**(5), 301–306.

Dyar, M. D., Wiedenbeck, M., Robertson, D., Cross, L. R., Delaney, J. S., Ferguson, K., Francis, C. A., Grew, E. S., Guidotti, C. V., Hervig, R. L., Hughes, J. M., Husler, J., Leeman, W., McGuire, A. V., Rhede, D., Rothe, H., Paul, R. L., Richards, I. and Yates, M. (2001), ‘Reference Minerals for the Microanalysis of Light Elements’, *Geostandards Newsletter* **25**(2-3), 441–463.
URL: *http://dx.doi.org/10.1111/j.1751-908X.2001.tb00616.x*

Eilu, P. and Groves, D. I. (2001), ‘Primary alteration and geochemical dispersion haloes of Archaean orogenic gold deposits in the Yilgarn Craton: the pre-weathering scenario’, *Geochemistry: Exploration, Environment, Analysis* **1**(3), 183–200.
URL: *http://geea.lyellcollection.org/lookup/doi/10.1144/geochem.1.3.183*

Emmanuel, S. and Berkowitz, B. (2006), ‘An experimental analogue for convection and phase separation in hydrothermal systems’, *Journal of Geophysical Research: Solid Earth* **111**(9), 1–12.

European Commission (2013), Tacking the challenges in commodity markets and on raw materials [COM(2011) 25 final], Technical report, European Commission.
URL: *https://publications.europa.eu/en/publication-detail/-/publication/e5b19725-e943-4c1c-8218-a0a415a8624f/language-en/format-PDF*

European Commission (2014), Report on critical raw materials for the EU, Report of the Ad hoc Working Group on defining critical raw materials, Technical Report May, European Commission.
URL: *http://ec.europa.eu/enterprise/policies/raw-materials/files/docs/crm-report-on-critical-raw-materials_en.pdf*

European Commission (2017), Study on the review of the list of critical raw materials. Non-critical raw materials factsheets., Technical Report June, European Commission.
URL: *https://publications.europa.eu/en/publication-detail/-/publication/7345e3e8-98fc-11e7-b92d-01aa75ed71a1/language-en*

Fekete, S., Weis, P., Driesner, T., Bouvier, A. S., Baumgartner, L. and Heinrich, C. A. (2016), ‘Contrasting hydrological processes of meteoric water incursion during magmatic–hydrothermal ore deposition: An oxygen isotope study by ion microprobe’, *Earth and Planetary Science Letters* **451**, 263–271.
URL: *http://dx.doi.org/10.1016/j.epsl.2016.07.009*

Fekete, S., Weis, P., Scott, S. and Driesner, T. (2018), ‘Multiple stable isotope fronts during non-isothermal fluid flow’, *Geochimica et Cosmochimica Acta* **223**, 537–557.
URL: *https://doi.org/10.1016/j.gca.2017.12.009*

Ferreira, N. M. R., Regêncio Macedo, C. A. and Bernardo de Sousa, M. (1987), Cronostratigrafia dos granitos da região de Moimenta da Beira-Tabuaço-Penedono, *in* 'Memórias / Museu e Laboratório Mineralógico e Geológico', Instituto Geológico e Mineiro, pp. 287–302.

Fonseca, N. d. C. (1943), 'Notas sobre o jazigo de volfrâmio da panasqueira', *Boletim da Sociedade Geológica de Portugal* **III**(I-II), 103–108.

Förster, H.-J., Tischendorf, G., Trumbull, R. B., Gottesmann, B., Forster, H.-J., Tischendorf, G., Trumbull, R. B. and Gottesmann, B. (1999), 'Late-Collisional Granites in the Variscan Erzgebirge, Germany', *Journal of Petrology* **40**(11), 1613–1645.
URL: *https://academic.oup.com/petrology/article/40/11/1613/1475500*

Fortey, R. A. and Cocks, L. M. (2003), 'Palaeontological evidence bearing on global Ordovician–Silurian continental reconstructions', *Earth-Science Reviews* **61**(3-4), 245–307.
URL: *http://linkinghub.elsevier.com/retrieve/pii/S0012825202001150*

Foxford, K. A., Nicholson, R. and Polya, D. A. (1991), 'Textural Evolution of W-Cu-Sn-bearing Hydrothermal Veins at Minas da Panasqueira, Portugal', *Mineralogical Magazine* **55**(380), 435–445.
URL: *http://www.minersoc.org/pages/Archive-MM/Volume_55/55-380-435.pdf*

Foxford, K. A., Nicholson, R., Polya, D. A. and Hebblethwaite, R. P. B. (2000), 'Extensional failure and hydraulic valving at Minas da Panasqueira, Portugal: Evidence from vein spatial distributions, displacements and geometries', *Journal of Structural Geology* **22**(8), 1065–1086.

Gaillard, N., Williams-Jones, A. E., Clark, J. R., Lypaczewski, P., Salvi, S., Perrouty, S., Piette-Lauzière, N., Guilmette, C. and Linnen, R. L. (2018), 'Mica composition as a vector to gold mineralization: Deciphering hydrothermal and metamorphic effects in the Malartic district, Quebec', *Ore Geology Reviews* **95**(January), 789–820.
URL: *https://doi.org/10.1016/j.oregeorev.2018.02.009*

Geiger, S., Driesner, T., Heinrich, C. A. and Matthäi, S. K. (2006*a*), 'Multiphase thermohaline convection in the earth's crust: I. A new finite element - Finite volume solution technique combined with a new equation of state for NaCl-H2O', *Transport in Porous Media* **63**(3), 399–434.

Geiger, S., Driesner, T., Heinrich, C. A. and Matthäi, S. K. (2006*b*), 'Multiphase thermohaline convection in the earth's crust: II. Benchmarking and application of a finite element - Finite volume solution technique with a NaCl-H2O equation of state', *Transport in Porous Media* **63**(3), 435–461.

Gilbert, N. (2009), 'Environment: The disappearing nutrient.', *Nature* **461**(7265), 716–718.
URL: *http://www.nature.com/doifinder/10.1038/461716a*

Gomes, G. L. (2016), Spatial simulation of the W-Sn ore grades of São Pedro das Águias skarn mineral deposit (Tabuaço , northern Portugal, Unpublished MSc Thesis, Universidade Nova de Lisboa.

Gonçalves, A., Lima, L., Ramos, V. and Noronha, F. (2018a), Santa Helena breccia pipe a new type of W deposit in Iberian W-Sn Metallogenic province (Borralha, N Portugal), *in* 'EGU General Assembly 2018', Vol. 20, EGU, p. 16190.

Gonçalves, M. A., Mateus, A., Pinto, F. and Vieira, R. (2018b), 'Using multifractal modelling, singularity mapping, and geochemical indexes for targeting buried mineralization: Application to the W-Sn Panasqueira ore-system, Portugal', *Journal of Geochemical Exploration* **189**, 42–53.
URL: *http://linkinghub.elsevier.com/retrieve/pii/S037567421730506X*

Graedel, T., Gunn, G. and Tercero Espinoza, L. (2013), Metal resources, use and Criticality, *in* 'Critical Metals Handbook', John Wiley & Sons, Oxford, pp. 1–19.
URL: *http://doi.wiley.com/10.1002/9781118755341.ch1*

Green, T. H. and Adam, J. (2003), 'Experimentally-determined trace element characteristics of aqueous fluid from partially dehydrated mafic oceanic crust at 3.0 GPa, 650-700°c', *European Journal of Mineralogy* **15**(5), 815–830.

Gruen, G., Weis, P., Driesner, T., De Ronde, C. E. and Heinrich, C. A. (2012), 'Fluid-flow patterns at brothers volcano, Southern Kermadec Arc: Insights from geologically constrained numerical simulations', *Economic Geology* **107**(8), 1595–1611.

Gruen, G., Weis, P., Driesner, T., Heinrich, C. A. and de Ronde, C. E. (2014), 'Hydrodynamic modeling of magmatic-hydrothermal activity at submarine arc volcanoes, with implications for ore formation', *Earth and Planetary Science Letters* **404**, 307–318.
URL: *http://dx.doi.org/10.1016/j.epsl.2014.07.041*

Guidotti, C. V. (1984), 'Micas in metamorphic rocks', *Reviews in Mineralogy and Geochemistry* **13**(1), 357–467.

Guillou-Frottier, L., Carre, C., Bourgine, B., Bouchot, V. and Genter, A. (2013), 'Structure of hydrothermal convection in the Upper Rhine Graben as inferred from corrected temperature data and basin-scale numerical models', *Journal of Volcanology and Geothermal Research* **256**, 29–49.

Guo, Z., Zhang, B., Guo, B., Dang, Y. and Hou, J. (2018), 'Zircon U-Pb and Wolframite Sm-Nd Dating of the Bayinsukhtu Tungsten Deposit in Southern Mongolia and its Geological Significance', *Resource Geology* **68**(4), 337–351.
URL: *http://doi.wiley.com/10.1111/rge.12173*

Gutiérrez-Alonso, G., Fernández-Suárez, J., Carlos Gutiérrez-Marco, J., Corfu, F., Murphy, J. B. and Suárez, M. (2007), U-Pb depositional age for the upper Barrios Formation (Armorican Quartzite facies) in the Cantabrian zone of Iberia: Implications for stratigraphic correlation and paleogeography, *in* U. Linnemann, R. D. Nance, P. Kraft and G. Zulauf, eds, 'The Evolution of the Rheic Ocean: From Avalonian-Cadomian Active Margin to Alleghenian-Variscan Collision', Geological Society of America.
URL: *http://dx.doi.org/10.1130/2007.2423(13)*

Harlaux, M. (2016), Tungsten and rare-metal (Nb, Ta, Sn) hydrothermal metallogenic systems in the late-Variscan orogenic context: example of the French Massif Central systems, Unpublished PhD Thesis, Université de Lorraine.

Harlaux, M., Marignac, C., Cuney, M., Mercadier, J., Magott, R. and Mouthier, B. (2015), 'Nb-Ti-Y-hree-W-U oxide minerals with uncommon compositions associated with the Tungsten Mineralization in the PUY-LES-vignes deposit (Massif Central, France): Evidence for rare-metal mobilization by late hydrothermal fluids with a peralkaline signature', *Canadian Mineralogist* **53**(4), 653–672.

Harlaux, M., Mercadier, J., Marignac, C., Peiffert, C., Cloquet, C. and Cuney, M. (2018), 'Tracing metal sources in peribatholitic hydrothermal W deposits based on the chemical composition of wolframite: The example of the Variscan French Massif Central', *Chemical Geology* **479**, 58–85.
URL: *http://linkinghub.elsevier.com/retrieve/pii/S0009254117307106*

Hart, C. J. R. (2007), Reduced Intrusion-related Gold Systems, *in* W. D. Goodfellow, ed., 'Mineral deposits of Canada: a synthesis of major deposit-types, district metallogeny, the evolution of geological provinces, and exploration method', number 5, Geological Association of Canada, Mineral Deposits Division, Special Publication, pp. 95–112.

Hawthorne, F. C. and Henry, D. J. (1999), 'Classification of the minerals of the tourmaline group', *European Journal of Mineralogy* **11**, 201–215.

Hazarika, P., Mishra, B. and Pruseth, K. L. (2015), 'Diverse tourmaline compositions from orogenic gold deposits in the Hutti-Maski greenstone belt, India: Implications for sources of ore-forming fluids', *Economic Geology* **110**(2), 337–353.

Hedenquist, J. W. and Lowenstern, J. B. (1994), 'The role of magmas in the formation of hydrothermal ore deposits', *Nature* **370**, 519.
URL: *http://dx.doi.org/10.1038/370519a0 http://10.0.4.14/370519a0*

Heinrich, C. A. (1990), 'The chemistry of hydrothermal tin(-tungsten) ore deposition', *Economic Geology* **85**(3), 457–481.
URL: *http://pubs.geoscienceworld.org/economicgeology/article/85/3/457/20750/The-chemistry-of-hydrothermal-tintungsten-ore*

Heinrich, C. and Candela, P. (2014), Fluids and Ore Formation in the Earth's Crust, *in* H. D. Holland and K. K. Turekian, eds, 'Treatise on Geochemistry', 2 edn, Vol. 13,

Elsevier, Oxford, chapter 13, pp. 1–28.
URL: *http://dx.doi.org/10.1016/B978-0-08-095975-7.01101-3 https://linkinghub.elsevier.com/retrieve/pii/B9780080959757011013*

Henry, D. J. and Dutrow, B. L. (1996), 'Metamorphic tourmaline and its petrologic applications', *Reviews in Mineralogy and Geochemistry* **33**(1), 503–557.

Henry, D. J. and Dutrow, B. L. (2018), 'Tourmaline studies through time: Contributions to scientific advancements', *Journal of Geosciences (Czech Republic)* **63**(2), 77–98.

Henry, D. J. and Guidotti, C. V. (1985), 'Tourmaline as a petrogenetic indicator mineral: an example from the staurolite-grade metapelites of NW Maine.', *American Mineralogist* **70**(1-2), 1–15.

Henry, D. J., Kirkland, B. L. and Kirkland, D. W. (1999), 'Sector-zoned tourmaline from the cap rock of a salt dome', *European Journal of Mineralogy* pp. 263–280.

Henry, D. J., Novák, M., Hawthorne, F. C., Ertl, A., Dutrow, B. L., Uher, P. and Pezzotta, F. (2011), 'Nomenclature of the tourmaline-supergroup minerals', *American Mineralogist* **96**(5-6), 895–913.

Herrero, M. J., Martín-Pérez, A., Alonso-Zarza, A. M., Gil-Peña, I., Meléndez, A. and Martín-García, R. (2011), 'Petrography and geochemistry of the magnesites and dolostones of the Ediacaran Ibor Group (635 to 542 Ma), Western Spain: Evidences of their hydrothermal origin', *Sedimentary Geology* **240**(3-4), 71–84.
URL: *http://dx.doi.org/10.1016/j.sedgeo.2011.08.007*

Hervig, R. L., Moore, G. M., Williams, L. B., Peacock, S. M., Holloway, J. R. and Roggensack, K. (2002), 'Isotopic and elemental partitioning of boron between hydrous fluid and silicate melt', *American Mineralogist* **87**(5-6), 769–774.

Hess, F. (1933), Tungsten, *in* O. Kiessling, ed., 'Minerals yearbook 1932-33', US Department of Commerce, Washington: United States Government Printing Office, pp. 271–280.
URL: *http://digital.library.wisc.edu/1711.dl/EcoNatRes.MinYB193132*

Hobbs, B. E., Zhang, Y., Ord, A. and Zhao, C. (2000), 'Application of coupled deformation, fluid flow, thermal and chemical modelling to predictive mineral exploration', *Journal of Geochemical Exploration* **69-70**, 505–509.

Hosking, K. F. G. (1969), The nature of primary tin ores of the southwest of England, *in* 'A second technical conference on tin', Bangkok, pp. 1157–1243.

Huang, R. and Audétat, A. (2012), 'The titanium-in-quartz (TitaniQ) thermobarometer: A critical examination and re-calibration', *Geochimica et Cosmochimica Acta* **84**(May), 75–89.

Ingebritsen, S. E. and Appold, M. S. (2012), 'The Physical Hydrogeology of Ore Deposits', *Economic Geology* **107**(4), 559–584.
URL: *https://pubs.geoscienceworld.org/economicgeology/article/107/4/559-584/128372*

Ingebritsen, S. E., Geiger, S., Hurwitz, S. and Driesner, T. (2010), 'Numerical simuation of magmatic hydrothermal systems', *Reviews of Geophysics* **47**(2009), 1–33.

Ingebritsen, S. E. and Manning, C. E. (2011), 'Permeability of the Continental Crust: Dynamic Variations Inferred from Seismicity and Metamorphism', *Frontiers in Geofluids* pp. 193–205.

Ingebritsen, S., Sanford, W. and Neuzil, C. (2006), *Groundwater in Geologic Processes*, 2 edn, Cambridge University Press, Cambridge.

ITA (2018), 'ITA survey shows weaker tin use growth in 2018'.
URL: *https://www.internationaltin.org/ita-survey-weaker-tin-use-growth-2018/*

ITRI (2016), '2016 Report on Global Tin Resources & Reserves', p. 20.

Jackson, N. J., Willis-Richards, J., Manning, D. A. C. and Sams, M. S. (1989), 'Evolution of the Cornubian ore field, southwest England: part II. Mineral deposits and ore-forming processes', *Economic Geology* **84**(5), 1101–1133.

Jackson, P., Changkakoti, A., Krouse, H. R. and Gray, J. (2000), 'The origin of greisen fluid of the Foley's zone, Cleveland tin deposit, Tasmania, Australia', *Economic Geology*

95(1), 227–236.
URL: *https://pubs.geoscienceworld.org/economicgeology/article/95/1/227-236/21931*

Jacques, D., Vieira, R., Muchez, P. and Sintubin, M. (2018), 'Transpressional folding and associated cross-fold jointing controlling the geometry of post-orogenic vein-type W-Sn mineralization: examples from Minas da Panasqueira, Portugal', *Mineralium Deposita* **53**(2), 171–194.
URL: *http://link.springer.com/10.1007/s00126-017-0728-6*

Jaques, L. and Pascal, C. (2017), 'Full paleostress tensor reconstruction using quartz veins of Panasqueira Mine, central Portugal; part I: Paleopressure determination', *Journal of Structural Geology* **102**, 58–74.
URL: *http://dx.doi.org/10.1016/j.jsg.2017.07.006*

Jiang, S. Y., Yu, J. M. and Lu, J. J. (2004), 'Trace and rare-earth element geochemistry in tourmaline and cassiterite from the Yunlong tin deposit, Yunnan, China: Implication for migmatitic-hydrothermal fluid evolution and ore genesis', *Chemical Geology* **209**(3-4), 193–213.

Jochum, K. P., Weis, U., Schwager, B., Stoll, B., Wilson, S. A., Haug, G. H., Andreae, M. O. and Enzweiler, J. (2016), 'Reference Values Following ISO Guidelines for Frequently Requested Rock Reference Materials', *Geostandards and Geoanalytical Research* **40**(3), 333–350.
URL: *http://doi.wiley.com/10.1111/j.1751-908X.2015.00392.x*

Johan, Z., Strnad, L. and Johan, V. (2012), 'Evolution of the Cínovec (Zinnwald) Granite Cupola, Czech Republic: Composition of feldspars and micas, a clue to the Origin of W, Sn mineralization', *Canadian Mineralogist* **50**(4), 1131–1148.

Julivert, M., Fontbote, J., Ribeiro, A. and Conde, L. (1974), 'Mapa Tectonico de la Peninsula Iberica y Baleares, escala 1:1.000.000'.

Kaliwoda, M., Marschall, H. R., Marks, M. A. W., Ludwig, T., Altherr, R. and Markl, G. (2011), 'Boron and boron isotope systematics in the peralkaline Ilímaussaq intrusion

(South Greenland) and its granitic country rocks: A record of magmatic and hydrothermal processes', *Lithos* **125**(1-2), 51–64.
URL: *http://dx.doi.org/10.1016/j.lithos.2011.01.006*

Kalliomäki, H., Wagner, T., Fusswinkel, T. and Sakellaris, G. (2017), 'Major and trace element geochemistry of tourmalines from Archean orogenic gold deposits: Proxies for the origin of gold mineralizing fluids?', *Ore Geology Reviews* **91**(July), 906–927.
URL: *https://doi.org/10.1016/j.oregeorev.2017.08.014*

Kelly, W. C. and Rye, R. O. (1979), 'Geologic, fluid inclusion, and stable isotope studies of the tin-tungsten deposits of Panasqueira, Portugal', *Economic Geology* **74**(8), 1721–1822.

Kelly, W. C. and Wagner, G. (1977), 'Paleothermometry by combined application of fluid inclusion and fission track methods', *Neues Jahrbuch fur Mineralogie* **1**, 1–15.

Kesler, S. E. and Simon, A. C. (2015), *Mineral Resources, Economics and the Environment*, Cambridge University Press.
URL: *https://www.cambridge.org/core/product/identifier/9781139871426/type/book*

Klemme, S., Marschall, H. R., Jacob, D. E., Prowatke, S. and Ludwig, T. (2011), 'Trace-element partitioning and boron isotope fractionation between white mica and tourmaline', *Canadian Mineralogist* **49**(1), 165–176.

Knutson, C., Peacor, D. R. and Kelly, W. C. (1985), 'Luminescence, color and fission track zoning in apatite crystals of the Panasqueira tin-tungsten deposit, Beira-Baixa, Portugal.', *American Mineralogist* **70**(7-8), 829–837.

Korges, M., Weis, P., Lüders, V. and Laurent, O. (2018), 'Depressurization and boiling of a single magmatic fluid as a mechanism for tin-tungsten deposit formation', *Geology* **46**(1), 75–78.

Kowalski, P. M. and Wunder, B. (2018), Boron Isotope Fractionation Among Vapor–Liquids–Solids–Melts: Experiments and Atomistic Modeling, *in* H. R. Marschall and G. L. Foster, eds, 'Advances in Isotope Geochemistry - Boron Isotopes - The Fifth

Element', Springer, Cham, Cham, pp. 33–69.
URL: *http://link.springer.com/10.1007/978-3-319-64666-4_3*

Kowalski, P. M., Wunder, B. and Jahn, S. (2013), 'Ab initio prediction of equilibrium boron isotope fractionation between minerals and aqueous fluids at high P and T', *Geochimica et Cosmochimica Acta* **101**, 285–301.
URL: *http://dx.doi.org/10.1016/j.gca.2012.10.007*

Kroner, U., Hahn, T., Romer, R. L. and Linnemann, U. (2007), 'The Variscan orogeny in the Saxo-Thuringian zone; Heterogenous overprint of Cadomian/Paleozoic Peri-Gondwana crust', *Special Paper 423: The Evolution of the Rheic Ocean: From Avalonian-Cadomian Active Margin to Alleghenian-Variscan Collision* **423**, 153–172.
URL: *http://dx.doi.org/10.1130/2007.2423(06)*

Kroner, U. and Romer, R. L. (2013), 'Two plates - Many subduction zones: The Variscan orogeny reconsidered', *Gondwana Research* **24**(1), 298–329.
URL: *http://dx.doi.org/10.1016/j.gr.2013.03.001*

Kroner, U., Roscher, M. and Romer, R. L. (2015), 'Ancient plate kinematics derived from the deformation pattern of continental crust: Paleo- and Neo-Tethys opening coeval with prolonged Gondwana–Laurussia convergence', *Tectonophysics* **681**, 220–233.
URL: *http://dx.doi.org/10.1016/j.tecto.2016.03.034*

Landing, E. (2005), 'Early Paleozoic Avalon-Gondwana unity: an obituary - response to "Palaeontological evidence bearing on global Ordovician-Silurian continental reconstructions" by R.A. Fortey and L.R.M. Cocks', *Earth-Science Reviews* **69**(1-2), 169–175.
URL: *http://linkinghub.elsevier.com/retrieve/pii/S0012825204001072*

Large, R. R. and McGoldrick, P. J. (1998), 'Lithogeochemical halos and geochemical vectors to stratiform sediment hosted Zn–Pb–Ag deposits, 1. Lady Loretta Deposit, Queensland', *Journal of Geochemical Exploration* **63**(1), 37–56.
URL: *http://linkinghub.elsevier.com/retrieve/pii/S0375674298000132*

Lassner, E. and Schubert, W.-D. (2005), 'The history of tungsten'.
URL: *https://www.itia.info/history.html*

Launay, G., Sizaret, S., Guillou-Frottier, L., Gloaguen, E. and Pinto, F. (2018), 'Deciphering fluid flow at the magmatic-hydrothermal transition: A case study from the world-class Panasqueira W–Sn–(Cu) ore deposit (Portugal)', *Earth and Planetary Science Letters* **499**, 1–12.
URL: *https://linkinghub.elsevier.com/retrieve/pii/S0012821X18304187*

Lecumberri-Sanchez, P., Heinrich, C. A., Wälle, M., Codeço, M. S., Weis, P., Sośnicka, M. and Pinto, F. (2018), Chemical controls on the paragenetic evolution at Panasqueira, Portugal, *in* 'SEG 2018: Metals, Minerals and Society', SEG, Keystone, Colorado.

Lecumberri-Sanchez, P., Vieira, R., Heinrich, C. A., Pinto, F. and W lle, M. (2017), 'Fluid-rock interaction is decisive for the formation of tungsten deposits', *Geology* **45**(7), 579–582.
URL: *https://pubs.geoscienceworld.org/geology/article/45/7/579-582/207856*

Lefebvre, M. G., Romer, R. L., Glodny, J., Kroner, U. and Roscher, M. (2019), 'The Hämmerlein skarn-hosted polymetallic deposit and the Eibenstock granite associated greisen, western Erzgebirge, Germany: two phases of mineralization—two Sn sources', *Mineralium Deposita* **54**(1), 193–216.
URL: *http://link.springer.com/10.1007/s00126-018-0830-4*

Legros, H., Marignac, C., Mercadier, J., Cuney, M., Richard, A., Wang, R. C., Charles, N. and Lespinasse, M. Y. (2016), 'Detailed paragenesis and Li-mica compositions as recorders of the magmatic-hydrothermal evolution of the Maoping W-Sn deposit (Jiangxi, China)', *Lithos* **264**, 108–124.
URL: *http://dx.doi.org/10.1016/j.lithos.2016.08.022*

Legros, H., Marignac, C., Tabary, T., Mercadier, J., Richard, A., Cuney, M., Wang, R.-C., Charles, N. and Lespinasse, M.-Y. (2018), 'The ore-forming magmatic-hydrothermal system of the Piaotang W-Sn deposit (Jiangxi, China) as seen from Li-mica geochemistry', *American Mineralogist* **103**(1), 39–54.
URL: *http://pubs.geoscienceworld.org/ammin/msa/ammin/article/103/1/39/525791/The-oreforming-magmatichydrothermal-system-of-the*

Lehmann, B. (1987), 'Tin granites, geochemical heritage, magmatic differentiation', *Geologische Rundschau* **76**(1), 177–185.

Lehmann, B. (1990*a*), Model of tin ore formation, *in* 'Metallogeny of Tin', Springer-Verlag, Berlin/Heidelberg, pp. 146–177.
URL: *http://www.springerlink.com/index/10.1007/BFb0010928*

Lehmann, B. (1990*b*), Petrological framework, *in* 'Metallogeny of Tin', Springer-Verlag, Berlin/Heidelberg, pp. 19–44.
URL: *http://www.springerlink.com/index/10.1007/BFb0010924*

Lewis, K. C. and Lowell, R. P. (2009*a*), 'Numerical modeling of two-phase flow in the NaCl-H 2 O system: Introduction of a numerical method and benchmarking', *Journal of Geophysical Research* **114**(B5), B05202.
URL: *http://doi.wiley.com/10.1029/2008JB006029*

Lewis, K. C. and Lowell, R. P. (2009*b*), 'Numerical modeling of two-phase flow in the NaCl-H2O system: 2. Examples', *Journal of Geophysical Research: Solid Earth* **114**(8), 1–16.

Li, C.-y., Zhang, R.-q., Ding, X., Ling, M.-x., Fan, W.-m. and Sun, W.-d. (2016), 'Dating cassiterite using laser ablation ICP-MS', *Ore Geology Reviews* **72**, 313–322.
URL: *https://linkinghub.elsevier.com/retrieve/pii/S0169136815002061*

Li, J., Huang, X. L., He, P. L., Li, W. X., Yu, Y., li Chen, L. and li Chen, L. (2015), 'In situ analyses of micas in the Yashan granite, South China: Constraints on magmatic and hydrothermal evolutions of W and Ta-Nb bearing granites', *Ore Geology Reviews* **65**(P4), 793–810.
URL: *http://dx.doi.org/10.1016/j.oregeorev.2014.09.028*

Li, Y., Li, X. H., Selby, D. and Li, J. W. (2018), 'Pulsed magmatic fluid release for the formation of porphyry deposits: Tracing fluid evolution in absolute time from the Tibetan Qulong Cu-Mo deposit', *Geology* **46**(1), 7–10.

Lichtervelde, M., Grégoire, M., Linnen, R. L., Béziat, D. and Salvi, S. (2008), 'Trace element geochemistry by laser ablation ICP-MS of micas associated with Ta mineralization in the Tanco pegmatite, Manitoba, Canada', *Contributions to Mineralogy and Petrology* **155**(6), 791–806.

Linnen, R. L. (1998), 'Depth of emplacement, fluid provenance and metallogeny in granitic terranes: a comparison of western Thailand with other tin belts', *Mineralium Deposita* **33**(5), 461–476.
URL: *http://link.springer.com/10.1007/s001260050163*

Liu, X., Xing, H. and Zhang, D. (2014), 'Fluid focusing and its link to vertical morphological zonation at the Dajishan vein-type tungsten deposit, South China', *Ore Geology Reviews* **62**, 245–258.
URL: *http://dx.doi.org/10.1016/j.oregeorev.2014.04.005*

Liu, X., Xing, H. and Zhang, D. (2015), 'The mechanisms of the infill textures and its implications for the five-floor zonation at the Dajishan vein-type tungsten deposit, China', *Ore Geology Reviews* **65**, 365–374.
URL: *http://dx.doi.org/10.1016/j.oregeorev.2014.10.011*

Llorens González, T., García Polonio, F., López Moro, F. J., Fernández Fernández, A., Sanz Contreras, J. L. and Moro Benito, M. C. (2017), 'Tin-tantalum-niobium mineralization in the Penouta deposit (NW Spain): Textural features and mineral chemistry to unravel the genesis and evolution of cassiterite and columbite group minerals in a peraluminous system', *Ore Geology Reviews* **81**, 79–95.
URL: *http://dx.doi.org/10.1016/j.oregeorev.2016.10.034*

Llorens, T. and Moro, M. C. (2012*a*), 'Oxide minerals in the granitic cupola of the Jálama Batholith, Salamanca, Spain. Part I: Accessory Sn, Nb, Ta and Ti minerals in leucogranites, aplites and pegmatites', *Journal of Geosciences* **57**(1), 25–43.

Llorens, T. and Moro, M. C. (2012*b*), 'Oxide minerals in the granitic cupola of the Jálama Batholith, Salamanca, Spain. Part II: Sn, W and Ti minerals in intra-granitic quartz veins', *Journal of GEOsciences* **57**(3), 155–171.
URL: *http://www.jgeosci.org/detail/jgeosci.119*

London, D. and Manning, D. A. C. (1995), 'Chemical variation and significance of tourmaline from southwest England', *Economic Geology* **90**(3), 495–519.

López-Moro, F. J., García Polonio, F., Llorens González, T., Sanz Contreras, J. L., Fernández Fernández, A. and Moro Benito, M. C. (2017), 'Ta and Sn concentration by muscovite fractionation and degassing in a lens-like granite body: The case study of the Penouta rare-metal albite granite (NW Spain)', *Ore Geology Reviews* **82**, 10–30.

López-Plaza, M. and Martínez Catalán, J. R. (1987), Síntesis estructural de los granitoides hercínicos del Macizo Hespérico, *in* F. Bea, A. Carnicero, J. Gonzalo, M. López-Plaza and M. Rodríguez Alonso, eds, 'Geología de los granitoides and rocas asociadas del Macizo Hespérico', Rueda, Madrid, pp. 195–210.

López-Plaza, M., Peinado, M., López-Moro, F.-J., Rodríguez-Alonso, M. D., Carnicero, A., Franco, M. P., Gonzalo, J. C. and Navidad, M. (2007), Contrasting mantle sources and processes involved in a peri-Gondwanan terrane: A case study of pre-Variscan mafic intrusives from the autochthon of the Central Iberian Zone, *in* 'Special Paper 423: The Evolution of the Rheic Ocean: From Avalonian-Cadomian Active Margin to Alleghenian-Variscan Collision', Geological Society of America, pp. 297–313.
URL: *http://specialpapers.gsapubs.org/cgi/doi/10.1130/2007.2423(14)*

Lötze, F. (1945), 'Zur Gliederung der Varisziden der Iberischen Mesetas.', *Geotekt Forsch* **6**, 78–92.

Lourenço, A. (2002), Paleofluidos e mineralizações associadas às fases tardias da Orogenia Hercínica, Unpublished PhD Thesis, Universidade do Porto.

Lowell, J. D. and Guilbert, J. M. (1970), 'Lateral and vertical alteration-mineralization zoning in porphyry ore deposits', *Economic Geology* **65**(4), 373–408.
URL: *http://econgeol.geoscienceworld.org/cgi/doi/10.2113/gsecongeo.65.4.373 http://pubs.geoscienceworld.org/economicgeology/article/65/4/373/18036/Lateral-and-vertical-alterationmineralization*

Lüders, V. (1996), 'Contribution of infrared microscopy to fluid inclusion studies in some opaque minerals (wolframite, stibnite, bournonite): metallogenic implications', *Economic Geology* **91**(8), 1462–1468.

Mangas, J. and Arribas, A. (1988), 'Hydrothermal fluid evolution of the Sn-W mineralization in the Parrilla ore deposit (Caceres, Spain)', *Journal of the Geological Society* **145**(1), 147–155.
URL: *http://jgs.lyellcollection.org/cgi/doi/10.1144/gsjgs.145.1.0147*

Marignac, C. (1973), 'Analyse structurale de l'environnement du gisement à tungstène-étain de Panasqueira (Beira-Baixa, Portugal): implication génétiques', *Comptes Rendus Académie des Sciences de Paris* **277**, 269–272.
URL: *http://gallica.bnf.fr/ark:/12148/bpt6k3086n*

Marignac, C. (1982), 'Geologic, fluid inclusions, and stable isotope studies of the tin-tungsten deposits of Panasqueira, Portugal; discussion', *Economic Geology* **77**(5), 1263–1266.
URL: *https://pubs.geoscienceworld.org/economicgeology/article/77/5/1263-1266/19686*

Marignac, C. and Cuney, M. (1999), 'Ore deposits of the French Massif Central: Insight into the metallogenesis of the Variscan collision belt', *Mineralium Deposita* **34**(5-6), 472–504.

Marschall, H. R. (2018), Boron Isotopes in the Ocean Floor Realm and the Mantle, *in* H. Marschall and G. Foster, eds, 'Boron Isotopes: The Fifth Element', Springer International Publishing, Cham, pp. 189–215.
URL: *https://doi.org/10.1007/978-3-319-64666-4_8 http://link.springer.com/10.1007/978-3-319-64666-4_8*

Marschall, H. R. and Jiang, S. Y. (2011), 'Tourmaline isotopes: No element left behind', *Elements* **7**(5), 313–319.

Marten & Co (2016), Wolf Minerals Ltd. New strategic metal producer, Technical Report March, QuotedData, London.

Martínez Catalán, J. R. (2012), 'The Central Iberian arc, an orocline centered in the Iberian Massif and some implications for the Variscan belt', *International Journal of Earth Sciences* **101**(5), 1299–1314.
URL: *http://link.springer.com/10.1007/s00531-011-0715-6*

Martínez Catalán, J. R., Arenas, R., Abati, J., Martínez, S. S., García, F. D., Suárez, J. F., Cuadra, P. G., Castiñeiras, P., Barreiro, J. G., Montes, A. D., Clavijo, E. G., Pascual, F. J. R., Andonaegui, P., Jeffries, T. E., Alcock, J. E., Fernández, R. D. and Carmona, A. L. (2009), 'A rootless suture and the loss of the roots of a mountain chain: The Variscan belt of NW Iberia', *Comptes Rendus Geoscience* **341**(2-3), 114–126.
URL: *http://linkinghub.elsevier.com/retrieve/pii/S1631071308002691*

Martínez Catalán, J. R., Arenas, R., Díaz García, F., González Cuadra, P., Gómez-Barreiro, J., Abati, J., Castiñeiras, P., Fernández-Suárez, J., Martínez Sánchez, S. and Andonaegui, P. (2007), 'Space and time in the tectonic evolution of the northwestern Iberian Massif : Implications for the Variscan belt', *Geological Society of America* **Memoir 200**(21), 403–423.

Martínez Catalán, J. R., Fernández-Suárez, J., Jenner, G. A., Belousova, E. and Montes, A. (2004), 'Provenance constraints from detrital zircon U-Pb ages in the NW Iberian Massif: implications for Palaeozoic plate configuration and Variscan evolution', *Journal of the Geological Society* **161**(3), 463–476.
URL: *http://10.0.4.120/0016-764903-054*

Martínez Catalán, J. R., Rubio Pascual, F. J., Montes, a. D., Fernandez, R. D., Barreiro, J. G., Dias Da Silva, I., Clavijo, E. G., Ayarza, P. and Alcock, J. E. (2014), 'The late Variscan HT/LP metamorphic event in NW and Central Iberia: relationships to crustal thickening, extension, orocline development and crustal evolution', *Geological Society, London, Special Publications* **405**(1), 225–247.
URL: *http://sp.lyellcollection.org/cgi/doi/10.1144/SP405.1*

Martins, H. C. B., Ribeiro, M. A., Sant'Ovaia, H., Abreu, J. and Madinabeitia, S. G. (2014), 'SHRIMP and LA-ICPMS U – Pb zircon geochronology of post-tectonic granitoid intrusions in NW of Central Iberian Zone', *Comunicações Geológicas* **101**(Especial

I), 147–150.
URL: *http://www.lneg.pt/iedt/unidades/16/paginas/26/30/185*

Martins, H. C. B., Sant'Ovaia, H. and Noronha, F. (2013), 'Late-Variscan emplacement and genesis of the Vieira do Minho composite pluton, Central Iberian Zone: Constraints from U-Pb zircon geochronology, AMS data and Sr-Nd-O isotope geochemistry', *Lithos* **162-163**, 221–235.

Martins, I. (2017), Microanálise elementar de sulfuretos, sulfossais e carbonatos constituintes das associações polifásicas que preenchem os sistemas filonianos de W(-Sn) suporte da mina da Panasqueira (Portugal); reconhecimento de marcadores metalogenéticos, Unpublished MSc Thesis, Universidade de Lisboa.

Martins, I., Mateus, A., Figueiras, J., Rodrigues, P., Vieira, R. and Pinto, F. (2017), Paragenetic meaning of the Bi- and Ag-rich phases from the Panasqueira lode system (Portugal), *in* 'Goldschmidt Conference Abstracts 2017', Paris.

Mateus, A. and Noronha, F. (2010), 'Sistemas mineralizantes epigenéticos na Zona Centro-Ibérica; expressão da estruturação orogénica meso- a tardi-Varisca', *Ciências Geológicas: Ensino, Investigação e sua História. Geologia Aplicada* **II**, 46–61.

Mathieu, L. (2018), 'Quantifying Hydrothermal Alteration: A Review of Methods', *Geosciences* **8**(7), 245.
URL: *http://www.mdpi.com/2076-3263/8/7/245*

Matte, P. (1991), 'Accretionary history and crustal evolution of the Variscan belt in Western Europe', *Tectonophysics* **196**(3-4), 309–337.
URL: *http://linkinghub.elsevier.com/retrieve/pii/004019519190328P*

Matthäi, S. K. and Belayneh, M. (2004), 'Fluid flow partitioning between fractures and a permeable rock matrix', *Geophysical Research Letters* **31**(7), 1–5.

Matthäi, S. K., Geiger, S., Roberts, S. G., Paluszny, A., Belayneh, M., Burri, A., Mezentsev, A., Lu, H., Coumou, D., Driesner, T. and Heinrich, C. A. (2007), 'Numerical simulation of multi-phase fluid flow in structurally complex reservoirs', *Geological Society, London, Special Publications* **292**(1), 405–429.

McGuire, A. V., Francis, C. A. and Dyar, M. D. (1992), ‘Mineral standards for electron microprobe analysis of oxygen’.

Medaris, L. G., Fournelle, J. H. and Henry, D. J. (2003), ‘Tourmaline-bearing quartz veins in the Baraboo quartzite, Wisconsin: Occurrence and significance of foitite and ”oxy-foitite”’, *Canadian Mineralogist* **41**(3), 749–758.

Melzer, S. and Wunder, B. (2001), ‘K-Rb-Cs partitioning between phlogopite and fluid: Experiments and consequences for the LILE signatures of island arc basalts’, *Lithos* **59**(1-2), 69–90.

Menand, T., Raw, A. and Woods, A. W. (2003), ‘Thermal inertia and reversing buoyancy in flow in porous media’, *Geophysical Research Letters* **30**(6), 1–3.

Menold, C. A., Grove, M., Sievers, N. E., Manning, C. E., Yin, A., Young, E. D. and Ziegler, K. (2016), ‘Argon, oxygen, and boron isotopic evidence documenting $^{40}\mathrm{Ar}_E$ accumulation in phengite during water-rich high-pressure subduction metasomatism of continental crust’, *Earth and Planetary Science Letters* **446**, 56–67.
URL: *http://dx.doi.org/10.1016/j.epsl.2016.04.010*

Meyer, C., Wunder, B., Meixner, A., Romer, R. L. and Heinrich, W. (2008), ‘Boron-isotope fractionation between tourmaline and fluid: An experimental re-investigation’, *Contributions to Mineralogy and Petrology* **156**(2), 259–267.

Micklethwaite, S., Ford, A., Witt, W. and Sheldon, H. A. (2015), ‘The where and how of faults, fluids and permeability - insights from fault stepovers, scaling properties and gold mineralisation’, *Geofluids* **15**(1-2), 240–251.

Mignardi, S., Ferrini, V., Masi, U., Conde, L. and Sousa, B. (1995*a*), Significance of the arsenopyrite composition from hydrothermal wolframite deposits of Panasqueira and Vale das Gatas (Portugal), *in* ‘Comun. XIII Reunion de Geologia del Oeste Peninsular’, Salamanca, Spain, pp. 187–190.

Mignardi, S., Ferrini, V., Masi, U., Conde, L. and Sousa, B. (1995*b*), Sphalerite-stannite relationships in the wolframite hydrothermal deposits of Panasqueira and Vale das

Gatas (Portugal), *in* 'Comun. XIII Reunion de Geologia del Oeste Peninsular', Salamanca, Spain, pp. 198–202.

Mlynarczyk, M. S. J. and Williams-Jones, A. E. (2006), 'Zoned tourmaline associated with cassiterite: Implications for fluid evolution and tin mineralization in the San Rafael Sn-Cu deposit, southeastern Peru', *Canadian Mineralogist* **44**(2), 347–365.

Monnier, L., Lach, P., Salvi, S., Melleton, J., Bailly, L., Béziat, D., Monnier, Y. and Gouy, S. (2018), 'Quartz trace-element composition by LA-ICP-MS as proxy for granite differentiation, hydrothermal episodes, and related mineralization: The Beauvoir Granite (Echassières district), France', *Lithos* **320-321**, 355–377.
URL: *https://linkinghub.elsevier.com/retrieve/pii/S0024493718303451*

Montero, P., Talavera, C., Bea, F., Lodeiro, F. G. and Whitehouse, M. J. (2009), 'Zircon Geochronology of the Ollo de Sapo Formation and the Age of the Cambro-Ordovician Rifting in Iberia', *The Journal of Geology* **117**(2), 174–191.
URL: *http://www.journals.uchicago.edu/doi/10.1086/595017*

Moura, A. (2005), 'Fluids from the Neves Corvo massive sulphide ores, Iberian Pyrite Belt, Portugal', *Chemical Geology* **223**(1-3), 153–169.

Moura, A., Dória, A., Neiva, A. M. R., Leal Gomes, C. and Creaser, R. A. (2014), 'Metallogenesis at the carris W-Mo-Sn deposit (Gerês, Portugal): Constraints from fluid inclusions, mineral geochemistry, Re-Os and He-Ar isotopes', *Ore Geology Reviews* **56**(July 2015), 73–93.
URL: *http://dx.doi.org/10.1016/j.oregeorev.2013.08.001*

Murphy, J. B. and Nance, R. D. (2008), 'The pangea conundrum', *Geology* **36**(9), 703–706.

Nance, R. D., Gutiérrez-Alonso, G., Keppie, J. D., Linnemann, U., Murphy, J. B., Quesada, C., Strachan, R. A. and Woodcock, N. H. (2012), 'A brief history of the Rheic Ocean', *Geoscience Frontiers* **3**(2), 125–135.

Neiva, A. M. R. (1987*a*), Geochemistry of Greisenized Granites and Metasomatic Schist of Tungsten-Tin Deposits in Portugal, *in* 'Chemical Transport in Metasomatic Processes',

Springer Netherlands, Dordrecht, pp. 681–699.
URL: *http://www.springerlink.com/index/10.1007/978-94-009-4013-0_26*

Neiva, A. M. R. (1987*b*), 'Geochemistry of white micas from Portuguese tin and tungsten deposits', *Chemical Geology* **63**(3-4), 299–317.
URL: *http://linkinghub.elsevier.com/retrieve/pii/0009254187901689*

Neiva, A. M. R. (2008), 'Geochemistry of cassiterite and wolframite from tin and tungsten quartz veins in Portugal', *Ore Geology Reviews* **33**(3-4), 221–238.
URL: *http://linkinghub.elsevier.com/retrieve/pii/S0169136807000972*

Neiva, A. M. R. and Gomes, M. E. P. (2001), 'Diferentes tipos de granitos e seus processos petrogenéticos: Granitos Hercínicos Portugueses', *Memórias da Academia das Ciências de Lisboa* **39**, 53–95.

Neiva, A. M. R., Silva, M. M. V. G. and Gomes, M. E. P. (2007), 'Crystal chemistry of tourmaline from Variscan granites, associated tin-tungsten- and gold deposits, and associated metamorphic and metasomatic rocks from northern Portugal', *Neues Jahrbuch für Mineralogie - Abhandlungen* **184**(1), 45–76.
URL: *http://openurl.ingenta.com/content/xref?genre=article&issn=0077-7757&volume=184&issue=1&spage=45*

Neiva, A. M. R., Williams, I. S., Lima, S. M. and Teixeira, R. J. S. (2012), 'U-Pb and ^{39}Ar/^{40}Ar data constraining the ages of the source, emplacement and recrystallization/cooling events from late- to post-D 3 Variscan granites of the Gouveia area, central Portugal', *Lithos* **153**(November), 72–83.
URL: *http://dx.doi.org/10.1016/j.lithos.2012.02.012*

Neiva, A. M. R., Williams, I. S., Ramos, J. M. F., Gomes, M. E. P., Silva, M. M. V. G. and Antunes, I. M. H. R. (2009), 'Geochemical and isotopic constraints on the petrogenesis of Early Ordovician granodiorite and Variscan two-mica granites from the Gouveia area, central Portugal', *Lithos* **111**(3-4), 186–202.
URL: *http://dx.doi.org/10.1016/j.lithos.2009.01.005*

Neymark, L. A., Holm-Denoma, C. S. and Moscati, R. J. (2018), 'In situ LA-ICPMS U–Pb dating of cassiterite without a known-age matrix-matched reference material: Examples from worldwide tin deposits spanning the Proterozoic to the Tertiary', *Chemical Geology* **483**, 410–425.
URL: *https://linkinghub.elsevier.com/retrieve/pii/S0009254118301190*

Noronha, F. A., Ramos, J. M. F., Rebelo, J. A., Ribeiro, A. and Ribeiro, M. L. (1979), 'Essai de corrélation des phases de déformation hercynienne dans le Nord-Ouest péninsulaire.', *Boletim da Sociedade Geológica de Portugal* **21**(II-III), 227–237.

Noronha, F., Cathelineau, M., Boiron, M. C., Banks, D. A., Dória, A., Ribeiro, M. A., Nogueira, P. and Guedes, A. (2000), 'A three stage fluid flow model for Variscan gold metallogenesis in northern Portugal', *Journal of Geochemical Exploration* **71**(2), 209–224.

Noronha, F., Doria, A., Dubessy, J. and Charoy, B. (1992), 'Characterization and timing of the different types of fluids present in the barren and ore-veins of the W-Sn deposit of Panasqueira, Central Portugal', *Mineralium Deposita* **27**(1), 72–79.

Noronha, F. M. P. (1983), Estudo metalogénico da área tungstífera da Borralha, Unpublished PhD Thesis, Universidade do Porto.

Noronha, F., Ramos, J. M. F., Rebelo, J. A., Ribeiro, A. and Ribeiro, L. (1981), 'Essai de corrélation des phases de déformation hercyniennes dans le Nord-Ouest Péninsulaire', *Leidse Geologische Mededelingen* **52**(1), 87–91.
URL: *http://www.repository.naturalis.nl/record/505951*

Noronha, F., Ribeiro, M. A., Almeida, A., Dória, A., Guedes, A., Lima, A., Martins, H. C., Sant'Ovaia, H., Nogueira, P., Martins, T., Ramos, R. and Vieira, R. (2013), Jazigos Filonianos Hidrotermais e Aplitopegmatíticos Espacialmente Associados a Granitos (Norte de Portugal), *in* R. Dias, A. Araújo, P. Terrinha and J. Kullberg, eds, 'Geologia de Portugal. Geologia Pré-Mesozóica de Portugal, Vol. I q q', first edit edn, Escolar Editora, Lisbon, pp. 403–438.

Noronha, F., Vindel, E., López, J. A., Dória, A., García, E., Boiron, M. C. and Cathelineau, M. (1999), 'Fluids related to tungsten ore deposits in northern Portugal and Spanish Central System: a comparative study'.

Oen, I. S. (1958), 'The geology, petrology and ore deposits of the Viseu region, northern Portugal', *Comunicações dos Serviços Geológicos de Portugal* **41**, 199.

Oen, I. S. (1970), 'Granite intrusion, folding and metamorphism in Central Northern Portugal', *Boletin Geológico y Minero de España* **81**, 271–298.

Oliver, N. H. and Bons, P. D. (2001), 'Mechanisms of fluid flow and fluid-rock interaction in fossil metamorphic hydrothermal systems inferred from vein-wall rock patterns, geometry and microstructure', *Geofluids* **1**(2), 137–162.

Oosterom, M. G., Bussink, R. W. and Vriend, S. P. (1984), 'Lithogeochemical studies of aureoles around the panasqueira tin-tungsten deposit, portugal', *Mineralium Deposita* **19**(4), 283–288.

Orejana, D., Villaseca, C., Valverde-Vaquero, P., Belousova, E. A. and Armstrong, R. A. (2012), 'U-Pb geochronology and zircon composition of late Variscan S- and I-type granitoids from the Spanish Central System batholith', *International Journal of Earth Sciences* **101**(7), 1789–1815.

Palmer, M. R. and Swihart, G. H. (1996), Boron Isotope Geochemistry: An Overview, *in* L. M. Anovitz and E. S. Grew, eds, 'Boron: Mineralogy, Petrology and Geochemistry', Mineralogical Society of America, Reviews in Mineralogy 33, pp. 709 – 744.

Pastor-Galán, D., Groenewegen, T., Brouwer, D., Krijgsman, W. and Dekkers, M. J. (2015), 'One or two oroclines in the Variscan orogen of Iberia? Implications for Pangea amalgamation', *Geology* **43**(6), 527–530.
URL: *http://pubs.geoscienceworld.org/geology/article/43/6/527/131905/One-or-two-oroclines-in-the-Variscan-orogen-of*

Patterson, J. W., Driesner, T. and Matthai, S. K. (2018a), 'Self-Organizing Fluid Convection Patterns in an en Echelon Fault Array', *Geophysical Research Letters* **45**(10), 4799–

4808.
URL: *http://doi.wiley.com/10.1029/2018GL078271*

Patterson, J. W., Driesner, T., Matthai, S. and Tomlinson, R. (2018b), 'Heat and Fluid Transport Induced by Convective Fluid Circulation Within a Fracture or Fault', *Journal of Geophysical Research: Solid Earth* **123**(4), 2658–2673.

Pawlowsky-Glahn, V., Egozcue, J. J. and Tolosana-Delgado, R. (2015), *Modelling and Analysis of Compositional Data*, John Wiley & Sons, Ltd, Chichester, UK.
URL: *http://doi.wiley.com/10.1002/9781119003144*

Pereira, E., Ribeiro, A. and Meireles, C. (1993), 'Cisalhamentos hercínicos e controlo das mineralizações de Sn-W, Au e U na Zona Centro-Ibérica em Portugal', *Cad. Lab. Xeol. Laxe* **18**(1980), 89–119.

Pereira, M. F., Castro, A. and Fernández, C. (2015), 'The inception of a Paleotethyan magmatic arc in Iberia', *Geoscience Frontiers* **6**(2), 297–306.
URL: *http://dx.doi.org/10.1016/j.gsf.2014.02.006*

Pereira, M. F., Chichorro, M., Silva, J. B., Ordóñez-Casado, B., Lee, J. K. W. and Williams, I. S. (2012), 'Early carboniferous wrenching, exhumation of high-grade metamorphic rocks and basin instability in SW Iberia: Constraints derived from structural geology and U-Pb and 40Ar- 39Ar geochronology', *Tectonophysics* **558-559**, 28–44.
URL: *http://dx.doi.org/10.1016/j.tecto.2012.06.020*

Pereira, M. F., Díez Fernández, R., Gama, C., Hofmann, M., Gärtner, A. and Linnemann, U. (2017), 'S-type granite generation and emplacement during a regional switch from extensional to contractional deformation (Central Iberian Zone, Iberian autochthonous domain, Variscan Orogeny)', *International Journal of Earth Sciences* pp. 1–17.

Pesquera, A., Torres-Ruiz, J., García-Casco, A. and Gil-Crespo, P. P. (2013), 'Evaluating the controls on tourmaline formation in granitic systems: A case study on peraluminous granites from the Central Iberian Zone (CIZ), Western Spain', *Journal of Petrology* **54**(3), 609–634.

Pesquera, A., Torres-Ruiz, J., Gil-Crespo, P. P. and Jiang, S. Y. (2005), 'Petrographic, chemical and B-isotopic insights into the origin of Tourmaline-Rich rocks and boron recycling in the Martinamor Antiform (Central Iberian Zone, Salamanca, Spain)', *Journal of Petrology* **46**(5), 1013–1044.

Pesquera, A., Torres-Ruiz, J., Gil-Crespo, P. P., Velilla, N., Torres Ruiz, J., Gil Crespo, P. P. and Velilla, N. (1999), 'Chemistry and genetic implications of tourmaline and Li-F-Cs micas from the Valdeflores area (Caceres, Spain)', *American Mineralogist* **84**(1-2), 55–69.

Pinto, F. M. (2014), Estudo da distribuição do Estanho na Mina da Panasqueira, Unpublished MSc Thesis, Universidade do Porto.

Pinto, F., Vieira, R., Ferraz, P. and Noronha, F. (2014), 'Study of Sn spatial distribution on W-Sn(Cu) Panasqueira ore deposit', *Comunicações Geológicas* **101**, 829–832.

Pinto, F., Vieira, R. and Noronha, F. (2015), 'Different Cassiterite Generations at the Panasqueira Deposit (Portugal): Implications for the Metal Zonation Model', *13th SGA Biennial Meeting* **1**.

Pokrovski, G. S., Schott, J. and Sergeyev, A. S. (1995), 'Experimental determination of the stability constants of NaSO4— and NaB (OH)40 in hydrothermal solutions using a new high-temperature sodium-selective glass electrode — Implications for boron isotopic fractionation', *Chemical Geology* **124**(3-4), 253–265.

Polya, D. A. (1987), Chemical behaviour of tungsten in hydrothermal fluids and genesis of the Panasqueira W-Cu-Sn deposit, Portugal. Na experimental, theoretical and field study, Upublished PhD Thesis, University of Manchester.

Polya, D. A. (1988*a*), 'Compositional variation in wolframites from the Barroca Grande mine, Portugal: evidence for fault-controlled ore formation', *Mineral. Mag* **52**(September), 497–503.

URL: *http://www.minersoc.org/pages/Archive-MM/Volume_52/52-367-497.pdf*

Polya, D. A. (1988*b*), 'Efficiency of hydrothermal ore formation and the Panasqueira W–Cu(Ag)–Sn vein deposit', *Nature* **333**(6176), 838–841.
URL: *http://www.nature.com/doifinder/10.1038/333838a0*

Polya, D. A. (1989), 'Chemistry of the main-stage ore-forming fluids of the Panasqueira W- Cu(Ag)-Sn deposit, Portugal: implications for models of ore genesis', *Economic Geology* **84**(5), 1134–1152.

Polya, D., Foxford, K., Stuart, F., Boyce, A. and Fallick, A. (2000), 'Evolution and paragenetic context of low δD hydrothermal fluids from the Panasqueira W-Sn deposit, Portugal: new evidence from microthermometric, stable isotope, noble gas and halogen analyses of primary fluid inclusions', *Geochimica et Cosmochimica Acta* **64**(19), 3357–3371.
URL: *http://linkinghub.elsevier.com/retrieve/pii/S0016703700004592*

Pretorius, W., Weis, D., Williams, G., Hanano, D., Kieffer, B. and Scoates, J. (2006), 'Complete trace elemental characterisation of granitoid (USGS G-2, GSP-2) reference materials by high resolution inductively coupled plasma-mass spectrometry', *Geostandards and Geoanalytical Research* **30**(1), 39–54.
URL: *http://doi.wiley.com/10.1111/j.1751-908X.2006.tb00910.x*

Pribnow, D. and Schellschmidt, R. (2000), 'Thermal tracking of upper crustal fluid flow in the Rhine graben', *Geophysical Research Letters* **27**(13), 1957–1960.
URL: *http://doi.wiley.com/10.1029/2000GL008494*

Priem, H. N. A. and den Tex, E. (1984), 'Tracing crustal evolution in the NW Iberian Peninsula through the RbSr and UPb systematics of Palaeozoic granitoids: a review', *Physics of the Earth and Planetary Interiors* **35**(1-3), 121–130.

Quesada, C. (1991), 'Geological constraints on the Paleozoic tectonic evolution of tectonostratigraphic terranes in the Iberian Massif', *Tectonophysics* **185**(3-4), 225–245.
URL: *http://linkinghub.elsevier.com/retrieve/pii/004019519190446Y*

Quesada, C., Fonseca, P. E., Munha, J., Oliveira, J. T. and Ribeiro, A. (1994), 'The Beja-

Acebuches Ophiolite (southern Iberia Variscan fold belt): geological characterization and geodynamic significance'.

Ragnarsdóttir, K. V. (2008), 'Rare metals getting rarer', *Nature Geoscience* **1**(11), 720–721.

Ramos, V., Guedes, A., Noronha, F., Dolgopolova, A., Seltmann, R., Armstrong, R., Stanley, C., Simons, B., Andersen, J. and Rollinson, G. (2017), Sn mineralization in W skarns from 'Douro Scheelite Belt': the example of Tabuaço (Portugal), *in* 'XII Congreso Nacional y XI Ibérico de Geoquímica', Linares (Jaén), Spain, pp. 24–28.

Ribeiro, A. (1974), 'Contribuition à l'étude tectonique de Trás-os-Montes Oriental.', *Comunicações dos Serviços Geológicos de Portugal* **24**, 1–168.

Ribeiro, A. (1990), Introduction, *in* 'Pre-Mesozoic Geology of Iberia', Springer Berlin Heidelberg, Berlin, Heidelberg, pp. 143–144.
URL: *http://www.springerlink.com/index/10.1007/978-3-642-83980-1_13*

Ribeiro, A. and Pereira, E. (1982), 'Controles paleogeográficos, petrológicos e estruturais na génese dos jazigos portugueses de estanho e volfrâmio', *Geonovas* **1**(3), 23–31.

Ribeiro, A., Quesada, C. and Dallmeyer, R. D. (1990), Geodynamic Evolution of the Iberian Massif, *in* 'Pre-Mesozoic Geology of Iberia', Springer Berlin Heidelberg, Berlin, Heidelberg, pp. 399–409.
URL: *http://www.springerlink.com/index/10.1007/978-3-642-83980-1_28*

Ribeiro da Costa, I., Mourão, C., Récio, C., Guimarães, F., Antunes, I. M., Ramos, J. F., Barriga, F. J. A. S., Palmer, M. R. and Milton, J. A. (2014), 'Tourmaline occurrences within the Penamacor-Monsanto granitic pluton and host-rocks (Central Portugal): genetic implications of crystal-chemical and isotopic features', *Contributions to Mineralogy and Petrology* **167**(4), 1–23.

Ribeiro, R. F. (2017), Gravimetric Modelling and Geological Interpretation of Argemela-Panasqueira Area, Upublished MSc thesis, Universidade do Porto.

Rieder, M., Cavazzini, G., D'Yakonov, Y. S., Frank-Kamenetskii, V. A., Gottardi, G., Guggenheim, S., Koval, P. V., Müller, G., Neiva, A. M. R., Radoslovich, E. W., Robert, J.-L., Sassi, F. P., Takeda, H., Weiss, Z. and Wones, D. R. (1998), 'Nomenclature of the Micas', *Canadian Mineralogist* **36**(3), 905–912.

Robardet, M. (2003), 'The Armorica 'microplate': fact or fiction? Critical review of the concept and contradictory palaeobiogeographical data', *Palaeogeography, Palaeoclimatology, Palaeoecology* **195**(1-2), 125–148.
URL: *http://linkinghub.elsevier.com/retrieve/pii/S0031018203003055*

Robb, L. (2005), *Introduction to Ore-Forming Processes*, Wiley-Blackwell.
URL: *https://www.wiley.com/en-gi/Introduction+to+Ore+Forming+Processes-p-9780632063789*

Rockwell, T., Fonseca, J., Madden, C., Dawson, T., Owen, L. A., Vilanova, S. and Figueiredo, P. (2009), 'Palaeoseismology of the Vilariça Segment of the Manteigas-Bragança Fault in northeastern Portugal', *Geological Society, London, Special Publications* **316**(1), 237–258.
URL: *http://sp.lyellcollection.org/content/316/1/237.abstract*

Roda-Robles, E., Pesquera, A., Gil-Crespo, P. P. and Torres-Ruiz, J. (2011), 'Occurrence, paragenesis and compositional evolution of tourmaline from the Tormes Dome area, central Iberian Zone, Spain', *Canadian Mineralogist* **49**(1), 207–224.

Roda-Robles, E., Pesquera, A., Gil-Crespo, P. P., Torres-Ruiz, J. and De Parseval, P. (2006), 'Mineralogy and geochemistry of micas from the Pinilla de Fermoselle pegmatite (Zamora, Spain)', *European Journal of Mineralogy* **18**(3), 369–377.
URL: *http://www.ingentaselect.com/rpsv/cgi-bin/cgi?ini=xref&body=linker&reqdoi=10.1127/093*
1221/2006/0018-0369

Roda-Robles, E., Pesquera, A., Gil-Crespo, P. P., Vieira, R., Lima, A., Garate-Olave, I., Martins, T. and Torres-Ruiz, J. (2016), 'Geology and mineralogy of Li mineralization in the Central Iberian Zone (Spain and Portugal)', *Mineralogical Magazine* **80**(1), 103–126.
URL: *http://www.ingentaconnect.com/content/10.1180/minmag.2016.080.049*

Roda-Robles, E., Pesquera, A., Lima, A., Vieira, R. and Gil-Crespo, P. P. (2012), Origin and significance of phosphate minerals in the Central Iberian Zone (Spain and Portugal): implications for the behaviour of P during the Variscan magmatism, *in* 'European Mineralogical Conference', Vol. 1, p. 381.

Rodríguez-Alonso, M. D., Peinado, M., López-Plaza, M., Franco, P., Carnicero, A. and Gonzalo, J. C. (2004), 'Neoproterozoic-Cambrian synsedimentary magmatism in the Central Iberian Zone (Spain): Geology, petrology and geodynamic significance', *International Journal of Earth Sciences* **93**(5), 897–920.

Roedder, E. (1986), *Fluid inclusions*, 12 edn, Reviews in Mineralogy, Mineralogical Society of America.

Romão, J., Metodiev, D., Dias, R. and Ribeiro, A. (2013), Evolução geodinâmica dos sectores meridionais da Zona Centro-Ibérica, *in* R. Dias, A. Araújo, P. Terrinha and J. Kullberg, eds, 'Geologia de Portugal. Geologia Pré-Mesozóica de Portugal, Vol.1', Escolar Editora, Lisbon, pp. 205–257.

Romer, R. L. and Hahne, K. (2010), 'Life of the Rheic Ocean: Scrolling through the shale record', *Gondwana Research* **17**(2-3), 236–253.
URL: *http://dx.doi.org/10.1016/j.gr.2009.09.004*

Romer, R. L. and Kroner, U. (2015), 'Sediment and weathering control on the distribution of Paleozoic magmatic tin-tungsten mineralization', *Mineralium Deposita* **50**(3), 327–338.

Romer, R. L. and Kroner, U. (2016), 'Phanerozoic tin and tungsten mineralization-Tectonic controls on the distribution of enriched protoliths and heat sources for crustal melting', *Gondwana Research* **31**, 60–95.
URL: *http://dx.doi.org/10.1016/j.gr.2015.11.002*

Romer, R. L., Meixner, A. and Hahne, K. (2014), 'Lithium and boron isotopic composition of sedimentary rocks - The role of source history and depositional environment: A 250Ma record from the Cadomian orogeny to the Variscan orogeny', *Gondwana Research* **26**(3-4), 1093–1110.

Rubio-Ordóñez, A., Valverde-Vaquero, P., Corretgé, L. G., Cuesta-Fernández, A., Gallastegui, G., Fernández-González, M. and Gerdes, A. (2012), 'An Early Ordovician tonalitic–granodioritic belt along the Schistose-Greywacke Domain of the Central Iberian Zone (Iberian Massif, Variscan Belt)', *Geological Magazine* **149**(05), 927–939.
URL: *http://www.journals.cambridge.org/abstract_S0016756811001129*

Rubio Pascual, F. J., Arenas, R., Martínez Catalán, J. R., Rodríguez Fernández, L. R. and Wijbrans, J. R. (2013), 'Thickening and exhumation of the Variscan roots in the Iberian Central System: Tectonothermal processes and ^{40}Ar/^{39}Ar ages', *Tectonophysics* **587**, 207–221.
URL: *http://dx.doi.org/10.1016/j.tecto.2012.10.005*

Rudnick, R. L. and Gao, S. (2014), Composition of the Continental Crust, *in* 'Treatise on Geochemistry', 2 edn, Vol. 4, Elsevier, pp. 1–51.
URL: *http://dx.doi.org/10.1016/B978-0-08-095975-7.00301-6*

Sánchez-García, T., Bellido, F., Pereira, M. F., Chichorro, M., Quesada, C., Pin, C. and Silva, J. B. (2010), 'Rift-related volcanism predating the birth of the Rheic Ocean (Ossa-Morena zone, SW Iberia)', *Gondwana Research* **17**(2-3), 392–407.

Sanderson, D. J., Roberts, S., Gumiel, P. and Greenfield, C. (2008), 'Quantitative Analysis of Tin- and Tungsten-Bearing Sheeted Vein Systems', *Economic Geology* **103**(5), 1043–1056.
URL: *https://pubs.geoscienceworld.org/economicgeology/article/103/5/1043-1056/128006*

Sant'Ovaia, H., Martins, H. and Noronha, F. (2013), 'Oxidized and reduced Portuguese Variscan granites associated with W and Sn hydrothermal lode deposits: magnetic susceptibility results', *Comunicações Geológicas* **100**(1), 33–39.

Saraiva, M. (1971), 'A composição e distribuição das volframites no Jazigo das Minas da Panasqueira (Portugal Central).', *Inv. Mineira Sec. 41 Cong. Hispano-Luso-Americano de geologia Económica* **II**, 917–932.

Schardt, C. and Large, R. R. (2009), 'New insights into the genesis of volcanic-hosted massive sulfide deposits on the seafloor from numerical modeling studies', *Ore Geology Reviews* **35**(3-4), 333–351.
URL: *http://dx.doi.org/10.1016/j.oregeorev.2008.11.008*

Schardt, C., Yang, J. and Large, R. (2005), 'Numerical heat and fluid-flow modeling of the Panorama volcanic-hosted massive sulfide district, Western Australia', *Economic Geology* **100**(3), 547–566.

Schermerhorn, L. (1956), 'Igneous, metamorphic and ore geology of the Castro Daire-São Pedro do Sul-Sátão region (northern Portugal)', *Comunicações dos Serviços Geológicos de Portugal* **37**, 617.

Schmidt, C., Thomas, R. and Heinrich, W. (2005), 'Boron speciation in aqueous fluids at 22 to 600°C and 0.1 MPa to 2 GPa', *Geochimica et Cosmochimica Acta* **69**(2), 275–281.

Shaw, J., Johnston, S. T., Gutiérrez-Alonso, G. and Weil, A. B. (2012), 'Oroclines of the Variscan orogen of Iberia: Paleocurrent analysis and paleogeographic implications', *Earth and Planetary Science Letters* **329-330**, 60–70.
URL: *http://dx.doi.org/10.1016/j.epsl.2012.02.014*

Shedd, K. B. (2017), Tungsten, Technical report, U.S. Geological Survey, Mineral Commodity Summaries.
URL: *https://minerals.usgs.gov/minerals/pubs/commodity/tungsten/mcs-2017-tungs.pdf*

Simancas, J. F., Azor, A., Martínez-Poyatos, D., Tahiri, A., El Hadi, H., González-Lodeiro, F., Pérez-Estaún, A. and Carbonell, R. (2009), 'Tectonic relationships of Southwest Iberia with the allochthons of Northwest Iberia and the Moroccan Variscides', *Comptes Rendus - Geoscience* **341**(2-3), 103–113.

Simms, M. A. and Garven, G. (2004), 'Thermal convection in faulted extensional sedimentary basins: Theoretical results from finite-element modeling', *Geofluids* **4**(2), 109–130.

Sinclair, W. D. (1996), Vein-stockwork tin, tungsten, *in* O. Eckstrand, W. Sinclair and

T. R.I., eds, ‘Geology of Canadian Mineral Deposit Types’, Vol. 8, Geological Survey of Canada, pp. 409–420.

Slack, J. F. (1996), ‘Tourmaline associations with hydrothermal ore deposits’, *Reviews in Mineralogy and Geochemistry* **33**(1), 559–643.
URL: *http://dx.doi.org/*

Slack, J. F. and Trumbull, R. B. (2011), ‘Tourmaline as a recorder of ore-forming processes’, *Elements* **7**(5), 321–326.

Smith, M. P. and Yardley, B. W. D. (1996), ‘The boron isotopic composition of tourmaline as a guide to fluid processes in the southwestern England orefield: An ion microprobe study’, *Geochimica et Cosmochimica Acta* **60**(8), 1415–1427.

Snee, L. W., Sutter, J. F. and Kelly, W. C. (1988), ‘Thermochronology of economic mineral deposits: dating the stages of mineralization at Panasqueira, Portugal, by high-precision ^{40}Ar/^{39}Ar age spectrum techniques on muscovite’, *Economic Geology* **83**(2), 335–354.

Soltani Dehnavi, A., Lentz, D. R., McFarlane, C. R. and Walker, J. A. (2018), ‘Quantification of fluid-mobile elements in white mica by LA-ICP-MS: From chemical composition to a potential micro-chemical vectoring tool in VMS exploration’, *Journal of Geochemical Exploration* **188**, 290–307.
URL: *https://doi.org/10.1016/j.gexplo.2018.01.017*

Spruzeniece, L., Andersen, J., Rollinson, G., Simons, B., Noronha, F., Ramos, V. and Seltma (2018), A microstructural study of tungsten-(tin) skarns in Tabuaço, NE Portugal, *in* ‘Goldschmidt Conference Abstracts 2018’, Boston, USA.

Štemprok, M. (1980), ‘Tin and tungsten deposits of the west-central European Variscides’, *Proceedings of the Fifth Quadrennial IAGOD Symposium* **1**(January 1980), 495–512.

Štemprok, M. and Steltmann, R. (1994), The Metallogeny of the Erzgebirge (Krusne Hory), *in* R. Seltmann, H. Kämpf and P. Möller, eds, ‘Metallogeny of Collisional Orogens’, Czech Geol. Survey, Prague, pp. 61–69.

Stussi, J.-M. (1989), ‘Granitoid chemistry and associated mineralization in the French Variscan’, *Economic Geology* **84**(5), 1363–1381.
URL: *http://pubs.geoscienceworld.org/economicgeology/article/84/5/1363/20708/Granitoid-chemistry-and-associated-mineralization*

Sverdrup, H. and Robert, K. H. (2009), Towards a world of limits: The issue of human resource follies’, *in* ‘19th Annual VM Goldschmidt Conference’, Vol. 73, Geochimica et Cosmochimica Acta, pp. A1298–A1298.
URL: *http://lup.lub.lu.se/record/1461625*

Taylor, R. G. (1979), *Geology of Tin Deposits*, 1 edn, Elsevier Science.

Teixeira, R. J. S., Neiva, A. M. R., Silva, P. B., Gomes, M. E. P., Andersen, T. and Ramos, J. M. F. (2011), ‘Combined U-Pb geochronology and Lu-Hf isotope systematics by LAM-ICPMS of zircons from granites and metasedimentary rocks of Carrazeda de Ansiães and Sabugal areas, Portugal, to constrain granite sources’, *Lithos* **125**(1-2), 321–334.
URL: *http://dx.doi.org/10.1016/j.lithos.2011.02.015*

Thadeu, D. (1951*a*), ‘Geologia do Couto Mineiro da Panasqueira’, *Comunicações dos Serviços Geológicos de Portugal* **32**, 5–64.

Thadeu, D. (1951*b*), ‘Geologia e jazigos de chumbo e zinco da Beira Baixa’, *Boletim Sociedade Geológica de Portugal* **9**, 1–144.

Thadeu, D. (1979), ‘Le gisement stanno-wolframifère de Panasqueira (Portugal)’, *Chron. Rech. Min.* **450**, 35–42.

Thomas, J. B., Watson, E. B., Spear, F. S., Shemella, P. T., Nayak, S. K. and Lanzirotti, A. (2010), ‘TitaniQ under pressure: The effect of pressure and temperature on the solubility of Ti in quartz’, *Contributions to Mineralogy and Petrology* **160**(5), 743–759.

Thomas, J. B., Watson, E. B., Spear, F. S. and Wark, D. A. (2015), ‘TitaniQ recrystallized: experimental confirmation of the original Ti-in-quartz calibrations’, *Contributions to Mineralogy and Petrology* **169**(3).

Tindle, A. G. and Webb, P. C. (1990), 'Estimation of lithium contents in trioctahedral micas using microprobe data: application to micas from granitic rocks', *European Journal of Mineralogy* **2**(5), 595–610.
URL: *https://dx.doi.org/10.1127/ejm/2/5/0595*

Tischendorf, G., Gottesmann, B., Förster, H.-J., Trumbull, R. B., Forster, H.-J. and Trumbull, R. B. (1997), 'On Li-bearing Micas: Estimating Li from Electron Microprobe Analyses and an Improved Diagram for Graphical Representation', *Mineralogical Magazine* **61**(409), 809–834.

Tornos, F., Galindo, C., Crespo, J. L. and Espiro, B. F. (2008), 'Geochemistry and origin of calcic tungsten-bearing skarns, Los Santos, Central Iberian Zone, Spain', *Canadian Mineralogist* **46**(1), 87–109.

Tracy, R. T. (1987), 'High grade metamorphic reactions and partial melting in pelitic schist, West-central Massachusetts'.

Trumbull, R. B., Beurlen, H., Wiedenbeck, M. and Soares, D. R. (2013), 'The diversity of B-isotope variations in tourmaline from rare-element pegmatites in the Borborema Province of Brazil', *Chemical Geology* **352**, 47–62.
URL: *http://dx.doi.org/10.1016/j.chemgeo.2013.05.021*

Trumbull, R. B., Garda, G. M., Xavier, R. P., Cavalcanti, J. A. D. and Codeço, M. S. (2019), 'Tourmaline in the Passagem de Mariana gold deposit (Brazil) revisited: major-element, trace-element and B-isotope constraints on metallogenesis', *Mineralium Deposita* **54**(3), 395–414.
URL: *http://link.springer.com/10.1007/s00126-018-0819-z*

Trumbull, R. B. and Slack, J. F. (2018), Boron Isotopes in the Continental Crust: Granites, Pegmatites, Felsic Volcanic Rocks, and Related Ore Deposits, *in* H. R. Marschall and G. L. Foster, eds, 'Advances in Isotope Geochemistry - Boron Isotopes - The Fifth Element', Springer, Cham, Cham, pp. 249–272.
URL: *http://link.springer.com/10.1007/978-3-319-64666-4_10*

Ueki, K. and Iwamori, H. (2017), ‘Geochemical differentiation processes for arc magma of the Sengan volcanic cluster, Northeastern Japan, constrained from principal component analysis’, *Lithos* **290-291**, 60–75.
URL: *https://doi.org/10.1016/j.lithos.2017.08.001*

Ugidos, J. M., Sánchez-Santos, J. M., Barba, P. and Valladares, M. I. (2010), ‘Upper Neoproterozoic series in the Central Iberian, Cantabrian and West Asturian Leonese Zones (Spain): Geochemical data and statistical results as evidence for a shared homogenised source area’, *Precambrian Research* **178**(1-4), 51–58.

Uribe-Mogollon, C. and Maher, K. (2018), ‘White Mica Geochemistry of the Copper Cliff Porphyry Cu Deposit: Insights from a Vectoring Tool Applied to Exploration’, *Economic Geology* **113**(6), 1269–1295.
URL: *https://pubs.geoscienceworld.org/segweb/economicgeology/article/113/6/1269/565829/White-Mica-Geochemistry-of-the-Copper-Cliff*

US Geological Survey (2017), Mineral Commodity Summaries, Tin, Technical Report 703, USGS.

Vallance, J., Cathelineau, M., Marignac, C., Boiron, M.-c., Fourcade, S., Martineau, F. and Fabre, C. (2001), ‘Microfracturing and fluid mixing in granites: W–(Sn) ore deposition at Vaulry (NW French Massif Central)’, *Tectonophysics* **336**(1-4), 43–61.
URL: *http://linkinghub.elsevier.com/retrieve/pii/S0040195101000932*

Valle Aguado, B., Azevedo, M. R., Schaltegger, U., Martínez Catalán, J. R. and Nolan, J. (2005), ‘U-Pb zircon and monazite geochronology of Variscan magmatism related to syn-convergence extension in Central Northern Portugal’, *Lithos* **82**(1-2 SPEC. ISS.), 169–184.

van Hinsberg, V., Franz, G. and Wood, B. (2017), ‘Determining subduction-zone fluid composition using a tourmaline mineral probe’, *Geochemical Perspectives Letters* pp. 160–169.
URL: *http://www.geochemicalperspectivesletters.org/article1719*

van Hinsberg, V. J. (2011), ‘Preliminary experimental data on trace-element partitioning between tourmaline and silicate melt’, *Canadian Mineralogist* **49**(1), 153–163.

van Hinsberg, V. J., Henry, D. J. and Dutrow, B. L. (2011a), ‘Tourmaline as a petrologic forensic mineral: A unique recorder of its geologic past’, *Elements* **7**(5), 327–332.

van Hinsberg, V. J., Henry, D. J. and Marschall, H. R. (2011b), ‘Tourmaline: An ideal indicator of its host environment’, *Canadian Mineralogist* **49**(1), 1–16.

van Hinsberg, V. J., Migdisov, A. A. and Williams-Jones, A. E. (2010), ‘Reading the mineral record of fluid composition from element partitioning’, *Geology* **38**(9), 847–850.

Vieira, R., Roda-Robles, E., Pesquera, A. and Lima, A. (2011), ‘Chemical variation and significance of micas from the Fregeneda-Almendra pegmatitic field (Central-Iberian Zone, Spain and Portugal)’, *American Mineralogist* **96**(4), 637–645.

Villaseca, C., Castiñeiras, P. and Orejana, D. (2015), ‘Early Ordovician metabasites from the Spanish Central System: A remnant of intraplate HP rocks in the Central Iberian Zone’, *Gondwana Research* **27**(1), 392–409.
URL: *http://dx.doi.org/10.1016/j.gr.2013.10.007*

Villaseca, C., Merino, E., Oyarzun, R., Orejana, D., Pérez-Soba, C. and Chicharro, E. (2014), ‘Contrasting chemical and isotopic signatures from Neoproterozoic metasedimentary rocks in the Central Iberian Zone (Spain) of pre-Variscan Europe: Implications for terrane analysis and Early Ordovician magmatic belts’, *Precambrian Research* **245**, 131–145.

Villaseca, C., Merino Martínez, E., Orejana, D., Andersen, T. and Belousova, E. (2016), ‘Zircon Hf signatures from granitic orthogneisses of the Spanish Central System: Significance and sources of the Cambro-Ordovician magmatism in the Iberian Variscan Belt’, *Gondwana Research* **34**, 60–83.
URL: *http://dx.doi.org/10.1016/j.gr.2016.03.004*

Villaseca, C., Orejana, D. and Belousova, E. A. (2012), ‘Recycled metaigneous crustal sources for S- and I-type Variscan granitoids from the Spanish Central System batholith:

Constraints from Hf isotope zircon composition', *Lithos* **153**, 84–93.
URL: *http://dx.doi.org/10.1016/j.lithos.2012.03.024*

von Goerne, G., Franz, G. and Heinrich, W. (2001), 'Synthesis of tourmaline solid solutions in the system Na2O–MgO–Al2O3–SiO2–B2O3–H2O–HCl and the distribution of Na between tourmaline and fluid at 300 to 700°C and 200 MPa', *Contributions to Mineralogy and Petrology* **141**(2), 160–173.
URL: *http://link.springer.com/10.1007/s004100100243*

Weis, P. (2015), 'The dynamic interplay between saline fluid flow and rock permeability in magmatic-hydrothermal systems', *Geofluids* **15**(1-2), 350–371.
URL: *http://doi.wiley.com/10.1002/9781119166573.ch29 http://doi.wiley.com/10.1111/gfl.12100*

Weis, P., Driesner, T., Coumou, D. and Geiger, S. (2014), 'Hydrothermal, multiphase convection of H 2 O-NaCl fluids from ambient to magmatic temperatures: a new numerical scheme and benchmarks for code comparison', *Geofluids* **14**(3), 347–371.
URL: *http://doi.wiley.com/10.1111/gfl.12080*

Weis, P., Driesner, T. and Heinrich, C. A. (2012), 'Porphyry-Copper Ore Shells Form at Stable Pressure-Temperature Fronts Within Dynamic Fluid Plumes', *Science* **338**(6114), 1613–1616.
URL: *http://www.sciencemag.org/cgi/doi/10.1126/science.1225009*

Wernicke, B. P., England, P. C., Sonder, L. J. and Christiansen, R. L. (1987), 'Tectonomagmatic evolution of Cenozoic extension in the North American Cordillera', *Geological Society, London, Special Publications* **28**(1), 203–221.
URL: *http://sp.lyellcollection.org/lookup/doi/10.1144/GSL.SP.1987.028.01.15*

Wheeler, A. (2016), Technical Report on the Mineral Resources and Reserves of the Panasqueira Mine, Portugal, Technical Report February, Mining Consultant, Cornwall.

Wilkinson, J. J., Chang, Z., Cooke, D. R., Baker, M. J., Wilkinson, C. C., Inglis, S., Chen, H. and Bruce Gemmell, J. (2015), 'The chlorite proximitor: A new tool for detecting

porphyry ore deposits', *Journal of Geochemical Exploration* **152**, 10–26.
URL: *http://dx.doi.org/10.1016/j.gexplo.2015.01.005*

Wilkinson, J. J., Cooke, D. R., Baker, M. J., Chang, Z., Wilkinson, C. C., Chen, H., Fox, N., Hollings, P., White, N. C., Gemmell, J. B., Loader, M. A., Pacey, A., Sievwright, R. H., Hart, L. A. and Brugge, E. R. (2017), Porphyry indicator minerals and their mineral chemistry as vectoring and fertility tools, *in* M. B. McClenaghan and D. Layton-Matthews, eds, 'Exploration '17: Sixth Decennial International Conference on Mineral Exploration', Geological Survey of Canada, Toronto, pp. 67–77.

Wimmers, D. (1985), 'Silver minerals of Panasqueira, Portugal : a new occurrence of Te-bearing canfieldite', *Mineralogical Magazine* **49**(December), 745–748.

Wunder, B., Meixner, A., Romer, R. L., Wirth, R. and Heinrich, W. (2005), 'The geochemical cycle of boron: Constraints from boron isotope partitioning experiments between mica and fluid', *Lithos* **84**(3-4), 206–216.

Xie, L., Wang, R. C., Groat, L. A., Zhu, J. C., Huang, F. F. and Cempírek, J. (2015), 'A combined EMPA and LA-ICP-MS study of Li-bearing mica and Sn-Ti oxide minerals from the Qiguling topaz rhyolite (Qitianling District, China): The role of fluorine in origin of tin mineralization', *Ore Geology Reviews* **65**(P4), 779–792.
URL: *http://dx.doi.org/10.1016/j.oregeorev.2014.08.013*

Yapparova, A., Gabellone, T., Whitaker, F., Kulik, D. A. and Matthäi, S. K. (2017), 'Reactive transport modelling of hydrothermal dolomitisation using the CSMP++GEM coupled code: Effects of temperature and geological heterogeneity', *Chemical Geology* **466**, 562–574.
URL: *http://dx.doi.org/10.1016/j.chemgeo.2017.07.005*

Yavuz, F., Iskenderoğlu, A. and Jiang, S. Y. (1999), 'Tourmaline compositions from the Salikvan porphyry Cu-Mo deposit and vicinity, northeastern Turkey', *Canadian Mineralogist* **37**(4), 1007–1023.

Zhang, S., Ma, D., Lu, J., Zhang, R. and Gao, S. (2014), 'Chemical and Boron Isotopic

Composition of Tourmaline in Baotan Tin Deposit, Northern Guangxi, South China', *Acta Geologica Sinica* **88**, 485–486.

Zhang, Y., Robinson, J. and Schaubs, P. M. (2011), 'Numerical modelling of structural controls on fluid flow and mineralization', *Geoscience Frontiers* **2**(3), 449–461.
URL: *http://dx.doi.org/10.1016/j.gsf.2011.05.011*

Zhang, Y., Schaubs, P. M., Zhao, C., Ord, A., Hobbs, B. E. and Barnicoat, A. C. (2008), 'Fault-related dilation, permeability enhancement, fluid flow and mineral precipitation patterns: numerical models', *Geological Society, London, Special Publications* **299**(1), 239–255.
URL: *http://sp.lyellcollection.org/lookup/doi/10.1144/SP299.15*

Zheng, Z., Deng, X. H., Chen, H. J., Yue, S. W., Dong, L. H., Qu, X. and Chen, Y. J. (2016), 'Fluid sources and metallogenesis in the Baiganhu W-Sn deposit, East Kunlun, NW China: Insights from chemical and boron isotopic compositions of tourmaline', *Ore Geology Reviews* **72**, 1129–1142.
URL: *http://dx.doi.org/10.1016/j.oregeorev.2015.09.006*

Zhimin, Z. and Yali, S. (2013), 'Direct Re-Os Dating of chalcopyrite from the Lala IOCG deposit in the Kangdian Copper Belt, China', *Economic Geology* **108**(4), 871–882.
URL: *https://pubs.geoscienceworld.org/economicgeology/article/108/4/871-882/128547*

Zhu, C. and Sverjensky, D. A. (1991), 'Partitioning of F-Cl-OH between minerals and hydrothermal fluids', *Geochimica et Cosmochimica Acta* **55**(7), 1837–1858.

A

Sampling strategy

During the course of this study, two separate fieldwork and sampling campaigns were accomplished, in 2015 and 2016. In the first campaign (11th – 23rd October), we collected samples for petrographic and geochemical studies. The selection criteria for sample locations were based on the main objectives of the study: (1) constraining the tourmaline and mica variations within the vein and host-rock and its spatial variation in the deposit; (2) understanding tourmaline-mica relationship; (3) characterizing the variation of mica within the Panasqueira deposit, giving special attention to zones where mica selvages are absent; (4) characterizing ore stage paragenesis and its relation with tourmaline and micas and finally, (5) studying the behavior of tourmaline and mica near the faults. A total of seventy-three samples were collected in the mine, and ten samples were collected in selected drill-cores containing tourmaline. Figure A.1 shows the distribution of the samples collected in the mine; we attempted to obtain the best spatial coverage within current accessibilities at the mine. We also collected two additional samples about 5.5 and 10.5 km from the mine as reference material for the host-rocks A.2.

During the second campaign (10th – 14th October 2016), samples for new petrographic

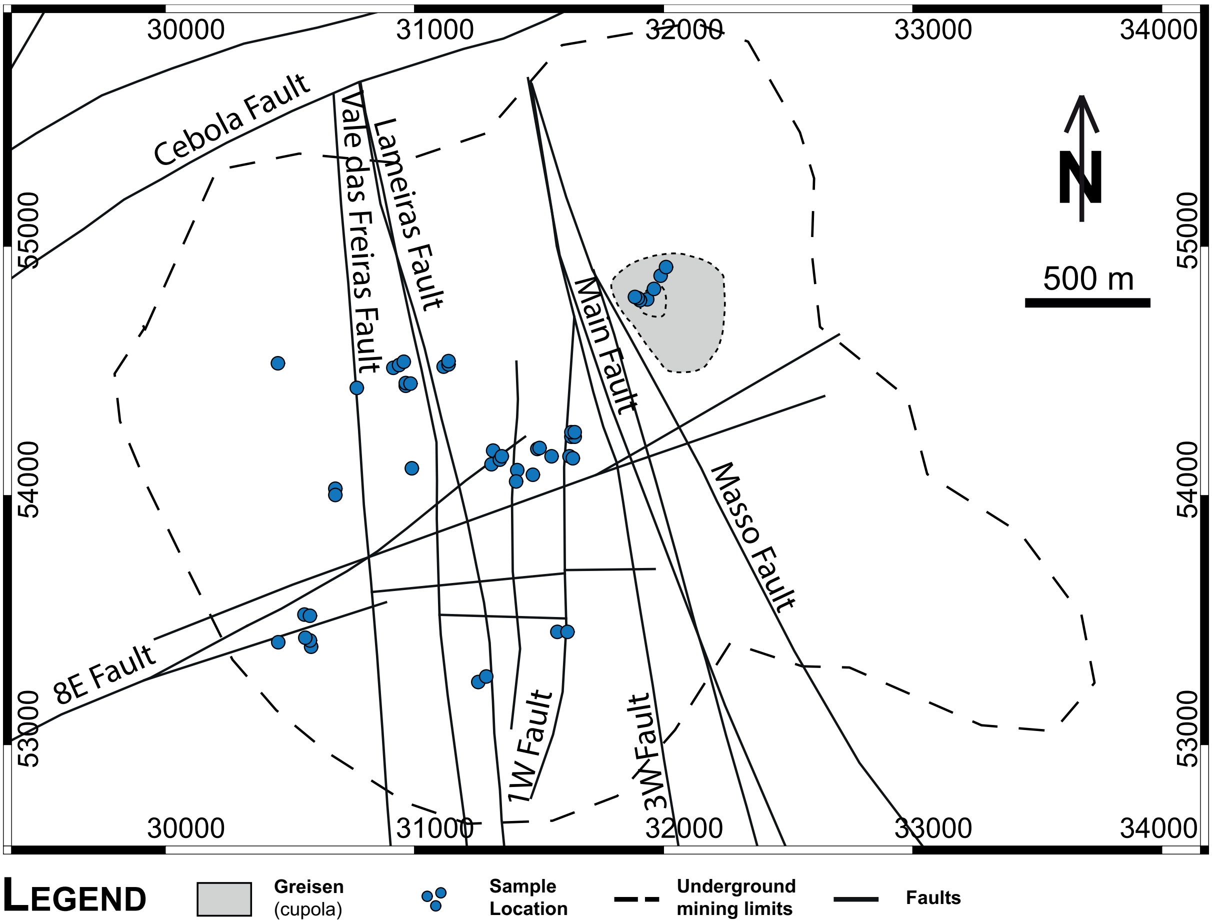

Figure A.1: Sampling map of the first campaign. Courtesy of Beralt Tin & Wolfram, SA.; coordinate system: ETRS89 / Portugal TM06 (EPSG:3763).

and geochemical studies (microprobe, whole rock geochemistry, and SIMS analysis) were collected. Selection criteria for the new samples included: (1) characterizing the variation of tourmaline farther from the mineralized veins, (2) understanding and characterizing the hydrothermal alteration farther from the mineralized veins and compare with unaltered specimens. A total of sixty-eight samples were collected in selected drill-cores. Figure A.3 shows the distribution of the samples collected in drill cores either performed at the mine and or in the surrounding area; we attempted to obtain the best spatial coverage considering the available drill-cores.

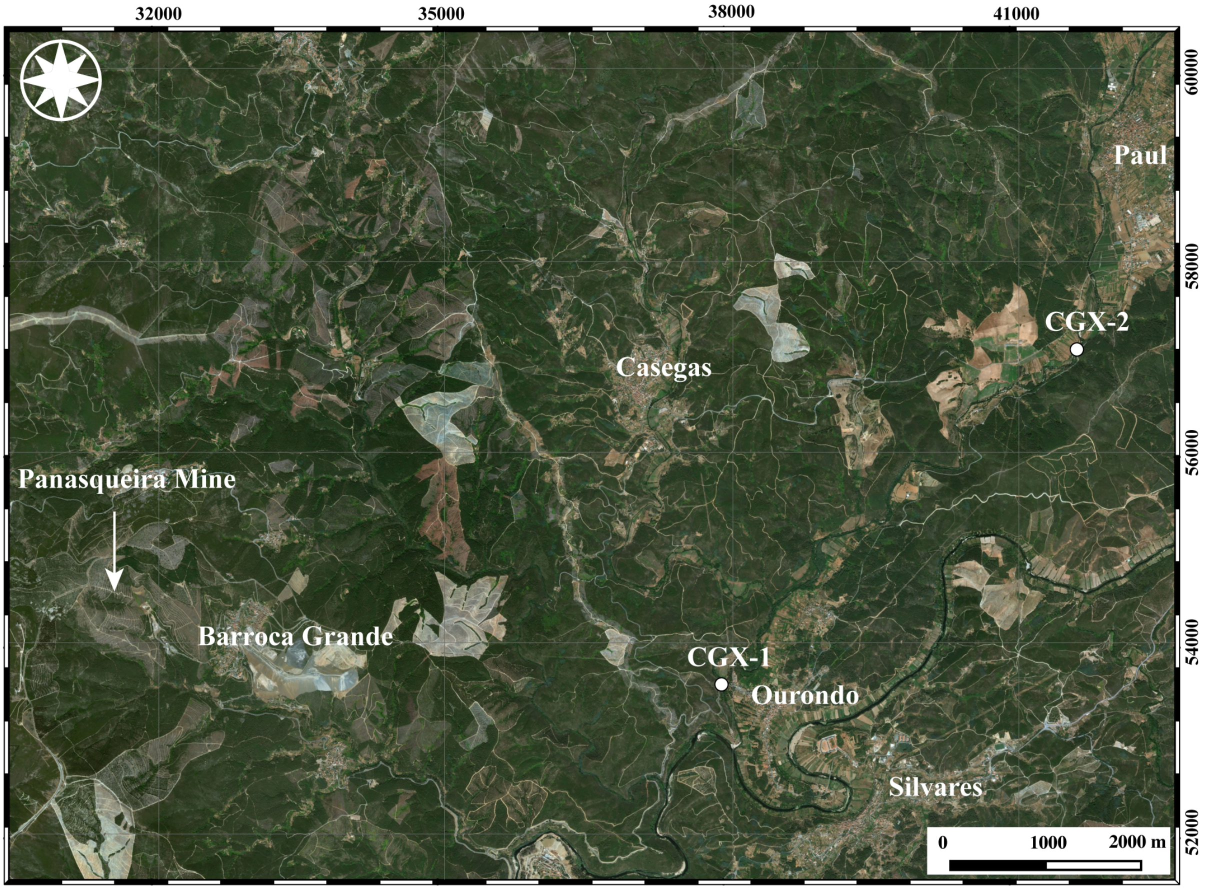

Figure A.2: Location of the samples collected from the two outcrops at ca. 5.5 and 10.5 km from the deposit. Adapted from ESRI; coordinate system: ETRS89 / Portugal TM06 (EPSG:3763)

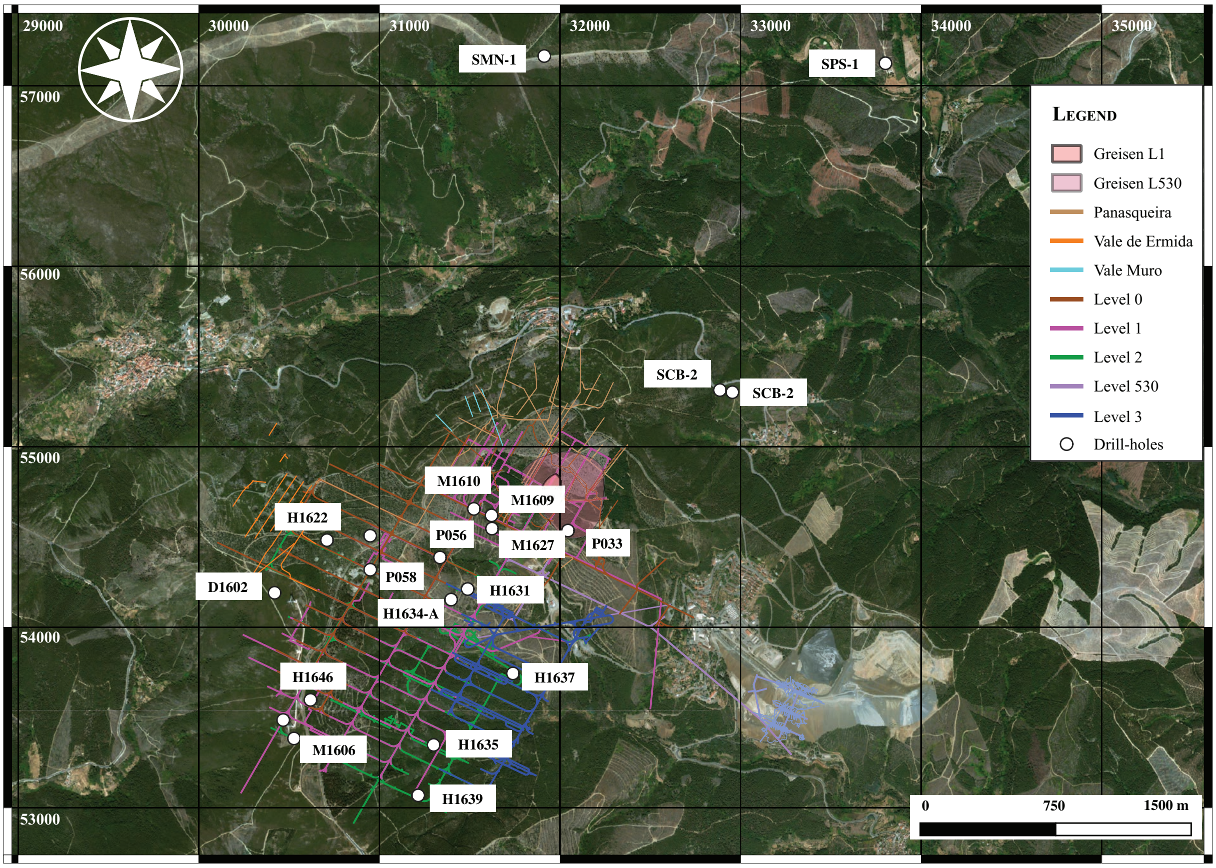

Figure A.3: Location of the drill-cores sampled during the second field campaign. Map: courtesy of Beralt Tin & Wolfram, SA.; coordinate system: ETRS89 / Portugal TM06 (EPSG:3763)

B

White mica normalization

Lithium may constitute an essential element in micas, in particular in trioctahedral micas, yet cannot be detected by microprobe analysis. The calculation of complete structural formulas requires the application of empirical regressions that yield calculated Li_2O^* contents as a function of F (or Rb_2O) (Lichtervelde et al., 2008; Pesquera et al., 1999; Roda-Robles et al., 2006; Tindle and Webb, 1990; Tischendorf et al., 1997). The application of such empirical regressions to the micas analyzed by microprobe in the present study proved to overestimate the Li contents. Thus, we re-measured the F contents of micas analyzed by LA-ICP-MS to compare both datasets. A good linear correlation can be found between F measured by microprobe and Li measured by laser ablation ICP-MS (Fig. B.1) that gives the relationship: $Li_2O* = 0.1721 \times F + 0.0168$ (R^2=0.8861). Therefore, this relationship was used for the calculation of structural formulae in white mica from the present study.

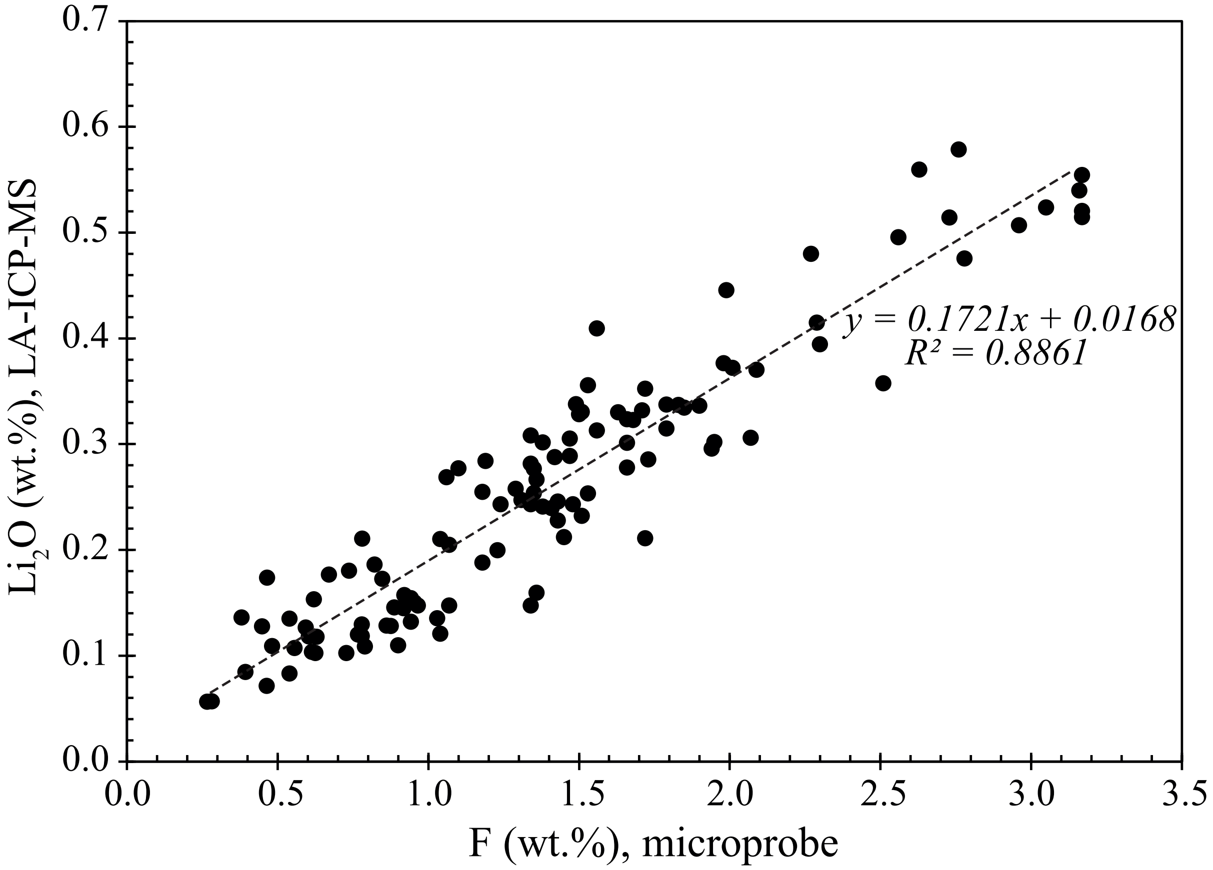

Figure B.1: Correlation between F and Li determined by microprobe and LA-ICP-MS, respectively

C

Supplement to Chapter 5

The tables and figures shown in this Appendix are supplementary to the Chapter 5. The complete dataset can be downloaded from the GFZ Data Services Website `http://doi.org/10.5880/GFZ.3.1.2019.001` and found in the CD enclosed with the printed version of this thesis.

Table C.1: Limits of detection (LOD) and precision of the LA-ICP-MS analyses of tourmaline

		^{7}Li	^{11}B	^{23}Na	^{24}Mg	^{29}Si	^{35}Cl	^{39}K	^{47}Ti	^{51}V	^{55}Mn	^{57}Fe	^{63}Cu	^{66}Zn
LOD (ppm)	Median	0.075	0.489	0.754	0.122	114.155	6.243	0.462	0.833	0.048	0.222	1.902	0.060	0.112
	Mean	0.116	2.086	2.826	2.071	135.454	7.895	1.273	1.418	0.082	0.269	5.915	0.079	0.191
	std	0.163	10.206	14.311	11.148	104.135	7.256	5.457	4.059	0.243	0.236	15.977	0.079	0.419
Precision (%)	Median	3.2	0.8	1.0	1.0	2.4	37.2	2.9	2.6	2.6	1.5	1.0	34.1	2.0
	Mean	4.4	1.1	1.2	1.3	2.5	56.4	4.5	3.7	3.1	2.2	1.2	50.3	2.5
	std	9.0	1.2	1.0	1.2	8.4	357.1	5.7	3.7	2.3	3.4	1.0	353.7	2.9
		^{85}Rb	^{86}Sr	^{89}Y	^{90}Zr	^{93}Nb	^{118}Sn	^{133}Cs	^{137}Ba	^{153}Eu	^{181}Ta	^{182}W	^{205}Tl	^{205}Pb
LOD (ppm)	Median	0.020	0.011	0.042	0.111	0.015	0.016	0.007	0.029	0.002	0.002	0.009	0.009	0.009
	Mean	0.057	0.047	0.145	0.346	0.018	0.028	0.012	0.096	0.008	0.005	0.021	0.011	0.014
	STD	0.201	0.184	0.283	0.615	0.015	0.065	0.019	0.133	0.016	0.011	0.081	0.010	0.024
Precision (%)	Median	21.0	2.7	26.7	12.9	31.4	5.9	29.5	21.7	30.0	29.8	21.5	24.5	7.5
	Mean	44.9	3.4	31.3	18.7	35.2	7.5	46.0	28.0	38.1	34.3	21.6	4.1	9.8
	STD	381.1	3.2	21.8	18.2	22.2	7.3	204.7	24.5	26.4	21.9	107.8	356.7	9.6

Table C.2: Limits of detection (LOD) and precision of the LA-ICP-MS analyses of white mica.

		^{7}Li	^{11}B	^{23}Na	^{24}Mg	^{29}Si	^{35}Cl	^{39}K	^{47}Ti	^{51}V	^{55}Mn	^{57}Fe	^{63}Cu	^{66}Zn
LOD (ppm)	Median	0.068	0.327	0.563	0.065	90.887	4.941	0.456	0.615	0.033	0.183	1.281	0.050	0.085
	Mean	0.087	0.755	0.798	0.432	114.052	6.423	0.894	0.860	0.045	0.203	2.202	0.089	0.113
	STD	0.085	1.506	0.810	1.386	101.215	5.300	2.786	0.780	0.037	0.136	3.876	0.150	0.101
Precision (%)	Median	1.0	4.2	0.7	1.1	1.0	27.6	0.5	2.3	3.6	1.1	0.9	17.0	2.3
	Mean	1.2	5.9	1.1	1.3	1.3	41.1	0.6	3.0	7.0	1.3	1.3	17.4	2.9
	STD	0.8	7.0	1.3	0.9	0.8	382.2	0.3	2.1	54.8	0.9	1.1	142.7	2.3

		^{85}Rb	^{86}Sr	^{89}Y	^{90}Zr	^{93}Nb	^{118}Sn	^{133}Cs	^{137}Ba	^{153}Eu	^{181}Ta	^{182}W	^{205}Tl	^{205}Pb
LOD (ppm)	Median	0.020	0.006	0.012	0.104	0.015	0.014	0.006	0.029	0.002	0.003	0.008	0.007	0.006
	Mean	0.040	0.014	0.021	0.087	0.015	0.021	0.008	0.047	0.003	0.003	0.010	0.009	0.008
	STD	0.089	0.016	0.020	0.046	0.005	0.025	0.007	0.050	0.003	0.001	0.009	0.006	0.011
Precision (%)	Median	0.7	3.1	13.2	22.0	4.6	1.0	1.0	1.5	19.4	5.5	1.5	1.6	3.4
	Mean	1.0	4.7	22.4	27.0	6.3	1.5	1.3	2.3	26.4	6.8	2.0	1.9	4.1
	STD	0.7	4.4	20.7	20.7	9.0	2.3	1.2	2.2	20.5	9.0	1.9	1.3	2.4

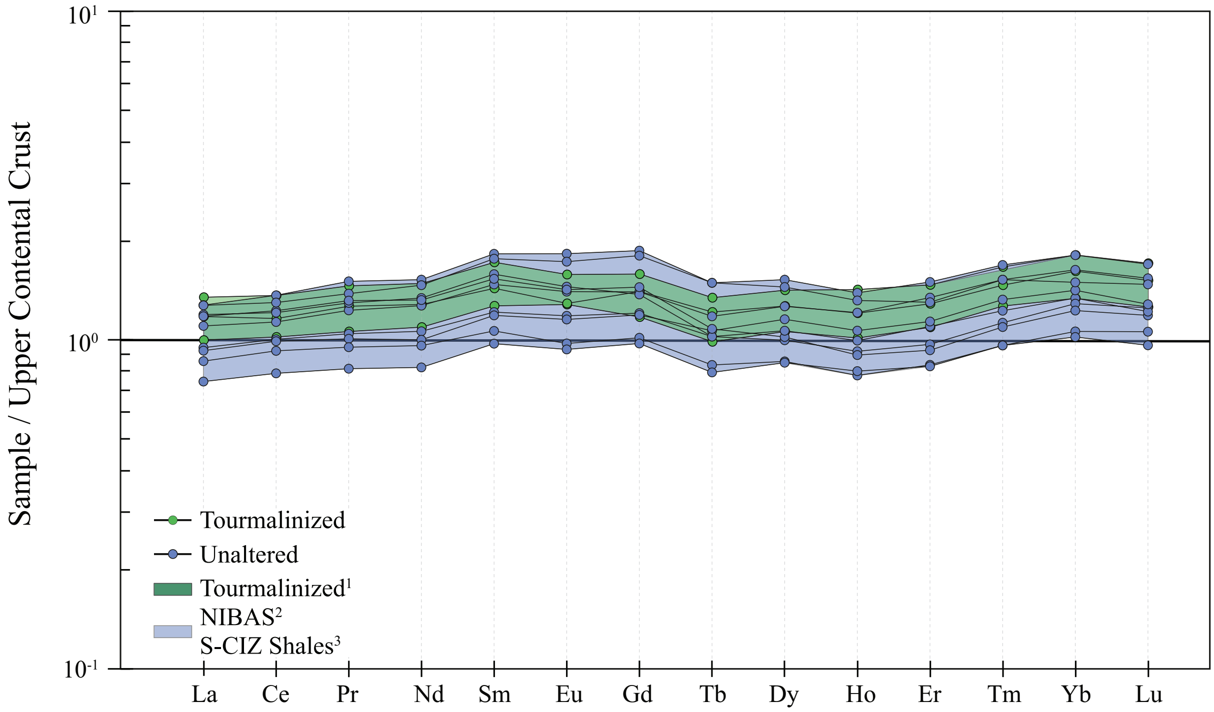

Figure C.1: Rare Earth Elements plot of altered and unaltered metasediments normalized to the Upper Continental Crust (Rudnick and Gao, 2014). Data sources: [1]Pinto et al. (2014), [2]Ugidos et al. (2010), [3]Villaseca et al. (2014), [4]Bussink (1984), and [5]Neiva (1987*a*).

Figures C.2 and C.3 show the comparison between the trace element and REE contents of unaltered metasediments analyzed during this study and the published regional data from Villaseca et al. (2014) and Ugidos et al. (2010).

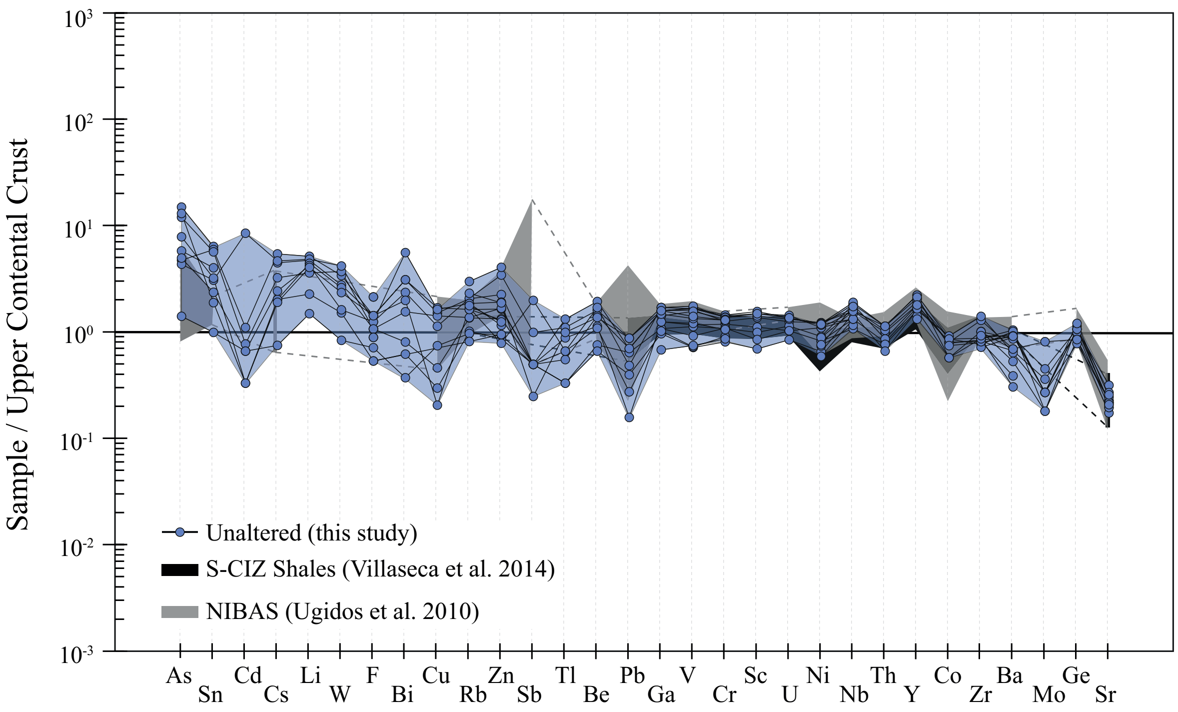

Figure C.2: Comparison between trace element contents of the unaltered metasediments from Panasqueira area and the published data from the Central Iberian Zone. Data was normalized to the Upper Continental Crust (Rudnick and Gao, 2014). Data sources: Ugidos et al. (2010) and Villaseca et al. (2014).

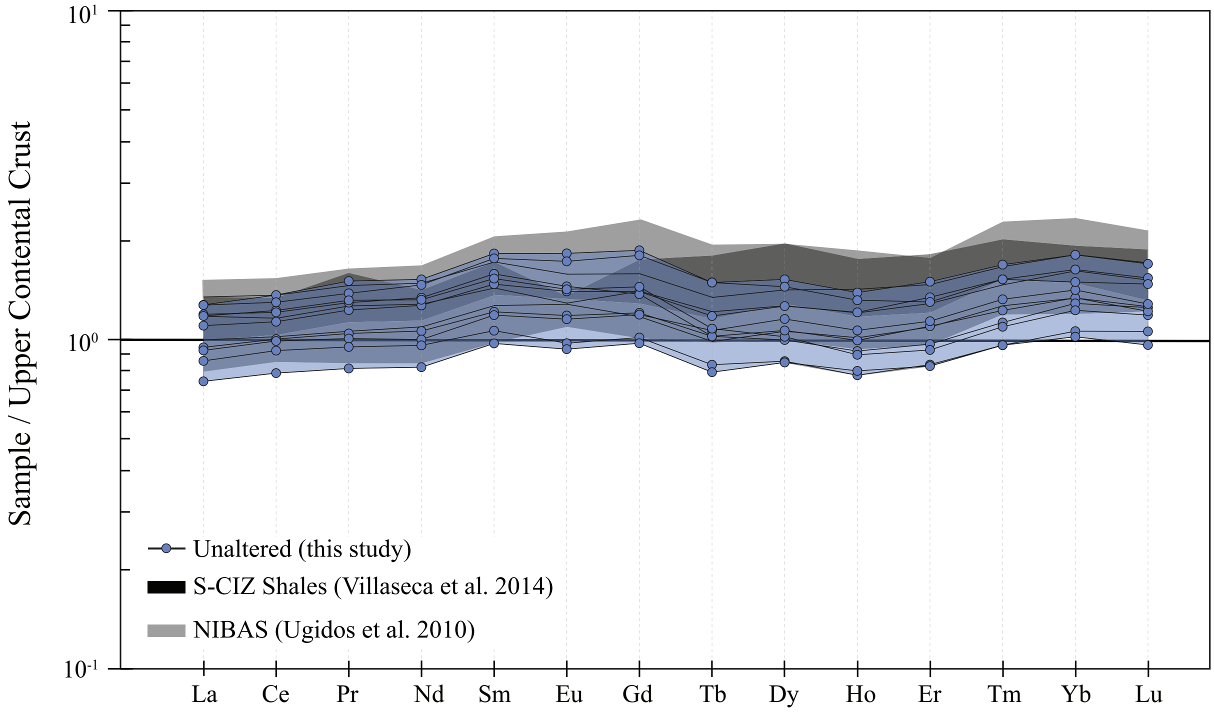

Figure C.3: Comparison of the Rare Earth Elements contents of unaltered metasediments from the Panasqueira area and published data from the Central Iberian Zone. Data was normalized to the Upper Continental Crust (Rudnick and Gao, 2014). Data sources: Ugidos et al. (2010) and Villaseca et al. (2014).

EVERYONE HAS INSIDE HIM A piece of good news. The good news is that you don't know how great you can be! How much you can love! What you can accomplish! And what your potential is!

–*Anne Frank*